Biologically Inspired Acoustic Systems – From Insect Ears to MEMS Microphone Structures

David J. Mackie

Submitted for the degree of Doctor of Philosophy,
August 2015

Centre for Ultrasonic Engineering

Department of Electronic and Electrical Engineering

University of Strathclyde

This thesis is the result of the author's original research. It has been composed by the author and has not been previously submitted for examination which has led to the award of a degree.

Signed: Date:

The thesis work has been published in part and is also under review for publication. The candidate carried out all the experimental work and contributed to all data analysis and writing of the manuscripts.

Signed: Date:

Abstract

Although difficult to notice initially, examples of bioinspired technology have now become commonplace in society today. Construction materials, aerodynamic transport design, photography equipment and robot technology are among many research fields which have benefitted from studying evolution-driven solutions to common engineering problems. One field of engineering research which has recently begun to take inspiration from the natural world is that of acoustical systems such as microphones and loudspeakers. Specifically, to solve the problems involved in the miniaturisation of these systems, the auditory organs of insects are inspiring new design strategies.

In this thesis, one such insect auditory system, that of the desert locust *Schistocerca gregaria*, was extensively studied beginning with a comprehensive review of the historical observations of the system. Micro-scanning laser Doppler vibrometry was then used to characterise the response of the locust ear, providing an explanation for the method behind frequency discrimination in the ear. Afterwards, finite element models, simulating the ear's features, were constructed with a view to furthering the understanding of each component of the hearing system. Directionality of the locust hearing system was also briefly investigated through computational modelling. All of these studies were performed with the overall aim of feeding into the future design of bioinspired acoustic sensors.

Devices constructed using micro-electro-mechanical systems fabrication techniques, with similar dimensions to the ear of the parasitoid fly, *Ormia ochracea*, were then experimentally tested using laser vibrometry and simulated using finite element analysis. Although not originally designed to operate as such, one MEMS structure exhibited some element of mechanical directionality in its response, found to be both predictable and repeatable. The objective of this section of the PhD research was to test the hypothesis that any system with sufficient degrees of freedom is capable of displaying an element of directionality in its vibrational response.

Acknowledgments

First and foremost I would like to express my thanks to my primary supervisor Dr. James Windmill for all of his advice, close support, encouragement and patience throughout my PhD research study. I really appreciate all of the opportunities and resources provided which contributed to a unique research experience. Thank you also to my secondary supervisors Dr. Joseph Jackson and Dr. Anthony Gachagan. Without Dr. Jackson's technical expertise and assistance throughout my practical experiments and data analysis, this thesis would not have been possible.

I would also like to thank the other members of the CUE Bioacoustics team, past and present, in particular Dr. Shira Gordon and Dr. Hannah Moir for their biology expertise and the endless amount of locust-related conversations we had. Thanks also to Andrew Reid and Yansheng Zhang for many helpful discussions about MEMS microphones, a vital part of my PhD project. Although many of the current members of CUE Bioacoustics are relatively new to the Centre for Ultrasonic Engineering, they have all been very encouraging and helpful during my PhD research.

Thank you also to my friends and colleagues within CUE out-with the bioacoustics team and in other research groups, particularly everyone that I have shared offices with and all of the guys and girls from 5-aside football. Thank you to the true engine room of CUE that is Walter, Tommy, Lynn, Rhona and previously Sylvia. Without your help, advice and kind words, my experience would not have been so special. My thanks also to the Friday night crew as by lending an ear or contributing to my leisurely past-times you have all assisted me more than you know. Thank you to the co-authors of my MEMS research publication, Prof. Deepak Uttamchandani and Gordon Brown from the Centre for Microsystems and Photonics, for all of your useful input. Thanks also to Dr. Gerald Harvey of Weidlinger Associates for all of his helpful conversation and assistance with PZFlex finite element modelling.

This PhD research would not have been possible without the help, guidance and patience of Dr. Richard Martin, manager of the ARCHIE-WeSt High Performance Computing facility at the University of Strathclyde.

Un grand merci à Dr. Jérôme Sueur of the Muséum National d'Histoire Naturelle in Paris for providing me with the opportunity to visit on multiple occasions and collaborate with his team, co-authoring the paper on the lesser water boatman. Thanks also to Associate Prof. Damian Elias of the University of California, Berkeley, and all of his team at the Elias lab for two excellent, informative and welcoming experiences.

Thank you to all of my School teachers and University lecturers over the years who have helped me become who I am today. I would like to reserve a special thank you for my Master's thesis supervisor, Prof. Gianluca Oppo, for providing an excellent introduction to the world of academic research.

Thank you to all of my friends, particularly Alistair, Ian, William and Stewart for your interest in my research and your constant encouragement. Thanks also to all of my gym buddies for providing a great atmosphere in which to unwind after long days in the lab or at my desk.

Love and thanks to all of my family, particularly my Mum, Dad, Stephen and Elaine, for all of your love and your kind, supporting and encouraging words – a special mention to my little niece Katie-Louise, my nephew Joseph and their mum Claire Frances.

Last but by no means least, a huge thank you to Solveig for all of your love and your inspirational and motivational words and actions. Without this thesis we would not have met so for that I am most grateful. Merci à ta famille for their kind encouragement and never-ending interest in my research work.

Results in this PhD thesis were obtained using the UK Engineering and Physical Sciences Research Council funded ARCHIE-WeSt High Performance Computer (www.archie-west.ac.uk). EPSRC grant no. EP/K000586/1.

The UK Engineering and Physical Sciences Research Council supported this thesis research via a PhD studentship.

Table of Contents

List of Figures

List of Tables

List of Abbreviations

ARCHIE-WeSt – Academic and research computer hosting industry and enterprise in the West of Scotland

BS – Beam-splitter

CAD – Computer-aided design

CF – Constant frequency

ChF – Characteristic frequency

CNS – Central nervous system

CPU – Central processing unit

dB SPL – Decibel sound pressure level

DOF – Degrees of freedom

EMM – Effective modal mass

EMMF – Effective modal mass fraction

EP – Elevated process

FB – Folded body

FEA – Finite element analysis

FEM – Finite element model or method

FFT – Fast Fourier transform

FM – Frequency modulated

FOI – Frequency of interest

HeNe – Helium Neon

IID – Interaural intensity difference

ITD – Interaural time difference

LDV – Laser Doppler vibrometry

MEMS – Micro-electro-mechanical systems

MO – Müller's organ

MPF – Modal participation factor

PCB – Printed circuit board

PV – Pyriform vesicle

PVC – Polyvinyl chloride

RAM – Random-access memory

RMS – Root mean square

SB – Styliform body

S-C Si – Single-crystal silicon

SEM – Scanning Electron Microscopy

SO – Subgenual organs

SOIMUMPS – Silicon-on-insulator multi-user MEMS process

TDOA – Time difference of arrival

TM – Tympanal membrane

TS – Trichoid sensilla

Chapter 1 : Introduction

"*Those who are inspired by a model other than Nature, a mistress above all masters, are labouring in vain*" - Leonardo Da Vinci

1.1 Introduction

From the observation of wild animals by the earliest humans, in order to hone their hunting and survival skills, to the development of cutting edge sharkskin-inspired swimming suits, bioinspired technology has developed to the point where examples are becoming increasingly common in our daily lives. Benefitting from millions of years of evolution-driven research and development, the natural world has already solved many problems which engineers are still facing today, with solutions often displaying unparalleled efficiency as well as sustainability.

By following the protocol of biomimicry, one such research field which is advancing rapidly is the design, manufacture and testing of biologically-inspired acoustic systems. An extensive range of hearing systems can be observed throughout the animal kingdom, often displaying sensitivity, compatibility with environmental conditions, sophistication and complexity of response, currently unmatched by any synthetically engineered acoustic sensor or transducer. Commonly associated problems such as miniaturisation, directional sensitivity and frequency selectivity are all solved in unique fashion by weird and wonderful creatures.

Since the Italian anatomist Alfonso Corti published his paper “Research on the organ of Corti of the mammalian ear” (Corti, 1851) over 150 years ago, researchers worldwide have explored the physiology and mechanisms active within the auditory system found throughout the animal kingdom. Analysing and modelling these natural systems provides the first step towards the manufacture of cutting-edge acoustic systems.

Fundamentally the auditory system forms one of a number of sensory systems which many organisms use to obtain information about their environment (Dusenberry, 1992). This information or feedback is processed by the animal and may elicit some response mechanism either by the individual or by another. Although the full extent of sensory system evolution and the driving forces for that evolution across the animal kingdom is unknown, it is widely believed that such sensory systems have evolved to perform one or more of the following functions.

The first of these functions, homeostasis, is defined as the use of feedback information (generally from an organism’s external environment) to regulate its

internal environment and maintain an equilibrium state of basic conditions including temperature, position and water content.

Timing of developmental, physiological or behavioural changes typically relies on sensory information from the surrounding environment.

Spatial orientation is another vital function of sensory information and incorporates the use of systems for identification of resources such as food, mates or certain habitats. Some species of bats have developed a highly sophisticated method of spatial orientation, known as echolocation, defined as biological sonar, for the detection of prey. This system used by bats will be briefly discussed in a later section.

Another function of sensory information is to provide protection or defence from threatening organisms, namely predators. In particular, some species of insects, which often fall prey to echolocating bats or other predators, have developed their own truly unique hearing system. Capable of not only detecting the sounds made by hunters (Frings & Frings, 1957; Miller & Surlykke, 2001; Lane et al., 2008) but in some cases tuning to a particular predator (Windmill et al., 2006), these systems are believed to have evolved due to the selective pressures associated with the arrival of new insect-hunting birds and mammals. These insect auditory systems display diverse variety in their morphology and location, dependent on species, and this gives rise to differing evasive manoeuvres and associated behaviour (Sales & Pye, 1975; Robert, 1989; Skals & Surlykke, 2000). Many of these systems are reviewed in **1.4**.

The analysis of the auditory system of one such insect, the desert locust, *Schistocerca gregaria*, is presented in this thesis. After an experimental study of the frequency response of the locust tympana, computational models of the ear are constructed and executed using numerical analysis techniques, with a view to better understanding the mechanisms involved in the observed response of the system. The overall aim is to study the locust ear with a view to directing the future of sensor and transducer technology.

The manufacture of biologically inspired acoustic systems utilises several different methods, whether in the design, fabrication or testing of a sensor or transducer. Fairly recent developments in silicon crystal fabrication techniques have

brought about a shift in miniaturised microphone design towards Micro- Electro-Mechanical Systems (MEMS) technology. The second part of this thesis presents some computational and experimental methods involved in the characterisation of such MEMS structures and considers their potential application as directional microphones.

There follows an introduction to many of the acoustics concepts and a description of the material properties, which are relevant to this thesis.

1.2 General Acoustics

1.2.1 Sound Principles

Loosely defined as a disturbance which travels through space and matter accompanied by an energy transfer, waves are classified as either mechanical or electromagnetic, depending on their origin and propagation method. Mechanical waves require a medium in which to travel and the transfer of energy is achieved through some deformation of the matter of this medium. Electromagnetic waves, which do not require a medium, are out with the scope of this work.

Sound waves are an example of a mechanical wave as they can be thought of as a disturbance in a fluidic medium (often air). This disturbance can be the end result of a vibrating body displacing surrounding air particles from their equilibrium position. Displaced particles collide with those in close proximity causing particle oscillations within the medium. These oscillations give rise to localised regions of increased pressure (compressions) and decreased pressure (rarefactions) through the medium (relative to equilibrium pressure), illustrating the characteristic energy transfer defined as the propagation of sound. The resultant auditory sensation in the ear caused by this disturbance is the basic definition of a sound. Sound waves are said to be longitudinal because the vibration of the particles in the medium is in the plane of the direction of propagation. The alternative wave type is transverse and refers to the situation when the vibration is at 90° to the perceived direction of propagation.

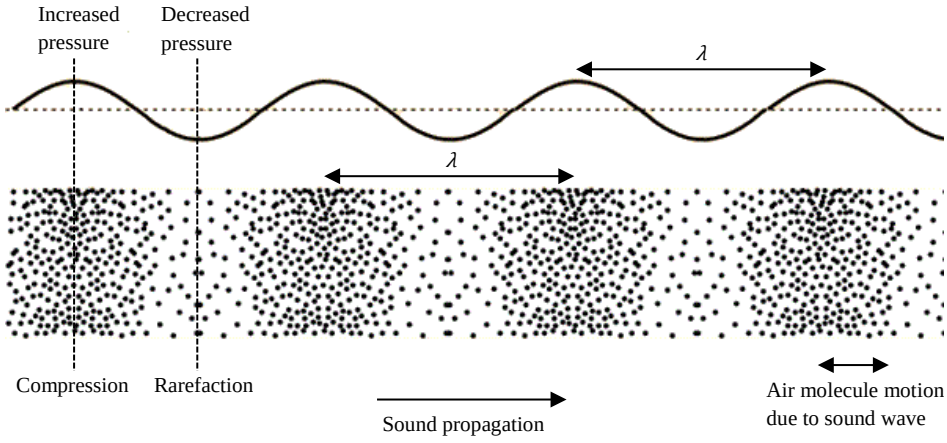

Figure 1.1 Basic illustration of a sound wave (adapted from HyperPhysics web resources http://hyperphysics.phy-astr.gsu.edu/hbase/hframe.html).

The sound field is quantified using two measures: the sound pressure, p (Pa) and the sound pressure level L_p (dB SPL). The former is simply the difference between the localised instantaneous pressure and the ambient or static, atmospheric pressure (1 atm. = 101.325 kPa). Defined as the lower threshold of audition, 20 µPa is used as the reference sound pressure, p_0, for sound propagating through air. In the real world, there exists a huge range of pressures encountered by animals that possess the sense of hearing. Therefore sound pressure level is defined as a base 10 logarithmic ratio calculated relative to p_0 as follows

$$L_p = 20 \log_{10} \frac{p}{p_0}$$

[1.1]

This means 20 µPa (the hearing threshold) is equivalent to 0 dB SPL. Both of these sound field quantities are usually quoted as root mean square (RMS) pressure values and usually also include a distance from the source, often 1 m. It should be noted that p_0 changes to 1 µPa for sound propagating through water.

Sound waves can be simplistically represented as a sinusoid with a measure of amplitude on the Y-axis and time on the X-axis. The peaks in this wave match the aforementioned compressions or areas of high pressure with the troughs corresponding to rarefactions. Fig. 1.1 shows an illustration of this wave. Several characteristics are used to define such a sound wave. The time taken for one complete cycle is known as the period, T (s). The frequency, f (Hz), of this sound is defined as the number of cycles per second and is related to the period by the equation

$$f = \frac{1}{T}$$

[1.2]

The perception of frequency is often known as the pitch of a sound and the human audible hearing range is generally accepted as being from 20 Hz to 20 kHz for a teenager with fully functional hearing.

The speed of sound, v (ms^{-1}), defined as the distance travelled by a sound wave per unit of time, varies depending on the medium of propagation. Since sound must have a medium through which to travel then it cannot propagate in vacuum

conditions. The arrangement of the constituent particles of the medium determines the speed at which sound will propagate and as a general rule sound travels faster through solids than liquids, and slower again through gases. Likewise the exact speed of sound in air is dependent on the temperature, relative humidity, barometric pressure and the fractions of constituent gases (e.g. variations in carbon dioxide content have a slight effect) as each of these can have an impact on air density. Through dry air at a temperature of 20 °C (often taken as room temperature), with a standard pressure of 100 kPa or 1 bar, the speed of sound is approximately 343 ms^{-1}. In comparison, the speed of sound in water at 25 °C is 1493 ms^{-1} or more than four times faster. Sound speed is also known as the group velocity of the envelope of a sound wave.

Defined as a particular point in a waveform cycle, the phase has the symbol φ, and is measured in degrees or radians. Fig. 1.2 shows one cycle of a basic sinusoid with phase on the X-axis. The wavelength is defined as the distance, in metres, between two consecutive points at the same phase of the cycle and has the symbol λ (the wavelength is labelled in Fig. 1.1). The above definitions for frequency, speed and wavelength of sound mean that they are all related through the universal wave equation

$$v = f\lambda. \qquad [1.3]$$

This means that for a sound wave propagating through an isotropic medium, i.e. at constant velocity, the frequency and wavelength are inversely proportional to each other.

The term frequency response is often used to describe the investigation of a particular vibrating object, either computationally or experimentally with both biological and artificially created specimens. In the case of vibrating bodies, it is simply a measure of the amplitude of vibration with respect to a range of operating frequencies.

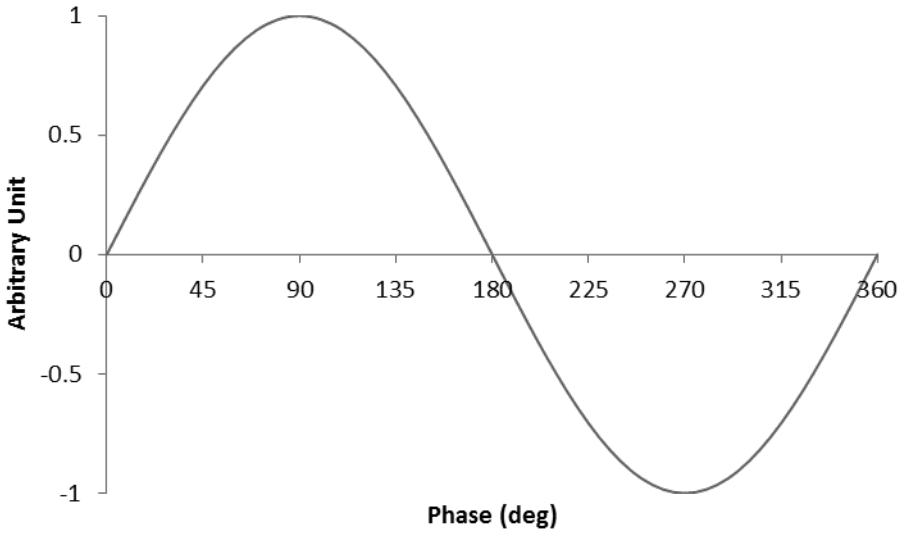

Figure 1.2 Basic sinusoid displaying phase along the X-axis.

1.2.2 Sound Wave Phenomena

As with all waves, sound waves exhibit the phenomena of reflection, refraction, diffraction and interference. All of these phenomena may take place when a sound wave encounters an interface between different media or approaches an obstacle. The extent of which each occurs is dependent upon the wavelength (and therefore frequency) of the sound, the size of the obstacle or interface boundary and the characteristic acoustic impedances of the media at each side of the interface. Additionally the characteristic specific acoustic impedance, Z (rayl), of a material is directly proportional to both the density ρ (defined later in ***1.3.1***) and speed of sound in the medium according to the equation

$$Z = \rho v.$$

[1.4]

Reflection of sound follows the same law of reflection as is defined in optics, i.e. for an incident sound wave reflecting off a stationary surface, the angle of incidence is equal to the angle of reflection (both angles being measured with respect to the surface normal (line perpendicular to the surface at the point of reflection)). An assumption is made that the incident beam of sound, the normal to the surface and the reflected beam are all coplanar.

When sound propagates across the interface from one medium of specific acoustic impedance to a medium of different impedance, there will be a corresponding change of speed usually with an accompanying change in wave propagation angle. From [1.4], if the sound travels from a lower to higher impedance medium then, for equally dense media, the speed will increase and according to [1.3] there will be a decrease in the wavelength of sound (frequency remains constant as it is dependent on the sound source). The relationship between the angle and speed of sound propagating from medium 1 into medium 2 follows Snell's Law

$$\frac{\sin\theta_i}{\sin\theta_r} = \frac{v_1}{v_2}$$

[1.5]

where θ_i and θ_r are the angles of incidence and refraction respectively.

When two or more coherent sound waves of comparable amplitudes propagate simultaneously through the same volume of a medium, e.g. an incident

wave and reflected wave, interference effects are observed according to the principle of wave superposition. The resultant wave is the point-wise sum with amplitude dependent on the instantaneous individual component wave amplitudes which are a function of the relative phase difference(s). The term constructive interference is given to the effect when two or more component waves have phase difference equal to some integer multiple of 2π and this results in the production of positive and negative maxima due to the superposition of two wave crests or two troughs. The opposite is termed destructive interference and occurs when the phase difference between two waves is some odd multiple of π, i.e. the crest of one wave meets the trough of the other and vice versa. Superposition in this circumstance results in a local minimum. The phase difference at a particular point is dependent on the difference in the distances between sources and that point (known as path length difference) and the wavelength of the sound. The corresponding pattern of maxima and minima is known as an interference pattern and this is also the basis behind optical interferometry as mentioned in the description of laser Doppler vibrometry in **2.1**.

When a sound wave meets an object or an opening then reflections and scattering cause a complex spatial arrangement of the original sources and, effectively, newly-created sound sources. If the wavelength of the sound is of the order of magnitude of the dimensions of the object then an interference pattern will form according to the phenomena mentioned above, manifesting itself as a pattern of reflections and diffraction fringes of maximum and minimum intensity. When the wavelength is much larger than the object dimensions then the corresponding diffraction pattern indicates that the sound has all curved around the object or through the opening. Therefore the word diffraction is used to define the way that waves curve around obstacles or through gaps in their propagation path. Sounds of wavelength shorter than an obstacle's size will reflect more than diffract, often resulting in a partial or full acoustic shadow behind the object. Echolocation using high frequency (therefore short wavelength according to [1.3]) ultrasound makes use of this very concept. Longer wavelength sounds will diffract more (or pass more easily) around the object in their path. These four phenomena introduced above have

major implications in the field of acoustics when applied to hearing, especially in sound localisation.

The theory of Helmholtz reciprocity also holds for acoustic waves i.e. the path of any sound wave travelling through linear, homogeneous media, undergoing any of the aforementioned phenomena, will perfectly match that of the same wave in the opposite direction. All other things remaining constant, switching the locations of a sound source and a receiver will make no change to the perceived sound at the receiver.

As mentioned previously, a vibrating object surrounded by a fluidic medium would act as a sound source. A spherical sound source, such as a sinusoidally pulsating sphere, will radiate equally in all directions and is therefore known as an omnidirectional acoustic monopole with a simple spherical directivity pattern.

Two monopoles of equal magnitude but opposite phase, some small distance apart, constitute an acoustic dipole source. This source shows a more complicated figure of eight directivity pattern. Quadrupole sound sources can also be constructed using two different configurations of dipole sources, resulting in characteristic directivity patterns with four lobes.

An important observation is made when either a sound source, a sound-reflecting body or a detector of sound move in space relative to one or both of the others. There becomes an apparent shift in the frequency of the sound, as detected by the receiver. If we assume the source and receiver are the same object and remain stationary, as is the surrounding medium of air, and the only moving object is the reflecting body, then this frequency or Doppler shift (after Christian Doppler, the physicist who first studied the concept now known as the Doppler effect) is proportional to the magnitude and direction of the velocity of the vibrating reflector. As is the case with many of the acoustic phenomena described here, this same observation can be made in the case of a source, receiver and reflector of light.

As sound propagates through a medium there is an attenuation of the sound pressure directly proportional to the distance from the source. Viscosity, density, pressure and fluctuations in the medium’s velocity all impact on this attenuation. For 3-D spherical spreading in a free field the sound pressure is proportional to the reciprocal of the distance from the source (in addition to any viscous losses). The

attenuation of propagating sound also displays frequency dependence which becomes particularly significant for higher frequencies such as ultrasound since higher frequency sound experiences greater viscous losses in the fluid medium.

Two regions exist with regards to sound sources and receivers: the near-field and the far-field. In relation to a sound source, the near-field is the region extending from the source boundary to some distance less than one wavelength of the sound. Within this region near-field sound can be thought of as a complex interference pattern of localised fluid motions, not characteristic of the normal propagation of sound. When the distance from a source is very much greater than the ratio of the wavelength to 2π, then far-field assumptions are made, whereby sound propagates according to the aforementioned basic principles and phenomena. This region extends infinitely and within it the sound is assumed to be travelling as a plane-wave.

1.3 Mechanical Properties and Structural Characteristics

1.3.1 Physical and Mechanical Properties

To analyse the vibrational patterns associated with a particular behaviour or response of a system, a number of material properties are important. These properties will of course depend on whether the material is homogeneous or nonhomogeneous. Isotropic materials are defined as those with uniform material properties in all directions. Conversely if the properties of a material vary systematically in a directionally dependent manner then the material is termed anisotropic.

The first important property, the volumetric density of a substance, is defined as its mass, m (in kg) per unit volume, V (in m^3), and is given the symbol ρ (kgm^{-3}).

$$\rho = \frac{m}{V} \qquad [1.6]$$

Density is dependent upon the temperature and pressure of the surrounding environment since they have a potential effect on the volume through increasing or decreasing the kinetic energy of the particles in the matter, thus affecting the particle distribution. The density of water is around 1000 kgm^{-3}, of Polyvinyl Chloride (PVC) is about 1300 kgm^{-3} and of iron is about 7860 kgm^{-3} (all at room temperature and pressure of 1 atm.). Vincent and Wegst (2004) found the density of insect cuticles to range from 1000 to 1300 kgm^{-3}.

Vibrational deflection as a result of incident sound waves is a type of mechanical strain caused by an engineering stress. The stress, σ (Nm^{-2} or Pa), is usually defined as the instantaneous applied load (F in N) divided by the initial cross-sectional area of the specimen under load (A_0 in m^2)

$$\sigma = \frac{F}{A_0} \qquad [1.7]$$

For a 3-D cube of material, the applied force, and therefore stress, may be in a number of different directions including normal to a face or in the plane of a face, with a component in a particular axis direction. Fig. 1.3 shows such a cube, with the possible stresses σ_{ij} defined according to the integers i and j which correspond to the surface and axis direction respectively.

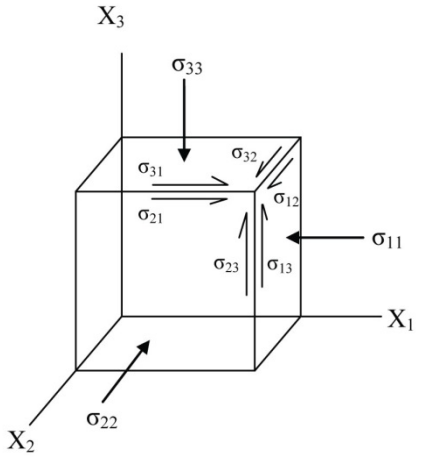

Figure 1.3 Cube of material showing possible normal and in-plane stresses and their corresponding indices.

The stress tensor for this cube is then defined as

$$[\sigma_{ij}] = \begin{bmatrix} \sigma_{11} & \sigma_{12} & \sigma_{13} \\ \sigma_{21} & \sigma_{22} & \sigma_{23} \\ \sigma_{31} & \sigma_{32} & \sigma_{33} \end{bmatrix}$$

[1.8]

Defined as the ratio between the change in length, Δl (m) of a specimen (in the same direction as the applied stress) and its original length, l_0 (m), the strain, ϵ (dimensionless), is calculated as

$$\epsilon = \frac{\Delta l}{l_0}$$

[1.9]

In the linear regime, the force, F, required to extend or compress a spring by a certain distance (x), is proportional to that distance. Known as Hooke's law this can be denoted as

$$F = kx$$

[1.10]

where k is known as the stiffness constant. This is applicable only to the elastic deformation of linear isotropic materials. If the deformation distance, x, is Δl from above, then substituting for F and x results in

$$\frac{F}{x} = k = \frac{\sigma A_0}{\epsilon l_0}$$

[1.11]

Cross-multiplying results in

$$\frac{Fl_0}{xA_0} = \frac{\sigma}{\epsilon} = E$$

[1.12]

where E (Pa) is the modulus of elasticity, or Young's modulus. This constant is often used as a measure of a material's stiffness or resistance to elastic deformation. The Young's modulus of a perfectly elastic, linear and isotropic material is usually defined as the ratio of stress to strain. Therefore Hooke's law can be interpreted as a direct proportionality between the strain of a material and the stress applied to that material. A material which obeys Hooke's law is often known as Hookean.

The Young's modulus of metals ranges from about 30 to 800 GPa (Callister, 2007). For bone this value tends to be 18 – 70 GPa (Wainwright, 1976) and for polymers such as PVC, E is between 1 and 4 GPa (Callister, 2007). Klocke and Schmitz (2011) reviewed insect cuticle mechanical properties and found the modulus of elasticity of cuticle from 11 orders of insect species ranged from 1.5 to 20 GPa. Wainwright (1976) reported the cuticle of the tibia of the locust as having a Young's modulus of 9.5 GPa, based on Jensen and Weis-Fogh (1962). Rubbers and mammalian skin are at the lower end of the spectrum when it comes to stiffness with elastic moduli in the range of 0.02 – 100 MPa (Callister, 2007; Agache et al., 1980; Gennisson et al., 2004; Liang & Boppart, 2010; Volandri et al., 2011).

When an object, consisting of isotropic material, undergoes a tensile stress in the Z-axis direction there is a corresponding strain, ϵ_z, in the same direction. This elongation usually causes constrictions in the X-axis and Y-axis directions orthogonal to the initial applied stress. In turn these contractions have associated compressive strains ϵ_x and ϵ_y. Assuming the stress is applied uniaxially then these strains are equal to each other, i.e. $\epsilon_x = \epsilon_y$. There exists a ratio, defined as one of the lateral strains divided by the axial strain, known as Poisson's ratio, ν.

$$\nu = -\frac{\epsilon_x}{\epsilon_z} = -\frac{\epsilon_y}{\epsilon_z}$$

[1.13]

Since ϵ_x and ϵ_z are usually of opposite sign, the negative sign is included to 'force' ν to be positive. Theoretically, for perfectly isotropic materials Poisson's ratio should

be exactly 0.25. Known as the incompressible limit, the maximum value of ν is 0.5, at which point there is no net volume change. Rubbers are often very close to this value whereas many metals and alloys have a ν ranging from 0.25 to 0.35, e.g. steel is 0.3 (Callister, 2007).

Anisotropic materials such as crystalline elements or compounds have slightly more complex material properties since the structural alignment of the crystal must be taken into account. To describe direction-dependent properties in 3-D crystal structures we must first consider the notification used for crystallographic planes and directions. Miller indices are used, consisting of three-integer triples, "*hkl*" which correspond to the XYZ Cartesian coordinate system. These are used to describe a direction or also a plane perpendicular to the direction. They are calculated by taking the reciprocal of the coordinates of the intercepts on the XYZ-axes and then simplifying by the lowest common denominator. For symmetrical crystal lattices, there exist groups of equivalent directions or planes which are called families. Miller indices are used to describe a number of concepts associated with crystallography, some of them explained in Table 1.1. Equations [1.9 – 1.11] above describe Hooke's law for isotropic materials however in the case of anisotropic materials, material properties differ in all of the X-, Y- and Z-axis directions. In these circumstances the elastic modulus from equation [1.12] becomes a fourth rank tensor, with 81 terms, called the stiffness matrix.

Notation	Meaning
[*hkl*]	Direction vector with components *h, k* and *l*
<*hkl*>	Family of symmetric direction vectors equivalent to *hkl*
(*hkl*)	Crystal plane orthogonal to vector *hkl*

Table 1.1 Selected Miller index notation for crystallography applications.

The properties introduced above are defined for a class termed the elastic materials whereby deformation is time independent i.e. strains due to stresses are assumed to be instantaneous. Most real materials display some form of anelasticity or time-dependent elastic response behaviours, particularly those which display viscoelasticity, including many polymeric and biological materials. Processes in the micro- and atomic scales are often time dependent, resulting in time dependent

deformation behaviour. Time and temperature affect the stress/strain behaviour of such materials, with concepts such as stress relaxation and hysteresis common.

1.3.2 An Introduction to Insect Cuticle – Material Properties and Microstructure

Insect integument is often subdivided into an epidermis layer and two layers of cuticle, the epicuticle (outermost layer) and the procuticle. The epidermis is the innermost single layer of cells responsible for the secretion of cuticle as the insect makes the transition from larval stage, through the nymphal instars, to imago or adulthood.

Epicuticle is a layered complex which can be divided into four parts: the outer cement layer, a waxy layer, the outer epicuticle and the inner cuticle. Proteins and lipids with polyphenols for stability constitute the hydrophobic cement layer and its function is believed to be protection of the underlying wax layer. The wax layer is a layer of lipidic hydrocarbons present for the purpose of cuticular transpiration and waterproofing. Cuticulin is the name given to outer epicuticle and it is universal in the insect world. Lining the finest tracheal tubes, called tracheoles, and being a part of muscle insertion points are the main presence of this laminar membrane. Also laminar in structure, a layer called the inner epicuticle is believed to be responsible for cuticle surface repairs.

Procuticle is the name given to the largest fraction of insect cuticle and in general its microstructure normally has three main constituents: a matrix of chitinous nanofibres, structural proteins and very rarely deposited calcium usually as calcium carbonate. Apart from in the cases of insect eggs, chitin is a structural component of all cuticles. With the chemical name poly-β-(1,4)-N-acetyl-D-glucosamine, this polysaccharide is closely related to cellulose in chemical properties. It is a crystallographic structural polymer consisting of packed nanofibres with an estimated stiffness of upwards of 150 GPa. However in reality chitin is viscoelastic in nature with its stiffness and extensibility displaying time-dependence i.e. a variation with deformation rate. The orientation of the microfibrils within the chitin in a particular section of cuticle is, of course, of great importance to the structural properties of the part of the insect's body where that cuticle is located. In the cuticle, chitin is always embedded within or closely tied into some form of protein matrix. The best-known of these proteins is called resilin which is analogous to rubber in many of its properties such as having a Poisson's ratio very close to the

incompressible limit of 0.5. Rubber-like cuticle has been discovered in the locust, consisting of heavily-hydrated resilin, a thicker layer of lamellae of solid chitin, all covered by thin epicuticle.

It should be noted that insect cuticle is a very difficult material to characterise, particularly because it is a complex composite material displaying a varied microstructure throughout the whole insect body. Although many textbooks and research papers have attempted to investigate the microstructure of different forms of cuticle in relation to the material and mechanical properties (Jensen & Weis-Fogh, 1962; Uvarov, 1966; Neville et al., 1976; Wainwright, 1976; Michel & Peterson, 1982; Blum, 1985; Vincent & Wegst, 2004; Liu et al., 2006) much has still to be discovered in this subfield including the construction of material models incorporating all of the aforementioned constituents and their properties, new methods for practical testing of cuticle mechanical properties and potentially even undiscovered cuticle compositions. The complexities and difficulties in analysing the cuticle of a particular insect body part, e.g. a sensory organ, are reflected in the modelling of insect systems since material property determination becomes problematic. In addition, many structures and regions of an insect body consist of specialised cuticles with unique properties suited to their required function. One such sensory organ is the locust's tympanal hearing system.

1.3.3 Analytical Eigenmodes of Clamped Circular Disc

Theoretically a circular plate which is fixed circumferentially and vibrating *in vacuo* has infinitely many eigenmodes or natural shapes of vibration, each having a corresponding eigenfrequency (or natural frequency). Fig. 1.4 below shows the first six of these modes with yellow representing areas of zero displacement, red for displacements towards the reader and green for vibration away from the reader, as seen on the side profile images above/below the corresponding plan view. This same red-outwards/green-inwards displacement convention is used throughout the thesis. Simple eigenmode analyses such as this, with no consideration of damping or loading, do not allow for a comparative investigation of the amplitude of deflection at each mode. However the amplitudes of the characteristic nodes within one particular mode can be accurately compared. Darker shades of red or green indicate greater amplitudes of displacement e.g. the darker red peak left of centre on mode 6 vs. the lighter red C-shaped peak on the right of the disc – see side profile of mode 6.

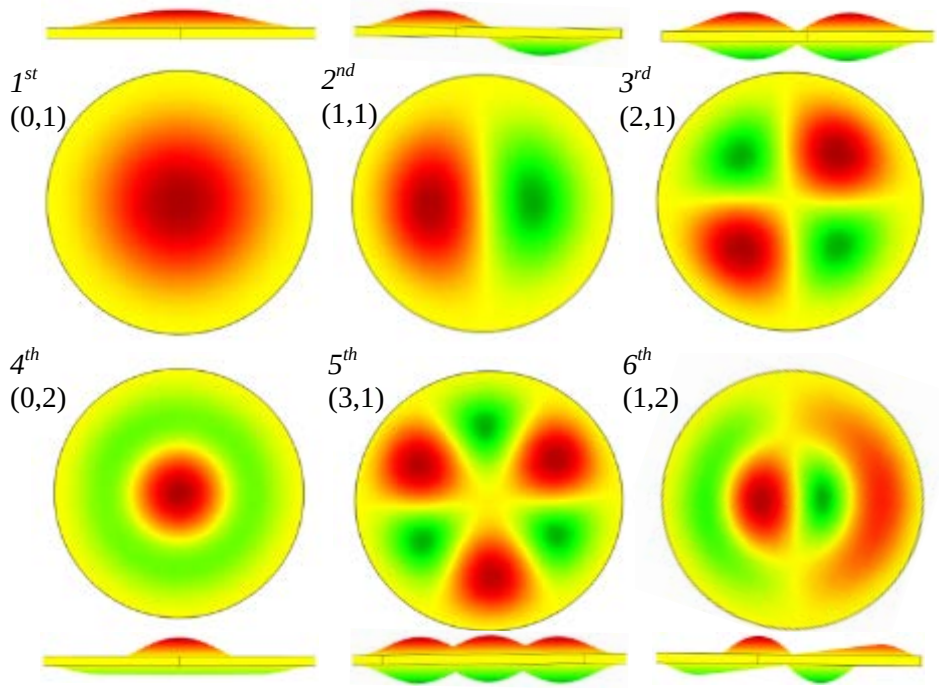

Figure 1.4 First 6 eigenmodes of ideal circular disc shown in plan view and side profile with mode numbers (number of nodal diameters, number of nodal circles).

Two concepts are used to describe such vibration patterns: the nodes, which are areas of constant zero displacement (yellow above); the antinodes which are areas of maximal deflection (darkest green and red). Nodes can be either a nodal circle e.g. around the perimeter of mode 1 or between the two antinodes in mode 4, or a nodal diameter e.g. the yellow line through the centre of mode 2. Every mode is designated a mode number (d, c) where d is the number of nodal diameters and c the number of nodal circles. The mode numbers for the first 6 modes are in Fig. 1.4.

Leissa (1969) studied the vibration of plates for various shapes with a selection of boundary conditions and concluded that the eigenfrequencies, ω_e, of a solid circular plate with circumferential clamping could be calculated using the formula

$$\omega_e = \frac{\lambda_e^2}{r^2}\sqrt{\frac{Eh^2}{12\rho(1-\nu^2)}} \qquad [1.14]$$

where λ_e is the eigenvalue, r the disc radius, E the Young's modulus of the plate material, h the thickness of the plate, ρ the density of the plate, and ν the Poisson's ratio. Part of the expression under the square root sign is defined as the flexural rigidity, D, where

$$D = \frac{Eh^2}{12(1-\nu^2)} \qquad [1.15]$$

Leissa tabulated λ_e^2 for a number of modes using Airey (1910), Carrington (1925) and Blanch (1952) as sources. Gorman et al. (2001) then used this data to calculate theoretical values for the first six eigenfrequencies of a clamped circular plate of radius 0.038 m, thickness 0.00038 m, Young's modulus 2.1×10^{11} Pa, density of 7800 kgm^{-3} and Poisson's ratio of 0.3, shown in Table 1.2.

Eigenmode	Eigenfrequency (Hz)
1^{st}	671.8
2^{nd}	1398
3^{rd}	2293
4^{th}	2615
5^{th}	3356
6^{th}	4000

Table 1.2 Theoretical eigenfrequencies of first 6 modes of a uniform circular plate with defined radius, thickness and material properties (Gorman et al. 2001).

These values can then be used to predict the natural frequencies of any isotropic linear circular plate, fixed circumferentially, assuming no damping or external loads.

1.4 Auditory Systems

1.4.1 Mammalian Hearing

1.4.1.1 The Human Ear

Corti's inaugural study documented the discovery of a "hearing organ", now known to be the core sensory component of the cochlea, a major part of the inner ear. This finding lead to other anatomists such as Reissner (1854), Deiters (1860) and Hensen (1863), among others, discovering components of the inner ear which they eventually gave their name to. The inner ear plus two other main sections, the outer (or external) ear and the middle ear constitute the mammalian hearing system, see Fig. 1.5. These are now examined briefly in the following Subchapter.

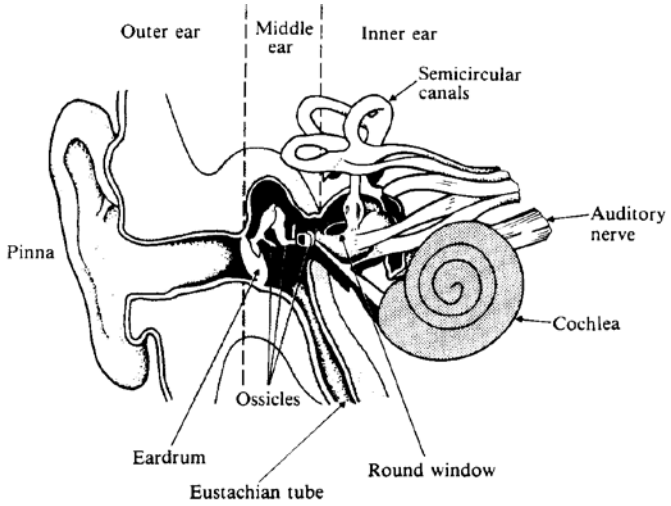

Figure 1.5 Schematic of human ear. From http://personal.cityu.edu.hk/~bsapplec/thehuman.htm.

Two substructures, the pinna (or auricle in humans) and the external auditory canal (meatus), make up the outer ear in the majority of mammals. The outer ear, as a whole, acts as a signal conditioner (Evans, 1992), emphasising frequencies of relevance to the species.

First, the pinna, the fleshy visible 'ear', is designed to funnel incident sound through the auditory canal. Both the ear canal and the physical structures of the head and external ears transform the spectrum of sound (Mehrgardt & Mellert, 1977; Musicant et al., 1989; Middlebrooks, 1999). With the auditory meatus acting as a resonator, a range of frequencies can be significantly amplified (Wiener & Ross,

1946). The bandwidth for a particular species (frequency range of sounds which an animal can hear) corresponds to sounds which are of biological relevance, i.e. may be used in interspecific communication or in some cases by potential predators.

Pinnae shape and size can vary considerably, e.g. among species of bats there is a belief that the unique structure of the pinna is a reflection of different echolocation behaviours (Vater & Kössl, 2004). Some bats (and other vertebrates) have incredibly mobile pinnae, capable of behaving as mobile directional acoustic antennae (Guppy & Coles, 1988; Obrist et al., 1993). Conversely some animals including echolocating cetaceans (whales, dolphins etc.) and some insectivorous mammals actually have no identifiable pinnae (Ketten, 1994).

The air-filled middle ear contains three tiny bones, the malleus (or hammer), the incus (or anvil) and the stapes (stirrup), collectively called the ossicles. These are bounded by the eardrum or tympanic membrane, located between the malleus and the internal end of the auditory canal, and the oval window on the inner side. “The function of the middle ear is to resolve the acoustic impedance mismatch between the air in the ear canal and the fluid of the inner ear.” (Fay et al., 2005). The process of transduction begins at the drum where sound pressure in the ear canal is converted into vibrations of the ossicles.

A number of factors contribute to the tympanic membrane’s efficiency as a transducer. Having developed a computer simulation of the meatus, eardrum and ossicles, Fay et al. (2006) concluded that at high frequencies, a cone-shaped eardrum transfers more force to the ossicles than a flat eardrum. In addition, the tilt of the eardrum within the canal allows a much larger area for the same canal size, increasing sound transmission to the cochlea. They also found that at high frequencies, optimal transmission is achieved by the creation of many intentionally mistuned resonances. Theoretically, at frequencies at and close to resonance the sensitivity of the eardrum will be at a maximum however because of the number and close proximity of the natural frequencies, the sum of these resonances at the malleus attachment results in a smooth transfer of pressure across all relevant frequencies.

The inner ear lies beyond the oval window and consists of a complex multi-chambered cavity containing the semicircular canals (important for balance but not involved in hearing) and the transduction centre of hearing, the cochlea. Shaped like

a snail shell, the cochlea has three membranous coiled tubes and is surrounded by a bony shell. The tubes are called the scala vestibuli, scala tympani and scala media respectively. The scala vestibuli and tympani contain a liquid called perilymph, whose ionic composition resembles that of other extracellular fluids. These two scalae have membrane-covered windows which open into the middle ear. In the scala vestibuli, the oval window is where the footplate of the stapes (one of the ossicles of the middle ear) lies. The scala tympani begin at a membrane covered window known as the round window. The scala media, lying between both vestibuli and tympani, is where the organ of Corti lies. This organ contains endolymph, a fluid with high potassium concentration, sustaining a large positive electrical potential. It also contains the basilar membrane on which Von Békésy (1960) observed the generation of different travelling waves which have propagation distances and shapes displaying a dependence on frequency. Three response characteristics are outlined below for a travelling wave on the basilar membrane of the mammalian cochlea (Robles & Ruggero, 2001).

Criterion 1: an increasing displacement phase lag is observed whereby the motion of the medium is increasingly lagging the motion of the point of origin, as the wave propagates across the membrane. This phase lag is also proportional to the stimulus frequency, i.e. increased stimulus frequency results in an increase in the phase lag.

Criterion 2: the envelope of the magnitude of the tympanum displacement is asymmetric around the area of maximal deflection, with the leading edge of the envelope steeper than the trailing edge. This point of maximal deflection coincides with where the wave compresses at its point of termination.

Criterion 3: the cochlear travelling waves are passive in that they are governed by the mechanical properties of the medium through which they propagate, i.e. mass, stiffness and damping.

Below the basilar membrane lie two types of hair cells, inner and outer, which are capable of transducing mechanical vibrations into receptor potentials. These receptor potentials lead to the “generation of action potentials in type I auditory nerve fibers” (Robles & Ruggero, 2001), resulting in the transmission of processed information from the cochlea to the brain. The outer hair cells have also

been shown to be capable of producing mechanical energy or self-oscillating and are therefore termed active, rather than passive, oscillators.

Two mechanisms have been proposed for frequency discrimination in vertebrate ears:

- The place principle where anatomical groups of receptor cells have different characteristic frequencies and therefore provide the central nervous system (CNS) with frequency information;
- Telephone principle at low frequencies when phase information may be encoded in nerve impulse trains.

Research into the workings of the inner ear is still very much on-going. In reality, due to the complexity of the active processes, mechanotransduction and neurology involved in hearing, constructing a model which fully and accurately describes the ear, has proven to be an arduous task. As a result, the development of our understanding of the auditory system is not nearly as advanced as that of the visual system.

1.4.1.2 Bat Echolocation

As mentioned previously, several species of bats have a complex, highly skilled method of spatial orientation, known as echolocation. This involves the emission of brief ultrasonic calls, or clicks, through either the nostrils or mouth. A spectrotemporal analysis of the reflections of these clicks from objects surrounding the bat, allows the animal to effectively navigate in complete darkness. Certain species can even accurately locate and successfully hunt their prey – small nocturnal insects such as moths.

A bat's gaze is defined as "the region of the environment a subject explores with the senses" (Ghose & Moss, 2006) and since this varies between species, the specific sonar call design including upper and lower frequencies (usually in the range of 20 kHz – 110 kHz), call duration and duty cycle also varies accordingly. Additionally, it follows that a particular bat's hearing system is tuned to the particular frequency range it uses to echolocate. If the echolocating calls are used for prey detection, the call design will match the physical characteristics of the prey, thus maximising the chance of successful capture. A higher frequency call (and therefore smaller wavelength) improves resolution however this is contrasted by a decrease in detection distance, due to greater attenuation.

From differences in perceived echo arrival time, intensity and spectrum, to both ears, the horizontal and vertical position of objects can be computed, sometimes even with sub-millimetre accuracy. Ulanovsky and Moss (2008) categorise echolocating bats into one of three types, based on their call or pulse design. FM (frequency modulated) bats use FM calls with durations 0.5 – 20 ms and this type is most common among all species. Constant frequency (CF) bats include several Microchiropteran bat species. With pulse durations of tens of milliseconds, the bats estimate target motion by analysing the Doppler shifts of the echoes. The final echolocation call design type belongs to bats of the genus *Rousettus* and they use very brief ultrasonic clicks, similar in nature to the biological sonar used by whales and dolphins and typically lasting 40 – 50 μs.

Due to the degree in which echolocating bats have honed their spatial orientating and prey detecting skills, a number of insects have developed hearing systems capable of detecting bat calls and use evasive manoeuvres to avoid capture.

1.4.2 Insect Hearing

1.4.2.1 General Insect Hearing Organs

The trend for auditory research rapidly extended into the invertebrate world in the beginning of the twentieth century with Schwabe (1906) being one of the earliest to study the morphology of the ear of Orthopteran insects (the order to which the locusts, grasshoppers and crickets belong). Insects are the most abundant and diverse class of animal in the world, with over one million species known and many more yet to be discovered and classified. Having existed on earth for approximately four hundred million years, it is reasonable to assume that a particular insect species has evolved to not only survive, but thrive in their varied and ever-changing environment (Grimaldi & Engel, 2005). Influenced by such selective pressures as changes to natural habitat or the requirement for new systems of predator detection and evasion, it is widely believed that several insect orders' sensory organs have developed to suit the needs of the species. Therefore it is logical that researchers of auditory systems would desire to investigate the links between the morphology, neurophysiological response and mechanical response of insect ears along with any associated behavioural responses.

An insect's well-evolved sensory organs are called mechanoreceptor organs, to which various types of auditory organs belong. Mechanoreception is broadly defined as the perception of any mechanical distortion of the body (Chapman, 1998) and specifically in the case of hearing, the detection of mechanical vibrations caused by sound propagating through the surrounding medium (usually air or water) which is incident on the insect.

Insect auditory systems may be used for intra-specific communication i.e. finding a mate or assisting with swarming behaviour, for predator detection and evasion and for localisation of prey. Due to the numerous different environments inhabited by different species, the auditory organs for a particular species are located in different positions of the body. Fig. 1.6 is a schematic diagram of a generalised insect showing 10 body locations for receptors believed to be organs of hearing.

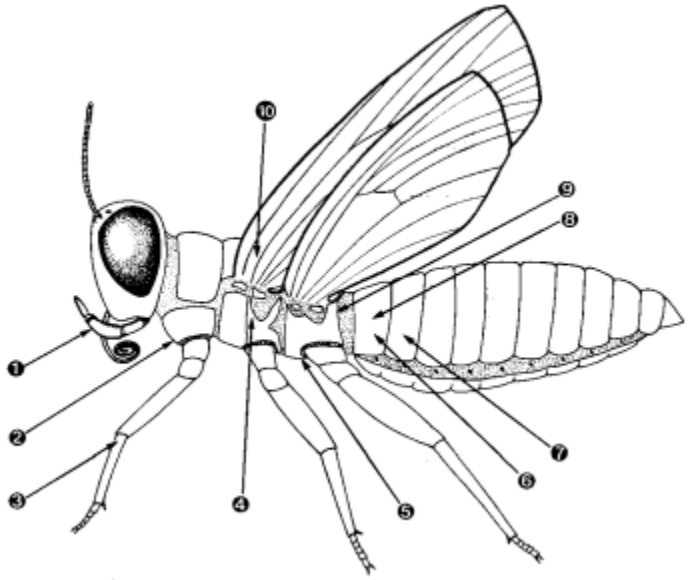

Figure 1.6 Generalised insect diagram showing 10 possible positions of auditory organs in different insect species (from Yack & Fullard, 1993). 1. – Lepidoptera: Sphingoidea, Choerocampinae, 2. – Diptera: Tachinidae, Ormiini, 3. – Orthoptera: Ensifera, 4. – Hemiptera: Corixidae, 5. – Mantodea: Mantidae, 6. – Lepidoptera: Geometroidea, Pyraloidea, 7. – Hemiptera: Cicadidae, 8. – Orthoptera: Acrididae, 9. – Lepidoptera: Noctuoidea, 10. – Neuroptera: Chrysopidae.

Yack (2004) reviewed the four main types of hearing organs which have been observed in insects: trichoid sensilla (TS), Johnston's organs, subgenual organs (SO), and tympanal organs (TM). These four hearing organ types are illustrated in Fig. 1.7 and further explained in this review.

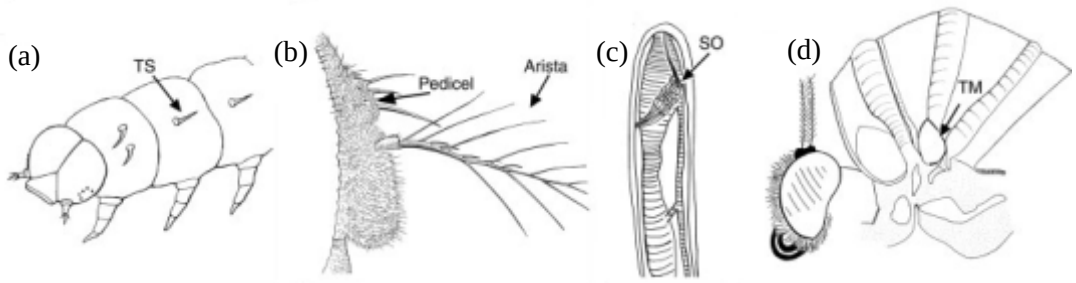

Figure 1.7 Four types of insect auditory mechanoreceptor organs (adapted from Yack, 2004). (a) Trichoid sensilla, (b) Johnston's organ, (c) subgenual organ and (d) tympanal organ.

Some species of caterpillar (including the caterpillar of lepidopteran moths in Fig. 1.7(a)) have trichoid sensilla located on their thorax. These are projections of cuticle, hair-like in shape, which usually have one or more bipolar nerve cells at their

base. Designed to vibrate in response to the air currents associated with sounds propagating through the surrounding medium, these usually act as simple near-field auditory mechanoreceptors.

Most insects have a non-connective chordotonal organ called Johnston's organ (Fig. 1.7(b)), located at the base of their antenna. The function and size of this organ varies significantly between species. Capable of detecting near-field sounds produced by the wing beats of conspecifics, the Johnston's organ is very complex in certain Dipteran flies including mosquitoes, midges and fruit flies. With up to 16,000 sensory cells in a mosquito's Johnston's organ, the antennae are extremely sensitive. The organ can even exhibit frequency selectivity as well as active sensory phenomena such as input amplification and self-generated oscillations (Göpfert & Robert, 2001; Göpfert & Robert, 2003; Jackson & Robert, 2006). Even the less sensitive female mosquito's Johnston's organ responds to antennal deflections of just ±0.0005° which are induced by ±11 nm air particle displacements in the sound field (Göpfert & Robert, 2000).

In the proximal tibia of each leg of most insects lies a subgenual organ (Fig. 1.7(c)) used primarily to detect substrate vibrations. This organ appears to be of importance to lacewings for mate-searching purposes (Devetak, 1998). Several species of insects are very sensitive to solid-borne vibrations including ants, cockroaches, crickets and wasps. Very little is still known about the function or structure of such mechanoreceptor organs across the insect species.

The last of the four known insect mechanosensory organ types is the tympanal organ (Fig. 1.7(d)). Insect tympanal ears consist of three main parts: the internal tracheal air sac, the tympanal membrane (TM) covering the sac and a mechanosensory organ with groups of sensilla, coupled to the membrane in some way. Pressure changes associated with a sound wave cause the tympanum to vibrate. The tympanal sensory organ is responsible for transducing this mechanical signal into neural signals. Specially shaped sensory cells, called chordotonal sensilla or scolopidia, are contained within the sensory organ.

Some species of moths and butterflies (Lepidoptera) have tympanal hearing organs that display a relatively simple morphology in comparison with other TM containing insect orders, e.g. they have fewer auditory receptor cells. However the

response of the organ is comparable to those insects with more complex organs with higher numbers of sensilla (Coro & Kössl, 1998). Röder (1966) concluded that the position of the two auditory organs of moths may allow directionality to be computed. Many moth ears are sensitive to the ultrasonic echolocating calls of insectivorous bats and moths have been observed making evasive manoeuvres when simulated bat calls are played.

Windmill et al. (2007) studied three species of noctuid moths and their corresponding tympanum vibrations in response to a variety of frequencies. When stimulated at high frequency (greater than 20 kHz), an area of the membrane called the opaque zone, where the scolopidia attach, vibrated with a greater displacement than the rest of the membrane. It was also found that a moth's auditory organs can tune up by mechanically changing sensitivity to higher frequencies, when they detect a hunting bat's calls. In fact they can remain tuned for a short period of time after, believed to be in case of an immediate return by a predatory bat (Windmill et al., 2006).

Compared with many other species which possess tympanal organs such as the noctuid moths and scarab beetles (Forrest et al., 1997), the locust auditory system has a slightly higher number of sensilla. However, locust tympanal systems appear relatively simple morphologically and overcome the common engineering problem of impedance mismatch whereby they are externally located i.e. in contact with surrounding air, and yet backed by air too. Additionally many interesting phenomena are displayed by the locust hearing system. The following subsection is a detailed review of the anatomy, morphology and response of the locust tympanal hearing system.

1.4.2.2 The Locust Tympanal Organ

The morphology of the ear of two different locust species (the desert locust, *Schistocerca gregaria* (Forskål), and the migratory locust, *Locusta migratoria* (Linnaeus)) has been well studied since the beginning of the 20th century (Schwabe, 1906; Pumphrey & Rawdon-Smith, 1936; Autrum, 1941; Gray, 1960; Horridge, 1960; Popov, 1965; Michelsen, 1966 & 1971a, b & c; Stephen & Bennet-Clark, 1982; Robert, 1989; Meyer & Hedwig, 1995; Jacobs et al., 1999). There follows an introduction to the desert locust and an overview of the ear structure and corresponding operation in response to incident sounds.

The desert locust, *Schistocerca gregaria* (Orthoptera: Acridoidea: Acrididae – Fig. 1.8) displays polyphenism, existing in two phases: solitarious and gregarious which depend on population density.

Figure 1.8 Adult desert locust in gregarious phase. Scale bar = 1 cm.

Desert locusts exist in the solitarious phase when the population density is low, however local changes in the distribution of vegetation can be enough to induce a spike in the locust population density. This can lead to prolonged physical contact between locusts which in turn drives the switch to the gregarious phase. Characteristics of the phase change include behavioural changes such as a move from slow short distance travel (and any long-distance flights done nocturnally) to increased diurnal activity. Morphological, physiological and appearance changes also take place. Mature adult solitary locusts are pale yellow (also displaying pale green and beige, depending on sex) whereas mature adult locusts in gregarious phase are bright yellow and dark brown when sexually mature and are also slightly smaller in body size (Ott & Rogers, 2010; Gordon et al., 2014). The dark patches on desert

locusts in the gregarious phase are believed to be a product of increased melanin production (Uvarov, 1966). Male desert locusts exhibit a bi-lobed subgenital plate, hence the Latin name *Schistocerca* meaning split-tail.

Adult desert locusts of each gender have a pair of tympana located laterally on their first abdominal segment (Fig. 1.9). Except when in flight, the tympana on either side are usually covered by their adjacent forewing.

The tympanal membrane has been described as both pear-shaped (Gray 1960) or bean-shaped (Fig. 1.10) and approximately 2.5 × 1.5 mm in size at its widest. Conversely Pumphrey and Rawdon-Smith (1936) described the ear of *Locusta migratoria* as a thin oval disk about 1.5 mm × 1 mm in size.

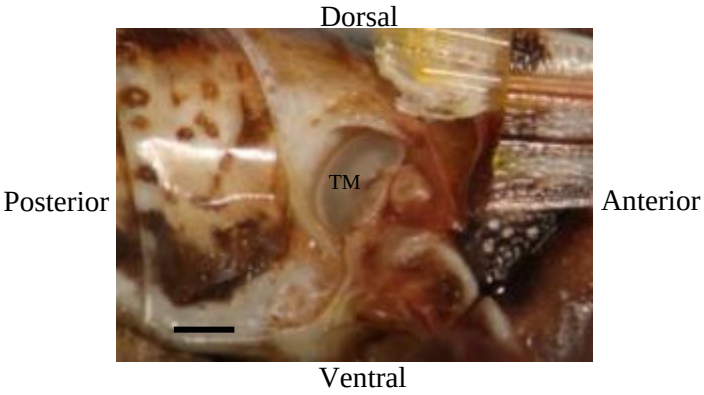

Figure 1.9 External right side first abdominal segment of *Schistocerca gregaria* with wings clipped, showing tympanum. Scale bar = 1 mm.

Fig. 1.10 shows that the membrane is reniform and has a rim of sclerotised cuticle which projects laterally, forming a shell-like structure around the posterior edge of the membrane. This shell, and the corresponding recess formed because of the slightly angled tympanum, have drawn comparison with both the fleshy pinna and auditory meatus of the ears of many mammalian species. No previously published studies have used numerical modelling techniques to investigate the function of this shell until the study in ***4.5.2*** of this thesis.

Externally in *Locusta migratoria* the sclerotised exocuticle surrounding the tympanum forms a flap which is similar in shape to the human tragus, projecting backwards covering about one third of the whole tympanum. The *Schistocerca* tympanal hearing system does not have this flap present.

Located anteriorly and in close proximity to the tympanum there is a respiratory spiracle with a connection to the system of tracheal air sacs behind the membrane. Gray (1960) suggests that this spiracle is perhaps analogous to the Eustachian tube present in the mammalian hearing system (see Pumphrey, 1940).

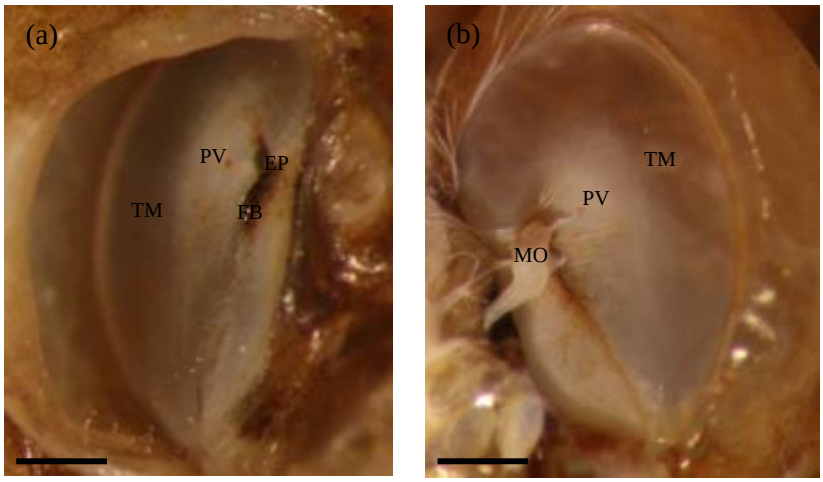

Figure 1.10 (a) External and (b) internal view of right side desert locust tympanal system. Scale bars = 0.5 mm. Pyriform vesicle, PV, is the darker spot visible externally and internally. FB is the dark folded body with the opening of the elevated process, EP. MO is the body of Müller's organ visible internally.

Two distinct areas of cuticle form the entirety of the membrane – the transparent thin region and the more opaque thicker region, with the latter located ventro-anteriorly from the former. These two areas are sometimes regarded as two different membranes and thus given the name thin membrane and thick membrane.

The tympanal membrane cuticle consists of three distinct layers usually given the names endocuticle (innermost layer), mesocuticle (middle layer) and exocuticle which is often described as sclerotised or tanned. The mesocuticle is reported to be impregnated with proteins or lipids leading to smaller interstitial spaces and a stiffer cuticle. The exocuticle is described as stiff and brittle (Stephen & Bennet-Clark, 1982). Spanning the interior face of the tympanum there is an epithelial layer of cuticle which is epicuticle of the air sac directly behind the membrane (also called a hypodermal layer). This layer is believed to be around one cell thick. Pumphrey and Rawdon-Smith (1936) quoted the thickness of the whole TM as varying from 0.5 µm at the posterior margin to 11 µm anteriorly. Gray (1960) described the tympanal membrane of *Locusta* as being approximately 2 to 3 µm thick apart from one thicker ventro-anterior area which is four times as thick. Spines about 1 to 2 µm long are

also visible on the TM cuticle. Stephen and Bennet-Clark (1982) used histology to construct a contour map of the systemic variation in thickness seen in the locust TM. The authors found the thickness to vary from a 0.5 – 0.6 µm thin arc-shaped region near the attachment to the shell to a maximum of 20 µm at the most ventro-anterior edge. More recently, Malkin et al. (2013) used focussed ion beam milling to etch slits into the TM after mounting and coating with gold using plasma-enhanced chemical vapour deposition. Measuring the thickness from the images captured at five of these slits they reported a value of 100 nm in the thin region of the membrane. This value increased to a range between 0.3 µm to 5 µm when moving ventro-anteriorly towards the PV. Etching a slit through the apex of the PV, the authors found the thickness there to be 15 µm.

Four specialised regions of sclerotised cuticle are visible on the membrane, providing the attachment sites for the internal mechanosensory organ. Michelsen (1971b) described three of these areas as “not just simple thickenings of cuticle”. The first of these, commonly called the folded body (FB), is a complex rigid plate of thicker sclerotised cuticle. Along the lateral edge where this cuticle body attaches to the thicker membrane, there is a fold and then the body becomes thinner eventually forming a ridge and a rod-shape continuation in the ventral direction. This ridge creates a boundary between the thick and thin regions of the whole tympanum. The shape and size of the folded body are shown on Fig. 4 of Stephen and Bennet-Clark (1982) and estimating using the scale bar it is approximately 800 µm long and 300 µm at its widest. Interiorly the FB protrudes approximately 70 µm from the membrane surface.

The second specialised region is called the elevated process (EP) and is an invagination protruding internally perpendicular to the TM to a depth of 100 µm. The EP is hollow and has been described as having a stretched cup shape or tubular, and lined with tuberculate cuticle, much thicker than any TM cuticle. The orifice of the EP is at the TM surface and at the bottom of the recess of the EP some non-spinous convex projections have been observed. The sclerotised cuticle of the EP and FB merge ventrally. Internally the EP appears to provide a strong connection between the external tympanal membrane and internal sensory organ.

The third sclerotised region of cuticle providing attachment between the membrane and the sensory organ is the styliform body (SB). Gray (1960) observed the SB as having a flattened concave surface. One end of the body widens to envelope part of the EP. Again the SB stands perpendicularly to the TM and Michelsen (1971b) described its form as an hour-glass as it has a wider neck near the EP which then narrows ventrally like a leg before widening again into an egg-shaped foot – a sclerotised plate of TM cuticle. Estimating from Stephen and Bennet-Clark (1982) the egg-shaped foot is approximately 300 x 200 μm in size. The cuticle is slightly thicker around the area of the styliform foot at the connection of the SB to membrane.

The fourth and final region of specialised cuticle is the pyriform vesicle (PV) and is the smallest of the four sclerites. Of Latin origin, pyriform means pear-shaped, and the PV is the one sclerotised region of the tympanal system that is a fairly simple thickening of the eardrum cuticle. Located about 250 μm from the orifice of the EP, the PV is connected to the body of the main internal sensory organ via the fusiform body which is a stretched ellipsoid in shape. Stephen & Bennet-Clark (1982) found a thinner region of cuticle, oval in shape, around the location of the PV.

These four specialised regions culminate in the main cell body called Müller's organ (MO) seen in Fig. 1.10, named after Johannes Peter Müller, the 19th century German anatomist. This end-organ (Schwabe, 1906) or ganglion (Gray, 1960) has been reported to contain anything between 60 and 120 sensory units or scolopidia, with 80 being the most widely reported figure. Michelsen (1971b) described the *Schistocerca gregaria* MO as being of irregular shape but if the main cell body is approximated as a prolate spheroid, Stephen and Bennet-Clark (1982) estimated it as being 400 × 200 μm at its maximum. Contrastingly Gray (1960) estimated the ganglion of the tympanal ear of *Locusta migratoria* as being 250 μm long and 150 μm at its widest. Internally, as well as the MO, there is also a series of three tracheal air sacs acting as protection for the auditory system, with one air sac in direct contact with the internal side of the membrane. It has been estimated that about 10 of the MO's sensory units attach to the FB (the so-called 'c' cells), 35 to the EP (the 'a' cells), 12 to the SB ('b' cells) and about 8 to the PV ('d' cells). Each scolopidium consists of three cells, one of which is called the scolopale cell. The

scolopales of the ‘a’, ‘c’ and ‘d’ cells have been observed to be arranged in mutually perpendicular planes with the ‘b’ cells in the same plane as the ‘a’ cells. Often, due to the close proximity of the ‘a’ cells in the EP to the ‘c’ cells in the FB, they are treated as just one group making a total of three groups of sensory units.

In *1.4.1.1* the two principles behind frequency discrimination in the mammalian ear were introduced. The place principle (cochlear hair cells are arranged tonotopically) is believed to be the main phenomenon underpinning frequency discrimination across the whole sensitive frequency range of the human ear with the telephone principle (CNS is sensitive to phase information of a sound wave) being significant only for low frequencies, less than 2 kHz. Early research into invertebrate hearing systems found no evidence of the use of place principle or in fact any frequency discrimination. Many neurophysiological studies have since been implemented on the frequency sensitivity of the sensory cells attached to the locust tympanal membrane. For pure tone stimuli from 500 Hz to 11 kHz, Pumphrey & Rawdon-Smith (1936) tested threshold sensitivities using electrophysiology. At 3 kHz the whole system was observed to display a maximum in sensitivity with the authors recording a threshold just 20 dB SPL above that of human hearing which is remarkable for an insect ear of such simple appearance. One major finding of this study was the lack of synchronisation between neural response and the frequency of the stimulus. This led to the conclusion, in line with the understanding of insects at the time, that the locust tympanal hearing system was incapable of frequency discrimination.

It was not until over twenty years later when Horridge (1960) measured electrophysiological activity from the auditory nerve of the locust tympanum and found evidence that the locust may in fact possess the ability to discriminate between frequencies. This led to work by both Popov (1965) and Michelsen (1966) leading to the publication of a three part study by Michelsen (1971a, b & c) on the physiology of the locust ear covering tympanal sensory cell frequency sensitivity in an excised ear, drum resonance-based pitch discrimination of the TM and the application of these findings to the ear *in situ* along with the acoustic influence of the whole body.

As mentioned previously the sensory cells in the locust tympanal system are allocated into three or four distinct groups. Michelsen opted for the four group, ‘a’ –

‘d’ notation mentioned previously. Pure tone stimuli with frequencies ranging from 0.5 – 30 kHz and sound pressure levels from 96 – 112 dB SPL were used throughout the three studies. In the first study electrophysiological recordings were made from each cell location, measuring the threshold sensitivity and calculating the average characteristic frequencies (ChF) of each cell type. It should be noted that the ears were isolated from the locust body by a fairly substantial surgical procedure.

The author found the ‘a’ cells, located in the region of the EP, to have an average first ChF of approximately 3.7 kHz, lying between 3.5 – 4 kHz for all ‘a’ cells measured. Another maximum was observed in the sensitivity response of many ‘a’ cells near 8 kHz with others displaying this maximum at 6 – 7 kHz or not at all.

Attached to the SB, the ‘b’ cells were recorded as having a ChF of around 3.4 kHz and displayed another maximum at 8 kHz as was the case for the ‘a’ cells. For around half of the ‘b’ cells tested another smaller maximum in sensitivity was observed at approximately 5 kHz.

Located in close proximity to the FB, most ‘c’ cells displayed high sensitivity to 1.5 kHz as well as a uniformly high sensitivity in the range of 2 – 3.5 kHz. A small number of units also displayed sensitivity to pure tone sounds of frequency in the region of 8 kHz, as was the case for the aforementioned sensory cells.

The last of the four sensory cell groups, the ‘d’ cells, with attachment to the PV, were found to be most sensitive across the range of frequencies from 10 to 14 kHz, with a ChF of 12 kHz. A second maximum appeared around 19 kHz in most ‘d’ cells and the sensitivity here was observed to be as high as at the 12 kHz peak. The observation was made that the sensitivity of ‘d’ cells showed significant drop-off at frequencies lower than 10 kHz and greater than 30 kHz, therefore the cell sensitivity is analogous to the function of a band-pass filter. Finally, ChF’s of all of the cells were observed to move significantly upwards as a function of the dryness of preparation.

The position and sensitivity of the mechanosensory cell units of the locust ear were revisited nearly thirty years later and the cell groups were reclassified slightly along with some changes in frequency ranges of sensitivity (Jacobs et al., 1999). Locusts were stimulated using single frequency pure tones between 100 Hz and 40 kHz at sound pressure levels of 35 to 90 dB SPL. Neurobiotin was used to mark

sensory cells and intracellular electrophysiological recordings were made of each cell type. The authors reported that, across the whole auditory range of the locust, maximum sensitivity is in the region of 2 to 5 kHz. Additionally a slight response was even observed for frequencies as low as 200 Hz for some sensory cells. The first cell unit type, named "Group I", was attached to the FB and consisted of around 20 cells in total. These low frequency detectors were found to be relatively insensitive having a ChF of 1.5 kHz and displaying a second maximum in the range of 400 to 700 Hz. All group I cells remained sensitive to frequencies up to 4 kHz and a few remained sensitive beyond this up to an upper limit of 10 kHz. Type II cells of which the authors counted 12 to 14, connect to the PV via the aforementioned fusiform body. These cells had ChF's in the region of 12 to 25 kHz and displayed broadband sensitivity tuned to frequencies between an upper limit of 40 kHz and lower limit of 4 to 7 kHz. The final sensory cell type, group III, linked to either the region of the EP or the SB, has a ChF of around 3 – 4 kHz. Electrophysiological recordings by Jacobs et al. found most examples of the third cell type to be narrowband low frequency receptors sensitive to sounds between a minimum of 2 kHz and a maximum of 10 kHz. No observation of the subdivision of this third cell type into two distinct groups (as previously reported) was made, leading the authors to classify locust ear mechanoreceptor cells into just three groups.

Michelsen (1971b) and Stephen & Bennet-Clark (1982) have both published data on either the estimated and/or measured masses of many features of the locust tympanal system including the TM itself along with the mass of cell bodies in the MO and FB. This data is collated in Table 1.3, with reference 1 being Stephen (1982) and 2 being Michelsen (1971b). 'Thin' corresponds to the mass of the thin region of the membrane plus the cells attached to this area. 'Thick' refers to the mass of the thick section of the membrane plus the cells. TM is the sum total of thin and thick (including cells). System mass is the sum of the whole TM (plus attached sensory cells) and Müller's organ.

Type	Estimated and Measured Masses / µg					Ref
	Thin	Thick	TM	MO	System	
Est	10.1	10.7	20.8	8.5 - 12.5	29.3 - 33.3	1
Est	10.8				40 - 45	2
Meas	7.7 aver.				30 aver., 50 max.	2

Table 1.3 Published data on masses of components of the locust hearing system. Reference 1 is Stephen & Bennet-Clark (1982) and reference 2 is Michelsen (1971b).

Michelsen (1971b) used the data in rows 2 and 3 above to estimate some of the resonance frequencies of the TM. These estimates were based on the existence of a thin membrane vibrating independently of the entire TM, therefore two sets of resonance frequencies were calculated, one for the thin membrane and another for the whole tympanum. A circular uniform thickness homogeneous membrane of effective radius 0.9 mm was assumed to be the thin membrane and only the circularly symmetric modes were considered. This yielded a fundamental mode of frequency 3.4 kHz for the thin membrane and frequencies of 8.1 kHz, 12.9 kHz and 17.9 kHz for the second, third and fourth circularly symmetric modes respectively. 1 mm was taken as the effective radius for the entire TM resulting in frequencies of 1.8 kHz, 4.2 kHz, 6.6 kHz, 9 kHz, 11.4 kHz, 13.8 kHz, 16.2 kHz and 18.6 kHz for the first eight circularly symmetric modes. The author reported close correlation between the observed frequencies of sensitivity of the receptor cells and the expected resonance frequencies however the observation was made that in the audible range of the locust there exists a large number of expected resonances therefore sensory cell selectivity could be an issue due to competing modes in the frequency range of sensitivity.

Laser holography has been used to observe the vibration shapes of the isolated locust TM in response to the same pure tone stimuli with frequencies ranging from 0.5 – 30 kHz and sound pressure levels from 96 – 112 dB SPL as previously (Michelsen, 1971b). Although capable of measuring the amplitude of vibration of the locust TM, the limited sensitivity of this method imposed the requirement for fairly high sound pressure levels, with the resulting measured displacements of the order of micrometres. These sound pressure levels are quite extreme, perhaps beyond the limit of the biologically relevant range for the locust. Considering the reported TM thicknesses, the measured amplitude of displacement is also alarmingly high. Additionally, laser holography provides no method of

quantifying temporal information therefore the phase of the vibration pattern is incalculable. Therefore, in conjunction with the holography, a dual platinum wire capacitance electrode was also used to measure the vibration of the isolated TM. Although measuring the absolute value of the displacement was impossible with this method, when used along with a reference microphone, the phase of the displacement relative to the source could be extracted. Similarly to laser holography, this method had limited sensitivity along with a total uncertainty rising from ±10° at low frequencies to ±20° at frequencies of about 15 kHz upwards. The author observed fairly close correlation between the measured resonant frequencies and the estimated frequencies mentioned previously, for both the thin membrane vibrations and the modes of the entire tympanum. However, a number of observations were made which appear to differ from the author's hypothetical idea that the TM response is due purely to the circularly symmetric modes of two separate membranes. Firstly, the antinode or centre of vibration was not always located at the geometrical centre of the membrane, as is the case for a theoretically ideal membrane. Great variation was found in the spatial location of the centre of vibration for changing frequency, both for the thin membrane and the entire tympanum vibrations. Secondly, Michelsen found the areas covered by maximal vibrations to be smaller than expected, with some vibration patterns localised only to small regions of the TM. Finally, some mode shapes were measured which appeared irregular and these did not fit theoretical predictions. However, the presence and frequencies of these modes appear to suggest an influence by asymmetric modes of the TM system on the overall vibrational response. Nonetheless, the author concluded that the locust tympanal hearing system is both a true resonance system and that frequency discrimination by the locust depends solely on the physical attributes of the ear. Also concluded was that the overall response is determined by interactions between the thin membrane vibrations and the vibrations of the entire membrane, with the thin membrane dominating across the whole frequency range.

Locust TM vibration patterns were also examined using stroboscopic illumination which was capable of recording both amplitude and phase data of the response of excised tympana. The same technique was also applied to analyse the motion of MO attached to the interior of the TM (Stephen, 1982). Maxima were

observed on the TM at frequencies of 3.25 kHz and 5.5 kHz with a relative minimum between the two and the former being the absolute maximum of sensitivity for the system, observed on locations on the TM, FB and SB. Rapid changes in phase were observed at both 5.5 kHz and beyond 6.5 kHz, believed to indicate potential resonances in the proximity of these frequencies. The TM vibrations corroborated previous findings using laser holography (Michelsen, 1971b). The authors calculated 0.58 kHz as an estimate of the resonant frequency of MO (based on rough dimensions and mass mentioned above) and using stroboscopy, they observed several complex vibrations and rotations of MO and the cuticular attachments to the TM. Simulations on the estimated natural frequency and the motion of MO have never been published prior to this research work. For frequencies from 2 to 5 kHz, the magnitude of the motion of MO relative to the motion of the TM clearly decreased as the frequency increased. However one limitation of this study was the narrowband response of the loudspeaker, practical only for the range from 1.75 kHz to 8 kHz. Additionally the sensitivity of stroboscopy was such that sound pressure levels were required to range from 102 dB SPL to 132 dB SPL, again perhaps extending beyond the range of biological relevance for the desert locust.

A more relevant sound stimulus of 60 dB SPL (equivalent to a sound pressure of 20 mPa) was later used in two studies of the mechanical response of the locust using micro-scanning laser Doppler vibrometry (LDV) (Windmill et al., 2005; Windmill et al., 2008). This sound pressure level was pre-conditioned to remain relatively flat across a wideband frequency sweep (or chirp) from a lower frequency limit of 1 kHz to an upper limit of 30 kHz. The earlier study concentrated on the frequency response of the locust, i.e. measuring the amplitude of vibration in the frequency domain. Acoustic impulses were then used as a new stimulus in the more recent research paper, which addressed the transient response of locust tympanum vibrations. Capable of measuring vibration amplitudes in the range of picometres, LDV is described further in **2.1**. Crucially the experimental setup for both papers ensured tympanal deflections remained within the linear regime. Additionally, the aforementioned studies were performed on fully intact locust ears, with excision of the wings being the only procedure implemented on all locust subjects, which remained alive throughout the main experimental procedure.

The first highlighted finding was increasing amplitude of vibration in the location of the PV as a function of frequency. Diffractive acoustics were postulated to be a cause of fluctuations in the response amplitude in the range of frequencies from 10 – 30 kHz, which corresponds to a wavelength range of approximately 3.4 – 1.1 cm respectively. Since this wavelength range is of the order of locust body dimensions one would expect the body to act as a partial barrier causing a complex mix of reflections, scattering and diffraction as the sound waves impinge on the body.

Four frequencies of interest (FOI's) were highlighted by the authors of the first paper: 3.3 kHz, 6.1 kHz, 12.21 kHz and 22.76 kHz. Rather than the standing wave patterns seen previously on the locust TM, travelling waves were observed to form at each frequency. With origin on the thin membrane, the waves propagated from left to right across the tympana when viewed externally as the ear is in Fig. 1.10. Dissipation of the waves was seen to occur at different locations dependent on frequency. At the lower FOI, 3.3 kHz, the wave extended beyond the PV to the FB. At the next FOI, 6.1 kHz, the approximate propagation direction was the same as at the lower frequency only the wave spreads a little more dorsally and ventrally forming a dual-peaked ridge with maxima dissipating at the EP and SF. 12.21 kHz and 22.76 kHz were the final two higher FOI's with the authors reporting a semi-concentric deflection shape at the location of origin in the thin membrane before travelling across the TM, converging to a much sharper peak spread across a smaller surface area which diminished at the location of the PV. This semi-concentric shape was not seen at the lower frequency range between 3 kHz and 7 kHz. At the two higher frequencies the TM deflection of the areas beyond the PV towards the FB was significantly smaller than at locations across the remainder of the membrane (and at the lower frequencies).

Notably, the authors reported no correlation between the angle of incident sound and the propagation path of the travelling waves i.e. the path direction at each frequency remained constant for all sample locusts throughout the study. Using the three travelling wave characterisation criteria, outlined in *1.4.1.1*, the locust TM travelling waves were compared to the cochlear travelling wave. In reference to criterion 1, an increase in stimulus frequency was reported to result in an increase in

the observed phase lag between the initiation point of the wave and the terminal point. The leading and trailing edge of a travelling peak were not always observed to be symmetrical particularly around the vibration maxima i.e. the envelope of the wave was asymmetrically shaped. To investigate the third and final criterion, the authors measured the tympanal deflection of dead desert locusts and compared the frequency response to that observed in live locusts. No difference in response was recorded between either of the sample groups across multiple stimulus frequencies indicating that no underlying physiological mechanisms are responsible for the locust TM travelling wave formation and propagation. Observing the deflection of the locust tympanum at one cycle phase angle, e.g. 0°, and comparing it to the deflection shape of the travelling wave after 180° in wave cycle phase shows that the second half of a travelling wave cycle is an inverted mirror image of the first with TM areas displaying positive displacement becoming equal but opposite negative displacement and vice versa.

In the more recent of the two papers, Windmill et al. (2008) used LDV to measure the vibration across 380 points on the whole TM with high spatial resolution and plotted the average gain response vs. frequency. The stimulus for this experiment was the same wideband chirp as before. A maximal peak was observed at around 24 kHz. Large peaks were also found at approximately 7 kHz, 10.8 kHz, and 12.5 kHz. Two smaller peaks were seen at 4.4 kHz and 19.9 kHz. The authors then allocated five points, A to E on the external surface of the TM, where the amplitude gain (in μmPa^{-1}) vs. frequency was found to display variable responses. Point A was located dorsally on the thin transparent area of the membrane, i.e. bottom left when looking at Fig. 1.10, point B at the PV and C was dorsal to the foot of the SB, i.e. in the top right region of the TM. Points D and E were on or near the FB with D at the ventral tip and E very near the EP. Points C, D and E showed no relative response beyond 10 kHz. The amplitude of the gain response at E was significantly smaller than at the other points and just two peaks were observed, the first at around 2 kHz and second slightly larger peak at 7 kHz. At point D, a double peak was observed with equal magnitudes at about 2 kHz and 4.4 kHz along with a relatively small peak at 5 kHz. Just one peak was observed at C, at 4.4 kHz, with a noticeable response between 5 kHz and 10 kHz. Several response maxima were found at point B including a high at

4.4 kHz and two peaks of almost equal sensitivity at approximately 7.5 kHz and 10.76 kHz. Smaller response spikes appeared at around 2 kHz, 12.5 kHz, 19.85 kHz and 24 kHz. Finally, point A displayed a maximum sharp double peak at 5 – 6 kHz as well as responses to frequencies in the range of 4.4 kHz and 10.76 kHz. A small response, matching the higher frequencies seen at point B, was also observed at this location on the TM. With different locations across the tympanum displaying all of these maxima in the frequency response, the authors concluded that TM vibrations appear more complex than simple drum mode resonances.

An acoustic impulse was also used as a stimulus to measure the locust tympanum's transient response. For a pulse of duration 15 μs, the TM continued to vibrate beyond the end of the impulse as the travelling wave propagated along a transect line formed between the thin membrane region, passing through the PV to the FB. The recordable response lasted around ten times the duration of the impulse.

In 2013, Malkin et al. modelled the locust tympanum as a membrane in tension with negligible stiffness. The authors modelled the TM as circular disc geometry with thick and thin geometric sections extruded from or cut into the disc. Modelling in the time domain i.e. as a transient analysis, their focus was on the travelling wave velocity and its evolution with respect to their membrane thickness measurements. Because of the dependence of a theoretical travelling wave velocity's on thickness, the tension-dominated system was chosen. For the thin membrane region they used a thickness of 3 μm and a cylinder of height 15 μm for the PV. A Young's modulus of 20 MPa, density of 1300 kgm^{-3} and Poisson's ratio of 0.3 were used for the cuticle material properties. Through time domain modelling using mechanical forces as simplified acoustic loads, at frequencies away from the modes of the system, Malkin et al. were able to show a travelling wave form at 15 kHz across their simulated locust tympanum.

Some researchers have studied the mechanism behind the perceived directional response of the locust hearing system with varying levels of success. Early research papers believed the TM to operate strictly as a pressure gradient receiver across all frequencies of sensitivity (Pumphrey, 1940; Autrum, 1941), that is, each tympanum is acted upon by both an external and internal component of pressure and therefore the tympanal vibratory response is the resultant of these two

contributions. Michelsen (1971c) and Miller (1977) then further elaborated that the locust TM likely operates as a pressure gradient receiver for frequencies below 10 kHz. This means each TM is acted upon by both an external and internal component of the sound pressure wave, and consequentially the overall vibration of the membrane would be a response to the relative magnitude and phase of both components. At frequencies beyond 10 kHz the authors concluded that the ears may operate as a pair of pressure difference receivers (or pressure receptors) i.e. most of the sound is incident externally and a slight difference in the external sound pressure at each ear is enough for the locust to discern source direction. Many findings alluded to this conclusion including first of all, the discovery of the relationship between the frequency of incident sound and the internal sound pressure level in dB (relative to the sound pressure level outside the body). At low frequencies, in the region of 1 – 5 kHz, when measured relative to the external sound level of the stimulus the internal sound was found to range from -2 dB SPL to -8 dB SPL indicating a fairly large percentage of sound is transmitted through the internal chamber between ears. Subchapter **4.6** attempts, for the first time, to model the influence of tympanal vibrations on the internal transmission of sound within the desert locust interaural cavity. Additionally, no significant difference in the sound pressure levels at each ear was measured for frequencies of 2 and 3.5 kHz and therefore no dependence on angle of incident sound either (Miller, 1977). Conversely a difference of 2 – 3 dB SPL was observed at 5 kHz, with this value increasing to 6 – 8 dB SPL at 15 kHz. With the wavelength of sound in air at the higher of these frequencies being of the order of magnitude of the locust body dimensions, one would expect the locust body to act more as a barrier to sound with more reflection at the ipsilateral side and less sound diffracting to the contralateral side, explaining this observation. Another finding from these directionality studies was the influence of the body mass, particularly of the tissue, tracheal air sacs and haemolymph, between both tympana on the measured sensitivity of the locust at the lower frequencies below 10 kHz. Abnormally meagre locusts displayed the highest hearing sensitivity to this range. No change in sensitivity was observed at frequencies beyond 10 kHz, with the tissue within the internal cavity of the locust hearing system compared to a low-pass filter.

Much can be learned from the sensitive, directional, impedance-matched (often air-to-air) and microscale hearing systems of insect species. One goal of this thesis is to further progress the understanding of the frequency-dependent formation of the travelling waves that propagate across the locust tympanum. For this, LDV will be used for a new characterisation of the waves at different frequency bands. Finally, approximating models are constructed and computed in the frequency domain using finite element analysis to investigate the characteristics which influence the formation and the frequency-specific shapes of the travelling waves. Particular interests are the shape of the locust TM, the mechanical properties of the cuticle, and the effect of both on the vibrational pattern of the membrane in response to incident sound. Many of the features of the locust hearing system mentioned in this review subchapter are simulated using novel finite element modelling methods.

1.4.2.3 The Tympanal Hearing System of Ormia ochracea

An example of a highly sensitive microscale directional acoustic sensor in the natural world is the ear of the parasitoid fly, *Ormia ochracea*. The gravid female *Ormia* larviposits on and around a host cricket, usually of the *Gryllus* genus and her predaceous larvae survive by feeding on their cricket host. In order for *Ormia* to be successful, the female must find a host cricket via phonotaxis to the mating call of the *Gryllus* spp. (Cade, 1975). Since the body size of the cricket enforces an evolutionary constraint on the maximum body size of the fly, there is a consequential impact on the size of the *Ormia* ear. The whole ormiine ear consists of two small tympanal membranes (less than 1 mm in diameter), both located within the same prosternal chamber between the fly's head and thorax and spanning a total edge-to-edge distance of around 1.68 mm (Edgecomb et al., 1995; Robert et al., 1998). Each tympanum has a tympanal pit, behind which the two mechanoreceptor organs or bulbae acusticae reside. With approximately 70 – 75 auditory receptor cells or neurons in each bulba acustica, vibration of the tympanal pit corresponds to deformation of the connected receptor organ. The separation distance between the tympanal pits of each ear, or interaural distance, is less than 0.5 mm, making them one of the smallest known ears in the insect world (Mason et al., 2001; Robert et al., 1996). One tympanal pit is coupled to the other via a unique structure of cuticle called the intertympanal bridge (Miles et al., 1995), described as being stiffer perhaps, than the surrounding cuticle of each tympanum. Behind the whole ear is only one undivided air chamber which connects externally via two tracheae and spiracles.

The mating call of a male *Gryllus* is narrow-band with a characteristic frequency between 4.5 kHz and 5.2 kHz corresponding to a wavelength in air of about 70 mm (Eq. [1.3]) (Ramsauer and Robert, 2000). As the whole body size of the fly is only ~ 7 × 3 mm one would expect the majority of the sound from the cricket call to easily diffract around the fly's body (see ***1.2.2***) (Rosen et al., 2009). Moreover, when the dimensions of the ormiine ears mentioned above are considered the hearing ability of this parasitoid fly becomes even more remarkable.

Most animals which possess directionally sensitive hearing use one or both of an interaural time difference (ITD) and interaural intensity difference (IID) to localise the origin of a biologically relevant sound source. For the *Ormia* the theoretical maximum ITD would be for sound travelling parallel to the plane of the ear with azimuthal angle of 90°, i.e. directly in line with the two tympanal pits. Robert et al. (1998) found that this corresponds to an ITD at this theoretical maximum of 1.45 μs (see ***1.2.1***). As mentioned previously most of the sound wave from the cricket mating call will easily diffract around the body of the fly leading to only a 1 dB SPL theoretical maximum IID. The combination of this undetectable IID and very small ITD should theoretically render impossible, the fly's ability to localise the cricket song.

However studies have shown that *Ormia ochracea* is capable of not only localising the cricket mating calls but with remarkable accuracy – a reported resolution of less than 2° in the azimuthal plane (Mason et al., 2001). The directional sensitivity of human hearing benefits from the fact that a human head is large enough to cause a significant IID at frequencies corresponding to human speech, as well as a much larger ITD compared to very small animals such as *Ormia ochracea*. Therefore for *Ormia* to achieve a directional sensitivity comparable to that of the human system is quite extraordinary. For sounds of frequency around 5 kHz, the parasitoid fly appears to amplify both the IID and ITD, by means of the intertympanal bridge mentioned above. The bridge, although stiff, is also flexible, resulting in a two degree of freedom system which consequently has two modes of vibration within the range of hearing of the fly. The first mode, termed the rocking mode, where the tympana are in antiphase i.e. 180° out of phase of each other, is excited by a sound pressure gradient between the tympanal membranes. The other mode, called the translational or bending mode where both tympana vibrate in-phase, is excited by the average pressure on both tympanal membranes (Miles & Hoy, 2006). The natural frequencies of these modes (and their proximity to one another and the cricket call), the strength of each mode and the coupling between them, all a result of the two degree of freedom system and unique morphology and mechanical properties of the ear, are the determining factors in ensuring the *Ormia* can successfully localise a cricket host on which to larviposit.

The combination of *Ormia ochracea's* phenomenal capability in sound localisation and superb sensitivity on a naturally miniaturised scale has inspired many engineers in the field of directional microphone design (Miles et al., 1995; Yoo et al., 2002; Miles & Hoy, 2006; Liu et al., 2008; Touse et al., 2010; Lisiewski et al., 2011; Chen & Cheng, 2012).

Arguably, however, no single researcher has managed to fully explain and therefore harness the ability of this remarkable fly with its own evolution-driven highly sensitive microscale directional acoustic sensor.

1.5 Microphone Technology

1.5.1 Microphone Types and Operation

A microphone, by design, must convert acoustical energy in a surrounding medium into an electrical signal. Incident sound waves cause a structure (often known as a diaphragm) to vibrate and this response is coupled to a system capable of transducing the mechanical energy into a measurable electrical output signal. Defined as devices which are capable of converting one form of energy into another, transducers are commonplace throughout the field of electronic and electrical engineering, with an electrical signal often being the outcome of the transduction process. Therefore the transducer and vibrating structure are the two main components of the majority of microphone systems and microphones are often categorised by their corresponding method of transduction.

Of these methods, dynamic microphones and condenser (otherwise known as capacitive) microphones are the types used in the majority of applications. Dynamic microphones operate using the principle of electromagnetic induction whereas condenser microphones operate by the detection of changes in capacitance. Microphones which use the concept of piezoelectricity (a piezoelectric material responds to stresses by generating an electric charge) also exist and are often known as crystal microphones.

Dynamic microphones are constructed with two major components: an annular magnet and a thin diaphragm which is attached to a wire coil. The response of the diaphragm to an incident sound pressure wave results in the vibration of the attached coil within a magnetic field, inducing an output voltage according to Faraday's Law.

Capacitive microphones consist of an electrically conductive backplate (often rigid and stationary) and a conductive diaphragm which is flexible enough to vibrate in response to impinging sound pressure waves. An initial bias voltage is applied to the plates setting them a specific distance apart. The diaphragm displacement results in a changing distance between the plates, which in turn is directly proportional to the capacitance (charge stored in the capacitor per unit volt).

Optical sensing methods are often used in some acoustics systems e.g. fibre optic microphones and laser microphones. Often the intensity or angle of reflected light is affected by the deflection of the vibrating surface or diaphragm. Interferometry can also be used to detect the diaphragm vibration.

Micro-electro-mechanical systems or MEMS microphones have made use of several of the aforementioned acoustic transduction methods although primarily they utilise some form of electrostatic capacitive sensing. This particular field of microphone design is increasingly finding applications in hearing aids and in portable devices such as tablets and smartphones, among many others, leading to an increase in research output in the field of MEMS microphones (Wang et al., 2004; Miles & Hoy, 2006). Single-crystal silicon (S-C Si) is often the chosen material used to fabricate such microphones as many benefits are associated with its unique properties. The use of S-C Si brings relative ease of incorporation of electronic functionality such as filtering and amplification, compatibility with semiconductor processing equipment and a consistent monolithic microstructure with no potential for grain boundary defects. Silicon's mechanical properties enable MEMS microphones to withstand harsh operating conditions and since microscale fabrication is possible, the results can be miniaturised, highly sensitive acoustic sensors.

1.5.2 MEMS Microphones

One feature of MEMS microphones includes the opportunity for small form factor designs making them highly suited to specialised applications in portable devices and hearing aids. Other features include superior sensitivity matching and a high tolerance for mechanical vibrations. Many MEMS microphone systems have an element of directionality about their mechanical response as a solution to reduce noise and therefore improvement of signal intelligibility. This attribute becomes particularly important in applications involving the recording of speech, pinpointing of sound source origin, and environmental monitoring (Ricketts, 2000; Gnewikow et al., 2009; Blumstein et al., 2011). While MEMS technology has already been applied in commercial microphones, achieving directionality within such devices is currently a subject of the research domain. Incorporating directionality into microphone systems often comes with great difficulties including an enforcement of size constraint. Some key sensor parameters when designing a commercially viable MEMS microphone include a predictable frequency response (often desired to be flat), a favourable SNR and a highly sensitive directional response.

Conventionally, directionality (which in three dimensions extends to localisation) is incorporated into microphone systems through an array of two or more pressure receivers (or elements), separated by a known distance preferably greater than the wavelength of the incoming sound. One or more of the time difference of arrival (TDOA), relative phase difference or pressure intensity difference at the receivers is measured and fed into sound source localisation algorithms. In applications requiring both directionality and miniaturisation, there exists an obvious conflict. As the microphone system decreases in size, there is the likelihood that the wavelength of incident sound will become greater than the inter-element spacing. At this point the phenomenon of diffraction, introduced in ***1.2.2***, becomes a significant issue. Diffraction adversely impacts the ability to measure the pressure difference or TDOA to the required degree of accuracy since the sound pressure reaching each pressure receiver will be almost equal. Applying this to a human's range of audio frequencies, where the wavelength of incident sound is of the order of centimetres, results in a significant physical constraint to the structure of

directional receiver arrays. Within this already space-limited system a means of transduction (***1.5.1***) must also be encompassed.

The parasitoid fly, *Ormia ochracea*, introduced in *1.4.2.3,* is one member of the animal kingdom which has cleverly overcome this size restriction imposed on directional acoustic sensor systems. Many bioinspired silicon MEMS microphone designs have appeared as a result of this evolution-driven solution to an engineering problem (Miles et al., 1995; Yoo et al., 2002; Miles & Hoy, 2006; Liu et al., 2008; Touse et al., 2010; Lisiewski et al., 2011; Chen & Cheng, 2012).

Biomimetically designed microphones are characterised either by their method of transduction or by the type of diaphragm or vibrating structure. The most common examples of the former are optical and electrostatic methods. Optical methods include reflecting a laser from diffraction gratings built into the MEMS structure using arrangements of gold sputter-coated fingers. The resultant pattern of interference fringes captured by photodiodes corresponds to the device displacement (similar to laser Doppler vibrometry as described in **2.1)**. However increased fabrication costs and space limitations often eliminate the feasibility of utilising optics for transducing mechanical signals into electrical signals in directional MEMS microphones. On the other hand, electrostatic sensing, usually either through a two-plate capacitor style like the conventional condenser microphone (described in ***1.5.1***) or via the use of electrostatic combs, can be intrinsically integrated into the microphone structure in a far more space-efficient manner (Cui et al., 2010).

The second directional MEMS microphone characteristic, structure type, can be further divided into three main types: the see-saw, the clamped-diaphragms (two or more) and the centre-supported or gimbal type.

Consisting of a diaphragm fixed centrally to a suspension beam, the unclamped nature of the see-saw microphone gives rise to both the name and characteristic two degrees-of-freedom mechanical response, similar to that of the fly *Ormia ochracea*. Gibbons and Miles (2000) designed and constructed a two degrees-of-freedom see-saw MEMS microphone consisting of a polysilicon rectangular diaphragm and perforated backplate. In a bid to counteract atmospheric pressure fluctuations behind the diaphragm, perforations were made in the backplate along with the inclusion of a fairly substantial air cavity behind the vibrating diaphragm. A

restraint on the maximum sound pressure level of this MEMS microphone is the potential for the diaphragm to implode onto the backplate as a result of the voltage between the two and excessive diaphragm deflections causing an accompanying decrease in the plate-to-plate air gap below a critical distance. The authors of this particular study fabricated a MEMS microphone capable of withstanding a maximum of 130 dB SPL with a corresponding 3 μm interspatial distance. Two mode shapes were predicted by finite element modelling, a rocking out of phase mode at 1272 Hz and a translational in-phase mode at 9349 Hz. Coupling and subsequent interactions between these modes were found to result in the system displaying mechanical directionality. On the diaphragm the authors also incorporated trenches or corrugations with a view to both increasing the mechanical sensitivity and decreasing any potential for residual in-plane stresses caused during fabrication.

This technique of strategically positioning trenches on microphones was one already used by Jerman (1990), Spiering et al. (1993) and Scheeper et al. (1994) among others. Yoo et al. (2001, 2002) also made use of corrugated diaphragms to construct biomimetic directional MEMS microphones taking inspiration from the ormiine ear, designing two microphones: one fabricated using polysilicon and the other using parylene. Not only did these devices feature corrugated trenches but they also incorporated silicon proof masses, tuning the resonant frequencies to specific values with frequency ratios significant to the desired response. By combining corrugations, proof masses and stiffening beams, many of the higher frequency modes were beneficially shifted beyond the audio frequency range. Modal responses of both of the devices were computed using finite element modelling and then measured experimentally using laser Doppler vibrometry.

Stiffening beams designed to drive a particular resonant frequency of a MEMS microphone upwards beyond the audible range of human hearing is a commonly used design technique (Miles et al., 2006 & 2009). In theory however, this can decrease the sensitivity of a particular microphone. Therefore extra design features, often influencing the damping properties of the device's mechanical response, are incorporated to address such losses of sensitivity. Thin-film or squeeze-film damping, a major potential source of damping in these highly sensitive, microscale devices, occurs in the presence of two parallel structures with a small

interspatial air cavity. When one or both plates move towards the other, a squeezing effect on the air film results in the exertion of a counteracting force on the structure. Many efforts are often made to release such damping from directional MEMS devices such as fabricating perforated backplates or etching slits into the diaphragm. It should be noted that such methods can sometimes be counterproductive as perforating holes in diaphragms is often mechanically inefficient since with decreased diaphragmatic surface area can come a loss of mechanical sensitivity.

Other directional MEMS microphones design types include structures consisting of two or three clamped discs (Lisiewski et al., 2011; Liu et al., 2013), more closely mimicking the ormiine auditory system, and gimbal-type devices with an extra central support (Ono et al., 2003).

Many studies in the field of directional MEMS microphones have centred on taking bioinspiration from the parasitoid fly, *Ormia ochracea*. While the degree of reported success varies from study to study, principally, any MEMS device with the correct degrees of freedom should display some element of mechanical directional acoustic sensitivity. The second goal of this thesis was to explore the modal and directional response of two such MEMS structures, see-saw type in form, which are similar in geometry and magnitude to the ear of *Ormia*. Physical and computational experiments were utilised to gauge the devices' performance with a view to their potential in applications such as directional microphones.

Chapter 2 : Methodology

"…great difficulties are felt at first and these cannot be overcome except by starting from experiments…and then be conceiving certain hypotheses…But even so, very much hard work remains to be done" – Christiaan Huygens

This chapter outlines the main methods used throughout this thesis to explore, analyse, predict and measure both insect auditory systems and micro-electro-mechanical systems microphone structures. An introduction to micro-scanning laser Doppler vibrometry is provided, followed by an overview of modelling using the finite element method, concluded with a step-by-step breakdown of some of the computer-aided design tools used for 3-D geometry creation. Laser vibrometry is the main physical experimentation technique utilised in this thesis research since it has become the class-leading technique for the accurate measurement of sub-nanometre vibrations. Finite element analysis, in conjunction with 3-D computer-aided design (CAD), has found applications throughout the field of computational modelling and it is vital when studying both structural mechanics and pressure acoustics. There follows an explanation of micro-scanning vibrometry, including the theory and application of this optical measurement system.

2.1 Micro-scanning Laser Doppler Vibrometry

One technique now widely used to investigate the mechanical response of a vibrating surface or body is micro-scanning laser Doppler vibrometry (LDV). Such is the significance of LDV, during the past thirty years it has rapidly increased in prevalence, becoming the norm in live insect dynamic vibration measurement techniques (Michelsen & Larsen, 1978; Yager, 1999; Windmill et al., 2005; Sueur et al., 2010; Moir et al., 2011). Making use of the Doppler Effect, explained in ***1.2.2***, a schematic diagram of the components of a typical LDV system is shown in Fig. 2.1. Firstly the output of one helium neon laser is split into two coherent laser beams, the reference beam and measurement beam, by passing it through beam-splitter 1 (BS1). After the measurement beam propagates through a second beam-splitter (BS2), refractive optics is used to focus it onto the sample surface via a manually adjustable lens. A detachable close-up attachment unit can also be used when scanning small samples, which acts like a microscope in magnifying the live video image of the sample as well as reducing the optimal stand-off distance for the laser light i.e. effectively reducing the working distance.

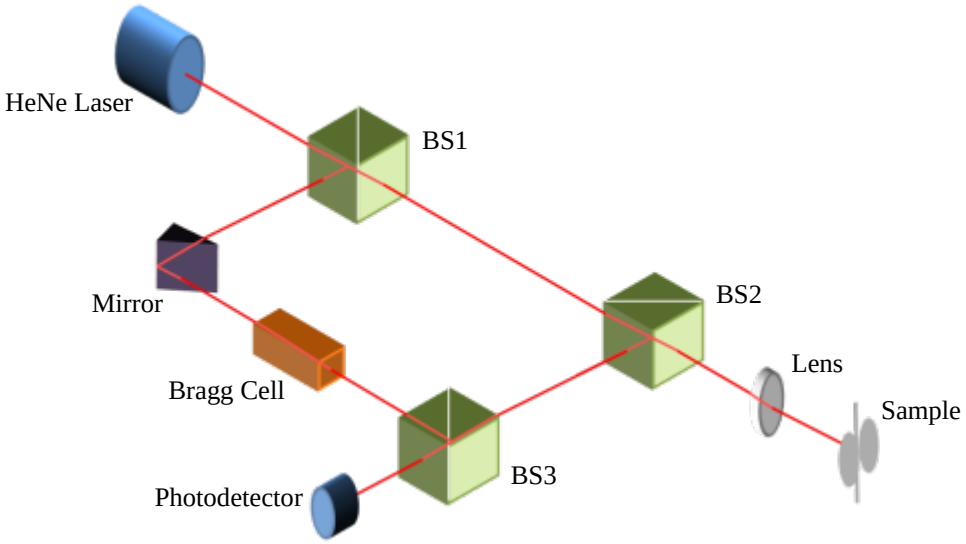

Figure 2.1 Internal components of a Laser Doppler Vibrometer. Illustration constructed using information from http://www.polytec.com/us/company/technologies/.

The sample reflects the laser light and the measurement beam re-enters the vibrometer where it is deflected by BS2 before being merged with the reference beam via a third beam-splitter (BS3). Finally, both beams then feed into a photodetector, often a photodiode. Laser interferometry is used to analyse the measurement beam with respect to the reference beam. Two coherent laser beams of light intensities I_1 and I_2 which overlap will constructively and/or destructively interfere creating an interference fringe pattern according to the formula

$$I_{tot} = I_1 + I_2 + 2\sqrt{(I_1 I_2 \cos[2\pi(r_1 - r_2)\lambda])} \quad [2.1]$$

where $r_1 - r_2$ is the path length difference between measurement beam and reference beam and λ the wavelength of the laser light. Assuming negligible thermal effects, the reference beam path length, r_2, remains constant with time while the path length of the measurement beam, r_1, varies transiently depending on the motion of the sample. There is direct proportionality between the magnitude of the sample vibrational velocity and the modulation frequency of the interferometer fringe pattern. Since the interference pattern would be identical for both motion towards and away the vibrometer, i.e. the direction of the velocity would be theoretically indiscernible, a Bragg cell is included to act as an acousto-optic modulator, shifting the frequency of the reference laser beam by 40 MHz. This integrated modulation of the fringe pattern frequency means that motion towards the detector decreases this 40 MHz frequency and conversely motion away from the interferometer shifts this modulation frequency upwards. Thus, the magnitude and direction of vibrational velocity of a sample can be measured.

1-D micro-scanning laser Doppler vibrometers are capable only of measuring movement in the plane of the measurement laser beam, i.e. optimally the beam should be positioned perpendicularly to the sample surface, meaning therefore that the technique is capable of measuring only the transverse (out of the surface plane) velocity. The LDV system has two acquisition modes available, time domain mode and Fast Fourier transform (FFT) mode. The acquisition and data presentation software used in conjunction with the vibrometer allowed for integration of the transverse velocity resulting in the computation of the transverse displacement of the

sample. Alternatively the velocity can be differentiated resulting in the computation of the sample's transverse acceleration.

The Polytec PSV-300-F system utilised for this research uses a He-Ne laser which, when focussed onto a sample 5 cm away, has a spot diameter of approximately 3-5 μm and can be consistently positioned with an accuracy of 1 μm in the XY-plane. Two laser acquisition modes are utilised – single point data capture and scanning mode. Scanning mode requires the user to create a grid of connected points and the vibrometer acquires multiple, consecutive single point measurements at each grid point. In the FFT acquisition mode some form of averaging is usually used at each scan point/single data point to reduce unwanted noise and increase the signal-to-noise ratio. The averaging algorithm types include magnitude, complex and peak-hold. Complex averaging is selected when an experiment has a known stimulus whereas magnitude averaging is reserved for stochastic vibrations and with this setting no phase information is captured. More info on these (and many other LDV concepts and settings) is available from the Polytec software and theory manuals or their website (http://www.polytec.com/us/company/technologies/).

LDV is usually used to measure the vibration of a sample in response to some known applied stimulus, in this case through the use of acoustic pressure wave loads. These sound stimuli can either be generated internally using the arbitrary waveform generator (National Instruments PCI-6111; Austin, TX) embedded within the vibrometer workstation or by the use of an external function generator (e.g. Agilent 33220A; Santa Clara, USA). The sound stimulus is usually then recorded using a reference microphone (Brüel & Kjær 4138; Nærum, Denmark) which feeds into the vibrometer. This allows the velocity gain of a sample to be computed as the transfer function of the transverse velocity to the reference sound level, using the formula

$$H_1 = \frac{G_{ab}(f)}{G_{aa}(f)} \qquad [2.2]$$

where H_1 is the transfer function, $G_{ab}(f)$ is the cross-spectrum of the reference and velocity signals and $G_{aa}(f)$ the auto-spectrum of the reference signal.

In summary, micro-scanning laser Doppler vibrometry can be used on biological samples to provide an *in vivo* analysis of the sub-nanometre scale

vibration of an insect tympanum in a non-contact and non-invasive way. Since phase and amplitude data is acquired simultaneously, animations can be reconstructed from a scan, allowing for the visualisation of complex-shaped vibrations of a sample of arbitrary shape. The same techniques can also be applied to the analysis of the mechanical deflections of silicon MEMS structures such as those analysed in this thesis.

2.2 The Finite Element Method

2.2.1 Introduction to FEM

Often, an engineering problem can be evaluated through a theoretical and mathematical approach, whereby the system is described using the underlying differential equations governing such principles as Newton's laws of motion, the conservation of energy and mass, equilibrium, the laws of thermodynamics and Maxwell's equations, among others. However when this approach is used for a 3-dimensional system, exhibiting complex arbitrary geometry, with varying length scales, multiple materials both isotropic and anisotropic, and perhaps encapsulating many aspects of physics such as structural mechanics, fluid dynamics and heat transfer, the method can rapidly become very cumbersome and any potential solution can even end up redundant of any real meaning. The theoretical approach is better suited to well-studied geometries of regular shape such as rectangles or circles, in combination with fairly simple boundary conditions. A numerical analysis technique called the finite element method or finite element analysis (FEA) is often the next best alternative. To this end, the ability of FEA to simulate structures exhibiting complex arbitrary geometry was one of the modelling technique's greatest driving forces. FEA is therefore a valuable tool particularly when modelling the complex geometry observed in nature such as that seen in the locust tympanal system.

A finite element model (FEM) is constructed with one or more domains, usually allocated depending on the state of matter of the material contained within the region i.e. a solid domain and/or fluid domain (liquid or gas). The system is then discretised by subdividing the domains using meshes of relatively simple-geometry elements of finite shape and size, hence the name finite element method. For 2-D models the form of these elements is often triangular or quadrilateral and for 3-D models tetrahedral or hexahedral elements are used. Between each element, often at the vertices or along intersecting mesh lines, there are a number of points or nodes. Depending on the particular application of FEA, a number of unknown parameters are then assigned to every node, known as the degrees of freedom (DOF). For a continuum, in reality there exists an infinite number of DOF whereas in an FEM the total number of DOF is finite and, for a given study type, is dependent solely on the

parameters of the model's meshing structure. Equations encapsulating these DOF, based around the aforementioned governing differential equations, are then formed. However instead of solving these on a complex system-wide scale they are applied only in simplified approximated form to each node. Since the position and behaviour of the nodes also indirectly controls that of the elements and inevitably nodes are shared between elements, the response of the system as a whole can then be approximated through the formulation and solving of a matrix containing a system of equations. These systemic equations incorporate the nodal DOF and the relative spatial positions of each node and element in addition to all model inputs such as material properties or specific boundary conditions which can often simplify the model slightly by reducing the DOF or eliminating some elements or nodes. Computationally solving this matrix formulation for all DOF is commonly known as using an implicit solver in FEA. Due to the nature of FEA, it should be noted that an FEM only approximates a solution and in general the accuracy is directly proportional to the mesh resolution.

FEA has found applications in structural mechanics, thermodynamics, fluid dynamics, acoustics and electrostatics among other fields. These physical concepts then branch out into many specific problem types. Stress analysis, for example, involves the computation of components of displacement, force, moment, strain and also failure criteria. Within fluid dynamics, Navier-Stokes equation problems consist of the computation of velocity components and pressures. Finally, eigenproblem formulation is very commonly used throughout FEA. This is the computation of a model's eigenvectors and corresponding eigenvalues which, in the context of structural mechanics, are usually the undamped unloaded natural shapes of vibration, the eigenmodes, and their associated eigenfrequencies. Most commercially available finite element modelling packages are reasonably similar in that they can simulate many of the different physics applications mentioned here, provide comparable capabilities in data input, post-processing and data output, and offer multiple solver types with some even incorporating effortless coupling of multiple applications from a wide variety of study applications. COMSOL Multiphysics® (version 5.0, COMSOL, Inc. Burlington, MA, USA), used extensively throughout this research, is one such FEM code with the versatility to model 'multiphysics' applications. Several

COMSOL application modules are available which, when combined, provide the user with a suite of available study types, some utilising coupled solvers and some not. Additionally, partial differential equations can be input in their raw form allowing the creation of a fully customised finite element model. In this thesis research the finite element models made extensive use of the structural mechanics, acoustics, MEMS and CAD geometry importation modules within COMSOL.

2.2.2 FEM Workstation Specifications

As mentioned previously, in simple terms the accuracy of any finite element model solution is a function of the mesh resolution. However the number of mesh elements (and therefore nodes and nodal DOF) is constrained by the physical specifications of the computer system on which the model is being executed. When modelling using the COMSOL FEA package, the defining factor for model size, and therefore estimation accuracy, is the physical random-access memory (RAM) installed in the system. On the other hand, total computational time can be influenced by three main factors. Since most of the default solvers make use of shared-memory parallel processing, multi-core processing is the first factor, and the memory architecture, through its influence on parallelisation efficiency, is the second factor. The third factor is when the model size is so large that the physical RAM becomes unable to fit the whole matrix formulation for the entire system. In this situation, COMSOL recruits part of the hard drive (virtual RAM) to complete the matrix computation, a process which is greatly affected by the hard drive's read/write speeds (COMSOL support base – http://www.comsol.com/community/).

To this end, three different computer systems were utilised when creating and executing the finite element models contained herein, the use of each being dependent primarily on model size. Two customised workstations were used, one with dual quad-core processors and 24 GB physical RAM and the other with dual octo-core processors and 64 GB physical RAM. The final system used was a 'Tier-2' supercomputer called ARCHIE-WeSt (**A**cademic and **R**esearch **C**omputer **H**osting **I**ndustry and **E**nterprise in the **West** of Scotland – http://www.archie-west.ac.uk/) which is a 3400+ core high performance computer hosted by the University of Strathclyde, regarded at launch date as one of the top ten most powerful high performance computers in the UK. Importantly ARCHIE-WeSt has eight specialised large memory 512 GB RAM or 'fat nodes', each with four octo-core Intel Xeon E7-430 CPUs. The largest models were computed on one of these nodes using anything from 16 to the full 32 cores and 512 GB physical RAM. In addition a new parallel environment was introduced specifically for the finite element modelling in this thesis which allowed the coupling of between two and four of these high-memory

nodes, leading to potentially 1 – 2 TB total physical RAM availability. ARCHIE-WeSt utilises the Linux operating system therefore to run COMSOL the user must create a job script which requests ‘x’ amount of cores of the fat node and points to a previously created COMSOL model file.

2.2.3 FEM Procedure

2.2.3.1 Fundamental Steps

The steps required in constructing most finite element models, particularly in the fields of acoustics and mechanics, usually follow the same underlying pattern. Before beginning to construct a model, parameters are stored as Global Definitions near the top of the COMSOL model tree (see left side of Fig. 2.2). These include (but are not limited to) geometrical dimensions and material properties, and parameterising the model in this fashion allows rapid future alterations as well as the execution of multiple iterations with one or more changing parameters through the use of COMSOL's built-in parametric sweeps – effectively providing the potential to create nested loops.

Often, the initial main step in formulating a finite element model is the creation or importation of the model geometry, which is then partitioned into one or more model domains. Where the model geometry used in this thesis was fairly simple and could be easily divided into primitive shapes then COMSOL's integrated geometry construction tools were used. In cases when more powerful geometry tools were required then the professional level 3-D CAD software SOLIDWORKS® (Dassault Systèmes SolidWorks Corp., Waltham, MA, USA) was used. SOLIDWORKS provides a number of exportable formats, many of which are compatible with COMSOL's CAD geometry import module, one of these being the native SOLIDWORKS .sldprt part file so for consistency, reliability and accuracy this format was used for importation. Occasionally the geometry was then re-scaled within the modelling environment for technical reasons explained in **2.3**. Fig. 2.2 shows the construction of a simple cylindrical disc within COMSOL with the radius and height fields visible and Fig. 2.3 is an example of CAD-created complex model geometry. The fact that no biological system consists purely of primitive geometry, coupled with FEM's ability to handle arbitrary geometry, means the easy importation of externally created geometries with advanced CAD features has become a powerful tool.

The next step is material specification within the model domain settings. Multiple material types (isotropic, anisotropic and orthotropic) and states (solid,

liquid and gas) can be combined along with the possible input of many custom properties. COMSOL comes with an in-built material library in which fields can also be edited accordingly to include additional experimental data. Fig. 2.4 displays the typical minimum material properties required for solid mechanics modelling of a linear isotropic material, the Young's modulus, Poisson's ratio and density (all defined in **1.3**).

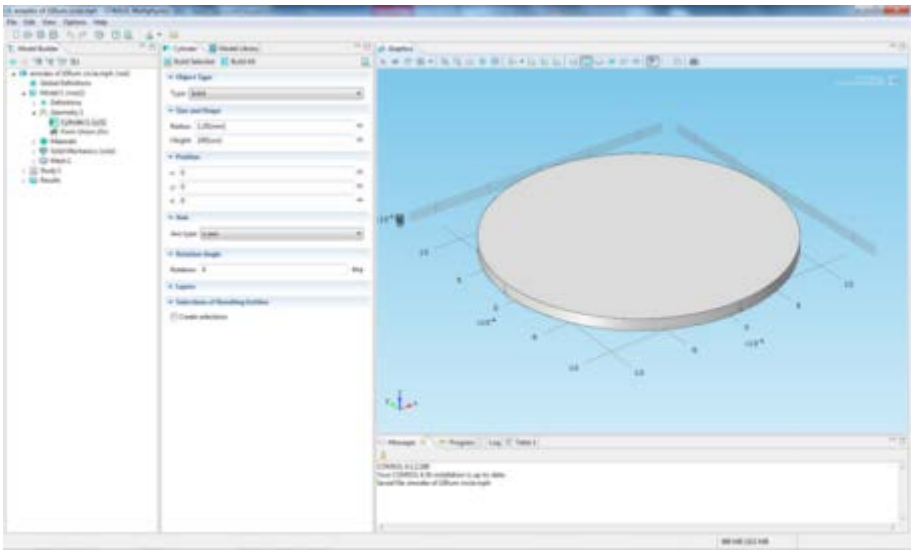

Figure 2.2 Cylindrical disc model geometry created in the COMSOL working environment.

The third main step in creating a FEM is the application of any boundary conditions which usually constrain the problem in some fashion, i.e. remove DOF from specific nodes or elements. Many options are provided here including external loads (forces, harmonic sinusoidal pressure loads) and initial conditions such as fixed constraints. Assuming applicability, these can be assigned to any point, line, 2-D boundary face or 3-D domain throughout the geometry. Fig. 2.5 illustrates the

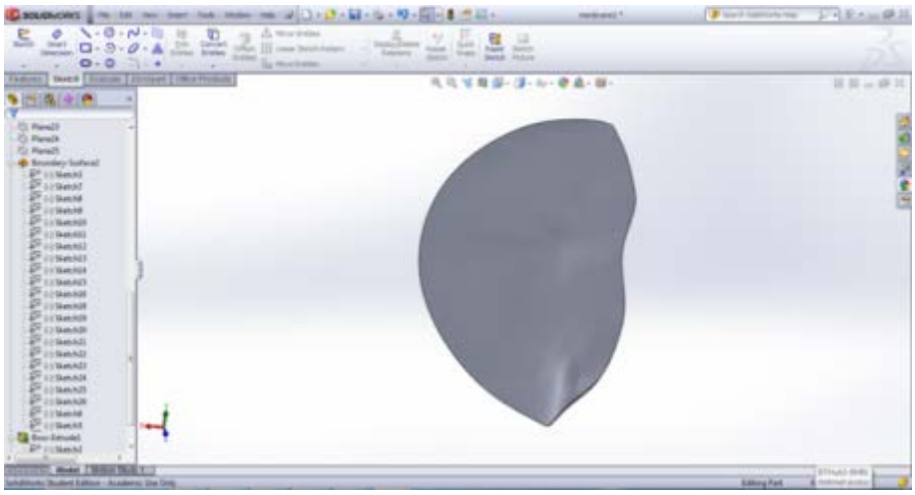

Figure 2.3 Complex CAD-built geometry in SOLIDWORKS.

application of a fixed constraint boundary condition on the four boundary faces at a disc's edge i.e. enforcing the displacement of all nodes (and therefore elements) on this 2-D boundary to be zero throughout computation.

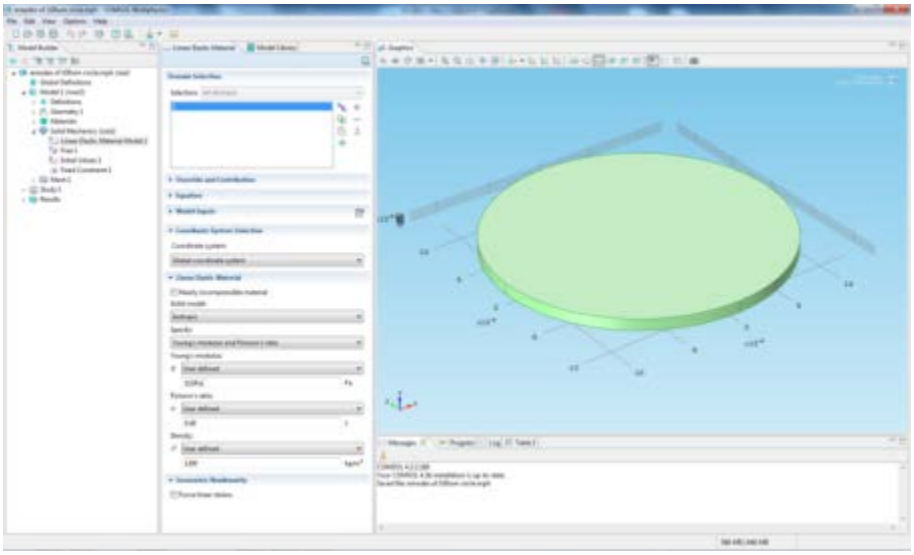

Figure 2.4 Setting material properties.

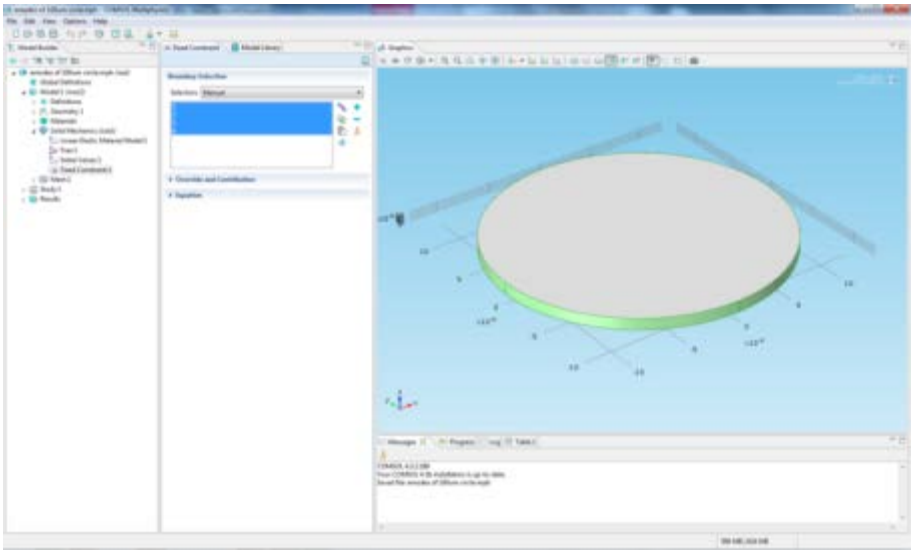

Figure 2.5 Applying fixed constraint boundary condition.

The penultimate major step in FEM formulation and computation is generation of the mesh. In COMSOL this vitally important step can either be controlled by the software known as physics-based meshing, or fully customised, in user-defined meshing. Meshing options range from single 1-D point or line insertion, 2-D boundary mesh creation, usually as triangular or quadrilateral elements, or full 3-D domain meshing using tetrahedral elements (among others). Most of the

meshing algorithms use adaptive meshing in that the element size increases and decreases throughout the mesh dependent upon the proximity to boundaries or specific features in the geometry structure such as areas of curvature, sharp corners and thin regions. Specific settings exist to improve the mesh resolution in all such areas. Integrated mesh sizes are included from ‘extremely coarse’ through ‘normal’ to ‘extremely fine’ and with each of these come specific element maximum and minimum sizes, growth rate and other parameters to control resolution. These can all be customised and a plethora of other meshing options exist including swept meshes for geometries of uniform cross-section. A particular problem can be the successful and efficient coupling of one domain’s mesh to the mesh of a surrounding domain and statistics are also available to assess the quality of a particular mesh. Fig. 2.6 shows a typical tetrahedral mesh with ‘normal’ element size setting.

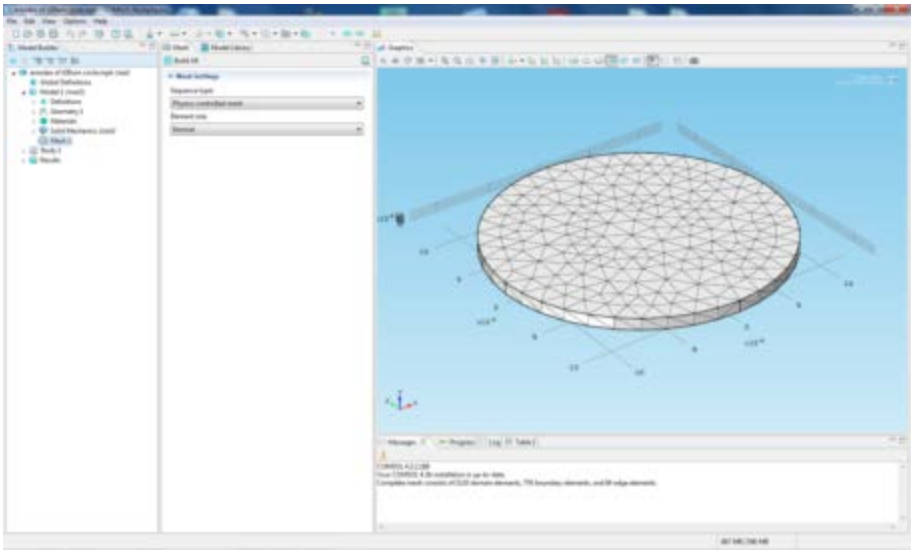

Figure 2.6 Tetrahedral normal sized mesh.

The final step is solver selection and settings and often the default solver type provided by COMSOL is the best option, providing accurate solution estimation and optimisation of computational costs both for simple one module applications or complex coupled multiphysics problems. Only occasionally are some settings tweaked to produce newly available output data.

Almost every numerical input to a COMSOL model can be parameterised and/or calculated using other model inputs, allowing the rapid automatic execution of multiple model iterations through nested loop parametric sweeps.

2.2.3.2 Eigenproblem Simulations

In theory, solid bodies have an infinite set of vibrational patterns which are known as the undamped or unforced normal modes of vibration or eigenmodes. The natural frequencies at which these vibrational patterns occur are called the eigenfrequencies (see **1.3.3** for theoretical modes of a circular plate). Each of these eigenfrequencies will depend on both the dimensions of the vibrating body and some material properties. In FEA of solid 3-D structures these properties are often the stiffness, density and Poisson's ratio. For isotropic linear Hookean materials the Young's modulus, E, is the measure of stiffness used most commonly.

COMSOL's solid mechanics eigenvalue solver, designed for rapid and accurate computation of eigenmodes and eigenfrequencies, was used extensively to predict the mode shapes and approximate natural frequencies of the model systems throughout this research. The COMSOL 5.0 Reference Manual and Structural Mechanics Module Users Guide along with Chapter 22 of the Springer Handbook of Acoustics (Rossing, 2007) provide the theory behind modal analysis of solid bodies including eigenvalue problem formulation and the particular solver used in FEA.

Implementation of such a modal analysis involved completion of each of the steps outlined in the previous section along with defining the study size by inputting a desired number of eigenfrequencies in the relevant solver settings field. Default output creation was of the mode shapes with their deformation exaggerated purely for visualisation purposes by an enlargement of the displacement using an automatic scale factor (which could be customised). The default solver setting for the output of eigenvectors (and therefore the one used here) is for normalisation via scaling against the RMS values. Consequently it should be noted that the colour scale for eigenmodes throughout this thesis indicates an arbitrary normalised out-of-plane displacement field, red indicating transverse displacement out of the page and green for displacements into the page. As mentioned previously, one cannot compare the amplitude of deflection of each mode in a simple eigenmode analyses, however the amplitudes of the characteristic nodes of a particular mode can be accurately compared.

In the modal analysis of any structure one further step can be implemented. Firstly the advanced solver setting of normalisation of outputs against the RMS values was changed to normalisation by the model mass matrix. Rerunning the eigenmode analysis solver resulted in the computation of the modal participation factors (MPF), of which there are 3 translational MPFs for each mode, one for each Cartesian axis direction. Squaring the MPF (in a particular direction) for each mode of the disc resulted in the effective modal mass (EMM) of that mode (kg).

$$EMM_{i\,j} = MPF_{i\,j}{}^{2} \tag{2.3}$$

where $EMM_{i\,j}$ is the effective modal mass of mode i where $i = 1,2, \dots, n$ in direction j where $j = X, Y$ or Z and $MPF_{i\,j}$ is the modal participation factor of that same mode in the same direction.

$$m_{tot} = \frac{\rho}{V_{tot}} \tag{2.4}$$

where m_{tot} is the total mass of the system, ρ is the density of the model material and V_{tot} is the total volume of the system.

For geometries with one uniform dimension and a constant cross-section,

$$V_{tot} = A_{c-s} \times th \tag{2.5}$$

where A_{c-s} is the cross-sectional area and th the uniform thickness.

For a cylindrical volume with circular cross-section of radius r,

$$A_{c-s} = \pi \times r^{2}. \tag{2.6}$$

For more complex geometries V_{tot} was calculated using a measure command in the geometry subnode. Alternatively m_{tot} can be defined and calculated in the software for complex multiple material model geometries by integrating the density of each material across the domain where that material is located, then summing all of these integrals.

Finally, dividing the EMM of each computed mode of the device in the same direction by the total mass of the system, resulted in the effective modal mass fractions for each calculated mode in that direction.

$$EMMF_{i\,j} = \frac{EMM_{i\,j}}{m_{tot}}$$

[2.7]

where $EMMF_{i\,j}$ is the effective modal mass fraction (%) of mode i in direction j where $j = X, Y$ or Z.

The effective modal mass fraction is an indication of the ease with which that mode would be excited by base excitation. Therefore the EMMF can be thought of as an estimate of the amount of energy which is found in a particular mode of the system.

2.2.3.3 Acoustic-structure Interaction with a Frequency Response Analysis

To simulate the frequency response of both model locust tympana and micro-electro-mechanical systems devices, COMSOL's acoustic-structure interaction application type, with an integrated frequency domain study, was used. This differs from the single domain, harmonic mechanical load, time domain analyses used by Malkin et al. in 2013. An acoustic-structure interaction analyses the two-way coupling between a structure's mechanical response and some load stimulus, in this case an incident pressure wave in the surrounding fluid. The propagation of this acoustic wave in the fluid domain, and any associated pressure fluctuations, are computed by the pressure acoustics frequency domain solver which revolves around resolving the Helmholtz equation

$$\nabla \cdot \left(-\frac{1}{\rho_c}\nabla p\right) - \frac{\omega^2 p}{\rho_c c^2} = 0 \qquad [2.8]$$

where ρ_c is the fluid density (in kgm^{-3}, c subscript denotes could be complex), p is the harmonic acoustic pressure of the form $p = p_a e^{i\omega t}$ (Nm^{-2} or Pa), ω is the angular frequency (rads^{-1}) and c the speed of sound (ms^{-1}).

This model application is designed specifically for external loads with harmonic pressure field variations. The simulated vibration of any solid body within the fluid is controlled by a corresponding frequency response analysis provided by the structural mechanics module. In response to a harmonic load, this FEA solver estimates the steady-state solution, by splitting the problem into the following components. A harmonic load of amplitude, F (N), and phase, F_{phase} (rad), is dependent on the excitation angular frequency, ω, where $\omega = 2\pi f$ and f is the excitation frequency (Hz), according to the equation

$$F_{\text{freq}} = F(\omega) \cdot \cos\left(\omega t + F_{\text{phase}}(\omega) \cdot \frac{\pi}{180}\right) \qquad [2.9]$$

A complex time-dependent displacement field is computed by this solid mechanics application with amplitude, u_{amp} (m), and phase angle u_{phase} (rad). Resultantly the instantaneous displacement is the real part of

$$u = u_{\text{amp}} \cos\left(2\pi f \cdot t + u_{\text{phase}}\right)$$

[2.10]

Two domains were usually created within the model and allocated a specific domain type, solid (the vibrating body) and fluid (air). Aside from any fixed boundary constraints similar to those seen in the eigenmode analysis and preceding fundamental FEA steps, most of the new required boundary conditions are controlled by the acoustic-structure boundary coupling. This unique two-way multiphysics interaction can be expressed mathematically by the two equations

$$-\mathbf{n} \cdot \left(-\frac{1}{\rho_c}(\nabla p_{\text{t}} - q_d)\right) = -\mathbf{n} \cdot \mathbf{u}_{tt}$$

[2.11]

$$\mathbf{F}_{\text{A}} = p_{\text{t}}\mathbf{n}$$

[2.12]

for exterior boundaries, where $\mathbf{n}$ is the surface unit normal vector, p_{t} is the total acoustic pressure (Pa), q_d is an optional dipole source, $\mathbf{u}_{tt}$ is the structural acceleration (ms^{-2}) and $\mathbf{F}_{\text{A}}$ is the load exerted on the solid (Nm^{-2}).
For interior boundaries this coupling is represented by

$$-\mathbf{n} \cdot \left(-\frac{1}{\rho_c}(\nabla p_{\text{t}} - q_d)\right)_1 = \mathbf{n} \cdot \mathbf{u}_{tt}$$

[2.13]

$$-\mathbf{n} \cdot \left(-\frac{1}{\rho_c}(\nabla p_{\text{t}} - q_d)\right)_2 = -\mathbf{n} \cdot \mathbf{u}_{tt}$$

[2.14]

$$\mathbf{F}_{\text{A}} = \left(p_{\text{t},1} - p_{\text{t},2}\right)\mathbf{n}$$

[2.15]

i.e. a pressure drop across the solid structure is related to the acoustic load.

The stimuli were simulated plane wave pressure fields of user-specified amplitude (p_a in Eq. [2.17], in Pa) at several frequencies in the vicinity of the

computed eigenfrequencies, applied to the external boundaries of the air domain. These same boundaries were allocated a radiation condition which eliminated any internal reflections within the domain, other than those of the sound wave impinging on the centrally positioned 3-D solid domain, i.e. at the extreme model boundaries the air domain behaves as if extended to infinity. Spherical wave radiation boundary conditions in COMSOL are formed by an expansion (in spherical coordinates) from Bayliss et al. (1982), which is

$$-\mathbf{n}\cdot\left(-\frac{1}{\rho_c}(\nabla p_{\mathrm{t}}-\mathbf{q}_d)\right)+\left(ik_{\mathrm{eq}}+\frac{1}{R}\right)\frac{p}{\rho_c}-\frac{R\Delta_{\mathrm{T}}p}{2\rho_c\left(ik_{\mathrm{eq}}R+1\right)}$$
$$=-\frac{R\Delta_{\mathrm{T}}p_i}{2\rho_{0c}\left(ik_{\mathrm{eq}}R+1\right)}+\left(ik_{\mathrm{eq}}+\frac{1}{R}\right)\frac{p_i}{\rho_c}+\mathbf{n}\cdot\frac{1}{\rho_c}\nabla p_{\mathrm{i}}$$

[2.16]

where k_{eq} is the wave number (radm^{-1}), R is the radius of the fluid domain (m), Δ_{T} is the Laplace operator in the tangent plane at a specific point, ρ_{0c} the static density (kgm^{-3}) and p_i the incident pressure field added as a subnode to the spherical wave radiation boundary. This pressure field is of the form

$$p_i=p_a e^{-i(\mathbf{k}\cdot\mathbf{r})}=p_a e^{-ik_{\mathrm{eq}}\left(\frac{\mathbf{r}\cdot\mathbf{e}_k}{\|\mathbf{e}_k\|}\right)}$$

[2.17]

where p_a is the pressure amplitude (Pa), $\mathbf{k}$ the wave vector with direction vector $\mathbf{e}_k$ and amplitude $|\mathbf{k}|=k_{\mathrm{eq}}$, and $\mathbf{r}$ the location on the boundary.

Two angles were created as parameters in the Global Definitions subnode, φ and ϑ (both in radians, bounded by the limits $0\leq\varphi\leq 2\pi$ and $0\leq\vartheta\leq\pi$), and defined as the anti-clockwise angle in the XY-plane starting from the X-axis and moving towards the Y-axis (sometimes known as angle of azimuth) and the angle between the Z-axis and the XY-plane (angle of elevation), respectively. Defined by these angles, three incident wave direction vector components k_1, k_2 and k_3 were then calculated, and input in the component fields defining $\mathbf{e}_k$ from [2.17] above. These were calculated using the trigonometric formulations below

$$\mathrm{k}_1=\sin(\vartheta)\times\cos(\varphi)$$

[2.18]

$$\mathrm{k}_2 = \sin(\vartheta) \times \sin(\varphi)$$

[2.19]

$$\mathrm{k}_3 = \cos(\vartheta).$$

[2.20]

The formula in ***1.2.1*** was adapted and used in the incident pressure field value for the pressure amplitude p_a (usually in Pa) so that the simulated sound stimulus could be input with an amplitude value in dB SPL using the formula

$$p_a = 2 \times 10^{-5} \times 10^{\left(\frac{dB\ SPL}{20}\right)}$$

[2.21]

Before executing acoustic-structure interactions, establishing the solver settings was the final important step with two main components – frequency selection and activation of the geometric nonlinearity solver option. The former of these settings is fairly self-explanatory and the chosen frequency controls that of the excitation frequency in tandem with the frequency content of the response output. Range input is available which involves choosing a minimum, step and maximum frequency. Enabling the 'Include geometric nonlinearity' option is advised for all finite element models displaying a number of common features:

- thin or high aspect ratio 3-D solid geometries (or regions) where the magnitude of deflection may approach the thickness values;
- situations where large rotational vibrations may be present – even just a few degrees for rigid bodies;
- all fluid-structure interaction problems.

With this option enabled pressure loads then act as true follower loads, i.e. the direction of their exerted forces reacts according to local deformations in material geometry.

Formulating every acoustic-structure interaction model in this thesis with full parameterisation of the geometry dimensions, all material properties, pressure load magnitudes, angles and their corresponding vector components as well as the solution frequencies, allowed multiple large-scale parametric sweeps (nested loops)

to be implemented, meaning automated and efficient computation of the simulated frequency response of model solid bodies for a range of incident sound waves.

Default output creation for 3-D acoustic-structure interactions is two 3-D plots: the first displaying the total displacement (in all axis directions) of the solid domain (m) and visualisation of an exaggerated deflection, as mentioned previously in the output for eigenfrequency analyses; the second being the total acoustic pressure throughout the fluid domain. The evolution of either of these variables can be visualised either by changing the solution phase angle and replotting or using the animation player to dynamically extend the data through a full harmonic cycle. Many other physical quantities from the fields of solid mechanics and pressure acoustics can be computed at a variety of model locations and visualised in a multitude of forms. 3-D cut points were used to extract any quantity at a particular point, specified by the point's coordinates in three dimensions or by selecting a point of existence already formed in the construction of the model geometry. Several mathematical functions and operators are also available as extra post-processing options.

2.3 Geometry Construction - Computer Aided Design

Several forms of geometry are used as inputs to the model tympana studied in this research and the first of these types is that of simple uniform thickness and constant cross-section. These structures are either constructed from primitive 3-D shapes such as cylinders and cuboids or for the slightly more complex geometry, a cross-section is drawn on a work plane and extruded, usually in the thickness direction, denoted Z (see **3.2** and **4.1** for examples). SOLIDWORKS 3-D CAD software was used to form model locust TMs with step changes in thickness using simple extruded sketch or extruded cut tools of particular features.

The final locust tympanal membrane model geometry was constructed using methods which allowed the completed geometry to be as close to the natural tympanum shape as possible. Fig. 2.7 below shows the first step in the process – importing the contour map from Stephen and Bennet-Clark (1982) which shows the thickness distribution and shape of the left tympanum of a desert locust, *Schistocerca gregaria* (see ***1.4.2*** for more detail).

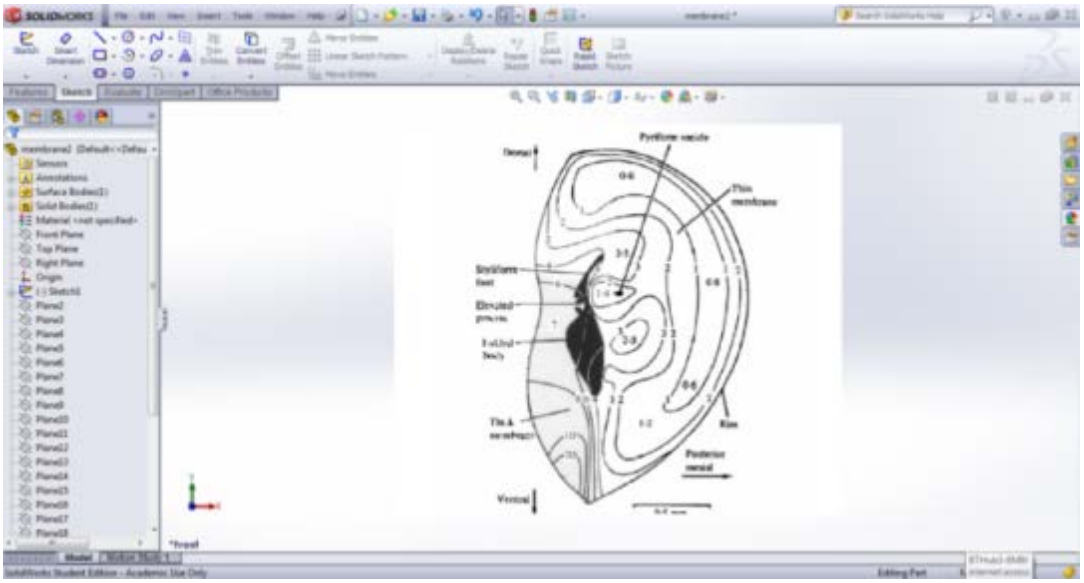

Figure 2.7 Inserted contour map (Stephen & Bennet-Clark, 1982) in SOLIDWORKS.

Although the values on the image are in µm, SOLIDWORKS can have some difficulty with dimensions in the region of 0.5 µm therefore isotropic scaling of the whole geometry by a scale factor of 1000 was implemented. COMSOL FEA software could then be used to reduce the geometry back to the desired size at the

geometry importation step. The scale bar on the Figure was used when resizing the whole image in order to correlate SOLIDWORKS' dimensions with those of the image. Secondly reference planes were inserted vertically across the contour map, equally spaced for the most part but packed more tightly at regions of importance and areas displaying steeper thickness changes. Notice in Fig. 2.8 that the planes continue beyond the extents of the membrane edge and two horizontal planes are inserted, one above the top edge and one below the bottom edge of the TM. The intersection of these planes forms a rectangular shape around the TM, with the geometry deliberately over-built to avoid any possibility of an instance of zero geometry at the membrane edges which could adversely affect meshing and matrix calculations within the modelling environment later.

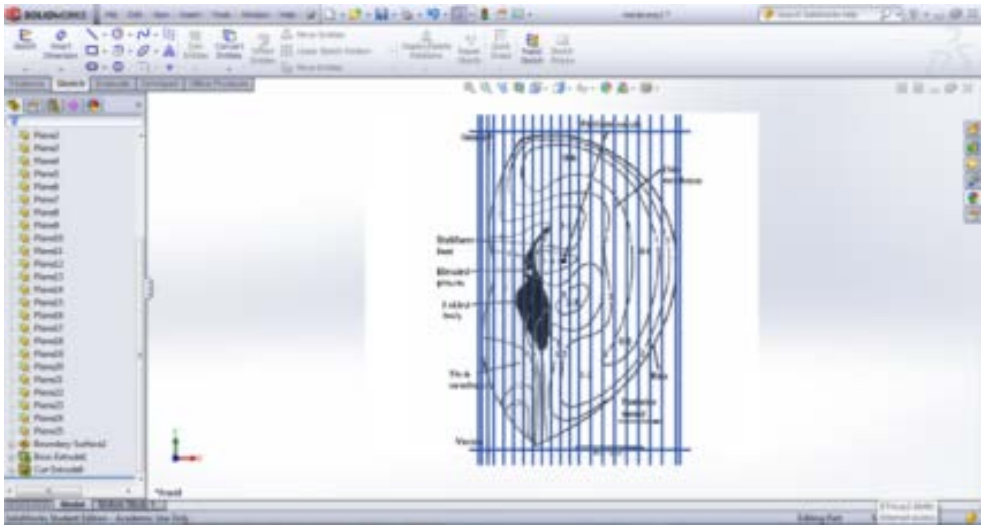

Figure 2.8 Reference planes inserted.

Next the whole sketch was flipped horizontally so that a right sided model ear was created, when visualising it from an external view, to match the majority of the literature on the ear of the desert locust. On each of the vertical planes a non-uniform rational B-spline was inserted, and a number of spline control points placed methodically along each spline, to roughly coincide with different contour lines. Each of these control points is then fixed at an exact height in the Z-axis direction (out of the page towards the reader), dependent on the closest contour thickness value. All of those points outside the edges of the TM were set at some constant height matching the nearest membrane edge thickness. Fig. 2.9 shows the culmination of these steps.

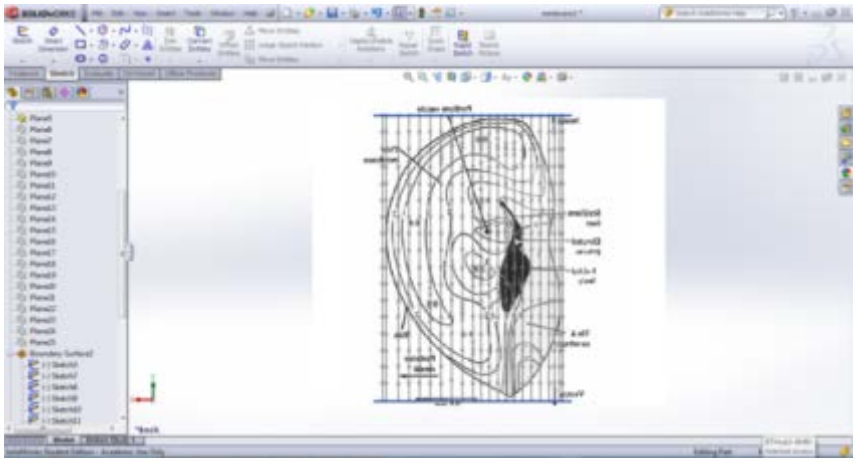

Figure 2.9 Splines (with multiple control points) drawn on planes.

All of the vertical profile splines were then carefully knitted together using the boundary surface tool, creating a shell with a contoured shape but no actual third dimension of thickness. Extruding from a plane exactly 0.6 mm below the surface i.e. 1000 times the smallest thickness on the contour map, resulted in a thin 3-D sheet which when viewed from the top has a rectangular profile but from the side has a profile with varying height depending on the tympanal membrane thickness at that point. The view in Fig. 2.10 is angled in a manner which clearly displays the thickness variations across the membrane surface and recognisable features such as the thin section around the PV area and also the thick region are clearly visible.

The final step was simply to trace the membrane outline using a spline and then use that sketch to extrude a cut through the whole 3-D solid leaving the geometry shown in plan elevation view in Fig. 2.11 and a slightly rotated and angled view in Fig. 2.12.

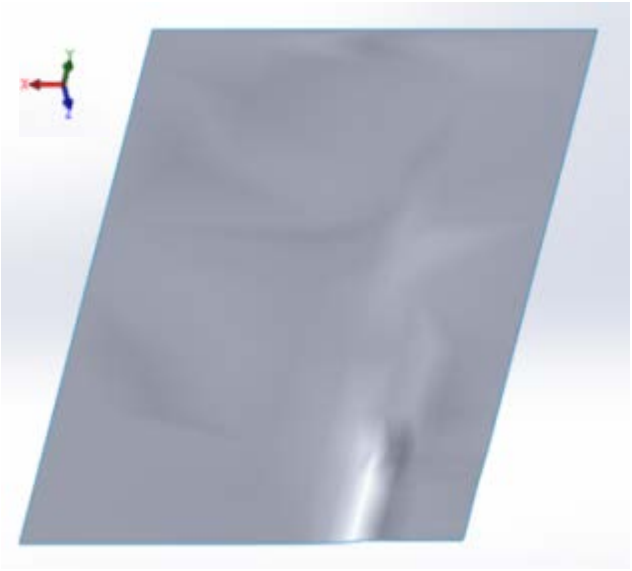

Figure 2.10 Boundary surface knit and thin extrusion edited screenshot from SOLIDWORKS.

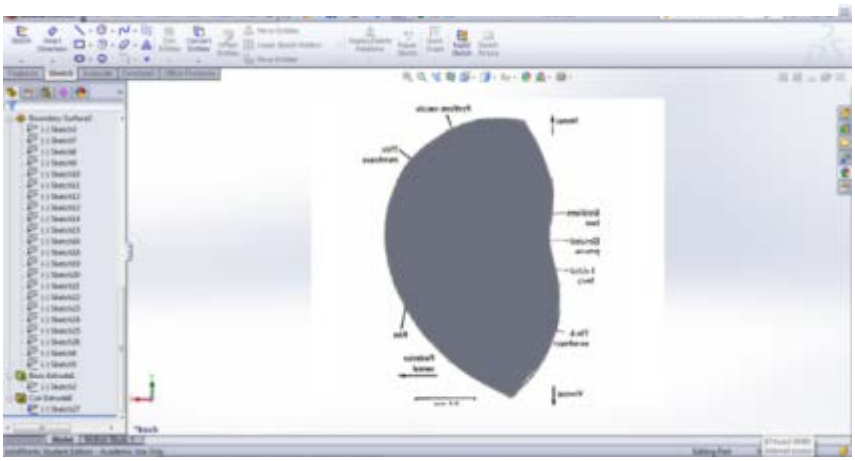

Figure 2.11 Extruded cut using spline which traces the TM outline.

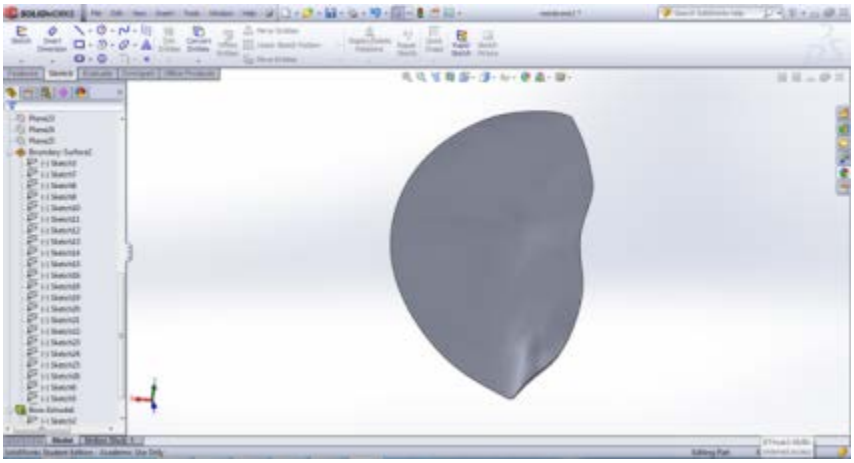

Figure 2.12 Final TM geometry angled to show varying thickness on surface.

In the following chapters, laser vibrometry, the finite element method and analytical modelling are all used to study the tympanal hearing system of a locust and to investigate the mechanical response of silicon MEMS structures. More in-depth, subject-specific methods are included in these subsequent chapters which fully explain the hardware, software and all settings and parameters utilised throughout the thesis.

Chapter 3 : Locust Hearing System – Laser Doppler Vibrometry and Introductory Finite Element Analysis

"*Look deep into nature, and then you will understand everything better*" – Albert Einstein

This chapter begins by characterising the vibrational response of the tympanal membrane of the desert locust using micro-scanning Laser Doppler Vibrometry. Finite Element Modelling is then used to analyse the response of simple 3-D circular disc models, in particular, using large sweeps on the defining characteristics and also simulating the acoustic-response of the discs.

3.1 Characterising the Response of the Locust Ear

The tympanal hearing system of the desert locust, *Schistocerca gregaria*, consists of a stretched tympanal membrane backed by a tracheal air sac. The mechanosensory Müller's organ is attached to the interior surface via a number of cuticle adaptations. Subchapter **1.3** covers the morphology as well as the neurophysiological and mechanical response of the hearing system in an extensive review. Fig. 1.10(a) shows an external view of the right side locust tympanum.

In 1971 (1971b), Michelsen concluded that the locust ear appeared to be a true resonance system and also that the origin of the ability to perform frequency discrimination was purely physical. Windmill et al. (2005 and 2008) found that travelling waves are generated on the tympanum as a response to sound with a variety of frequencies. Laser vibrometry showed two main travelling wave types, one at lower frequencies which channelled the energy to the folded body (and associated low frequency receptor cells), and the other at high frequencies which appeared to transfer energy to the pyriform vesicle (and attached high frequency tuned receptor cells).

This section is dedicated to the characterisation of the travelling waves seen on locust tympanal membranes for a variety of different stimulus frequencies, using micro-scanning laser Doppler vibrometry. The purpose of this investigation was to highlight any potential previously unreported features and categorise the locust TM vibration response into travelling wave pattern types.

The first step was the experimental frequency response analysis of 23 desert locusts (12 male – 7 in their gregarious phase and 5 solitary, and 11 female – 6 gregarious and 5 solitary) followed by an in-depth observation of the variety of travelling waves formed on the locust tympanum, each of which is dependent upon the frequency of the incident sound.

For this a micro-scanning laser Doppler vibrometer (Polytec PSV-300-F; Waldbronn, Germany) was used with a close-up scanning head unit (OFV-056) attached (see Subchapter **2.1**). Capable of measuring picometre vibrational displacements, this setup provides a non-invasive, non-contact method of studying the complex vibrational pattern of the locust tympanal membrane *in vivo*.

The environmental conditions in the laser vibrometer room were a temperature of 23°C and relative humidity of 50%. Both the vibrometer itself, including laser head, and any sample were mounted on a floor panel isolated from the rest of the room to reduce unwanted structural vibrations.

Each locust had its right forewing and hind wing removed allowing exposure of the majority of the tympanum to the laser which had a spot diameter, when sharply focussed on the membrane, of approximately 3 – 5 μm. The locust was positioned ventral side down, restrained with Blu-tack (Bostik-Findley; Stafford, UK) and rotated slightly until at an angle which facilitated a large area of the tympanum surface to be scanned, keeping the incident laser beam as close to perpendicular to the TM surface as possible. The sound stimulus consisted of a periodic chirp and was generated internally by the arbitrary waveform generator (National Instruments PCI-6111; Austin, TX) within the vibrometer workstation. The loudspeaker (ESS Heil Air Motion Transformer; South El Monte, USA) was connected to the generator output from the workstation via an amplifier (Sony TA-FE370; Tokyo, Japan). As a reference, a precision pressure microphone (Brüel & Kjær 4138; Nærum, Denmark), connected to a preamplifier (Brüel & Kjær Nexus 2690; Nærum, Denmark), was placed in close proximity to the TM of the locust and measured the incident sound spectrum as a signal voltage across the range of frequencies included in the broadband chirp. This sound spectrum was then inverted with respect to magnitude and the reciprocal values were used to create an amplitude correction data file. By importing this amplitude correction file into the vibrometer's software control panel the sound stimulus was then transformed to ensure a fairly constant RMS sound pressure of 35 mPa (≈ 65 dB SPL re 20 μPa) across the frequency spectrum. This process was repeated for each scan, i.e. whenever a new locust was used. Since frequency domain data was required, the Fast Fourier Transform acquisition mode of the LDV was utilised, with complex averaging selected and 15 averages acquired at each scan point. With this averaging technique enabled, the measurement noise floor was 3 pm, and was consistent for the vibrometry experiments throughout this thesis. Each scan consisted of approximately 330 – 350 scan points. The frequency content and duration of the sound stimulus were governed by the vibrometer bandwidth selection and Fast Fourier Transform

sampling characteristics. A bandwidth of 40 kHz was chosen with a lower cut-off frequency of 1 kHz and an upper cut-off of 30 kHz. Measurements for both laser and microphone signals were recorded at a sampling rate of 102.4 kHz. Conversion to the frequency domain via the FFT using a rectangular window and 3200 FFT lines resulted in a frequency resolution of 12.5 Hz and a sample time of 80 ms (optimised by the software based on the bandwidth and FFT settings). Using the method shown in Subchapter **2.1** the amplitude of the transverse velocity gain (in $ms^{-1}Pa^{-1}$) and the phase response of the locust hearing system was obtained for the chosen range of frequencies. Integrating this gives us the amplitude of the displacement gain (mPa^{-1}) across all frequencies. For each locust the amplitude of the displacement gain is displayed as well as the displacement phase averaged at each point across the TM for selected FOI's. The amplitude of the displacement gain and the phase is then combined to show the instantaneous transverse displacement gain at different cycle phase angles.

The first locust in the sample was male and in the solitary phase (approx. TM size 2.8 × 1.7 mm). Fig. 3.1 below shows the full amplitude-frequency response curve for the average spectrum with displacement gain on the Y-axis. Vertical cursor lines indicate FOI's where snapshots of the travelling waves were taken for later images. Areas of higher and lower sensitivity of auditory response (peaks and troughs respectively) are apparent. The frequency response curve in Fig. 3.2 illustrates the displacement gain of the membrane between 1 and 5 kHz.

1812.5 Hz was the first FOI (red line on Figs. 3.1 and 3.2) and for this locust tympanum the magnitude of the average displacement gain was 37 $nmPa^{-1}$. At this particular frequency the whole membrane appeared to deflect with uniform displacement phase, including parts in the thin region and also beyond the FB into the opaque thicker region.

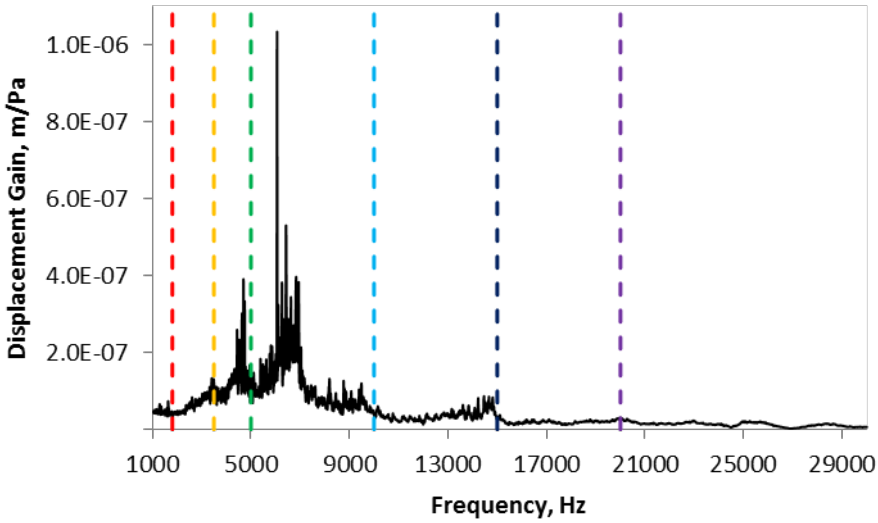

Figure 3.1 Frequency response curve for locust from 1 to 30 kHz.

Near the lower (ventral) end of the folded body the amplitude of displacement reached an instantaneous maximum of approximately 104 $nmPa^{-1}$, close to the ridged interface between thin membrane and thick membrane. Snapshots of the vibration pattern at wave cycle phases of 0°, 45°, 90°,……, 360° (Fig. 3.3) show the whole membrane moving coherently, almost like the standing wave seen at the fundamental drum mode of a circular membrane. Red depicts displacement towards the reader and green for deflection into the page. The maximal deflection (see vibrational pattern at 45°) covers an area which ranges from near the PV position, ventro-anteriorly across most of the folded body and includes an area on the opaque thick membrane.

3.5 kHz (orange line on Figs. 3.1 and 3.2) was the next FOI and the average magnitude of the displacement gain was approximately 122 $nmPa^{-1}$ at this frequency. The displacement phase was fairly constant across the entire TM apart from a small region of the thick opaque membrane at the membrane's most extreme anterior edge. Fig. 3.4 shows the full dynamic cycle at this frequency from 0° to 360° with a 45° step.

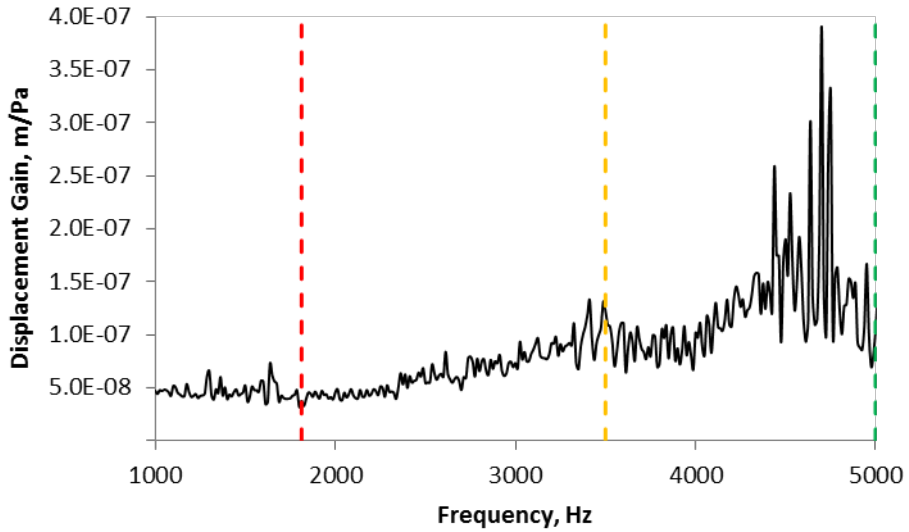

Figure 3.2 Locust's frequency response for 1 to 5 kHz.

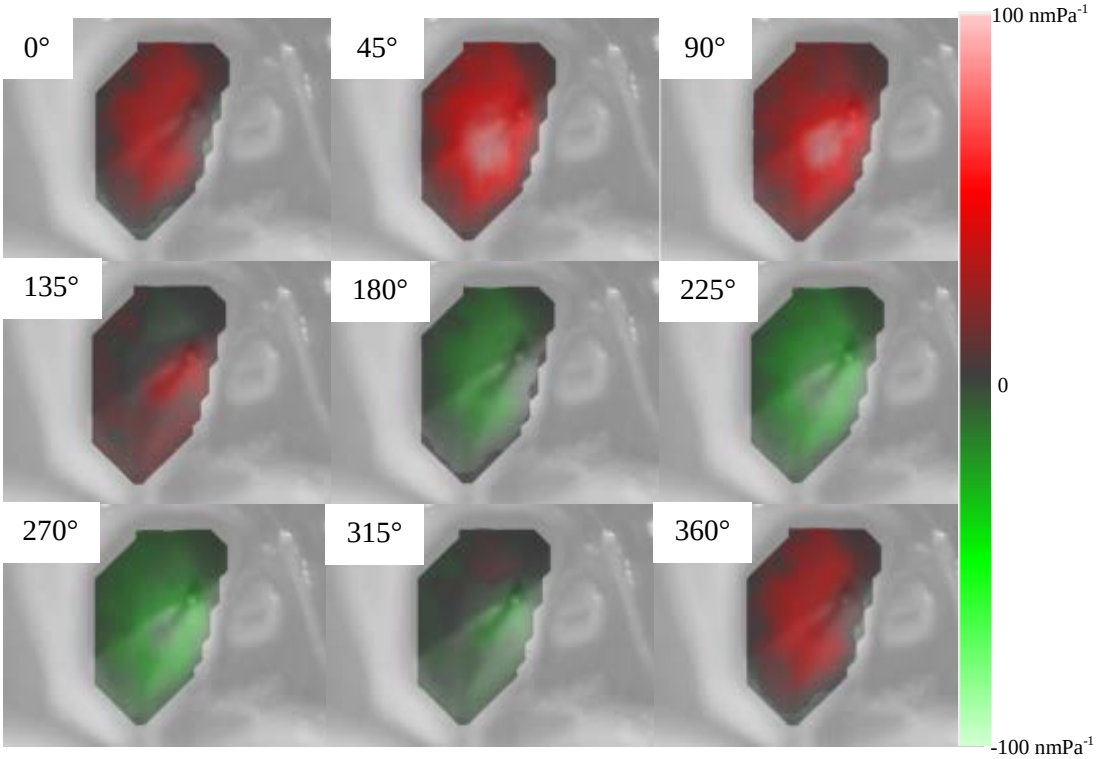

Figure 3.3 Dynamic cycle of locust tympanum vibration at 1.8 kHz.

The vibration now displays a travelling wave, with origin towards the top left of the TM on the thin membrane and travelling diagonally, both downwards and right, towards the FB where it reaches a maximum displacement gain of nearly 400 $nmPa^{-1}$ in the region of the FB. The majority of the maximum deflection was concentrated on an area close to that seen for 1.813 kHz, but perhaps a little higher

and further left, with the maximum spread much further along the length of the FB (see cycle phase angles 135° and 180°). There is still some propagation of the wave beyond the FB region into the opaque thick region. Interestingly when the frequency was manually switched up in small steps from 1.813 kHz to 3.5 kHz the motion of the tympanum moved gradually away from the initial standing wave (with fully coherent nature) towards a gradual development of the diagonal travelling wave with the observed travel clearly strengthening as the frequency increased towards the slight peak seen in response between 4 and 5 kHz.

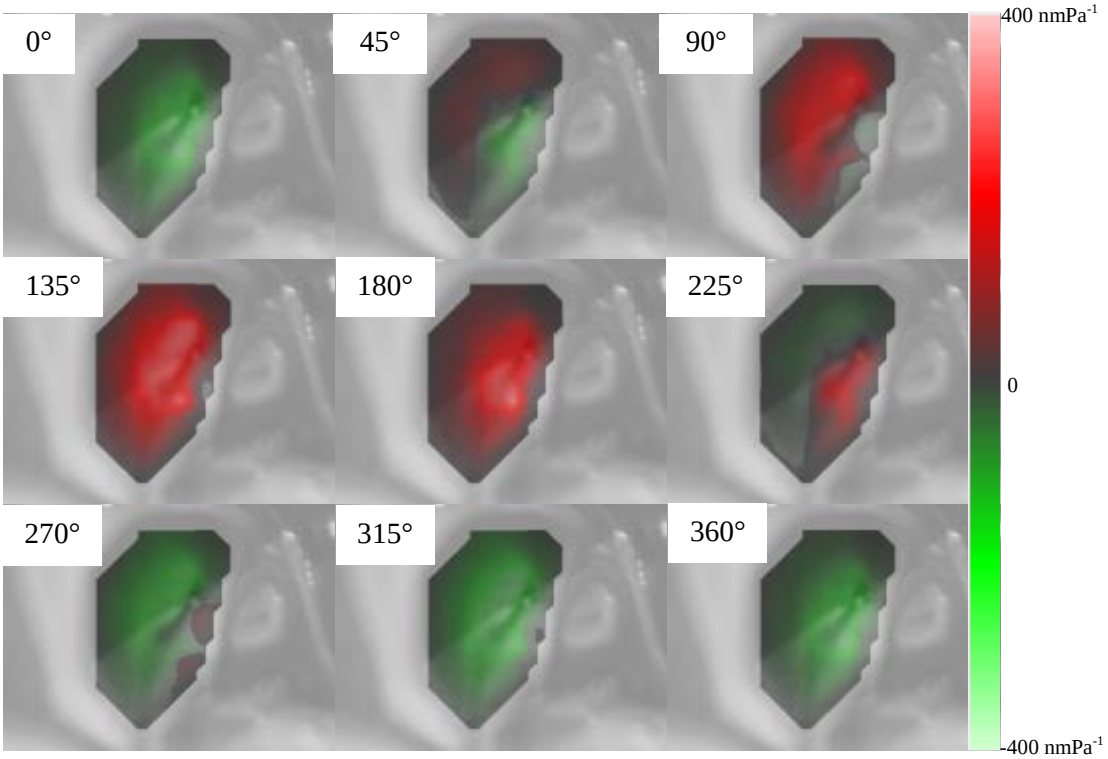

Figure 3.4 Dynamic cycle of locust tympanum vibration at 3.5 kHz.

Fig. 3.5 displays the frequency response curve for the displacement gain of the membrane between 4 kHz and 11 kHz, as measured by LDV. Green and blue vertical markers indicate the next two FOI's of 5 kHz and 10 kHz respectively. At 5 kHz the average magnitude displacement gain was ~ 105 $nmPa^{-1}$ and the displacement phase showed a central divide in the membrane with one half clearly out of phase with the other.

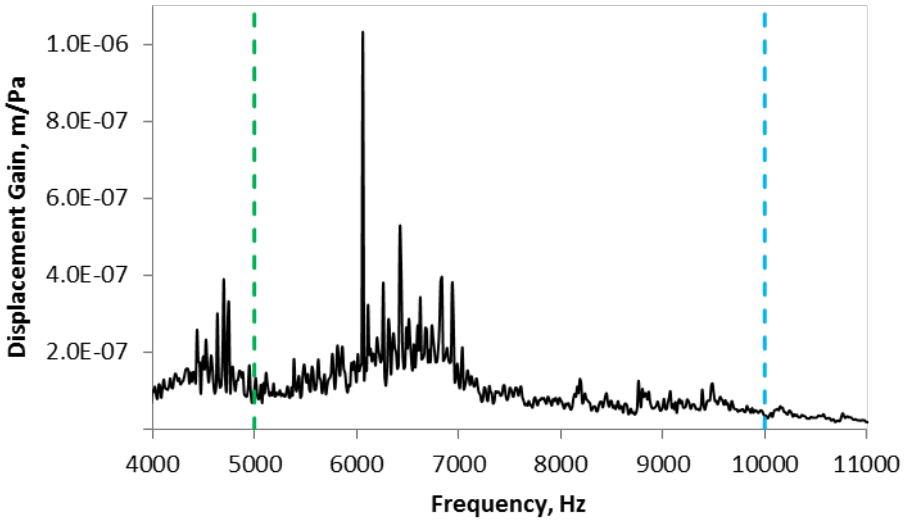

Figure 3.5 Frequency response curve for locust from 4 to 11 kHz.

Displacement gain maximum was approximately 250 $nmPa^{-1}$ and Fig. 3.6 shows the full cycle TM deflection pattern for this frequency. The travelling wave at this frequency took a more noticeably horizontal path than at 3.5 kHz, with no visible downward component to the wave progression. The change from the diagonal motion towards the horizontal motion was observed as gradual as the frequency was increased towards 5 kHz and then beyond up to 6 and 7 where the same horizontal travelling became even more apparent. The maximum outwards deflection appears at a cycle phase equal to 180° – 225° where the strongest motion of the tympanum is now far more widespread than previously covering a large region around and over the whole FB. The displacement still appears strong immediately beyond the FB, even more so perhaps than at lower frequencies.

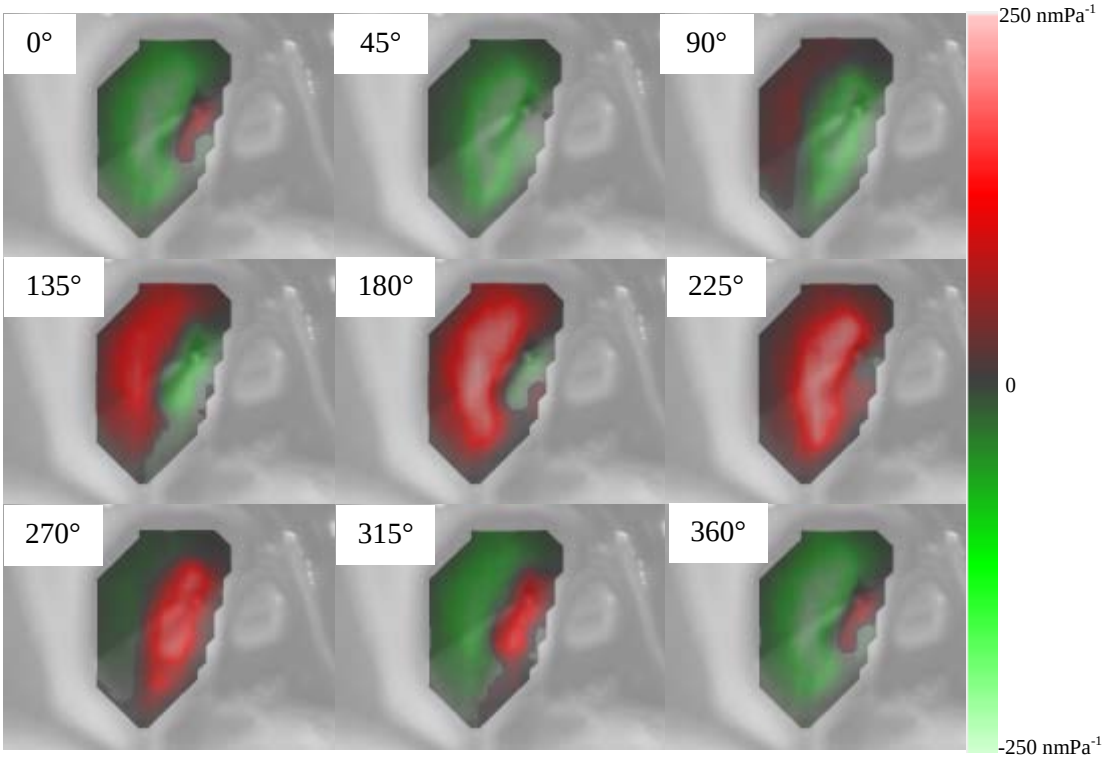

Figure 3.6 Dynamic response of TM at 5 kHz.

Indicated by the blue line on Fig. 3.5, the next FOI was 10 kHz where the average displacement gain was ~ 35 $nmPa^{-1}$ and the displacement phase pattern showed a semi-concentric (‘C-shaped’) region out of phase with the region around and including the FB. Fig. 3.7 shows the full dynamic cycle of the vibration of the TM at 10 kHz at each phase angle. The travelling wave has clearly switched from the earlier horizontal motion to a more complex pattern, beginning with a semi-concentric C-shaped outwards displacement at the thin region while the central area of the TM is deflected inwards. The FB appears to be in phase with the movement of the thin region. This C-shape then converges into a smaller surface area and becomes a greater outward deflection, forming a maximum in the region immediately surrounding the PV (180° – 225°). The total area of the main deflection immediately surrounding this maximum is far smaller than that seen previously at 5 kHz at 225° in Fig. 3.6. The switch from the travelling wave at 5 kHz to that seen below was observed to occur quite abruptly in the region of 7 – 8 kHz.

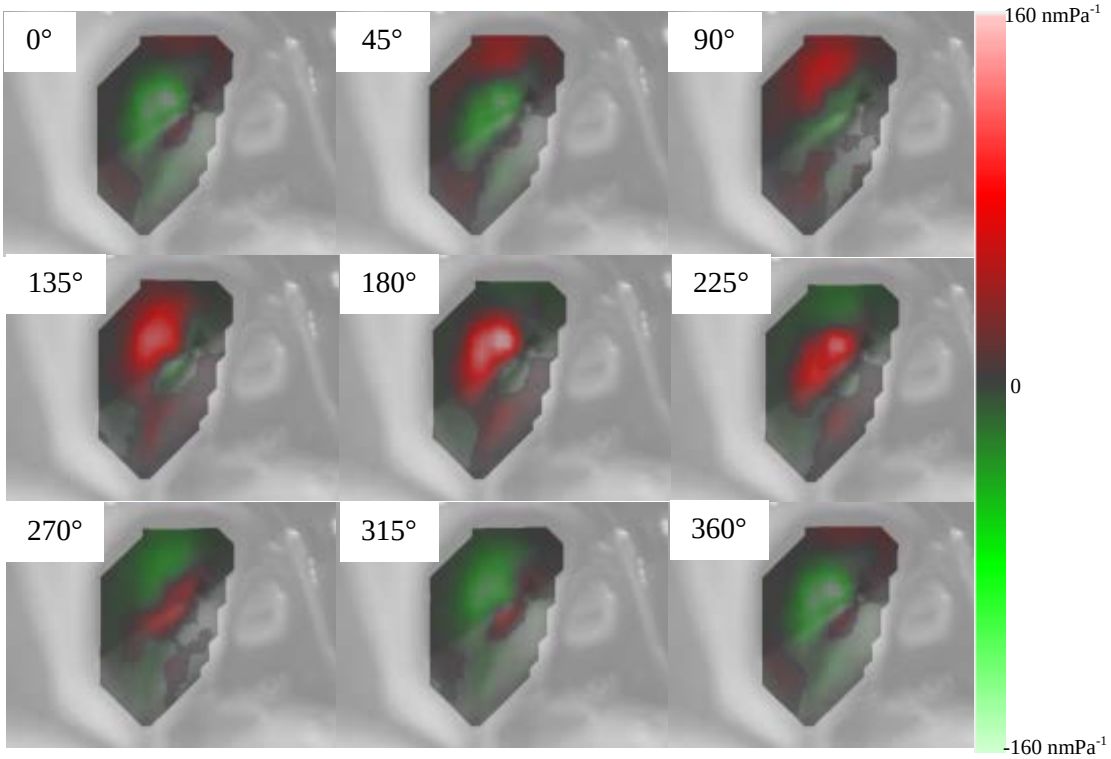

Figure 3.7 Vibration of TM at 10 kHz.

The penultimate FOI was 15 kHz, as indicated by the indigo coloured marker on Fig. 3.8. At this frequency, the TM displayed an average displacement magnitude of ~ 33 $nmPa^{-1}$. Fig. 3.9 shows the progression of this travelling wave pattern for a full cycle. Although quite similar to that observed at 10 kHz closer inspection revealed that the C-shaped outward displacement seen at 270° – 315° was spread over a far greater area of the tympanum surface. There was also a concentration of the wave into a much smaller area while travelling to the PV than that seen at 10 kHz.

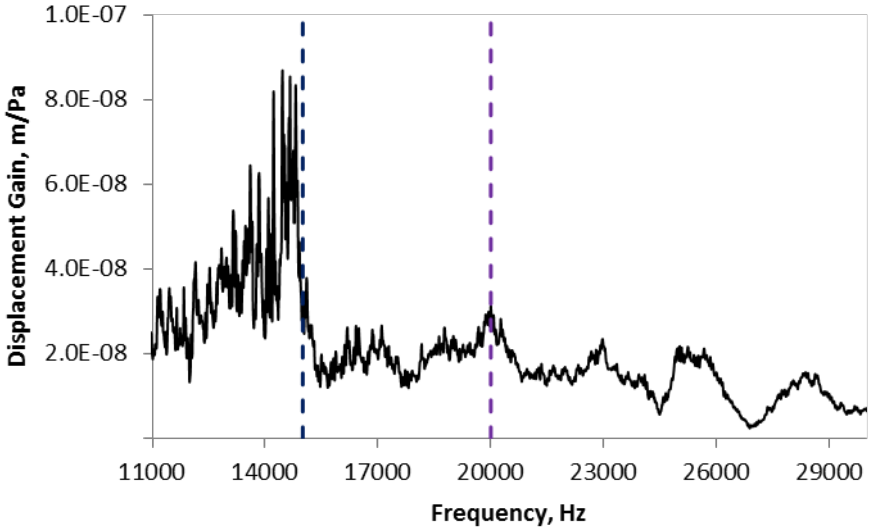

Figure 3.8 Frequency response of locust TM from 11 to 30 kHz.

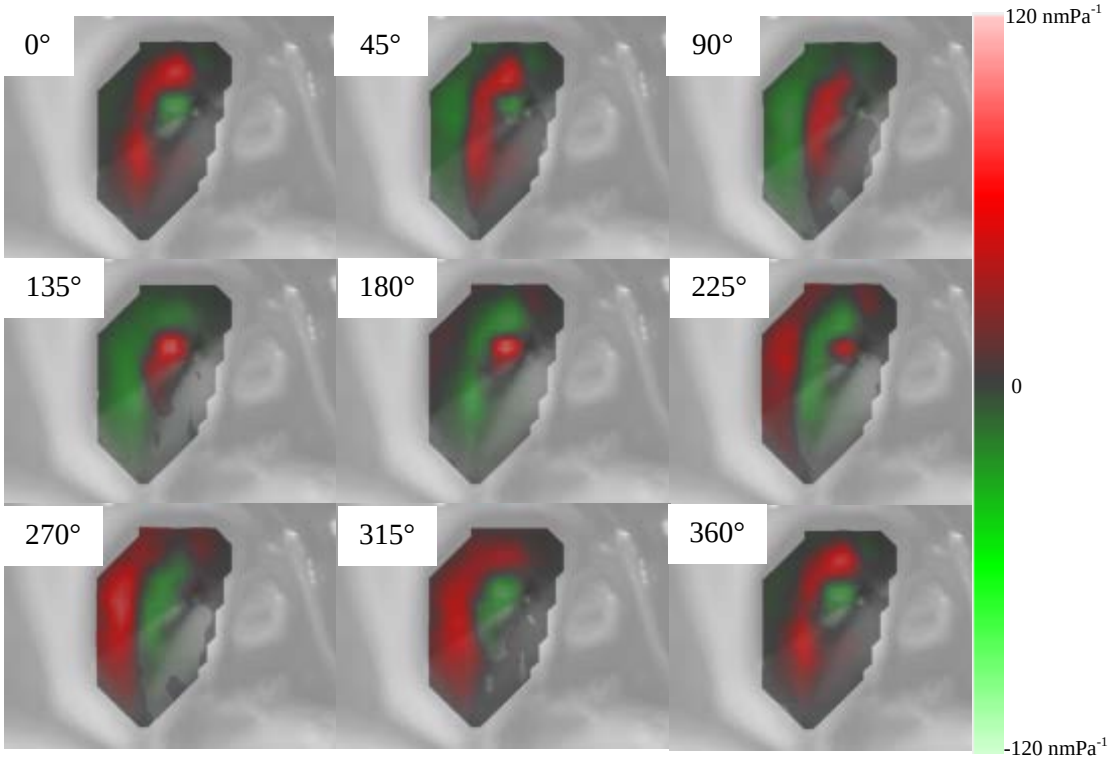

Figure 3.9 Travelling wave pattern on tympanum at 15 kHz.

The final difference is that while the PV area still had a noticeably red outwards displacement, the characteristic C-shape of the travelling wave had already

begun forming on the far left of the TM whereas previously at 10 kHz the wave had almost completely faded out at the PV before the C-shape began to form. With the addition of a new antinode as the frequency increased, this change in response is characteristic of a modal system. In the region of 13.5 kHz is where the change in vibration pattern was observed to occur.

Below in Fig. 3.10 the full dynamic cycle at the final FOI of 20 kHz is displayed. An average displacement of 31 $nmPa^{-1}$ was observed for this frequency and the travelling wave propagation across the tympanum appeared very similar to that seen at 15 kHz. This trend continued from 20 kHz right up to the 30 kHz maximum frequency of the chirp sound stimulus.

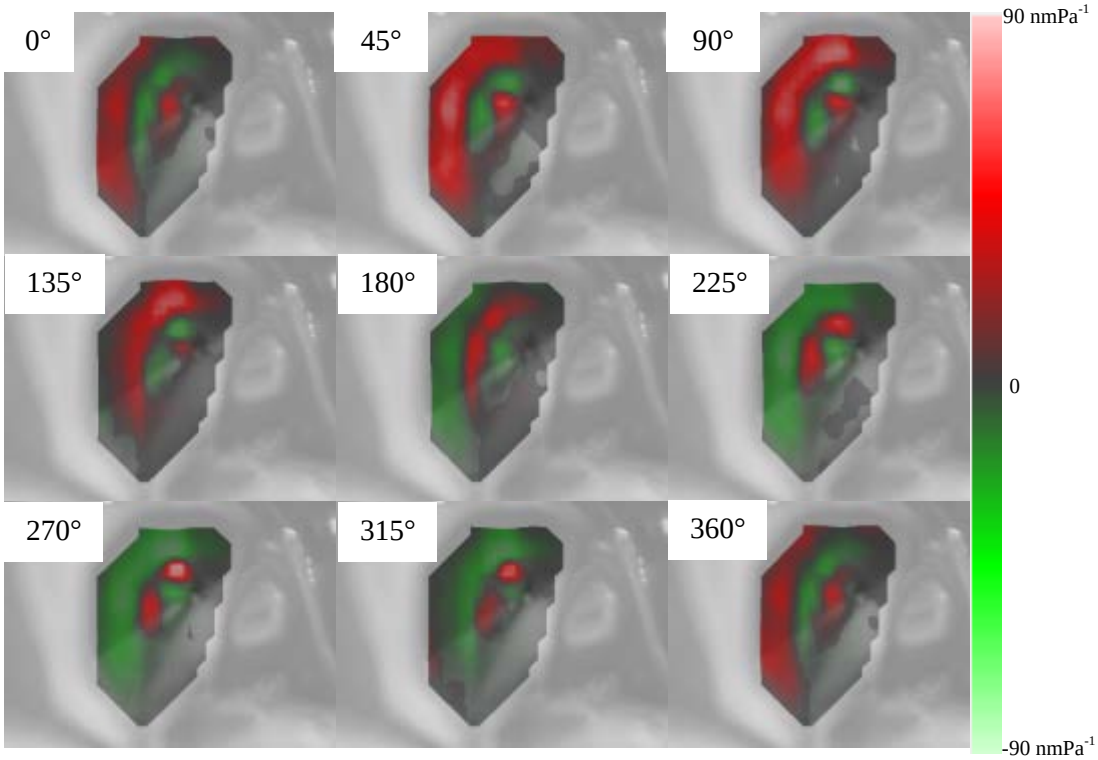

Figure 3.10 Dynamic response of TM at 20 kHz.

The second locust in the sample was female and in the gregarious phase (approx. TM size 3.0 × 1.6 mm). Fig. 3.11 below shows the full amplitude-frequency response curve for the average spectrum with displacement gain on the Y-axis. Vertical lines, with the same colour scheme as in Figs. 3.1, 3.2, 3.5 and 3.8, mark the identical frequencies of interest at 1812.5 Hz, 3.5 kHz, 5 kHz, 10 kHz, 15 kHz and

20 kHz. Similarly to Fig. 3.1 there were visible peaks and troughs in the auditory response.

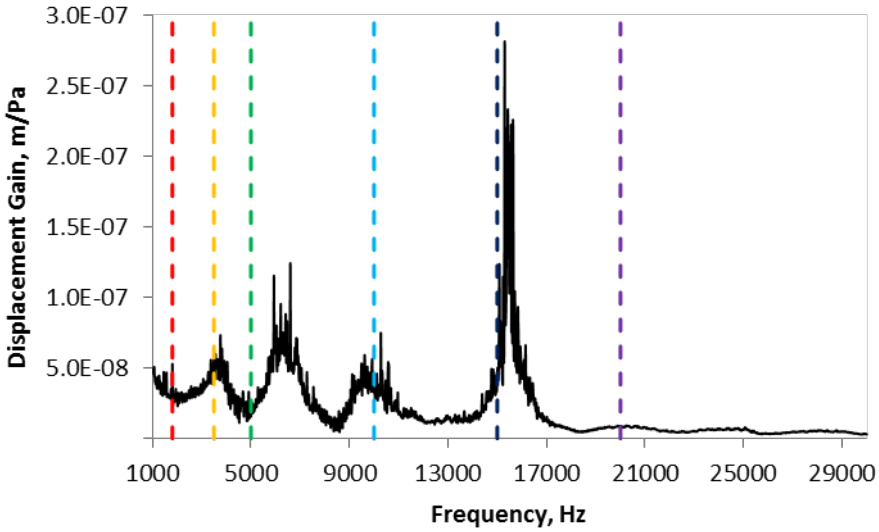

Figure 3.11 Full frequency response of locust TM from 1 to 30 kHz.

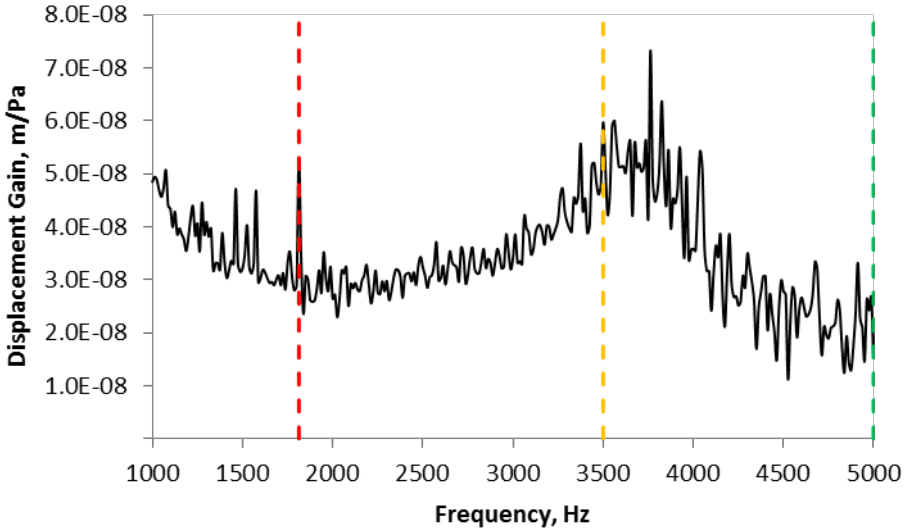

Figure 3.12 Snapshot of response from 1 to 5 kHz.

The vibrational response of this locust tympanum at 1.8 kHz is shown by the instantaneous displacement gain snapshots below and again the transverse displacement displayed uniform phase across the whole membrane. Thinking of the vibration at this frequency as a standing wave, the position of the antinode, as shown

in Fig. 3.13 at 45° phase, was shifted slightly both dorsally and posteriorly when compared to the male locust's response, although it remained maximal around the lower edge of the FB. The total surface area of the maximal deflection was approximately the same size as previously and the instantaneous maximum amplitude of displacement gain was approximately 140 $nmPa^{-1}$, again in the location where the FB stops and the ridged boundary between the two membrane zones begins. An average magnitude displacement gain across the points of ~ 53 $nmPa^{-1}$ was recorded at this frequency for this insect.

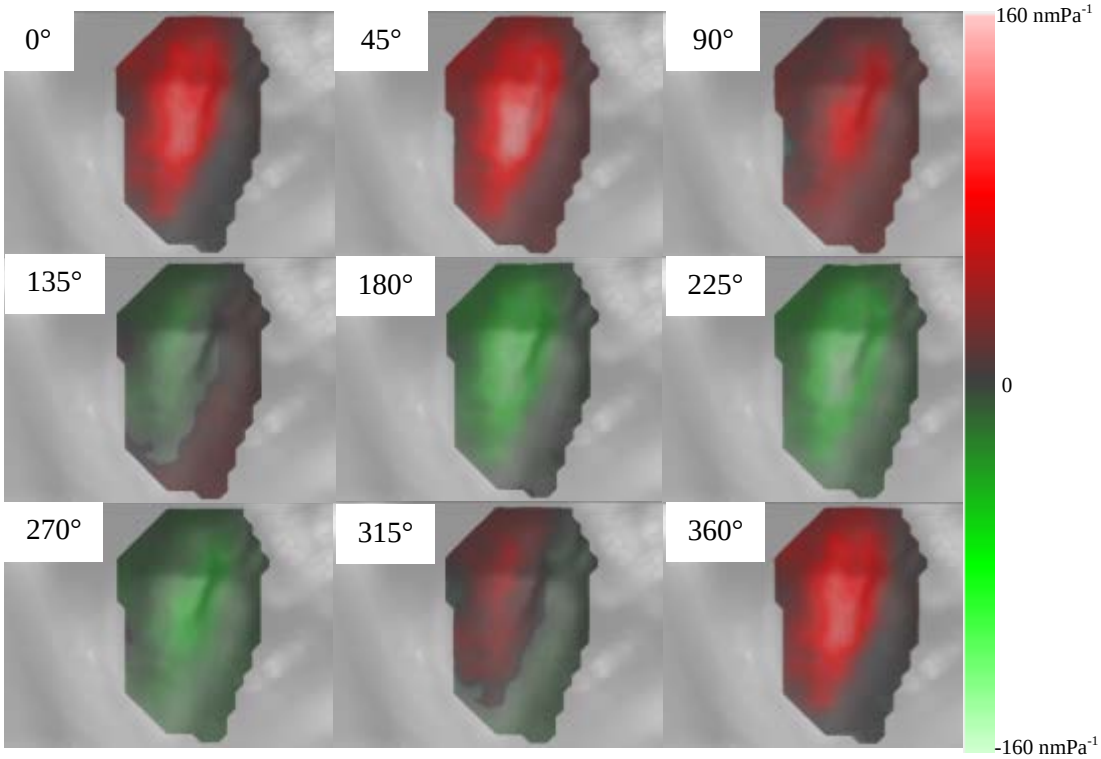

Figure 3.13 Mechanical vibration of TM at 1.8 kHz.

At 3.5 kHz the response of this locust had an average magnitude of 60 $nmPa^{-1}$ and a full dynamic cycle of the travelling wave is shown in Fig. 3.14. The same diagonal travelling wave as in Fig. 3.4 was observed, from the thin region across to (and beyond) the FB.

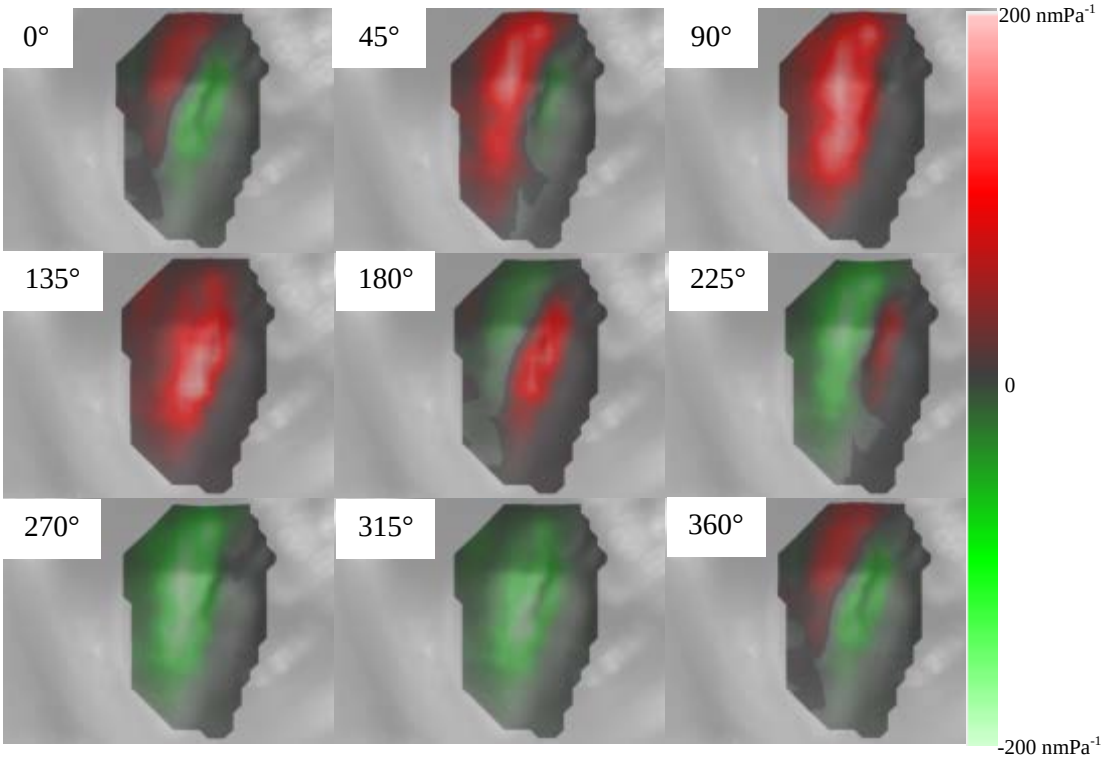

Figure 3.14 Vibration of TM at 3.5 kHz.

Wave phase cycle snapshots of the response at 5 kHz are in Fig. 3.16 and the average magnitude for this frequency was 15.7 $nmPa^{-1}$. The same travelling pattern can be seen as that observed in Fig. 3.7, with slightly more horizontal motion than the diagonal motion at lower frequencies.

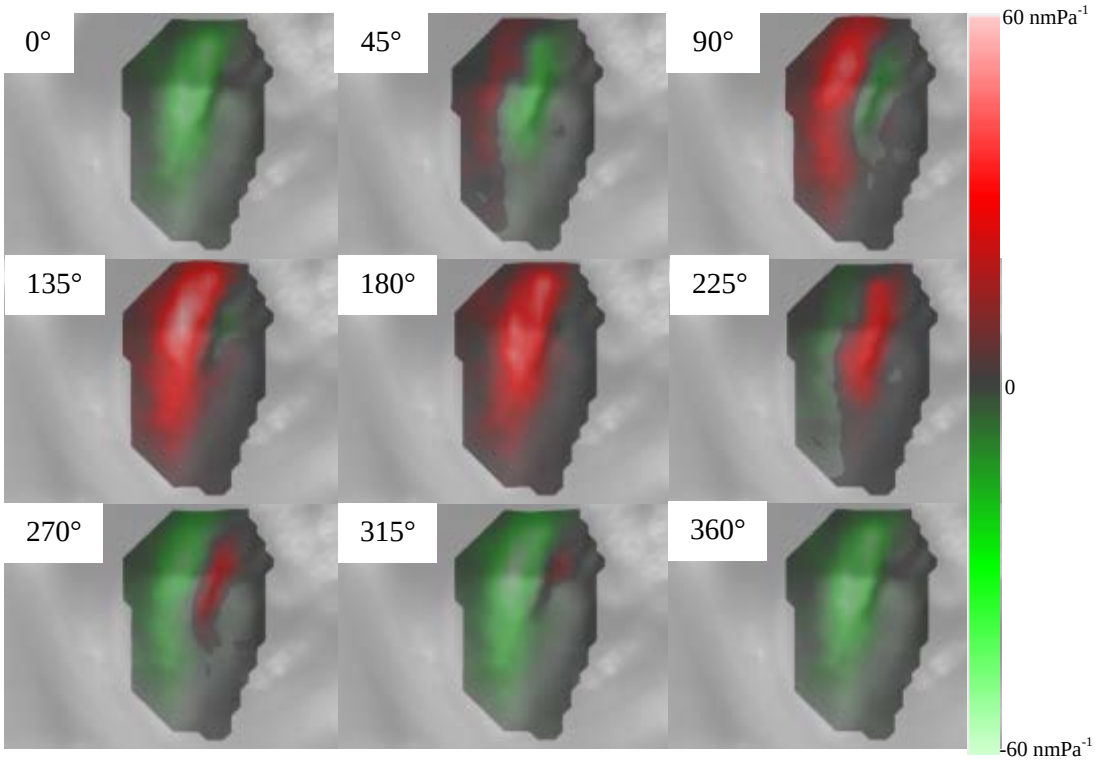

Figure 3.15 Dynamic response of membrane at 5 kHz.

Fig. 3.16 shows the blue line for 10 kHz where the average displacement gain was ~ 35 $nmPa^{-1}$. The full dynamic cycle of the vibration of the TM at this frequency is in Fig. 3.17. The same complex pattern, beginning with a semi-concentric C-shaped displacement in the thin region out of phase with the central area of the TM, (as in Fig. 3.7) was observed. Again, the switch from the wave seen at 5 kHz to that seen at 10 kHz occurred in the region of 7 – 8 kHz.

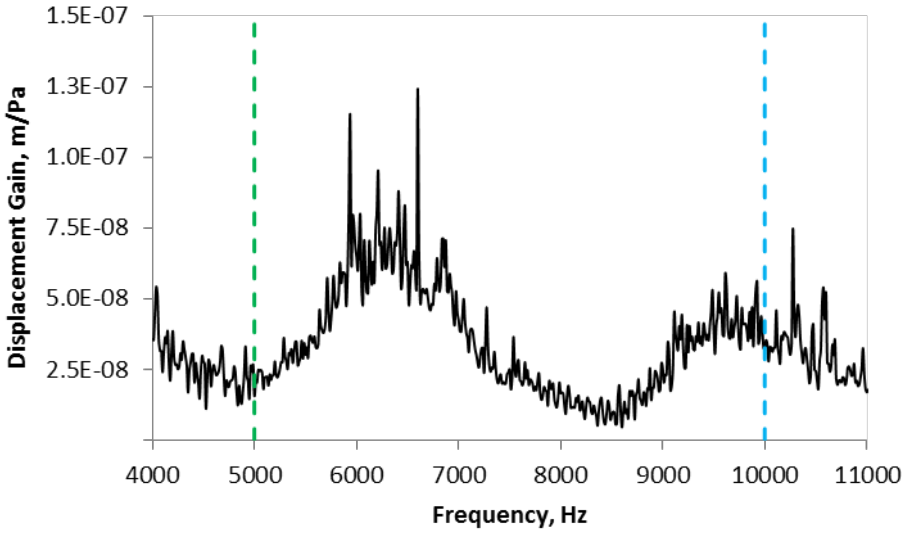

Figure 3.16 Frequency response of TM from 4 to 11 kHz.

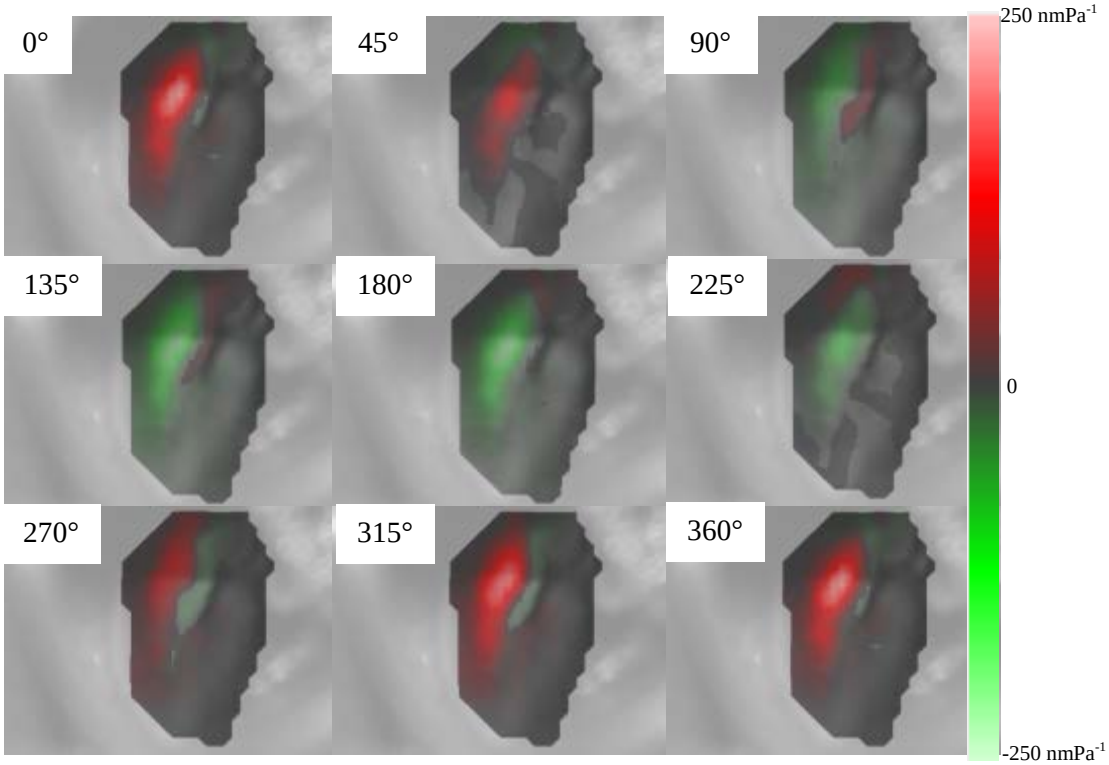

Figure 3.17 Travelling wave pattern on tympanum at 10 kHz.

The indigo marker on Fig. 3.18 is at 15 kHz where the TM displayed an average displacement magnitude of ~ 48 $nmPa^{-1}$. Fig. 3.19 shows the progression of

this travelling wave pattern for a full cycle. This is almost identical to that seen on the tympanum of the male locust (Fig. 3.9).

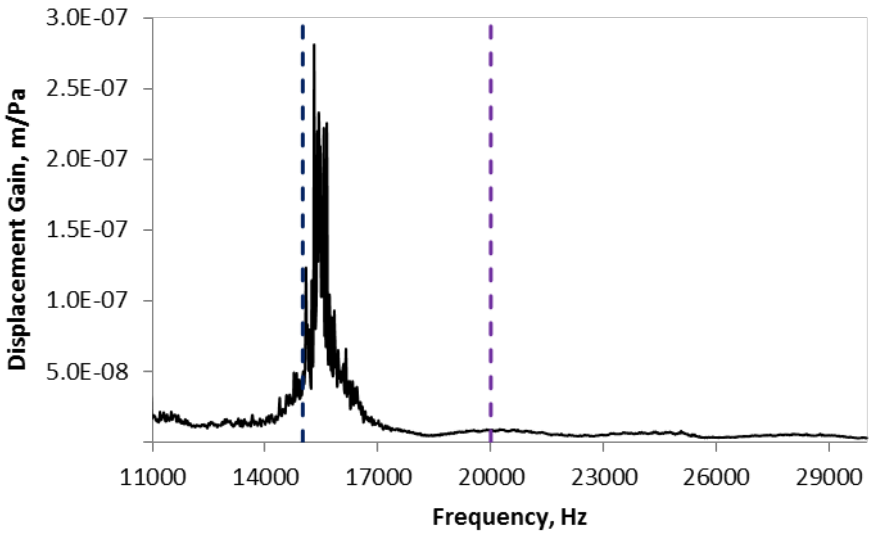

Figure 3.18 Response of TM for frequencies from 11 to 30 kHz.

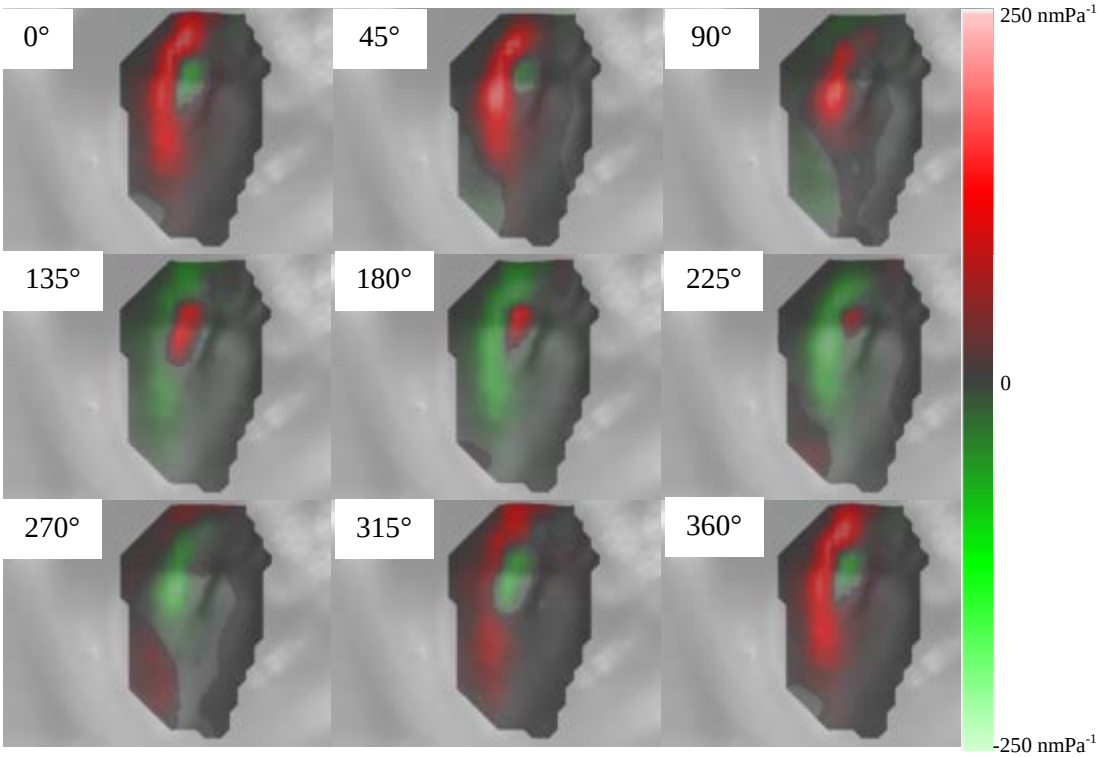

Figure 3.19 Travelling wave pattern at 15 kHz.

20 kHz is the final FOI and the full dynamic cycle is below. An average displacement of about 9 $nmPa^{-1}$ was observed for this frequency and the travelling wave propagation across the tympana is exactly the same shape as seen in Fig. 3.10.

Visual inspection of the frequency and phase response of every other locust in the sample showed a similar vibration pattern on the tympana at each of the frequencies highlighted above, regardless of locust sex or phase. Some specimens were more sensitive than others, but the displacement gain across all frequencies was usually of roughly the same order of magnitude for all specimens.

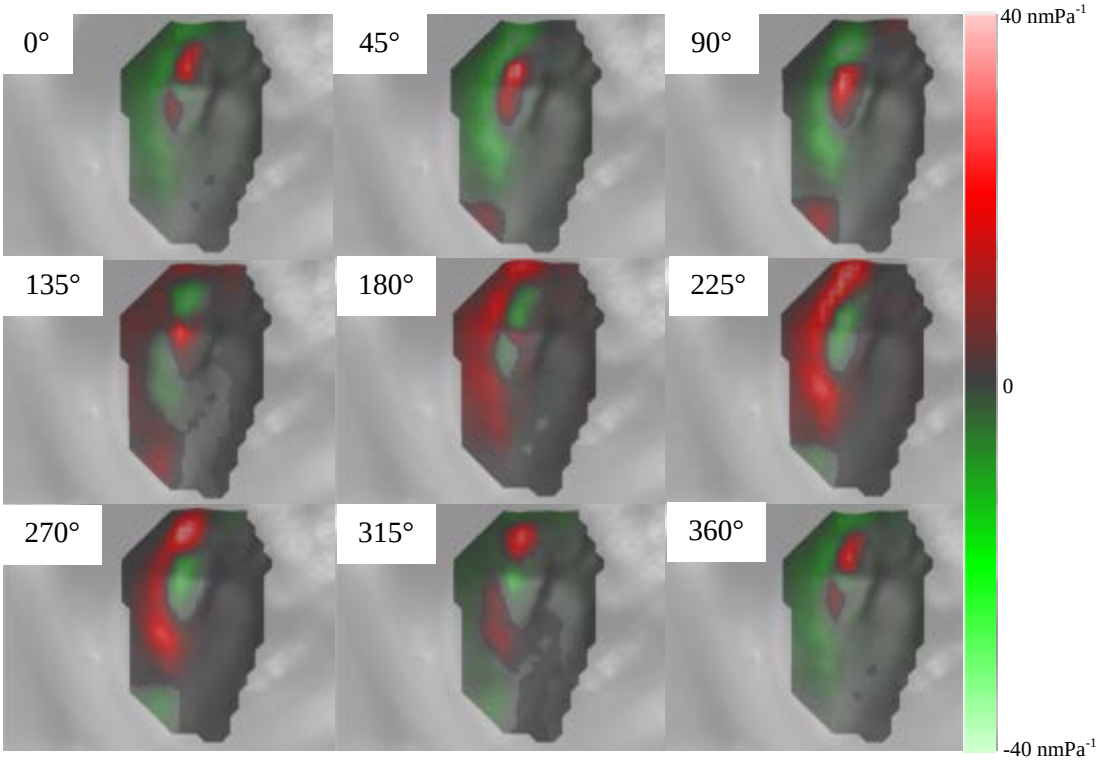

Figure 3.20 Dynamic cycle of deflection of TM at 20 kHz.

The second half of a travelling wave cycle is a direct opposite mirror image of the first half, with TM areas displaying positive displacement becoming equal but opposite negative displacement and vice versa.

Two features became apparent in this study of the formation of the locust tympanum travelling waves. Firstly, there existed characteristic frequencies, consistent across all locusts in the sample, at which there were abrupt switches from one travelling wave type to alternative patterns, depending on whether the stimulus frequency was decreased or increased. Secondly, components of the travelling wave deflection patterns such as the 180° phase switch through the centre of the TM seen at 3.5 kHz (and 5 kHz), the sharp peak travelling near the centre of the TM and the C-shaped maximum seen at higher frequencies were all reminiscent of elements of

the 2nd, 4th and 6th mode, respectively, of the circular disc modes displayed in Fig. 1.4. Combined with the observations made by Windmill et al. (2008) of large peaks in the average frequency response curve and in the response curves measured at strategically located points across the tympanum, this could indicate the presence of a complex system of coupled modes, with not only the equivalent circularly symmetric modes but also the asymmetric modes (such as numbers 2 and 6 of the uniform disc) having a strong influence on the overall response. The lack of observed nodal lines in the vibrational response of the locust TM could perhaps be attributed to a unique system of damping and the complicated superposition of both external and internal components of incident sound. In the following subsections these ideas are investigated further through the use of computational modelling of simplified components of the locust tympanal system.

3.2 Circular Disc Models

3.2.1 Eigenmode Analysis of Uniform Circular Discs

For a better understanding of membrane mechanics, the first step was a computational study of the modal response of circumferentially clamped circular discs which were reasonably similar in size to the locust tympanum. COMSOL Multiphysics was used to perform initial eigenmode analyses of these 3-D models (see *2.2.3.2*).

Theoretically, for a uniform thickness circular disc such as this there are infinite eigenmodes with each mode increasing in complexity through the addition of one or more nodal diameters or circles. In practice, due to the nature of FEA, the total number of modes solvable using this numerical analysis method is actually limited by the requirement for a finite number of elements and hence corresponding number of degrees of freedom.

Geometrical construction of the model membrane was the first step and for uniform discs this was implemented using the tools within the COMSOL modelling environment. The cylinder 3-D drawing tool was used specifying both the radius and thickness to create circular discs with their uniform thickness aligned with the Z-axis and the centre of the bottom face of the disc located at the origin (0,0,0) of the modelling workspace.

Material model type selection is the next step and a new isotropic material was created and defined by one physical property – the density, and two mechanical properties – the Young's modulus and Poisson's ratio. The effect of each of these properties on the model output was investigated.

The main boundary condition was setting a permanent zero displacement on the edges of the disc, i.e. a fixed constraint boundary condition. The remainder of the disc was left free to vibrate.

Initially COMSOL's physics-defined meshing was utilised with a mesh size setting of "normal" but a number of coarser and finer options were explored along with custom user-defined meshes. This setting uses 2-D triangular mesh elements to mesh boundaries and these connect to 3-D tetrahedral elements expanding across domains. Tetrahedral elements in COMSOL support adaptive mesh refinement,

meaning regions in close proximity to edges, points, boundaries and any unique geometry or area of particular importance, are meshed at a higher density than the rest of the domain.

The final input before running the default eigenvalue solver was the total number of eigenmodes to compute and therefore corresponding eigenfrequencies to calculate.

Initial dimensions for the uniform thickness circular disc were a radius of 0.75 mm and thickness of 50 μm. The effect on the eigenfrequencies, and therefore the disc's vibrational response, of changing these dimensions is included in this analysis. For these dimensions and mesh settings outlined above, the initial total tetrahedral mesh element count was 1434.

1.3.1 includes a thorough explanation and discussion about cuticle mechanical properties. As an initial value for locust TM cuticle density, the quoted value of 1200 kgm^{-3} was used (Jensen & Weis-Fogh, 1962; Wainwright, 1976). For Young's modulus an initial value of 1 GPa was used which is of the same order of magnitude as reported in a number of previous studies. A Poisson's ratio of 0.49 is used initially based on Liu et al.'s (2006) statement that "the Poisson ratio of most soft biological tissues is very close to 0.5". ν has no profound effect for values less than 0.4, however values greater than 0.4 have a significant effect on membrane mechanics (Aernouts et al., 2010; Malkin et al., 2013). The chosen values here contrasted the values of 1300 kgm^{-3} for the density, 20 MPa as E and ν of 0.3 used in a previous study on the finite element modelling of the locust tympanal ear by Malkin et al. (2013) (with E in MPa being of the order of published mammalian skin data). Ranges of each of these properties are tested using parametric sweeps to investigate their effect on the vibrational response. Modelling insect cuticle, understood to be a complex, viscoelastic and anisotropic laminar material, as an isotropic elastic material is obviously a simplification of the true model material type but combined with the published literature on insect cuticle properties, it provides a good baseline from which to investigate and simulate the response of insect systems.

Using the parameters above and running the simulation for the first six eigenmodes of this structure results in the mode shapes shown in Fig. 3.21 (seen in ***1.3.2***). As explained in *2.2.3.2* the colour scale for modes 1 – 6 represents the

normalised out-of-plane displacement field, red indicating transverse displacement towards the reader and green for displacements away from the reader with darker shades of red or green indicating greater amplitudes of displacement.

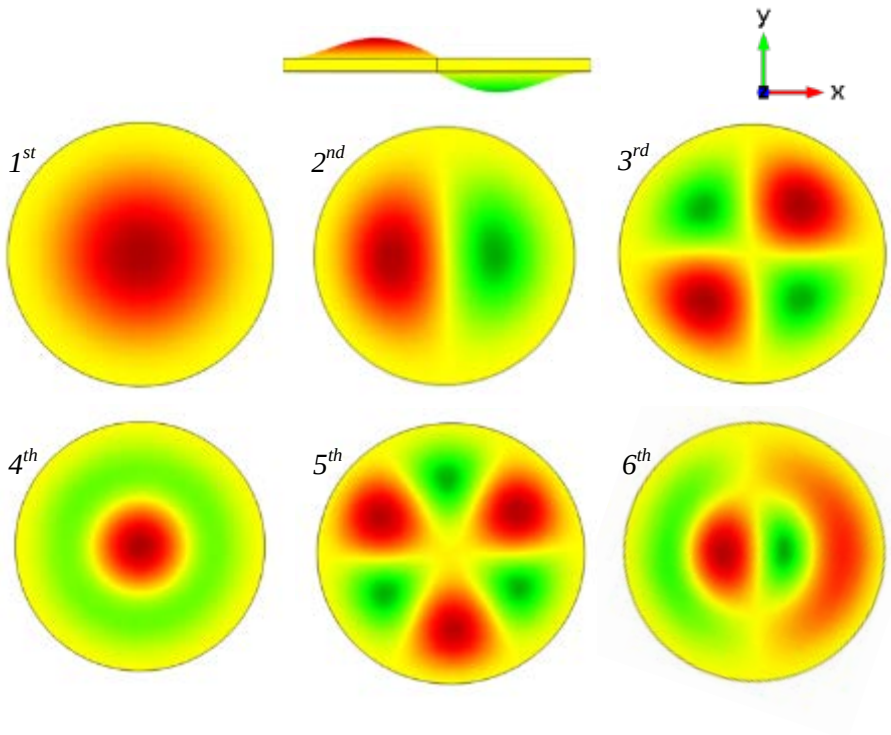

Figure 3.21 First 6 FEM-computed eigenmodes of uniform circular disc.

Using the method outlined in *2.2.3.2*, i.e. switching the normalisation type in the solver setting and re-computing the model, resulted in the calculation of effective modal mass fractions for each of these modes in each axis direction. Table 3.1 shows the corresponding eigenfrequencies and EMMF in the Z-axis direction of each of the 6 modes shown in Fig. 3.21.

Eigenmode	Eigenfrequency / kHz	$EMMF_z$ / %
1^{st}	48.85	49.36
$2^{nd}(1)$	100.11	6.02×10^{-5}
$2^{nd}(2)$	100.24	5.11×10^{-5}
$3^{rd}(1)$	162.13	3.66×10^{-4}
$3^{rd}(2)$	162.39	7.73×10^{-6}
4^{th}	185.10	17.83
$5^{th}(1)$	234.70	1.93×10^{-5}
$5^{th}(2)$	234.92	6.82×10^{-5}
$6^{th}(1)$	277.75	1.23×10^{-6}
$6^{th}(2)$	278.78	5.44×10^{-5}

Table 3.1 Eigenfrequencies of first 6 eigenmodes of circular disc and $EMMF_z$.

The fundamental mode (Fig. 3.21 and row 1 in Table 3.1), distinguishable by a centrally located antinode, has no nodal diameters and one nodal circle around the outside of the disc and is therefore denoted as the (0,1) mode. FEA computed the eigenfrequency of this mode as approximately 49 kHz with an $EMMF_z$ of almost 50%, by far the largest EMMF for any of these modes. With a constant displacement phase across the disc and the deflection spread across the majority of the top surface, this high $EMMF_z$ is to be expected.

The 2^{nd} mode (Fig. 3.21 and row 2 in Table 3.1) has one nodal diameter and one nodal circle, therefore it is the (1,1) mode, with an antinode on each half of the disc, moving 180° out of phase of each other. COMSOL finds the eigenfrequency of this mode at around 100 kHz, approximately two times the fundamental frequency. For modes 2, 3, 5 and 6 (known as the asymmetric modes), if a plane is constructed dissecting 3 points – point one on the disc edge which is geometrically closest to an antinode (for the case of mode 6 it must be one of the outer two antinodes), point two being the centre of the disc, and the third point on the other edge of the disc (a diameter across from the first point) – then this plane will be a plane of symmetry for this mode. Each of these planes of symmetry will dissect at least two antinodes and in the case of mode 6, all four antinodes are coincident to the plane. The antinodes which constitute these mode shapes can be rotated infinitely many times yet the mode shape will remain the same, defined by these planes of symmetry. Due to this cyclic symmetry and the numerical analysis techniques involved in FEA, these eigenmodes are found twice, each being orthogonal to the other, with very similar

computed eigenfrequencies (compare rows 2 and 3, rows 4 and 5, rows 7 and 8, and rows 9 and 10). Increasing the mesh density improves the convergence of these computed frequencies. Mode 2 (in both arrangements) has EMMFs ranging from about 5 to 6×10^{-5} %.

The 3rd mode (Fig. 3.21 and row 4 in Table 3.1) has two orthogonal nodal diameters and one circumferential nodal circle. This (2,1) mode is characterised by a quartering of the disc into four antinodes, with one pair of in-phase diagonally adjacent antinodes deflecting 180° out of phase from the other pair. Again, this eigenmode was found twice with a 90° rotation between the two and a frequency of approximately 162 kHz. EMMFs for this mode range from a minimum of about 7.7×10^{-6} % to a maximum of 3.7×10^{-4} %.

Similar to the fundamental mode, the 4th mode also has a centrally located antinode, this time confined to a far smaller area, and no nodal diameters but two nodal circles. These two nodal circles mean that this (0,2) mode has a second antinode, an annular deflection, concentric but 180° out of phase from the central antinode. COMSOL computes the eigenfrequency for this mode at around 185 kHz and the EMMF in the Z direction was nearly 18%.

The 5th mode has three nodal diameters and one circumferential nodal circle such that this (3,1) mode has the disc split into six equal parts (antinodes) with each rotationally consecutive antinode vibrating in antiphase with that adjacent to it. Due to the symmetry of this mode, COMSOL again computes it twice, at a frequency of approximately 235 kHz. EMMFs for this mode range from approximately 2×10^{-5} % to 7×10^{-5} %.

The 6th and final mode in this eigenmode analysis displays features of modes 2 and 4. One nodal diameter divides the disc in half and two nodal circles, one circumferential and one between the outer edge and centre, split the disc into a pair of larger area out of phase semi-annular deflections located peripherally and a pair of smaller area semi-circular deflections in antiphase located centrally. The antinode of one peripheral semi-annular deflection is 180° out of phase from the adjacent antinode of the central semi-circular deflection. The eigenfrequency of this mode is calculated as about 278 kHz and EMMF range from approximately 1.2×10^{-6} % to 5.4×10^{-5} %.

Clearly modes 1 and 4 are the strongest i.e. most likely to be excited through base excitation, with a combined $EMMF_z$ of about 68%. Due to the shape of these modes (and their distinct lack of nodal diameters) they are part of a subset called the circularly symmetric modes. Drawing any diameter and extruding it infinitely in the positive and negative thickness directions results in a plane of symmetry. This can then be rotated (keeping the centre point in common) infinitely many times resulting in an infinite number of planes of symmetry. The rest of the modes appear to share the effective modal mass fairly evenly, albeit in relatively small amounts.

3.2.2 FEA Result Verification – Theoretical Circular Discs

When using FEM, good practice is to verify the accuracy of any solution using known analytical solutions as theoretical benchmarks. As discussed previously in ***1.3.2***, the eigenfrequencies of a circumferentially clamped circular plate have been calculated theoretically for a disc with the parameters listed in Table 3.2 below. The dimensions and parameters of the disc modelled in the previous section are included in the 2nd row of the table.

	r / m	E / Pa	h / m	ρ / kgm^{-3}	ν
Gorman (2001)	0.038	2.1×10^{11}	0.00038	7800	0.3
1st Circular Disc	0.00075	1×10^{9}	0.00005	1200	0.49

Table 3.2 Dimensions and material properties of theoretical circular disc (Gorman et al., 2001) and FEM disc.

From Chapter 1, equation [1.12] states

$$\omega_{\mathrm{e}} = \frac{\lambda_{\mathrm{e}}^2}{r^2}\sqrt{\frac{Eh^2}{12\rho(1-\nu^2)}} \qquad [3.1]$$

Two circular discs, both fixed at the edge, have radii r_1 and r_2, Young's moduli E_1 and E_2, thicknesses h_1 and h_2, densities ρ_1 and ρ_2 and Poisson's ratios ν_1 and ν_2, respectively, where each of the properties of the second disc are some constant multiplied by the corresponding property of the first disc. From equation [3.1], the theoretical eigenfrequencies of disc 1, ω_{e1}, are proportional to the dimensions and properties according to this relationship

$$\omega_{\mathrm{e1}} \propto \frac{h_1\sqrt{E_1}}{r_1^2\sqrt{\rho_1}\sqrt{(1-\nu_1^2)}} \qquad [3.2]$$

It then follows that the theoretical eigenfrequencies of the new disc 2, ω_{e2}, are proportional to the properties of both the new and old disc by the statement

$$\omega_{\mathrm{e2}} \propto \frac{h_2}{h_1}\frac{r_1^2}{r_2^2}\frac{\sqrt{E_2}}{\sqrt{E_1}}\frac{\sqrt{\rho_1}}{\sqrt{\rho_2}}\frac{\sqrt{(1-\nu_1^2)}}{\sqrt{(1-\nu_2^2)}}\times\omega_{\mathrm{e1}} \qquad [3.3]$$

The above proportionality statement can be used to calculate the multipliers shown in Table 3.3. Using these multipliers to calculate one overall coefficient of proportionality and then re-evaluating the theoretical eigenfrequencies in Table 1.2 resulted in the values in Table 3.4 for the theoretical eigenfrequencies (rounded to the nearest Hz) of the same circular disc studied using FEA in this Subchapter.

	r / m	E / Pa	h / m	ρ / kgm^{-3}	ν
Gorman (2001)	0.038	2.1×10^{11}	0.00038	7800	0.3
1st Circ Disc	0.00075	1×10^{9}	0.00005	1200	0.49
Multiplier	$\frac{0.038^2}{0.00075^2}$	$\frac{\sqrt{1 \times 10^9}}{\sqrt{2.1 \times 10^{11}}}$	$\frac{0.00005}{0.00038}$	$\frac{\sqrt{7800}}{\sqrt{1200}}$	$\frac{\sqrt{(1-0.3^2)}}{\sqrt{(1-0.49^2)}}$

Table 3.3 Multipliers for scaling factor from theoretical disc's parameters to FEM disc's parameters.

Eigenmode	**Theoretical Eigenfrequency (Hz)**	**Computational Eigenfrequency (Hz)**
1st	43688	48850
2nd	90913	100175
3rd	149116	162260
4th	170056	185100
5th	218244	234810
6th	260124	278265

Table 3.4 Scaled theoretical eigenfrequencies vs. FEM computed eigenfrequencies for first 6 modes

The third column above is a repeat of the 2nd column of Table 3.1 displaying the eigenfrequencies estimated using FEA (where 2 values occurred i.e. for the asymmetrical modes, the average of the 2 was used). Plotting these two columns with the theoretical eigenfrequencies on the X-axis (kHz) vs. the computationally estimated eigenfrequencies on the Z-axis (kHz) resulted in the triangular data points seen in Fig. 3.22. The Pearson product-moment correlation coefficient, r_{P}, is defined as

$$r_{\mathrm{P}} = \frac{\sum(x-\bar{x})(y-\bar{y})}{\sqrt{\sum(x-\bar{x})^2 \sum(y-\bar{y})^2}} \qquad [3.4]$$

where $\bar{x}$, the mean x-data value, $= \frac{\sum_1^n x}{n}$, and n is the total number of data points. Using this formula r_{P} was 0.99994.

With the origin as a common point, fitting a linear trend line to the data, the rate of change along the line, b, was then calculated by

$$b = \frac{\Delta y_{\text{tre}}}{\Delta x_{\text{tre}}}$$

[3.5]

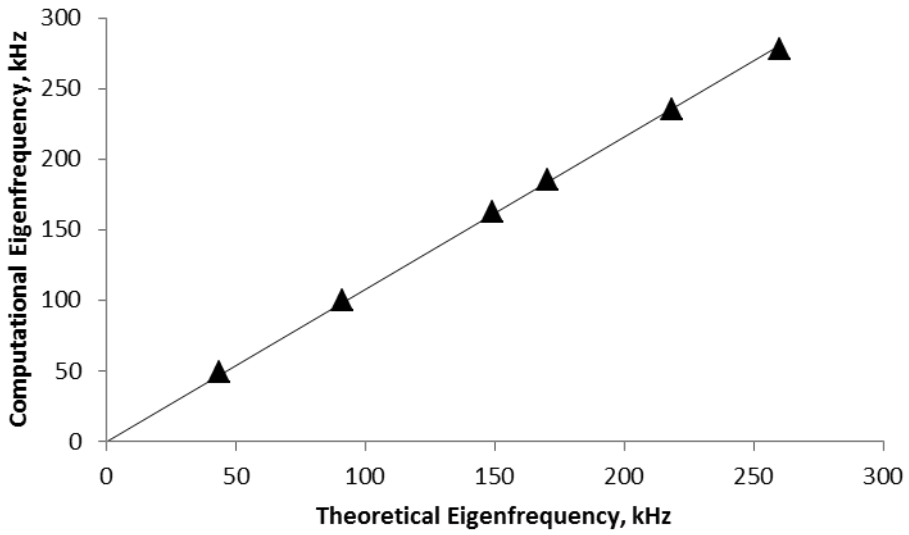

Figure 3.22 Relationship between theoretical and computed eigenfrequency of fundamental mode.

The goodness-of-fit R-squared value, which assesses the representation of the data by the linear trend line, is defined as

$$R^2 = 1 - \frac{\text{SS}_{\text{res}}}{\text{SS}_{\text{t}}}$$

[3.6]

where the sum of the squares of the residuals,

$$\text{SS}_{\text{res}} = \sum_{0}^{n} (y - y_{\text{tre}})^2$$

[3.7]

and

$$\text{SS}_{\text{t}} = \left(\sum_{0}^{n} y^2\right) - \frac{\left(\sum_{0}^{n} y\right)^2}{n}.$$

[3.8]

For this dataset b = 1.0788 and R^2 = 0.9995 (R^2 = 1 indicates a perfect fit between the X-Y data and the linear trend line). Therefore with a Pearson coefficient, rate of change of the trend line, and R-squared value for the trend line, all very close to 1, there clearly exists a direct linear relationship between the theoretical and computational eigenfrequencies with one-to-one correspondence and very close correlation.

3.2.3 Analysing the Finite Element Model Mesh

FEM solution accuracy is highly dependent on the quality of the mesh used to discretise a model into finite elements with spurious results often computed as a consequence of inadequate mesh densities. As mentioned in *3.2.1.1*, COMSOL's physics-based meshing with a mesh size setting of "Normal" was used when carrying out an initial FEM eigenmode analysis of a solid circular disc. This resulted in a net mesh element count of 1434. In total, nine mesh size pre-sets were available, ranging from the lowest net number of elements (and therefore low mesh density quality), called "Extremely coarse" (*Ext C*), to the setting for the highest number of elements known as "Extremely fine" (*Ext F*). Between these selections there are "Extra coarse" (*E C*), "Coarser" (*Cr*), "Coarse" (*C*), "Normal" (*N*), "Fine" (*F*), "Finer" (*Fr*) and "Extra fine" (*E F*), each with a gradual increase in number of elements along with improvements in the resolution of areas of curvature and thin regions. The eigenmode analysis described in *3.2.1.1* was iteratively computed using all nine mesh settings and then displayed in Table 3.5 below.

	Eigenfrequencies / kHz								
EM	*Ext C*	*E C*	*Cr*	*C*	*N*	*F*	*Fr*	*E F*	*Ext F*
1st	79.28	59.80	52.79	50.30	48.85	47.50	46.61	45.18	43.93
2nd(1)	164.00	124.36	108.55	103.74	100.11	97.19	95.43	92.55	90.11
2nd(2)	169.25	127.37	109.92	104.01	100.24	97.31	95.62	92.77	90.13
3rd(1)	268.84	209.94	177.13	168.96	162.13	156.90	154.28	149.52	145.42
3rd(2)	275.69	213.80	180.09	169.40	162.39	157.39	154.56	149.73	145.47
4th	329.14	245.55	204.97	194.12	185.10	179.02	175.87	170.00	165.23
5th(1)	392.26	313.99	262.49	246.60	234.70	226.21	222.22	215.25	209.02
5th(2)	408.89	314.70	262.78	247.21	234.92	226.55	222.57	215.45	209.08
6th(1)	432.04	381.73	309.49	292.32	277.75	268.66	263.58	254.74	247.27
6th(2)	451.77	391.87	316.80	293.02	278.78	268.81	264.21	255.15	247.32

Table 3.5 Eigenfrequencies of first 6 modes for the range of mesh density size settings.

The total mesh size for this model at each of these settings was 131, 280, 578, 849, 1434, 2243, 3132, 9183 and 38708 elements respectively. To compare the performance of each of these meshes, firstly the computed eigenfrequency for a particular mesh density setting was divided by the corresponding analytical value from the middle column of Table 3.4, and these quotients are displayed in Table 3.6. As the mesh density increases these values tend towards the ideal value of 1. There is a marked improvement between a mesh density setting of extremely coarse (average

quotient value of 1.81) and the normal mesh density setting (average value of 1.09). Extra fine mesh density and extremely fine mesh density had average quotient values of 1.00 and 0.97 respectively.

	Computed / Theoretical								
EM	*Ext C*	*E C*	*Cr*	*C*	*N*	*F*	*Fr*	*E F*	*Ext F*
1st	1.81	1.37	1.21	1.15	1.12	1.09	1.07	1.03	1.01
2nd(1)	1.80	1.37	1.19	1.14	1.10	1.07	1.05	1.02	0.99
2nd(2)	1.86	1.40	1.21	1.14	1.10	1.07	1.05	1.02	0.99
3rd(1)	1.80	1.41	1.19	1.13	1.09	1.05	1.03	1.00	0.98
3rd(2)	1.85	1.43	1.21	1.14	1.09	1.06	1.04	1.00	0.98
4th	1.94	1.44	1.21	1.14	1.09	1.05	1.03	1.00	0.97
5th(1)	1.80	1.44	1.20	1.13	1.08	1.04	1.02	0.99	0.96
5th(2)	1.87	1.44	1.20	1.13	1.08	1.04	1.02	0.99	0.96
6th(1)	1.66	1.47	1.19	1.12	1.07	1.03	1.01	0.98	0.95
6th(2)	1.74	1.51	1.22	1.13	1.07	1.03	1.02	0.98	0.95

Table 3.6 Ratio of computed to theoretical eigenfrequency for 6 eigenmodes at each mesh density.

Another simple way to analyse the mesh suitability was to compare the frequencies of the 'dual-computed' asymmetric eigenmode $2^{nd}(2)$ vs $2^{nd}(1)$, $3^{rd}(2)$ vs $3^{rd}(1)$, $5^{th}(2)$ vs $5^{th}(1)$ and finally $6^{th}(2)$ vs $6^{th}(1)$. Each of these mode pairs, in reality, is just one mode but the nature of FEA and meshing means they are found twice rotated orthogonally. The percentage difference in magnitude between the second and first computed values was calculated according to the formula

$$\%EF(2) = \left(\frac{EF(2) - EF(1)}{EF(1)}\right) \times 100\% \qquad [3.9]$$

Table 3.7 shows these percentage differences for each of these asymmetric modes. Clearly as the mesh density increases modes $2^{nd}(2)$ and $2^{nd}(1)$, $3^{rd}(2)$ and $3^{rd}(1)$, $5^{th}(2)$ and $5^{th}(1)$ and $6^{th}(2)$ and $6^{th}(1)$ all begin to noticeably converge (i.e. the percentage change tends to zero).

Additionally there is a noticeable difference again between the performance of the extremely coarse mesh (average percentage change of 3.64%) and the normal mesh (average percentage difference of 0.19%) and then even more so for the extremely fine mesh with an average of 0.03%.

	%EF(2)								
EM	*Ext C*	*E C*	*Cr*	*C*	*N*	*F*	*Fr*	*E F*	*Ext F*
2nd	3.20	2.42	1.26	0.26	0.13	0.12	0.20	0.24	0.02
3rd	2.55	1.84	1.67	0.26	0.16	0.31	0.18	0.14	0.03
5th	4.24	0.23	0.11	0.25	0.09	0.15	0.16	0.09	0.03
6th	4.57	2.66	2.36	0.24	0.37	0.06	0.24	0.16	0.02

Table 3.7 Percentage difference between the 2 computed eigenfrequency values for the same mode, for the first 4 asymmetric eigenmodes.

Increasing the number of elements and therefore number of degrees of freedom in the system was found to decrease each of the computed eigenfrequencies. Plotting the frequency of the 1st eigenmode against the total number of elements resulted in Fig. 3.23. There is a clear levelling off of the computed eigenfrequency beyond about 2500 elements, indicating that this number of mesh elements is approaching the optimal mesh size for convergence on reasonably accurate values for eigenfrequency. This, however, is not the deciding factor to consider during mesh optimisation, as COMSOL also calculates mesh statistics for qualitative assessment.

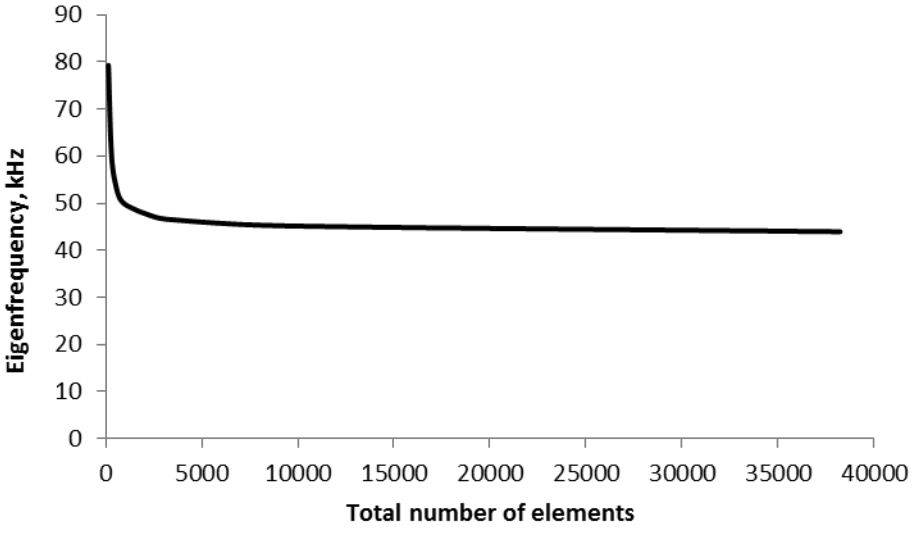

Figure 3.23 Relationship between total element number and eigenfrequency of 1st mode.

For total element numbers greater than 1434 elements (i.e. normal mesh size settings or finer) the effective modal mass fractions (EMMF), particularly those in the Z-axis direction and for the circularly symmetric modes ((0,1) and (0,2)), were observed to remain relatively constant across all mesh densities.

3.2.4 Changing the Parameters

3.2.4.1 Disc Radius

Several defining factors influence the predicted eigenfrequencies of a given uniform circular plate, according to Eq. [3.2] in ***3.2.2***. By confirming that each of these factors affected the eigenfrequencies in the expected manner, predictions or adjustments could be made to FEM results aligning them more closely with the known characteristics of the real locust tympanal system. Of these factors, disc radius was chosen as the first model parameter to be tested for impact on both the frequency and the EMMF of the eigenmodes. A parametric sweep was utilised to vary the radius from 0.2 mm to 2 mm with a step size of 50 µm. All other dimensions, mechanical properties and mesh settings were unchanged from the model in ***3.2.1***.

Plotting the eigenfrequency of the fundamental mode on the Y-axis versus disc radius on the X-axis resulted in the triangular data points in Fig. 3.24. Fitting a power trend line (of the form $y = bx^c$ where b and c are constants) to this data using the method of least squares polynomial regression analysis yielded a value for b of 26.346 and c of -1.993. The solid line in Fig. 3.24 shows this trend line which had a goodness-of-fit R^2 value of 0.9989, indicating strong correlation with the data. The c value of approximately -2 was expected since theoretically for an isotropic Hookean circular plate the eigenfrequency, $\omega_e \propto \frac{1}{r^2}$ (Eq. [3.2] in ***3.2.2***) where r is the disc radius.

This same relationship was observed across all eigenmodes with the power constant, c, always equal to approximately -2. Effective modal mass fractions, recalculated for each new radius due to increasing total model mass, were observed not to vary with radius in any logical fashion.

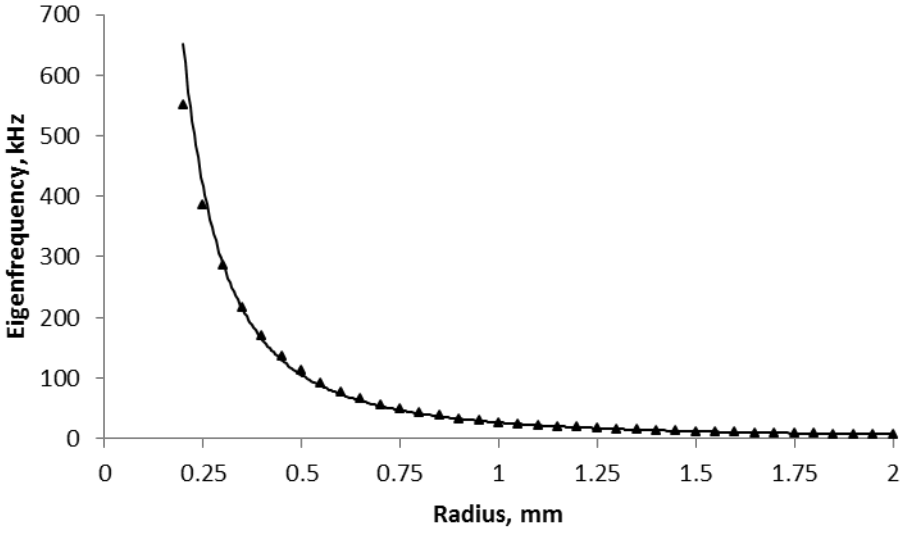

Figure 3.24 Relationship between radius of disc and eigenfrequency of fundamental mode.

3.2.4.2 Changing Parameters – Thickness

The effect on the eigenmodes of altering disc thickness was tested next. A lower limit of 10 µm, step size of 5 µm and upper limit of 200 µm were the defining features in this parametric sweep. All other dimensions, mechanical properties and mesh settings were unchanged from the model in ***3.2.1***.

Fundamental mode eigenfrequency on the Y-axis versus disc thickness on the X-axis is displayed by the triangular data points in Fig. 3.25. Using linear regression analysis to fit a linear trend line, passing through the origin (of the form $y = mx$ where m is the constant gradient) to this data resulted in a gradient of 0.9708 and a goodness-of-fit R^2 value of 0.9984. Fig. 3.25 displays this linear relationship as a solid black line, closely correlated with the data points. m was expected to be 1 since theoretically the eigenfrequency, $\omega_e \propto h$ (see *3.2.1.2*) where h is the disc thickness.

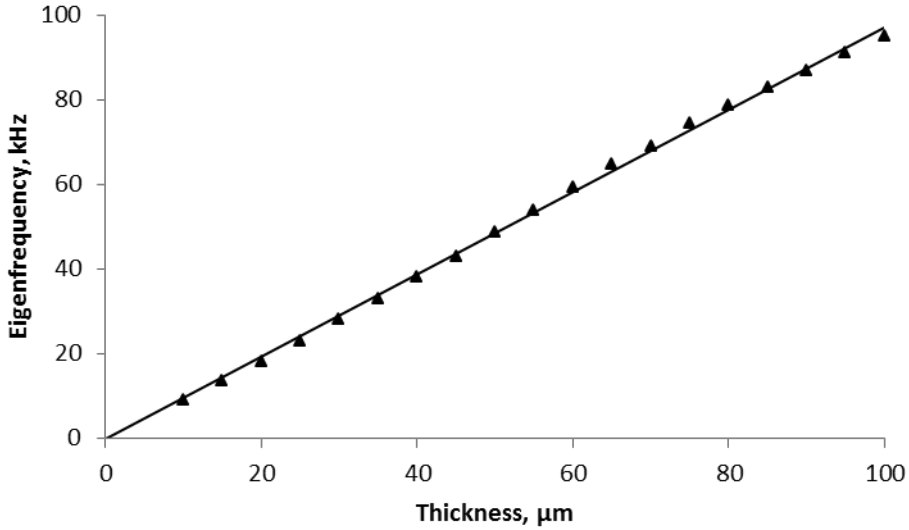

Figure 3.25 Relationship between thickness of disc and frequency of 1st mode.

All eigenmodes displayed this same linear relationship between thickness and modal frequency with the gradient always equal to approximately 1. Effective modal mass fractions, recalculated for each new thickness due to increasing total model mass, were observed not to vary with thickness in any logical pattern.

3.2.4.3 Changing Parameters – Young's Modulus

In theory, an isotropic, linear elastic circular plate, has eigenfrequencies, $\omega_e \propto \sqrt{E}$, where E is the Young's modulus of the disc material (***3.2.2***). Varying the modulus of elasticity from 1 MPa to 961 MPa with a step of 40 MPa, and then plotting the eigenfrequency of the first eigenmode on the Y-axis against Young's modulus on the X-axis resulted in the data points on Fig. 3.26 below.

Using polynomial regression again to fit a power trend line (of the form $y = bx^c$) to this data produced the solid black line in the Figure. For this power relationship the coefficient, b was 1.5448 and the power, c was 0.5 (correct to 6 decimal places). The R-squared goodness-of-fit value was 1 (correct to 9 decimal places). This computed relationship between eigenfrequency and Young's modulus matched the aforementioned theory perfectly and the 0.5 power value and close correlation occurred across all of the modes. EMMF were constant for all of the eigenmodes across all the Young's moduli.

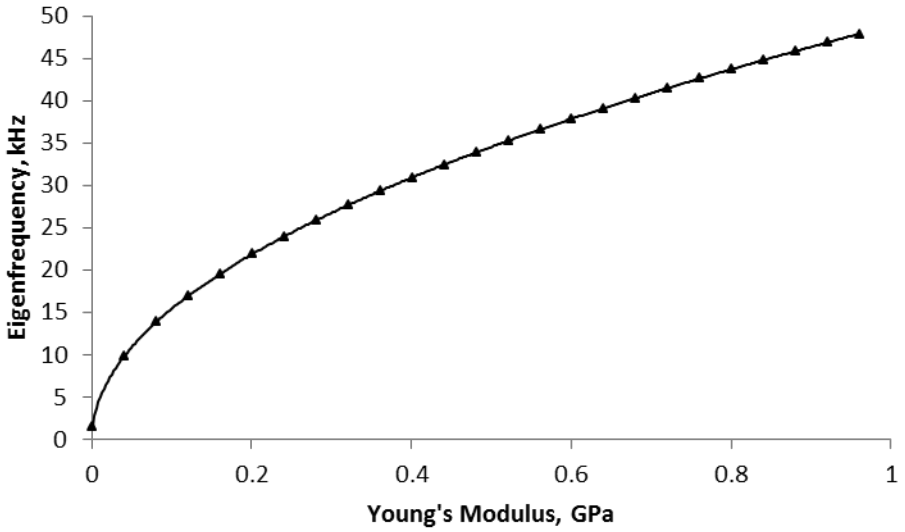

Figure 3.26 Relationship between Young's modulus and fundamental mode eigenfrequency.

3.2.4.4 Changing Parameters – Density

The penultimate parameter to be tested was the density and an upper value of 2000 kgm^{-3}, lower value of 100 kgm^{-3} and step size of 100 kgm^{-3} were the chosen sweep values. Fig. 3.27 shows the triangular data points for the fundamental mode's eigenfrequency on the Y-axis against the density on the X-axis. Theoretically, the eigenfrequencies, $\omega_e \propto \frac{1}{\sqrt{\rho}}$, where ρ is the density of the disc material (***3.2.2***).

Fitting a power trend line (of the form $y = bx^c$) to this data using the least squares method of polynomial regression produced the solid black line in the Figure. With a coefficient, b of approximately 1.69×10^6 and power, c of -0.5 (correct to 5 d. p.) the relationship was exactly as expected. The R-squared goodness-of-fit value was 1 (correct to 9 d. p.). Close correlation occurred across all of the modes as did the power value of -0.5. Once the total modelled mass was adjusted for the new densities, EMMF were observed to be constant for all of the eigenmodes across all densities.

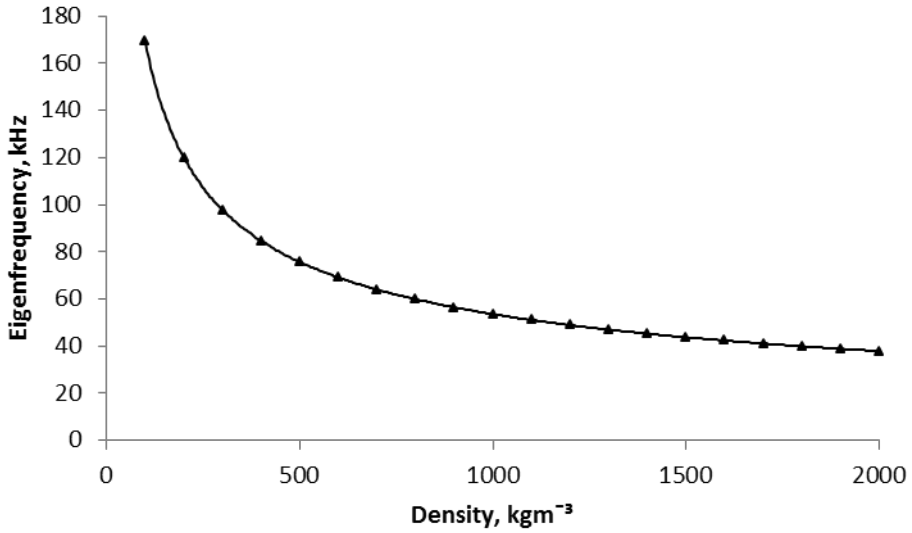

Figure 3.27 Relationship between density of disc material and eigenfrequency of 1st mode.

3.2.4.5 Changing Parameters – Poisson's Ratio

Poisson's ratio was the final parameter to be tested and the parametric sweep was executed across a range from 0.1 to 0.49 with a step size of 0.01. From ***3.2.2***, the eigenfrequency of a particular eigenmode of a circular plate,

$$\omega_e \propto \frac{1}{\sqrt{1-\nu^2}} \tag{3.10}$$

where ν is the Poisson's ratio and all other parameters remain constant. This can be rewritten as

$$\omega_e = \frac{k}{\sqrt{1-\nu^2}} \tag{3.11}$$

where k is some arbitrary constant. Taking the natural logarithm of each side, becomes

$$\ln \omega_e = \ln\left(\frac{k}{\sqrt{1-\nu^2}}\right) \tag{3.12}$$

which can be rewritten as

$$\ln \omega_e = \ln k - \ln(1-\nu^2)^{\frac{1}{2}} \tag{3.13}$$

Rearranging gives

$$\ln \omega_e = -\frac{1}{2}\ln(1-\nu^2) + k_2 \tag{3.14}$$

since $\ln k$ is a constant, k_2. This equation is of the form

$$Y = -\frac{1}{2}X + k_2 \tag{3.15}$$

where $Y = \ln \omega_e$ and $X = \ln(1-\nu^2)$. This theoretical expression is a linear relationship with gradient -0.5 and Y-axis intercept of k_2.

Calculating $\ln \omega_e$ for the eigenfrequency of the fundamental mode of the circular disc and $\ln(1-\nu^2)$ for the Poisson's ratios in the sweep, then plotting this data on the Y-axis and X-axis respectively, resulted in Fig. 3.28. Normal mesh size

(total of 1434 elements) and the same parameter values as previous model computations were used.

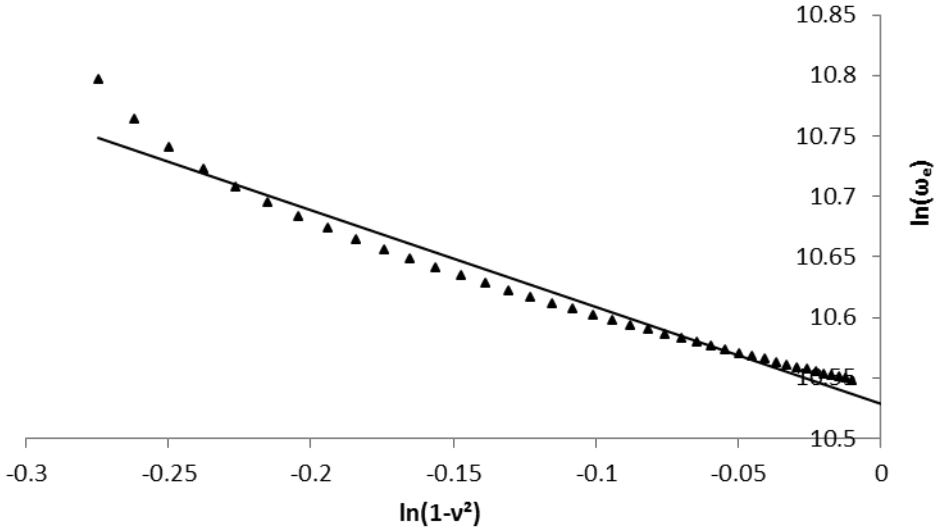

Figure 3.28 Linear relationship between logarithmic expressions of Poisson's ratio and the eigenfrequency of the 1st mode for normal mesh size.

Again, using linear regression analysis to fit a linear trend line (of the form $y = mx + c$) to this data resulted in a gradient of -0.7991, a Y-axis intercept of 10.529 and a goodness-of-fit R^2 value of 0.9662. This gradient was not the predicted -0.5 and the data points above visibly deviate from an obvious linear relationship. Additionally the R^2 value was far from the values computed for the previously tested parameters.

Mesh quality was suspected to be influencing this solution and mesh statistics can be computed for any mesh which has been successfully constructed in COMSOL. One of these statistics is the minimum element quality, which provides a good overall estimate of a particular mesh's quality. It is recommended that the minimum element quality remains above 0.1 for accurate discretisation of finite element models in COMSOL. Since the value was below 0.1 for this model mesh, the model was recomputed at four finer meshing size settings: fine, finer, extra fine and extremely fine, respectively (total element numbers are in Table 3.8).

Fig. 3.29 displays the data for all five mesh density settings, normal through to extremely fine. The red data and linear trend line are for normal mesh size, orange for fine, green for finer, blue for extra fine and finally purple for the largest mesh

size of extremely fine. Clearly the linear fit is improving as the total number of mesh elements increases and the gradient of the line is also decreasing. Table 3.8 displays the gradient and R^2 for each of these refinements. The gradient was observed to be approaching the expected -0.5 and there is a marked improvement in the R^2 values as the mesh becomes more dense. As a final step, customising the mesh density to create a 407335 element mesh resulted in the computation of a gradient of -0.5112 with a goodness-of-fit R^2 value of 0.9998. Evidently the accurate modelling of high aspect ratio thin plates depends greatly on the mesh density and in particular the number of elements used to discretise a particular thin section due to the influence of Poisson's ratio on the elements in such a region.

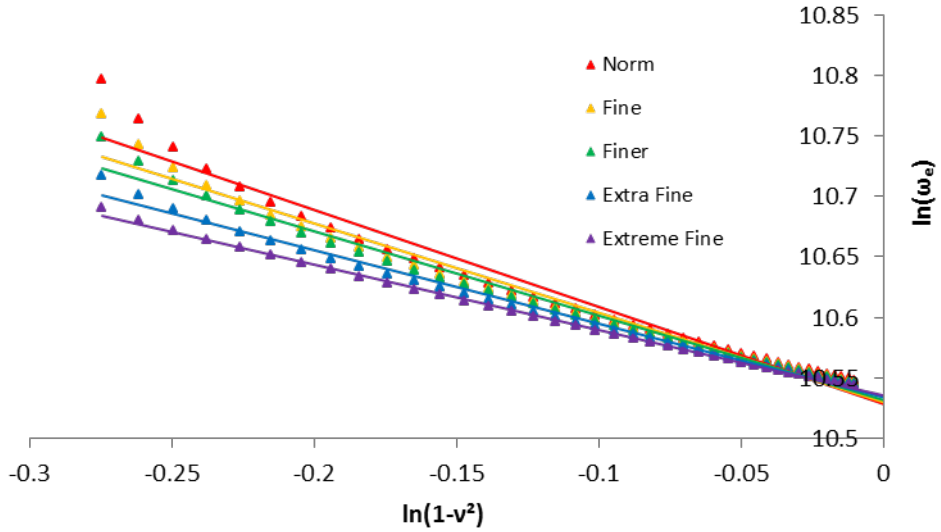

Figure 3.29 Linear relationship between natural logarithmic expression of Poisson's ratio and the eigenfrequency of the 1st mode for various mesh densities.

Mesh Density	Total Element Number	Gradient of Linear Fit	R^2 value
Normal	1434	-0.7991	0.9662
Fine	2243	-0.7362	0.9776
Finer	3132	-0.6961	0.9848
Extra Fine	9183	-0.6068	0.9933
Extremely Fine	38708	-0.5390	0.9986

Table 3.8 Gradients and R^2 values for the linear relationship between logarithmic expressions of ν and eigenfrequency, for different mesh densities.

These results for a varying Poisson's ratio are a clear warning that, although a model's mesh density may be sufficiently fine to accurately predict the shape of

eigenmodes and the value of their eigenfrequencies, the mesh density may need to be increased in other modelling contexts.

Investigating the influence of changing the Poisson's ratio on the effective modal mass fractions of the disc's modes was the next step. For all previous parameters, both mechanical properties and physical, no significant effect was observed on the EMMF of each mode by a change in the parameter value. For Poisson's ratio, however, this was not observed to be the case. Using the custom high density mesh with 400000+ elements, the $EMMF_{1Z}$ in the transverse Z-axis direction, of the fundamental mode, was calculated for each value of ν from 0.1 to 0.49, by the method outlined in *2.2.3.2*. Looking at Fig. 3.30, clearly the $EMMF_{1Z}$ decreases as the Poisson's ratio increases, with the diminution becoming more severe as $\nu > 0.3$. Next, $EMMF_{2Z}$ was analysed, i.e. for the second eigenmode, as a function of the Poisson's ratio. This result is displayed in Fig. 3.31 and shows substantial increase in the effective modal mass fraction of the second mode as the Poisson's ratio increases, with a steep increase observed beyond $\nu = 0.45$. Interestingly, this increasing EMMF pattern was observed for all of the asymmetric modes. Conversely, the decreasing EMMF shown in Fig. 3.30 was observed to occur for both modes 1 and 4, i.e. all of the circularly symmetric modes in the first 6 eigenmodes.

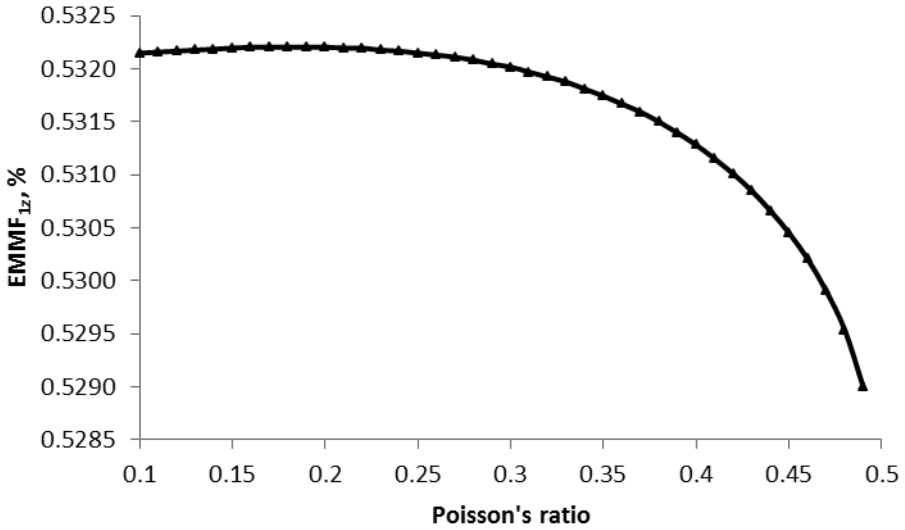

Figure 3.30 Poisson's ratio against Z-axis EMMF of the 1st mode.

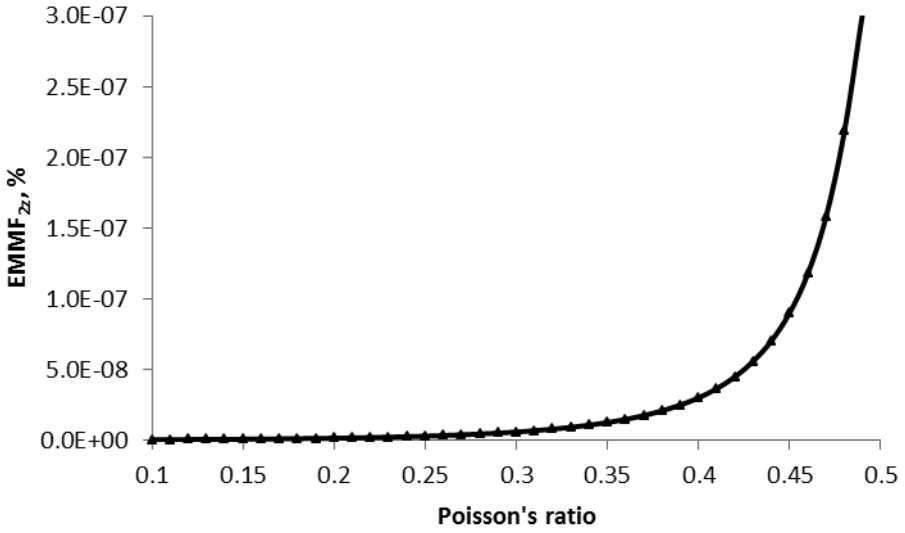

Figure 3.31 Poisson's ratio against Z-axis EMMF of the 2nd mode.

3.2.5 Acoustic-Structure Interaction with Frequency Response – Circular Discs

In **3.1** it was observed that locust ear travelling wave shapes switch at specific frequencies and also show components of the natural modes of vibrating membranes. Therefore, equipped with a better understanding of both the frequencies and relative strength of the modes of thin circular disc membranes, the natural next step was to explore the possibility of the coupling of these modes as a mechanism for the formation of frequency specific travelling waves. *2.2.3.3* describes the acoustic-structure interaction application study used to investigate the response of the model tympanal membranes to harmonic acoustic pressure loads in a surrounding fluid of air. This differs from Malkin et al.'s approach (2013) where harmonic loads were applied as a mechanical load to a model membrane surface, treating the model TM as a tensed membrane with frequency dependent damping, stimulated at frequencies not in the region of the natural modes.

This study type requires the addition of a fluid domain to the model and a hemisphere of radius 40 mm was chosen as the main component of the fluid domain. The centre point of the hemisphere was coincident with the centre of the bottom face of the circular disc such that the entire disc, excluding the bottom face, was surrounded by the hemispherical fluid domain. Defined as a circular disc of radius 0.75 mm and thickness 50 μm, the solid domain remained as in ***3.2.1*** with the same material properties as the initial eigenmode analysis. Directly beneath the solid domain, a cylinder, of radius equal to the disc and a height of 0.5 mm, was constructed as a second fluid domain separate from the hemispherical part. Air, included in COMSOL's in-built material library, was then assigned to both fluid domains i.e. the hemisphere dome and larger cylinder. The material properties of air used in the computation were a fluid density, ρ_c, of 1.1839 kgm^{-3} and speed of sound, c, of 346.13 ms^{-1}. Several boundary conditions were then set including applying a fixed constraint boundary to the entire disc edges in the solid mechanics boundary options.

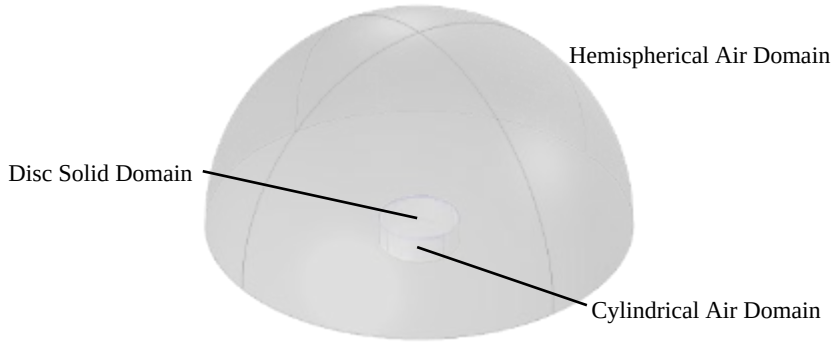

Figure 3.32 3-D geometry used to simulate acoustic response of the model tympana.

Fig. 3.32 shows an isometric view of the 3-D model geometry with image transparency switched on and the fixed boundaries highlighted in darker blue. The sound stimuli for the computational experiment were simulated plane wave pressure fields with sound pressure level of 65 dB SPL re 20 μPa (≈ 35 mPa) at several frequencies in the range of the computed eigenfrequencies and incident from a variety of angles.

The incident acoustic pressure field was applied to the external boundaries of the hemisphere of air and radiation boundary conditions were also applied to the bottom face of the dome and all boundaries of the air domain cylinder. The top and bottom face of the thinner circular disc i.e. the solid domain, were the only acoustic-structure boundaries in the model formulation.

Constructing the problem in this fashion benefitted the model in three major ways:

- the fluid air domain extended infinitely in all directions eliminating any unwanted reflections and ensuring the model tympanum was effectively in the far-field of the source of the incident sound;
- the bottom surface of the dome acted as a baffle to the circular disc-shaped model tympanum by isolating the external from the internal surface, as is the case in the locust since the surrounding body parts of the locust create a natural baffle to incoming sound;
- use of a hemispherical air domain instead of the traditional full spherical domain efficiently kept the total element number to a minimum without compromising model accuracy.

Initially, the wave vector defining angles, φ and ϑ (as defined in *2.2.3.3*), were set to π radians and $\frac{3\pi}{4}$ radians respectively, corresponding to an incident sound pressure wave with equal magnitude components in the negative X- and Z-axis directions and negligible Y component, i.e. downwards at 45° to the plane of the circular disc. Physics-defined meshing was selected with the 'extra fine' mesh size settings yielding a total element count of 135449. An overview of the theory behind the acoustic-structure interaction and all of the required boundary conditions along with the remaining solver settings is provided in *2.2.3.3*. To define the parametric sweep of frequencies, the lower and upper bounding frequencies were 20 kHz and 300 kHz respectively, with a step of 5 kHz i.e. 57 model iterations. A snapshot of an incident sound wave of frequency 150 kHz is shown in Fig. 3.33. Clearly there are no unwanted reflections at any of the model boundaries and sound can be seen transmitting through to the internal part of the air domain due to the vibration of the centrally located disc, similar to transmitted sound from the deflection of one TM of the locust (see later subsections ***4.6.1*** and ***4.6.2***).

Fig. 3.34 shows the frequency response across this frequency range, with the total displacement in picometres on the Y-axis. Five peaks are visible on the response curve, 45 kHz, 95 kHz, 175 kHz, 220 kHz and 260 kHz.

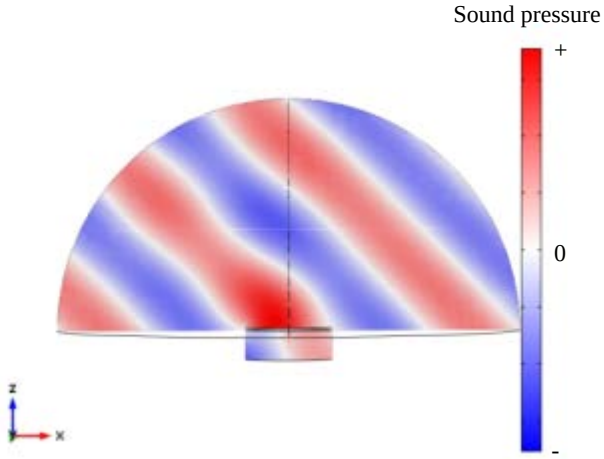

Figure 3.33 Snapshot of simulated acoustic-structure interaction at 150 kHz showing distribution of acoustic pressure.

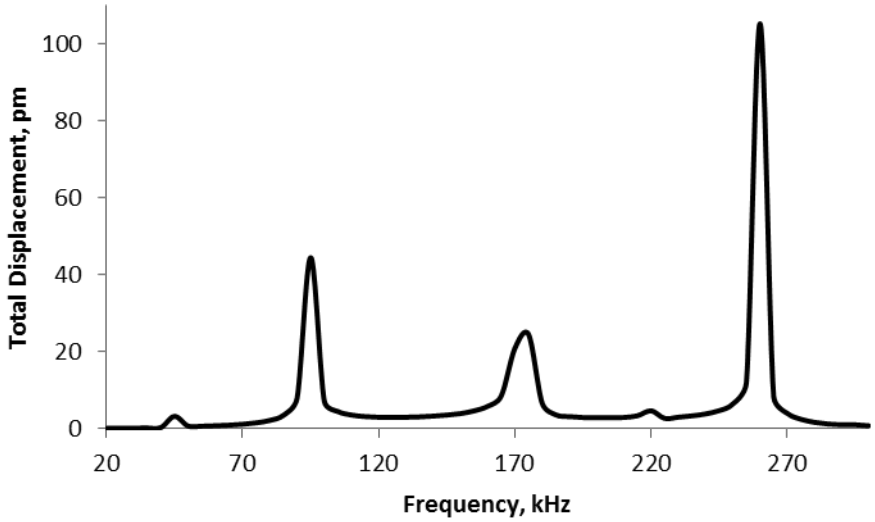

Figure 3.34 Computed frequency response from 20 kHz to 300 kHz.

To further increase the resolution in the vicinity of these peaks, five new frequency sweeps were executed, each with a 1 kHz step. These were 41 – 49 kHz, 91 – 99 kHz, 171 – 179 kHz, 211 – 219 kHz and finally, 256 – 264 kHz. Fig. 3.35 displays the new frequency response curve with five vertical lines marking specific frequencies of interest chosen to illustrate the various vibrational responses which were observed.

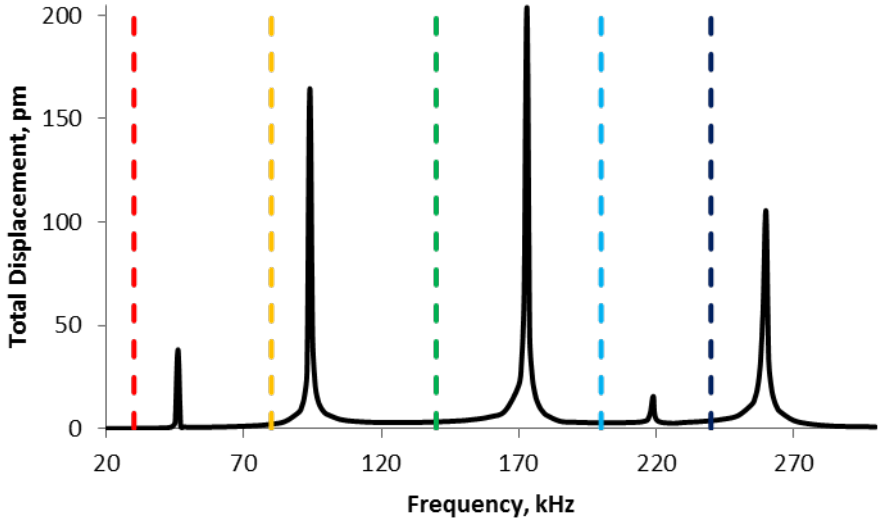

Figure 3.35 Refined computational frequency response from 20 kHz to 300 kHz.

These frequencies of interest were red - 30 kHz, orange - 80 kHz, green - 140 kHz, light blue - 200 kHz and dark blue - 240 kHz. At each frequency, the

instantaneous Z-axis component of displacement was computed and displayed as snapshots of the dynamic cycle of the vibration of the model tympanum.

As in previous sections, red indicates transverse displacement towards the reader and green represents deflection into the page. The vibration cycle at 30 kHz is shown in Fig. 3.36 and at this frequency the model membrane vibrates like the fundamental drum mode with an antinode, of maximum displacement around 7.1 pm at 90°, remaining centrally positioned and one circumferential nodal line.

Fig. 3.37 illustrates the dynamic cycle at 80 kHz (the yellow line in Fig. 3.35) from 0° through to 360°. Instantaneous maximum and minimum displacements at each wave cycle phase are marked by black dots on the Figure and a maximum of 6.7 pm was predicted at 270°.

Following the black dot at phase angles 45°, 90° and 135°, the point of maximum deflection can clearly be seen travelling from left to right i.e. in the positive X-axis direction, peaking in the very centre of the disc.

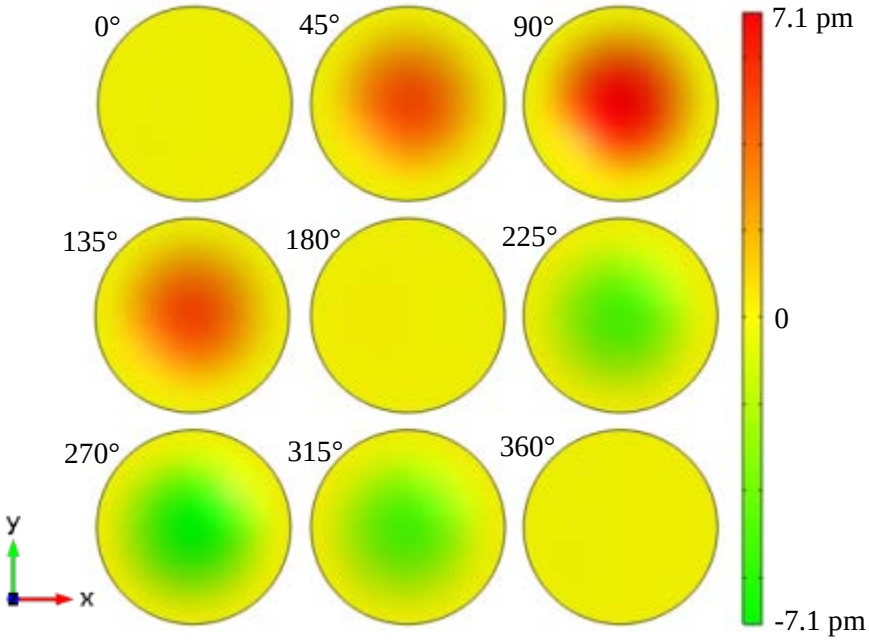

Figure 3.36 Dynamic cycle of vibration of basic model tympanum at 30 kHz.

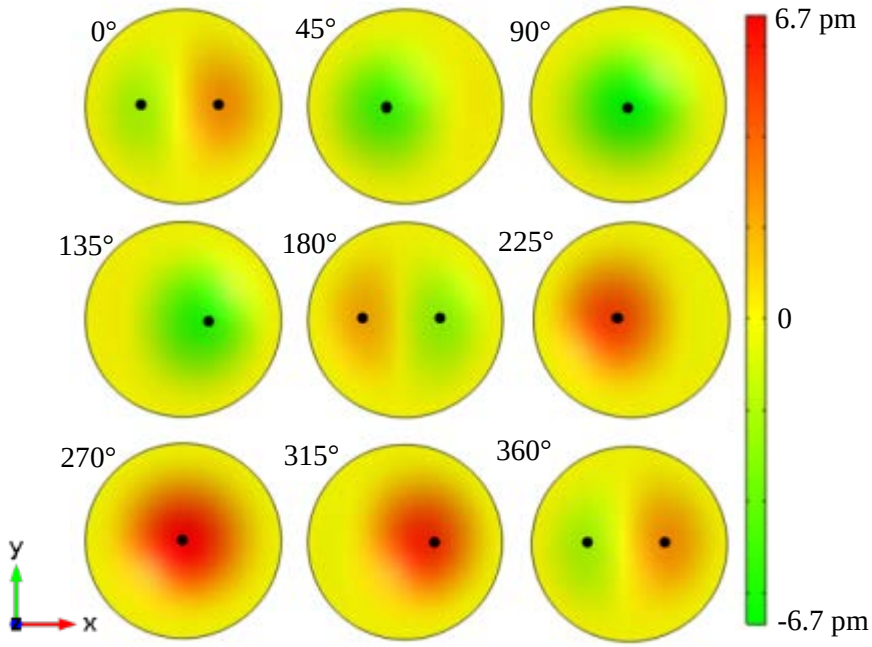

Figure 3.37 Dynamic cycle of vibration of basic model tympanum at 80 kHz. Black spots indicate points of maximum inward/outward displacement at that cycle phase angle.

The shift from the vibration seen in Fig. 3.36 to this travelling wave became just observable at 65 kHz, becoming more noticeable at 70 kHz and the travelling motion strengthening as the frequency was increased towards 95 kHz.

At 140 kHz (the green line in Fig. 3.35), the vibrational pattern of the simple model tympanum, shown in Fig. 3.38, displayed a different travelling wave from that at lower frequencies. At this frequency the point of maximum deflection is clearly travelling from right to left i.e. in the negative X-axis direction, and the shape of the maximum area of deflection is now more elongated than at 80 kHz, particularly at 270° and 315°, where the displacement was predicted at a maximum of 5.4 pm. Additionally, the maximum deflection clearly occurred off-centre, in stark contrast to at the lower frequencies. This switching of the travelling wave pattern was observed to take place at frequencies greater than the second peak in Fig. 3.35 (94 kHz) with the travelling motion continuing to strengthening towards the next peak at 173 kHz.

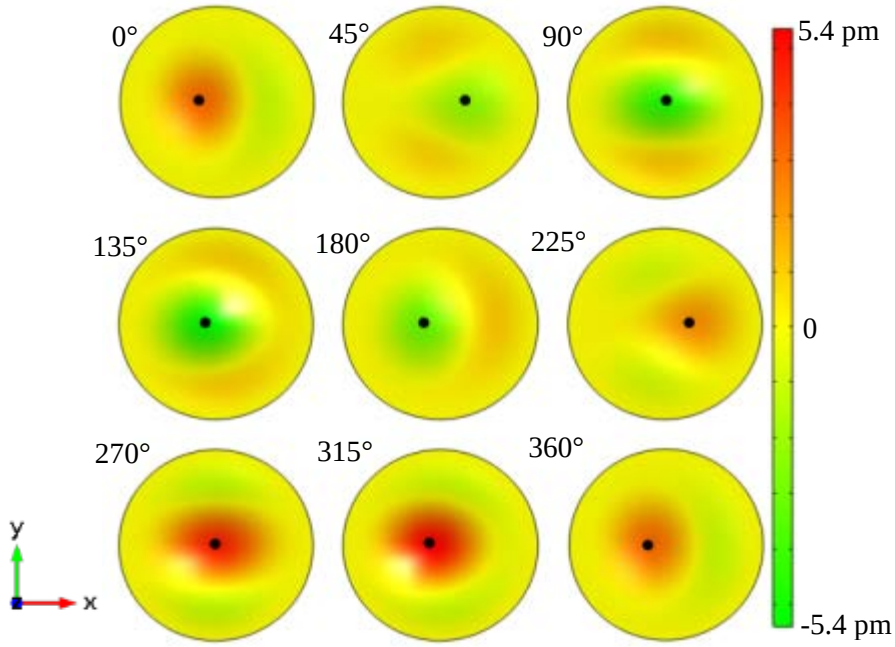

Figure 3.38 Dynamic cycle of vibration of basic model tympanum at 140 kHz. Black spots indicate points of maximum inward/outward displacement at that cycle phase angle.

The next FOI was 200 kHz (the light blue line in Fig. 3.35) and the dynamic cycle at this frequency is displayed in Fig. 3.39. At this frequency an almost C-shaped maximum forms on the left of the disc before shrinking into a maximum covering a smaller area which travels across the disc in the positive X-axis direction. This more condensed maximum travels beyond the disc's centre before dissipating and appears out of phase from the initial C-shaped deflection. The maximum displacement at this frequency was 3.9 pm at 45°. Beyond the third peak of the frequency response, at 173 kHz, was where this change in travelling wave deflection pattern was observed to occur.

240 kHz was the final FOI and the dynamic cycle at this frequency is shown in Fig. 3.40. Again a C-shaped deflection occurs near the edge of the model tympanum but this time it begins to form on the disc while the smaller area of maximum deflection is still apparent. At 45° the maximum displacement was predicted as approximately 3.9 pm.

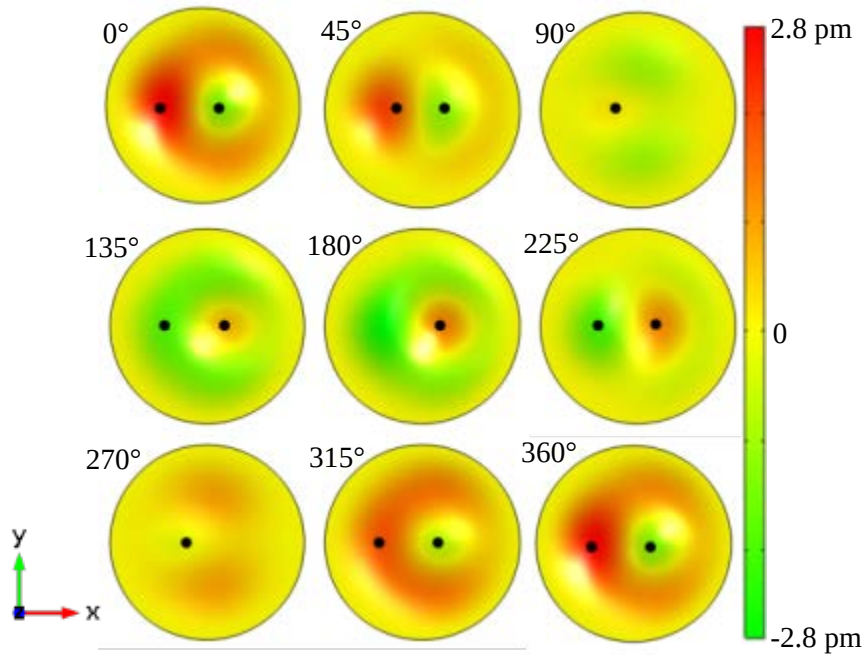

Figure 3.39 Dynamic cycle of vibration of basic model tympanum at 200 kHz. Black spots indicate points of maximum inward/outward displacement at that cycle phase angle.

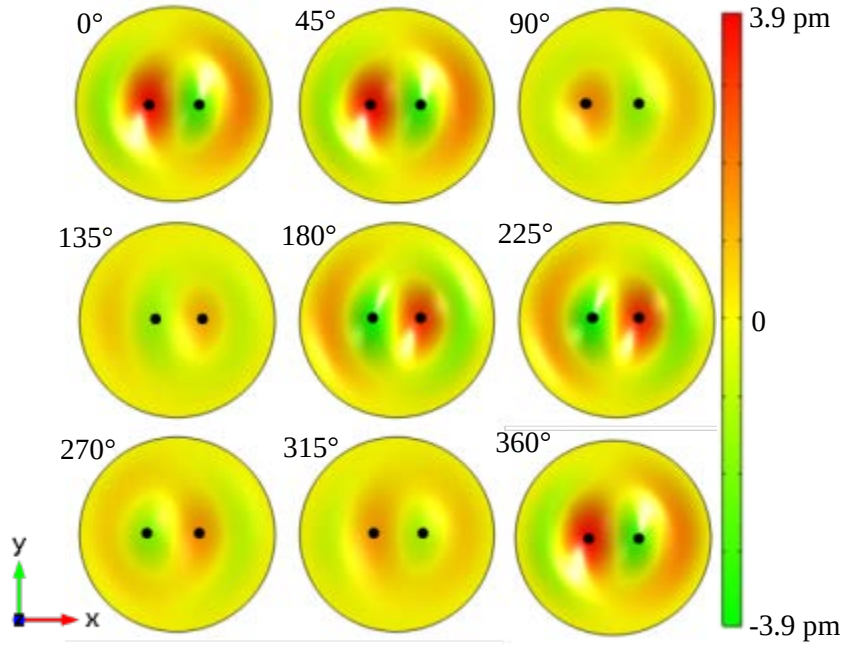

Figure 3.40 Dynamic cycle of vibration of basic model tympanum at 240 kHz. Black spots indicate points of maximum inward/outward displacement at that cycle phase angle.

3.3 Discussion

Using micro-scanning laser Doppler vibrometry the vibrational response of the tympanal ear of the desert locust, *Schistocerca gregaria*, was measured using a periodic chirp from 1 kHz to 30 kHz as a stimulus. Six frequencies of interest were identified, 1.8 kHz, 3.5 kHz, 5 kHz, 10 kHz, 15 kHz and 20 kHz and analysed further resulting in the observation of five possibly distinct frequency-dependent travelling wave patterns, each with more maxima (anti-nodes) added as the frequency increased.

At 1.8 kHz nearly the whole tympanal membrane, thick and thin regions, displaced coherently with the maximal point of deflection in the region of the attachments of Müller's organ.

Conversely, at 3.5 kHz there was a noticeable phase change in the displacement across the TM, particularly noticeable at 45° in Fig. 3.4. The travelling wave motion appeared to follow a diagonal path, from a dorsal-posterior area of origin to the ventral-anterior edge of the tympanum.

5 kHz was the next frequency of interest and at this frequency the phase switch across the membrane was even more prominent. The motion appeared to be slightly less diagonal and more horizontal from posterior to anterior, again dissipating on the far edge of the membrane within the thick region.

At 10 kHz the travelling wave began as a long thin maximum aligned dorso-ventrally which converged to more of a peak as it traversed across the TM towards the PV where the motion dissipated significantly, with the relative deflection amplitude far weaker in the thick membrane region.

15 kHz and 20 kHz were the last two FOI's and at these frequencies a C-shaped maximum propagated anteriorly across the tympanum, quickly converging into a very sharp peak in the region of the PV. At 20 kHz the formation of the C-shape began while the sharp peak was still present at the PV.

Every locust in the sample displayed the same travelling wave patterns and four frequencies were identified where the travelling wave was seen to switch shape, 2.7 kHz, 4.5 kHz, 7.5 kHz and 13.5 kHz. With this consistent observation, in conjunction with the familiarity of many of the features of the travelling wave

patterns, the chosen next step was an in-depth FEM study of a uniform circular disc with dimensions of the order of magnitude of the locust tympanum and material properties aligned with values reported for insect cuticle. Six eigenmodes were predicted, two high EMMF circularly symmetric modes and four much lower EMMF asymmetric modes. The accuracy and validity of the eigenfrequencies were assessed using numerical methods and the predicted values were found to be supported by theory. Computationally predicted values were found to converge strongly on the theoretical values as the mesh density was increased to an extremely fine setting.

Five parameters defined the circular disc model geometry, two dimensions and three material properties. Looping eigenmode analyses using a linearly increasing radius resulted in confirmation of the inverse square law between eigenfrequency and disc radius. Implementing the same technique, this time varying the disc thickness, lead to the theoretically expected direct linear relationship between eigenfrequency and thickness. Young's modulus was next to be varied linearly and circular plate theory predicted a square root relationship between the eigenfrequency and E which was consequently validated by the FEA predictions. An inverse square root relationship should exist between the density of the material and the eigenfrequencies of a circular disc and this was confirmed when plotting the density on the X-axis versus the FEM computed eigenfrequency of the fundamental mode of a circular disc. Theoretically, the effect of Poisson's ratio on the eigenfrequency was shown to follow a logarithmic expression, Eq. [3.14]. Using FEA this relationship was confirmed although the accuracy of these predicted values was found to depend very strongly on mesh quality with a high density mesh required for observation of the full effect of a Poisson's ratio approaching 0.5. In addition, while the other parameters were predicted to have no profound effect on EMMF, ν approaching 0.5 greatly enhanced the relative strength of otherwise weak asymmetric modes.

As a last step, acoustic-structure interactions with frequency response analyses were implemented on the circular disc model and the response at five frequencies was highlighted. The resulting response at each of these frequencies was found to contain elements of the eigenmodes in close proximity to the stimulus frequency. Travelling waves were observed to form on the model membranes at

frequencies of 80 kHz, 140 kHz, 200 kHz and 240 kHz, all as a result of the coupling of vibrational modes of the membrane. Although these frequencies are higher than the frequencies of interest where real locust tympanal travelling waves were measured (**3.1)**, the following Chapter is dedicated to addressing this point and introducing some more features of model locust hearing systems.

Chapter 4 : Application of the Finite Element Method to the Locust Hearing System

"*In all things of nature there is something of the marvellous*" – Aristotle

In this chapter finite element modelling is used to computationally investigate the components of the locust hearing system and their influence on phenomena observed on the locust tympanal ear as well as the locust's overall hearing ability.

4.1 Application of Initial FEM Results to Real Locust Frequency Response

Clearly some differences were observed between the results in the previous Chapter and those published historically and reported in this thesis on the frequency response of the real locust TM, with this Chapter dedicated to highlighting and addressing these differences. The very basic uniform thickness circular disc model tympanum introduced in the previous section displayed five different frequency-dependent responses including four travelling wave patterns. Frequency discrimination at the most basic level was therefore displayed by this model but it must be noted that the range of frequencies selected for simulation (20 kHz to 300 kHz) was not of biological relevance to the real desert locust since the locust's hearing is known to function over a range of around 1 kHz (or less) to 30 kHz. However, the modelled circular disc had a thickness of 50 μm which is significantly thicker than quoted thicknesses of 2-3 μm for the most part (Gray, 1960) and ranging from 0.6 μm to 4 μm for the thin part and 6 μm to 20 μm for the thick (Stephen & Bennet-Clark, 1982).

In *3.2.1.5* it was shown that the eigenfrequency of a particular circular plate mode scales linearly with the thickness of the plate i.e. a simple linear adjustment of the frequencies can be applied to the results of the 50 μm model tympanum effectively scaling the disc to thicknesses much closer to the actual thickness of the real locust TM. Using the example of a 3 μm uniform circular disc this would equate to a scale factor of 0.06 (3/50) applied to the FOI's in ***3.2.2***. Incidentally, a quick calculation of the mass of a 0.75 mm radius, 3 μm thick circular disc using the density of 1200 kgm^{-3} and the formula for the volume, $V = \pi r^2 h$ gives a mass of about 6.4 μg, which is of the order of magnitude of the mass reported in Table 1.3.

For the real locust, five vibration shape types were allocated to the observed TM response displayed in ***3.1.1***. Response type 1 is the standing wave fundamental mode-like response seen in Figs. 3.3 and 3.13. The travelling wave pattern illustrated in Figs. 3.4 and 3.14 is assigned as response type 2. Response type 3 is the deflection pattern seen in Figs. 3.6 and 3.15. The penultimate response type, 4, is allocated to the travelling wave displayed in Figs. 3.9 and 3.17 with the final response type being that of Figs. 3.10 and 3.19.

Five vibration shapes were then used to categorise the different patterns of vibration seen during the acoustic-structure interaction of the finite element model. Response types 1 to 5 were allocated to the vibrations seen in Figs. 3.36 to 3.40 respectively.

Finally, the frequency cut-off values were recorded at which each of the 5 responses was observed to begin and end for both real locust and the basic model tympanum. All of this data was collated in Table 4.1, with the frequency range of the real locust truncated to 1.2 – 18 kHz with a step size of 0.6 kHz and the model frequencies ranged from 20 – 300 kHz with a 10 kHz step as this allowed correlation in the number of rows between locust and model. The fifth and sixth columns of the table are with the linear scale adjustment of the simulated frequencies applied, assuming a 0.75 mm radius circular disc of 3 μm thickness with the same material properties as previously.

Real Locust		**Circular Disc Model 50 μm**		**Scaled Model 3 μm**	
Freq. / kHz	*Vib. Shape*	*Freq. / kHz*	*Vib. Shape*	*Freq. / kHz*	*Vib. Shape*
1.2	1	20	1	1.2	1
1.8		30		1.8	
2.4		40		2.4	
3	2	50		3	
3.6		60		3.6	
4.2	3	70	2	4.2	2
4.8		80		4.8	
5.4		90		5.4	
6		100	3	6	3
6.6		110		6.6	
7.2		120		7.2	
7.8	4	130		7.8	
8.4		140		8.4	
9		150		9	
9.6		160		9.6	
10.2		170	4	10.2	4
10.8		180		10.8	
11.4		190		11.4	
12		200		12	
12.6		210		12.6	
13.2	5	220	5	13.2	5
13.8		230		13.8	
14.4		240		14.4	
15		250		15	
15.6		260		15.6	
16.2		270		16.2	
16.8		280		16.8	
17.4		290		17.4	
18		300		18	

Table 4.1 Vibration shape types for real locusts vs. FEM model vs. thickness/frequency scaled model results.

Looking at the spread of the vibration shapes there are some similarities between the scaled model results and those of the real locust. In addition, both real locust and model displayed the same standing wave, fundamental mode-like first vibration shape. They also both display similar low frequency travelling waves with the maximum of the deflection moving across the membrane along with a similar higher frequency travelling wave with the characteristic semi-concentric C-shape which transforms into a more concentrated maximum as it travels across the membrane. However, the model displayed one travelling wave, called vibration shape 3 and shown in Fig. 3.38, where the motion moved in the opposite direction from the travelling waves seen at other frequencies. This is not analogous to the real locust where the travelling wave motion follows the same general direction with origin in the thin region and movement towards the thick region for all frequencies. Non-uniformity in the thickness distribution of the real locust TM could be responsible for this lack of travelling waves moving across the centre of the membrane in the opposite direction; this initial model was a perfectly uniform disc. Finally, picometre scale displacements were computed for the 50 μm disc model in FEA acoustic-structure interactions. Running single frequency acoustic-structure interaction models (keeping the model size and computation time reasonable) of much thinner circular disc models, closer to the real locust TM cuticle thickness, yielded displacements in the nanometre per Pascal range, as expected due to the experimentally measured displacements from LDV.

4.2 The Effect of a Non-Uniform Thickness – Circular Disc with a Step Thickness Change

An obvious difference between the model in Chapter 3 and the real locust TM is the stark contrast in the distribution of cuticle thickness. Therefore the subsequent step was to investigate the effect of having a slight variation in thickness of the membrane. For this the majority of a 0.75 mm radius circle was extruded a Z-axis distance of 25 μm excluding a segment on the far right edge of the disc (positive X-axis direction) where the extrusion distance was 50 μm, with the step, running in the direction of the Y-axis, located exactly half a radius from the disc edge. Fig. 4.1 shows the 3-D geometry for this model which was meshed at a fine density beyond that of the extremely fine setting using custom mesh size parameters which yielded a 196803 element mesh.

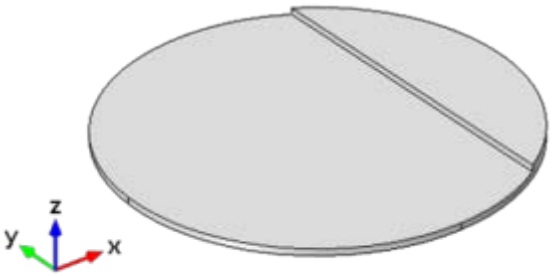

Figure 4.1 Two-step thickness circular model TM.

Using the same material properties as previous models and applying a fixed constraint to the disc edges then computing the first ten eigenmodes of this 3-D model resulted in the mode shapes seen in Fig. 4.2. Using COMSOL to output the total solid domain volume then calculating the new total mass (63.3 μg), the EMMF of each mode was computed via the method described in *2.2.3.2* and collated in Table 4.2. Worth noting is the change to the fundamental mode with the antinode now no longer central on the disc but instead shifting to the relative centre of the thinner section of the model tympanum. In actual fact all of the antinodes of each eigenmode display this same shift in the negative X direction favouring the thinner part of the disc. The 2nd mode, as seen on the uniform disc in Fig. 3.21, has now become two separate modes with slightly different eigenfrequencies. With a nodal line perpendicular to the step, the lower of these two eigenmodes had an

eigenfrequency of 49.9 kHz and the higher, mode 3, characterised by a nodal line parallel to the step, had a frequency of 55.9 kHz. Comparing the third row of Table 4.2 to the second and third rows of Table 3.1, there has been a substantial shift in the EMMF of mode 3 where the nodal line is parallel to the step, with a 10^4 order of magnitude increase from this mode on the uniform disc to the same mode on a step thickness change disc. Meanwhile the other two-antinode asymmetric mode, number 2 in Fig. 4.2, with antinodes aligned on the Y-axis, still appears to be somewhat suppressed by the system.

Furthermore there was an appearance of two new modes, the moderately strong 4th mode and much weaker 8th mode, characterised by three and four antinodes arranged in antiphase along the Y-axis. These mode shapes have arisen due to the unusual cross-sectional shape of the thin region of the membrane and analogous modes shapes are observed on uniform rectangular plates where the three or four antinodes usually split the plate into thirds or quarters respectively.

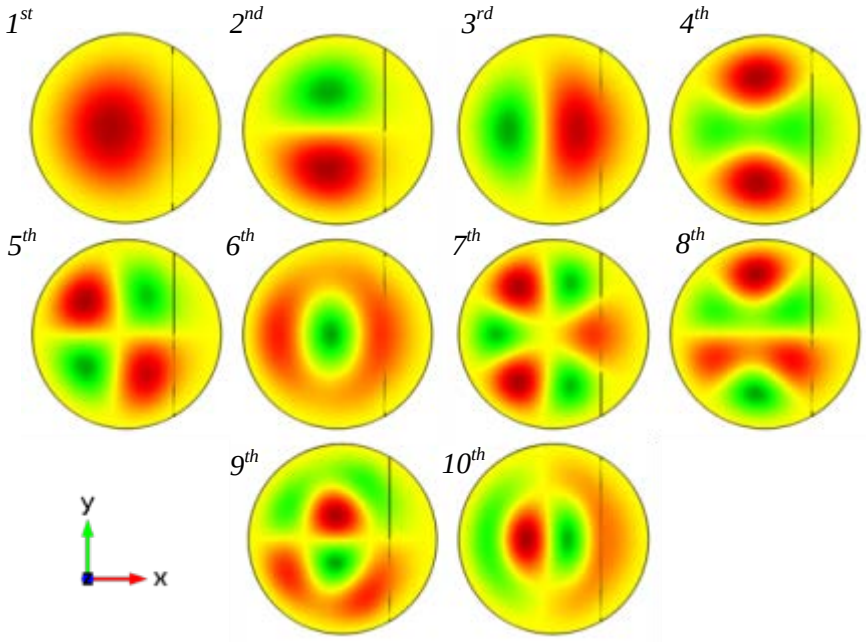

Figure 4.2 FEM computed mode shapes of two-step thickness membrane.

A similar if slightly lesser shift can be seen in eigenmode 10 when compared to the analogous mode 6 of the uniform disc. Mode 4 also has a reasonably high EMMF, indicating it is the 3rd strongest mode of the first 10 however in general the

system seems to favour mode shapes with the antinodes arranged in a perpendicular fashion with respect to the step thickness change i.e. along the X-axis.

Eigenmode	Eigenfrequency / kHz	$EMMF_z$ / %
1^{st}	26.90	42.38
2^{nd}	49.90	1.60×10^{-06}
3^{rd}	55.90	1.71
4^{th}	80.85	0.49
5^{th}	86.35	5.67×10^{-05}
6^{th}	93.70	18.43
7^{th}	120.78	0.06
8^{th}	121.15	1.06×10^{-04}
9^{th}	136.96	2.32×10^{-06}
10^{th}	143.86	0.35

Table 4.2 FEM computed eigenfrequencies and $EMMF_z$ of first 10 eigenmodes of two-step thickness circular model.

Acoustic-structure interaction with a frequency response, using the model settings outlined in ***3.2.5***, was the obvious next step. Meshing was increased to the extremely fine setting yielding more than 1.6 million elements. Several frequency-dependent travelling waves formed on this model membrane with three examples highlighted in Figs. 4.3, 4.4 and 4.5.

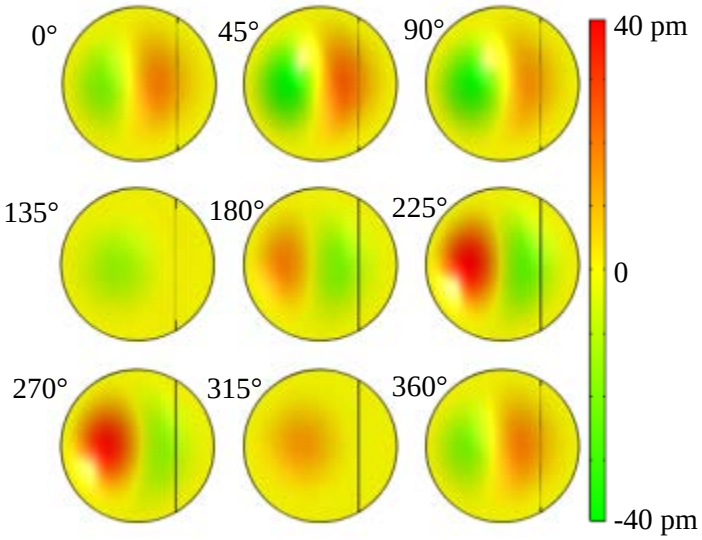

Figure 4.3 Dynamic cycle of vibration of basic model tympanum at 55 kHz.

All three of the travelling waves show the area of maximum deflection travel from left to right across the membrane. In Fig. 4.3, the frequency response at 55 kHz is shown and many features are worth noting. Firstly, a large area of the model

membrane is strongly displaced throughout the cycle. Secondly, there is just one region of maximal deflection which is spread widely in the plane of the membrane and travels to the thicker part of the membrane and partially beyond the ridge between thick and thin.

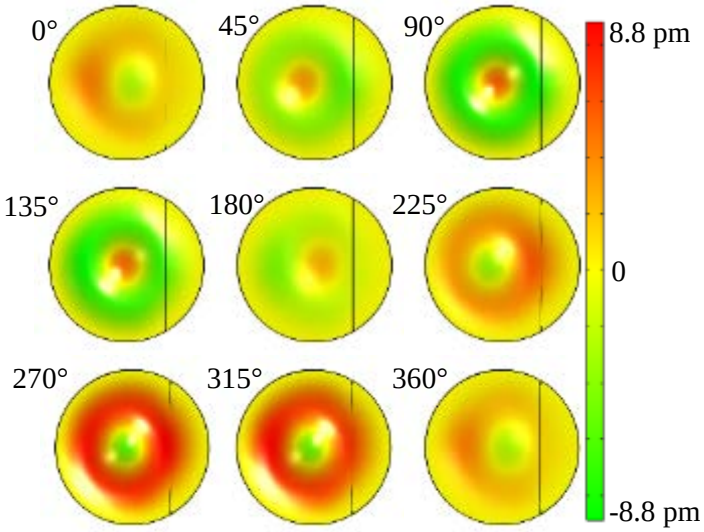

Figure 4.4 Dynamic cycle of vibration of basic model tympanum at 110 kHz.

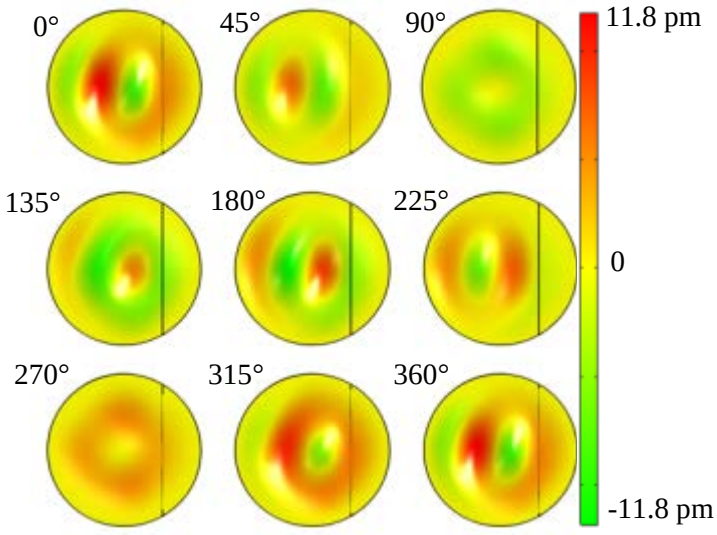

Figure 4.5 Dynamic cycle of vibration of basic model tympanum at 140 kHz.

Lastly, the travelling peak forms on the far left of the disc (180°), initially gaining amplitude as it travels (270°) before diminishing in amplitude near the thin

region centre (315°) and then finally increasing again near the maximum's terminal location (45°). The final positive displacement amplitude observed at 45° is clearly slightly stronger than at 315° yet weaker than at 180°. Eigenmode 3 on Fig. 4.2, with its eigenfrequency around 55.9 kHz, seems to dominate the shape of this travelling wave, as predicted at this frequency.

Fig. 4.4 displays the response of this model to 110 kHz initiating with the now familiar semi-concentric shape of the travelling wave (0°) which then evolves into a very condensed area or sharp peak of maximal deflection (90°). Fairly circular in shape when viewed from above with a slight flattening towards the thickness transition, this peak travels across the geometrical centre of the thin section. Enlarging in displacement amplitude just once as it progresses across the mode TM, the peak dissipates well short of the boundary between thick and thin membrane regions (180°). Eigenmode 6 from Fig. 4.2, with its corresponding eigenfrequency of 93.7 kHz, appears to dominate the motion at this frequency.

140 kHz is the last of the three highlighted frequencies and Fig. 4.5 shows the dynamic cycle at this frequency. Similar in appearance to the initial semi-concentric shape seen at the lower 110 kHz, the main differences at this frequency are that the concentrated peak which travels across the disc is stretched in the Y-axis direction (or constricted in the X direction) and the semi-concentric almost C-shaped maximum clearly begins to form while this sharp maximum is still present on the membrane. Additionally, the converged peak has fairly large amplitude at 45° before dissipating slightly at 90° then increasing again to a higher maximum value at 180°. The 10^{th} mode of the system, with a frequency of approximately 143.9 kHz dominated the motion of the vibration.

The ever-evolving nature of the amplitude of these deflection maxima and minima, seen throughout each travelling wave cycle, was not observed on the uniform membrane implying that this phenomenon is due to the thickness distribution's influence on the mode shapes. Unsurprisingly the eigenmodes which dominated the motion at each of these frequencies were among the strongest modes as indicated by the 3^{rd} column of Table 4.2. Worth noting is that the frequencies of the travelling waves observed above were exceptionally high in comparison to the observed response of the real locust TM however this dual step thickness model was

significantly thicker and therefore had a mass of 5 to 6 times more than that reported for the real TM. An eigenfrequency FEA was utilised to study the effect of reducing the thickness of the whole disc by one fifth, resulting in a change from a 25 µm to 50 µm, 63.3 µg model membrane to a more realistic 5 µm to 10 µm, 12.7 µg model TM. With the same ultra-fine mesh parameters, this 4 million DOF model yielded the same eigenmode shapes as previously but the eigenfrequencies were approximately one fifth of those listed in Table 4.2 bringing them closer to the experimentally determined transitional frequencies where changes in real locust TM travelling waves occur.

4.3 Elliptical Disc Model Locust Tympana

Model tympana with circular cross-sections are evidently a large approximation of the reniform real locust TM. Consequently, elliptically shaped discs were investigated as a possible closer approximation to the shape of the locust TM since the length of the real tympanum is significantly greater than the width. Defined by a semi-major axis of 1.25 mm, a semi-minor axis of 0.75 mm and a thickness of 5 µm, a uniform elliptical disc was the next model geometry. The material properties remained as for earlier models and the disc edges were again held stationary. Computing the first ten eigenmodes of this 3-D model resulted in the mode shapes seen in Fig. 4.6. With a total mass of 17.68 µg, this ellipse was in the range of the masses quoted in Table 1.3 and this yielded the eigenfrequencies and transverse EMMF values shown in Table 4.3.

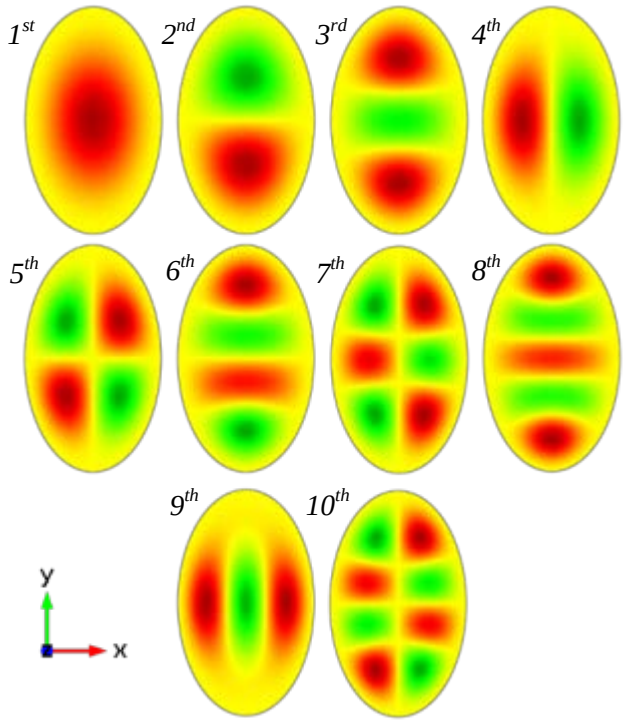

Figure 4.6 FEM computed mode shapes of elliptical membrane.

As was the case for the varying thickness circular disc models, the first asymmetric mode has again separated with one asymmetric mode defined by a nodal line across the minor axis (the 2nd mode in Fig. 4.6) and another asymmetric mode with the nodal line along the major axis (mode 4 in the Figure). However, some

differences exist between these particular eigenmodes and their analogous modes observed on the step thickness circular disc. Firstly, the relative difference in eigenfrequency between the two is now much larger than previously, owing to the fact the frequency of the elliptical disc mode with nodal line across the minor axis has shifted substantially upwards due to the fact that the minor axis of the ellipse is 60% of the major axis. Looking at rows 2 and 4 in Table 4.3, both of these asymmetric modes, numbers 2 and 4, are very weak compared to some other modes of the system.

Secondly, the apparent elliptical equivalent of the 2nd circularly symmetric mode (6th mode in Fig. 3.21) has shifted position considerably, from mode 6 of the circular two thickness model to mode 9 of the uniform elliptical membrane. Again it is the second strongest eigenmode according to EMMF in the Z direction, after the dominating fundamental mode.

Finally, more asymmetric modes are predicted for this model distinguished by their antinodes aligned along the Y-axis. Looking at the third column of Table 4.3, two of these asymmetric modes have relatively high EMMF, namely eigenmodes number 3 and 8. In their current form on an elliptical disc, these modes bear no apparent resemblance to any elements of the travelling wave patterns seen on the real locust TM.

Eigenmode	**Eigenfrequency / kHz**	**$EMMF_z$ / %**
1st	3.12	51.22
2nd	4.90	3.36E-11
3rd	7.39	8.53
4th	7.73	2.45E-08
5th	10.26	4.99E-09
6th	10.58	7.01E-12
7th	13.38	2.29E-08
8th	14.48	2.14
9th	14.51	9.16
10th	17.11	1.64E-10

Table 4.3 FEM computed eigenfrequencies and $EMMF_z$ of first 10 eigenmodes of uniform elliptical model.

Acoustic-structure interaction simulations of elliptical disc shaped model tympana in the frequency domain using the methods outlined previously resulted in the formation of frequency specific travelling waves. However, no significantly new results were observed beyond those seen for the circular disc models and certainly nothing which more closely resembled the frequency response of the real locust ear.

4.4 Reniform Model Locust Tympana

4.4.1 Uniform Thickness Model Tympanum – Eigenmode Analysis

The final geometry used to create 3-D finite element models of the locust TM was kidney-shaped discs, more closely resembling the actual eardrum of a desert locust. Initially a reniform disc of uniform thickness 50 μm was created in SOLIDWORKS using an extrusion of the TM outline shape in the contour map in Fig. 5 of Stephen and Bennet-Clark (1982). An eigenvector analysis of the first 20 modes of this model TM was computed, resulting in the output of the predicted mode shapes along with their corresponding eigenfrequencies and $EMMF_z$. Sorting these modes in descending order by their $EMMF_z$, the strongest 10 modes are displayed in an ordered fashion in Fig. 4.7 below.

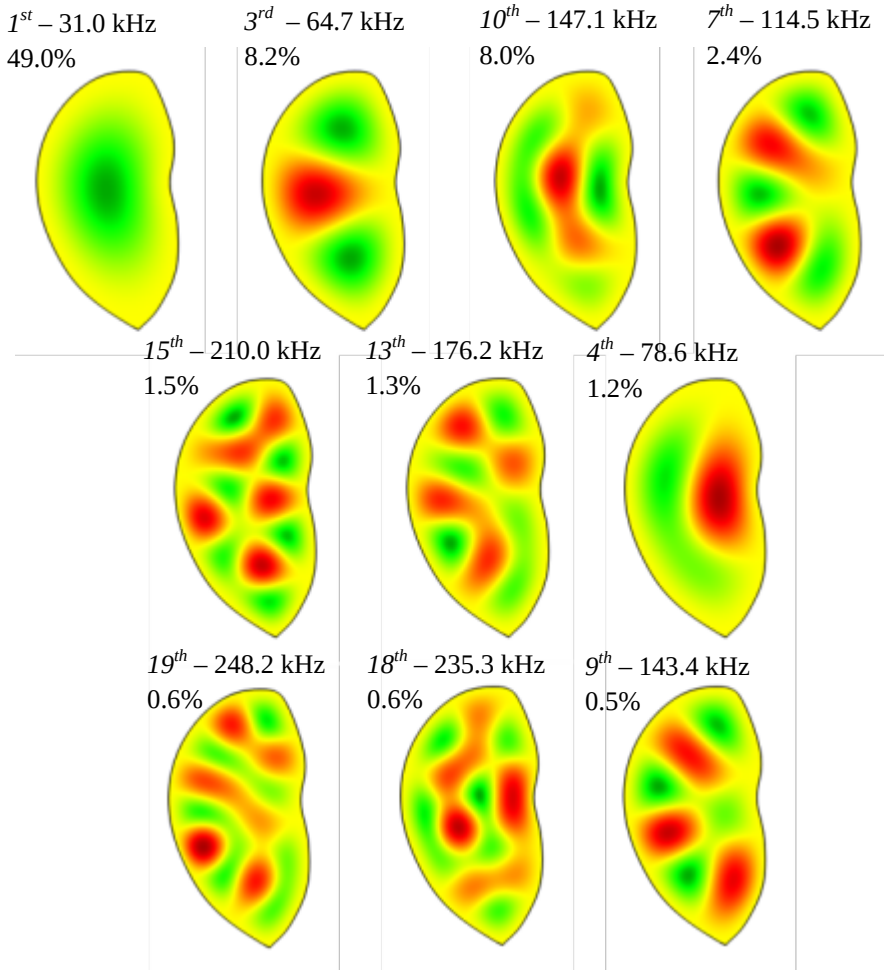

Figure 4.7 Strongest ten lower frequency eigenmodes of reniform 50 μm uniform model TM with mode position number, eigenfrequency and $EMMF_z$.

Similarly to the elliptical disc, the fundamental mode of the kidney-shaped uniform thickness model TM encapsulated approximately 50% of the $EMMF_z$, and the antinode was located centrally. Another common feature between the two models is the relative strength of both the third mode and the tenth mode above (analogous to the ninth mode of the elliptical model in Fig. 4.6), again having the second and third greatest EMMF of all predicted modes. This appears to be where the similarities end however, as there are several clear differences between the eigenmodes of the elliptical disc model and that of the reniform model.

Firstly, although modes 3 and 10 in Fig. 4.7 correspond to modes 3 and 9 of the elliptical model in Fig. 4.6, switching the disc cross-section from an ellipse to a kidney shape altered the mode shapes somewhat. In the case of mode 3, rather than the three antinodes being stacked along the Y-axis as they are in Fig. 4.6, they now have an element of both horizontal and vertical spacing i.e. they are diagonally aligned. The result of this is a single maximum on the left side of the membrane and almost a dual-peaked minimum on the right side. Mode 10 (9 for the ellipse) has switched from consisting of three equally sized antinodes each in antiphase with its neighbour and all aligned perfectly across the minor axis of the ellipse (see Fig. 4.6 9^{th} mode) to three distinctively shaped antinodes occupying very diverse regions of the model tympanum. Starting at the left, the first antinode is C-shaped and covers a large area of the membrane surface, closely following the form of the left edge from the top of the membrane to the bottom. Contrastingly, on the far right, the third antinode is very convergent with a large amplitude (greatest of the three) confined to a much smaller region. The central antinode of the three sits both within the first C-shaped antinode and around the small peaked antinode to its right, almost replicating the C-shape to a degree, but spanning a smaller area. Comparing the relative magnitudes of the antinodes, the antinode on the right, concentrated into a smaller area, appears to have a much greater displacement than the antinode on the left of the model tympanum, illustrated by the much darker shade of green of this maximum. The final highlighted difference between the modes of the elliptical disc models and those of the kidney-shaped membrane model here is the relative strength of the 4^{th} mode in Fig. 4.7. Analogies of this mode appear in Fig. 3.21 mode 2, Fig. 4.2 mode 3 and Fig. 4.6 mode 4 however within these systems this mode is relatively weak,

particularly in uniform circular and elliptical models, strengthening a little with the introduction of the thickness change in **4.2**. Modelling the locust TM with the more realistic reniform shape presented here resulted in a significant strengthening of the influence of this mode on the system. A final observation of this mode is that the antinodes again display unequal maximum amplitudes with the antinode on the right clearly greater in amplitude than the antinode on the left.

It appears that one impact of a reniform shaped tympanal membrane is an alteration of the conventional circularly symmetric modes into asymmetric style modes, stronger than those seen on a simple circular plate. Consequently, modes 3, 4 and 10 more closely resemble potential components of the locust TM travelling waves seen in ***3.1.1***. These subtle differences in model predictions may be missed in oversimplified circular or elliptical membrane models.

4.4.2 Uniform Thickness Model Tympanum – Frequency Response Analysis

Frequency response analysis of this model tympanum using the acoustic-structure interaction multi-physics application of the COMSOL FEM package was the obvious next step. As in previous acoustic-structure interactions, the stimulus consisted of simulated plane wave pressure fields with a sound pressure level of 65 dB SPL re 20 µPa and single frequencies guided by the previous eigenfrequency results.

60 kHz was the first chosen stimulus frequency and the response at this frequency is shown in Fig. 4.8. Travelling diagonally from the top left to the bottom right, the deflection looked to be heavily influenced by both the strong fundamental mode at 31 kHz and a weak second mode found near 45 kHz, analogous to mode 2 of the elliptical disc in Fig. 4.6 but too weak to be included in Fig. 4.7. A maximum displacement of about 18.5 pm was predicted for this model at this frequency. This travelling wave is similar to the diagonally downwards travelling waves observed on the real locust tympanum at lower frequencies in the range of 3 kHz e.g. at 3.5 kHz in Figs. 3.4 and 3.14.

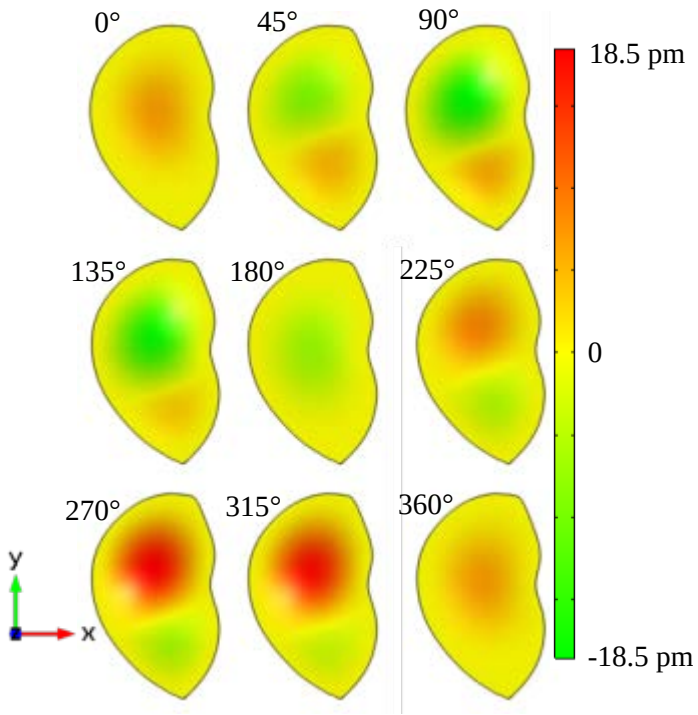

Figure 4.8 Frequency response at 60 kHz with maximum displacement of approximately 18.5 pm.

80 kHz was the next chosen frequency which lies near modes 3 and 4 in Fig. 4.7 and the response is displayed in Fig. 4.9. Coupling of these modes resulted in a travelling wave where the maximum of deflection propagates horizontally from left to right across the membrane. Although the direction of travel is very similar to that seen on the real locust TM at 5 kHz (Figs. 3.6 and 3.15), the shape of the maxima, particularly at its terminal location towards the right side of the model membrane, is somewhat different. The maximum amplitude of deflection at this frequency was approximately 14 pm.

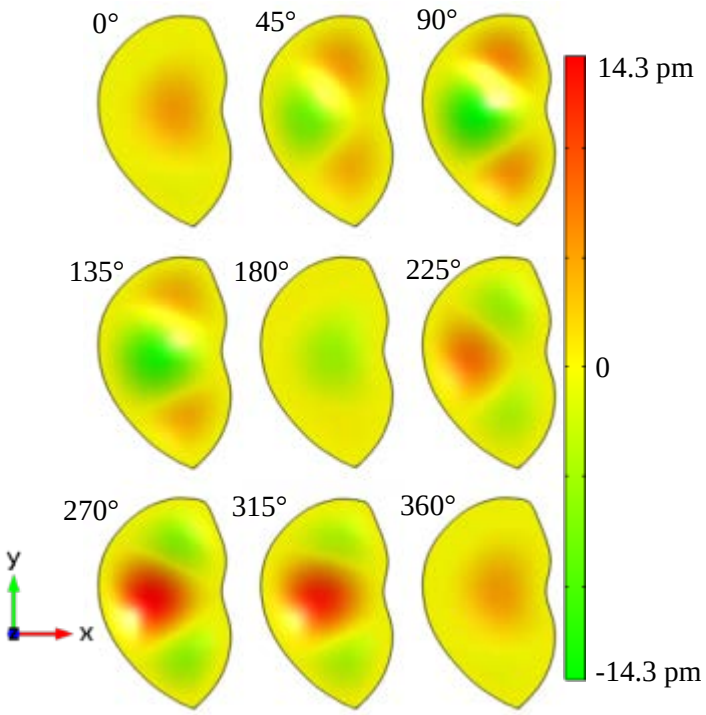

Figure 4.9 Travelling wave at 80 kHz with maximum transverse displacement of 14 pm.

The final highlighted frequency of interest was 157 kHz, slightly higher than the eigenfrequency of the 10th mode (Fig. 4.7), and the response at this frequency is shown in Fig. 4.10. At this frequency, modes 9 and 10 in Fig. 4.7 appear to combine, resulting in a C-shaped maximum (seen at 0° in the wave cycle) travelling from left to right across the membrane and eventually becoming a sharper peak at the right side (see 135° or 180° in the cycle). Approximately 4.5 pm was the maximum amplitude in this simulated frequency response.

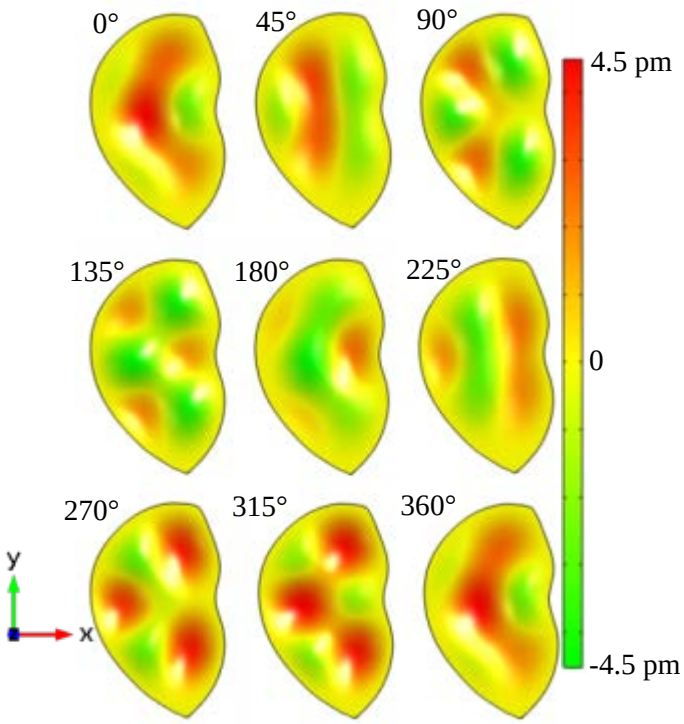

Figure 4.10 Travelling wave at 157 kHz with maximum transverse displacement of about 5 pm.

4.4.3 Contoured Complex Thickness Distribution Model Tympanum

SOLIDWORKS' advanced 3-D CAD complex shape modelling and surfacing tools were utilised to construct the final kidney-shaped model locust tympanum. Outlined in its entirety in Subchapter **2.3**, this method involved building a surface with realistic smooth thickness variations, closely following the aforementioned contour map of the locust TM (Stephen and Bennet-Clark, 1982). Fig. 4.11(a) below shows the next geometry which was imported into COMSOL Multiphysics, tilted to show the contouring on the top surface. In 4.11(b) a plan view of the model TM is displayed along with five slots which were cut into the geometry, rotated and then enlarged in the small dotted rectangles to show an example of the sweeping contours of the TM. A measured volume of 8.6×10^{-12} m^3 for the model geometry yielded a model tympanum mass of approximately 10.3 µg, around the same order of magnitude as reported locust tympanum masses (*1.4.2.2*).

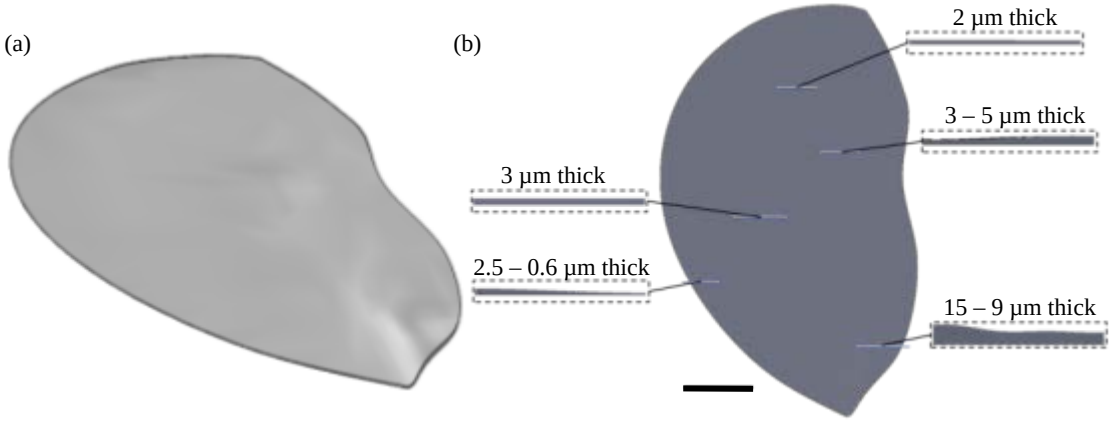

Figure 4.11 (a) Complex locust tympanum model geometry, angled to highlight contouring. (b) Plan view with 5 slices and their cross-section enhanced with exaggerated thickness. Scale bar for (b) represents 0.5 mm on plan view only.

The geometry was meshed with an adaptive growth mesh algorithm resulting in areas of thinner (denser meshing with smaller element size) and thicker (sparser meshing with larger element size) cuticle, visible in Fig. 4.12.

With other model parameters set as previously, an eigenmode analysis was implemented using a total mesh size of 207107 elements initially. The motivation of this eigenmode computation was a search for mode shapes, with frequencies relevant to the real locust system, and which closely resemble components of the travelling

wave patterns seen on real locust eardrums. To fully encapsulate the perceived sensitivity range of the locust hearing, a large number of eigenmodes were simulated, from the fundamental mode with an estimated eigenfrequency of 2.1 kHz to an eigenmode at 43.6 kHz. Ten of these eigenmodes are displayed in Fig. 4.13, arranged in descending order by EMMF. An extra fine mesh in excess of 1.2 million elements (considerably large for a pure solid mechanics eigenfrequency analysis) was used as a final verification of the first ten eigenmodes.

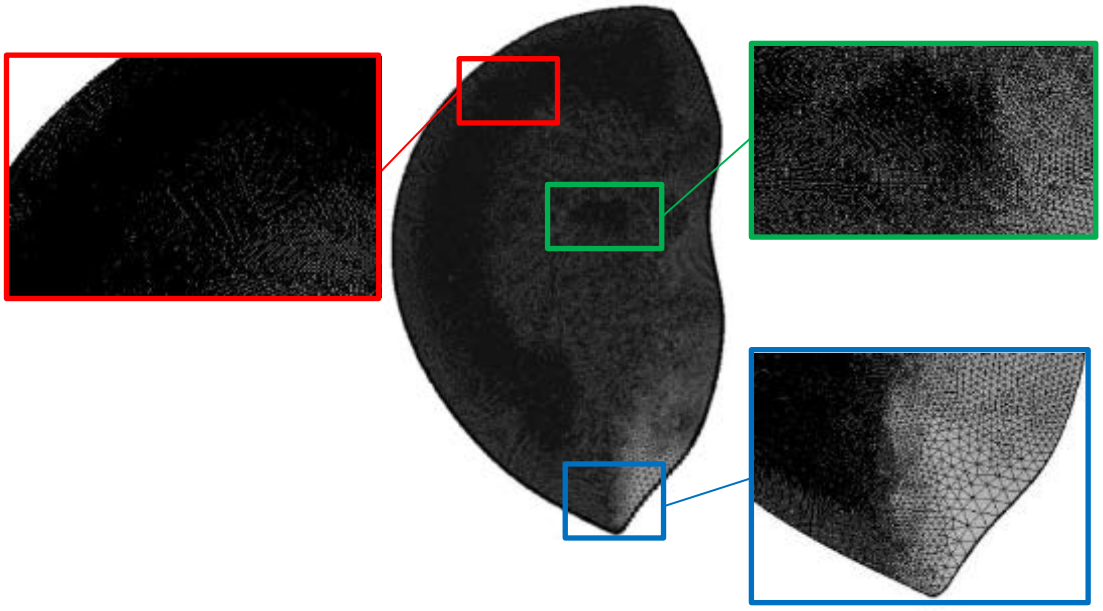

Figure 4.12 COMSOL FE mesh of model TM with three regions enlarged showing thickness-dependent adaptive mesh density.

An apparent similarity between the eigenmodes of this model tympanum and those of the uniform membrane in the previous subsection is the shape and relative strength of modes 3 and 4 of the systems. However some major differences arise between the computationally predicted responses of each model system. Firstly, and particularly clear for modes 1 and 3, there is an obvious shift of the majority of the membrane deflection away from the centre and into the thin region of the model TM. Modes 1, 3 and 4 have changed from the horizontal arrangements of antinodes of the uniform model TM to a slight diagonal arrangement which also matches the direction of travelling wave propagation, through the PV area, seen on a real locust TM (see transect line in Windmill et al., 2008). Higher order modes display far fewer large amplitude antinodes in the thicker section of the model TM and the higher the

eigenfrequency, the less displacement observed in the thick section, with mode 35 showing this point well. Many of the higher order modes were very similar to mode number 35 in shape with their patterns of antinodes rotated slightly and their eigenfrequencies in very close proximity to each other, with strong coupling potentially giving rise to the characteristic narrow rotating peaks of the high frequency travelling waves on the real locust TM.

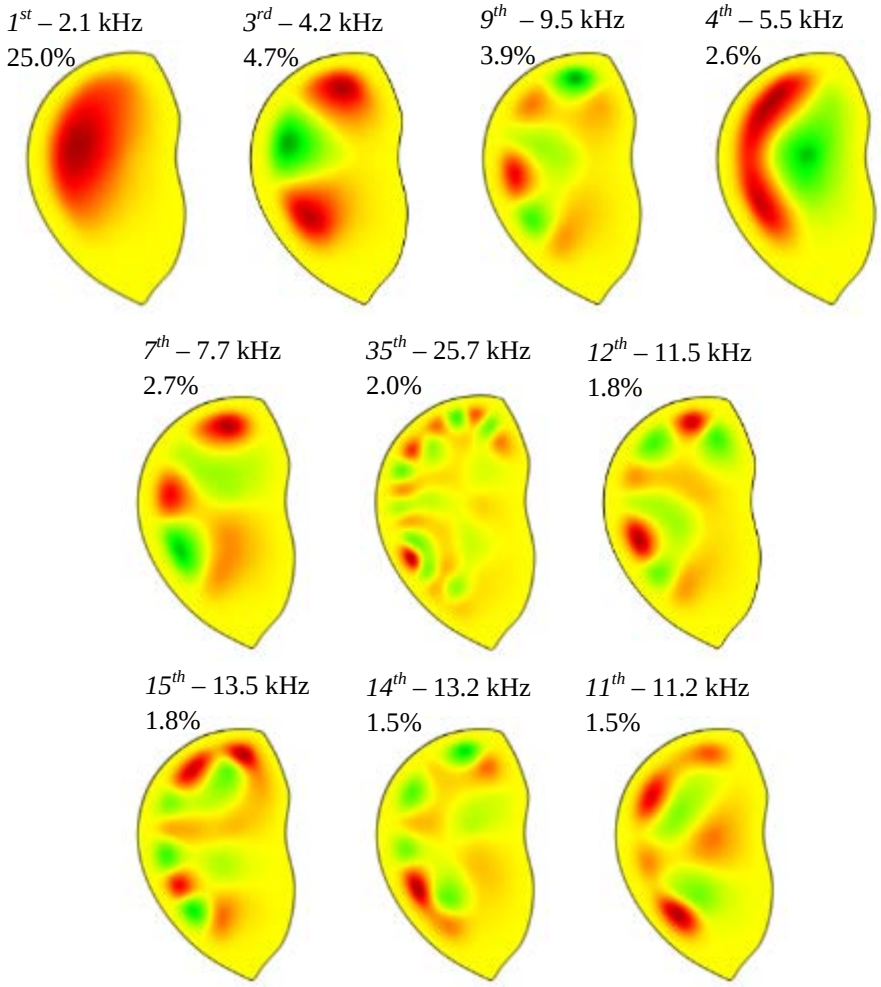

Figure 4.13 Strongest ten lower frequency eigenmodes of contoured thickness model TM with mode position number, eigenfrequency and $EMMF_z$.

Interestingly, the fundamental mode has dropped significantly in $EMMF_z$, from 50% to 25%, indicating that more of the energy of the system has been transferred into higher order modes. The shape of the first mode does not quite predict the vibrational response seen at the lowest frequencies on the real locust however the attachment of the mass of MO could perhaps have a large influence on the response at this range. Importantly, the frequencies are now aligned with the real

locust hearing range and the close proximity, mode shape and high $EMMF_z$ i.e. modal strengths of modes 1 and 3 could lead to the coupled response seen at frequencies around 3.5 kHz on the real locust. For frequencies slightly higher near the value of 5 kHz, the effect of mode 4, also with a high EMMF and close frequency, could be the horizontal motion observed previously. Modes 7, 9, and higher, particularly 11 may combine to result in the characteristic C-shape (see left side antinode of the 11^{th} mode) converging to peaks which meet at the PV. Overlapping an image of the real TM with modes 4 and 11 above (among others) showed the antinodes on the right to be aligned perfectly for the position of the PV. Additionally, all of these complex modes in close proximity, with antinodes arranged in patterns on the model membrane, could explain the peaks measured by Windmill et al. (2008) when studying the frequency spectra of five points of interest on the locust tympanum.

4.5 Additional Features of the Locust Hearing System

4.5.1 Model Müller's Organ

In reality, the locust hearing system has several components which contribute to the overall response of the system, with one of the major components being Müller's organ. To test for the first time, the effect of the addition of MO as an off-centre mass on a model TM, a model was constructed using a simple circular disc of radius 1.125 mm and thickness of just over 3 μm i.e. a thin cylinder of volume 1.24×10^{-11} m^3. Using the same material properties as with previous models yielded a mass of approximately 14.9 μg for the disc. A prolate spheroid of dimensions 200 μm × 600 μm × 200 μm was constructed and connected to the disc via three long hollow cylindrical bodies, a simulated SB, EP and fusiform body. Of the three, the EP was widest and its interior hole was extruded from inside the model MO right through the entire membrane thickness to the external surface, leaving a hollow invagination as described in *1.4.2.2* for the EP. This model cell body and attachments had an overall volume of 1.20×10^{-11} m^3, and therefore a mass of 14.4 μg. As a result both masses were therefore consistent with the published data on the estimated and measured masses of both of the major locust tympanal system components. Multiple views of the geometry are shown in Fig. 4.14 with a transparent plan view making the modelled MO visible behind the disc.

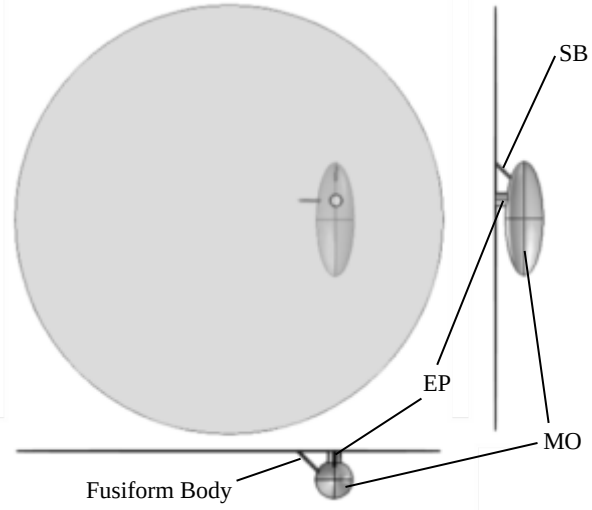

Figure 4.14 Model tympanum disc and Müller's organ. Simplified body of Müller's organ, styliform body, elevated process and fusiform body all labelled.

Initially, an eigenmode analysis was computed using this model geometry and a high mesh density leading to a 13 million DOF model. The fundamental mode was predicted to have an eigenfrequency of 0.58 kHz, an $EMMF_z$ of 64% and a mode shape as shown in Fig. 4.15. This value is the same as the 0.58 kHz natural frequency of Müller's organ predicted by Stephen and Bennet-Clark (1982 – see p.42) of this thesis. The motion seen at this eigenmode was dominated by a rocking motion of the simulated Müller's organ behind the model tympanum causing the membrane to displace. Visible in the Figure are parts of the simulated MO at its zero position, closer to the reader than the inwardly deflected tympanum.

Figure 4.15 Fundamental mode of an approximately 3 µm thick circular membrane with a model MO attached.

When the MO was removed from the model and an eigenmode analysis of the fundamental mode of a circular disc with the same radius and thickness was executed the resulting image was that seen of the 1st mode in Fig. 3.21, as expected, with an eigenfrequency of approximately 1.22 kHz. Doubling the thickness to approximately 6 µm and therefore increasing the mass of the system to that of the previous disc plus MO model, resulted in the predictable value of 2.46 kHz for the eigenfrequency of the fundamental mode. Therefore the addition of the simulated MO had a significant effect on both the shape and eigenfrequency of the first eigenmode.

Two acoustic-structure interaction frequency response analyses were then performed using the same stimulus of a plane wave of sound pressure level 65 dB SPL and frequency of 1 kHz. The first was executed with the stimulus acting externally on the surface of the model tympanum and the second with the sound incident internally onto MO and the internal surface of the membrane. For the external stimulus, a maximum Z direction displacement of 115 nm was observed whereas for the internal stimulus this maximum more than doubled to 272 nm.

Relative to the circular face of the model membrane, the simulated Müller's organ had a surface area five to six times greater, and this, along with the addition of the strong mode in close proximity to the 1 kHz stimulus, could perhaps explain this observation of increased sensitivity to internal stimuli.

4.5.2 Cuticular Shell

Another major component of locust hearing is the external cuticular shell which covers a large part of the tympanum (see the left image of Fig. 1.10), previously unstudied computationally until this subchapter. To investigate the effect of this shell the same circular disc as in ***4.5.1***, minus the model MO, was used along with a quarter of a hollowed-out sphere. With an external radius of 1.25 mm and an internal radius of 1.125 mm, the quarter sphere resulted in the shell of thickness 125 µm shown in Fig. 4.16 below.

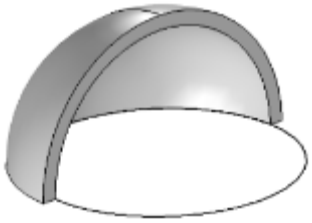

Figure 4.16 Geometry showing circular disc model tympanum and quarter sphere shell.

Acoustic-structure interactions were computed with two different stimuli, the first at a frequency of 5 kHz and the second at 10 kHz. The maximum transverse displacement of the model membrane was extracted at each frequency and then compared to the maximum displacement for frequency response analyses at the same frequencies for the same modelled disc minus the shell structure. At 5 kHz the maximum displacement in the out-of-plane Z direction for the disc without the shell was approximately 15 nm and at the same frequency the model with shell yielded a maximum transverse displacement of 14 nm. 10 kHz was the next frequency of interest and at this frequency the maximum displacement increased from 46 nm without the shell to 65 nm with the shell. Incident sound at a higher frequency appeared to have been amplified by the presence of the shell around the membrane.

4.6 Directionality

4.6.1 Internal Sound Transmission

Another phenomenon observed in real locusts is that of the sound propagating internally through the body i.e. sound waves transmitted by (or through) the ear. Hypothesising that the vibrational shapes of the tympanum influence the frequency dependency of the sound pressure level of internally propagating sound, a new method was devised using the simulation results from the acoustic-structure interaction of a 50 μm circular disc in ***3.2.5***. As seen in Figs. 3.32 and 3.33, the finite element model has a small cylindrical air domain located behind the model tympanum in which the pressure is disturbed by vibrations of the disc. The average sound pressure (Pa) was computed in this domain for every frequency of the parametric sweeps used in ***3.2.5***. Complex number representations of the pressure behind the membrane were obtained as a result of this post-processing computation (see *2.2.3.3*). The absolute values of these complex expressions are the pressure amplitudes (Pa) which were converted into sound pressure levels (dB SPL) using Eq. [1.1] and then the external value of 65 dB SPL was subtracted yielding computation of the relative internal sound pressure level.

Plotting this sound pressure level on the Y-axis against simulation stimulus frequency on the X-axis resulted in Fig. 4.17.

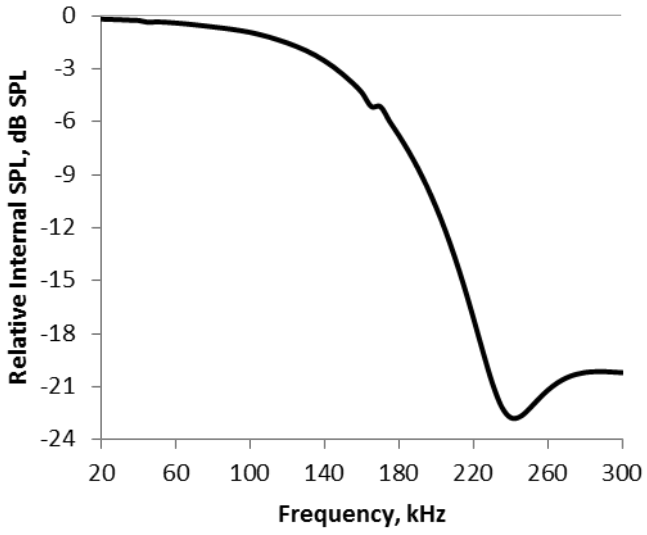

Figure 4.17 Frequency vs. relative internal sound pressure level for simple model TM.

To scale the frequencies on the X-axis of Fig. 4.17, which were relevant for a 50 µm circular disc, to the equivalent for a 3 µm disc (of mass much closer to the real locust TM mass) the same linear scale factor of 0.06 was used as previously, resulting in the following new version of the Figure.

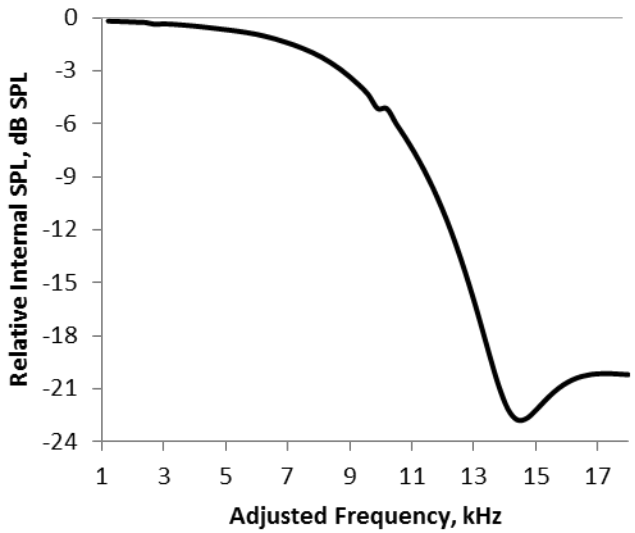

Figure 4.18 Linearly-adjusted frequency vs. relative internal sound pressure level.

Considering this computation was for only one very basic model TM of uniform thickness and perfectly circular shape and therefore a somewhat simplified version of the real system which has two tympana separated by a specific distance, interconnected by a series of air sacs and positioned laterally on a locust body, the above relationship bears a striking resemblance to historical experimental data (Fig. 9 of Michelsen, 1971c and also Fig. 2 of Miller, 1977). This indicates that the varying shape of tympanum deflection and moreover the distribution of maximum displacement across the membrane surface could indeed have a strong influence on the transfer of sound energy into the internal part of the locust's acoustic system.

4.6.2 Full Body Effects

Over a specific range of frequencies, locust body dimensions are thought to cause disturbances in an incident sound field, potentially allowing for a method of perception of the direction of a sound source. Therefore as a final step, a model was constructed to investigate the combination of the influence of the locust body on the sound field and the extent of internal sound transmission from an ear contralateral to a sound source, to the interior of the ipsilateral ear. For this a simplified locust head and thorax were constructed as a cylinder of length 1.9 cm and radius 0.5 cm based on simple observational measurements. Next, the abdomen was simulated as a cylinder of length 3.6 cm and radius 0.35 cm. Two model ears were constructed as 0.77 mm radius, 3 μm thick circular membranes tilted diagonally inwards at their posterior edge at an angle of 30° to the external body surface (again based on personal observations). A chamber of elliptical cross-section was extracted from between the two ears with semi-major axis equal to the model ear radius and semi-minor axis calculated using the exact ear diameter and angle of tilt to calculate the required width. The result was the geometry shown with transparency activated in Fig. 4.19 below.

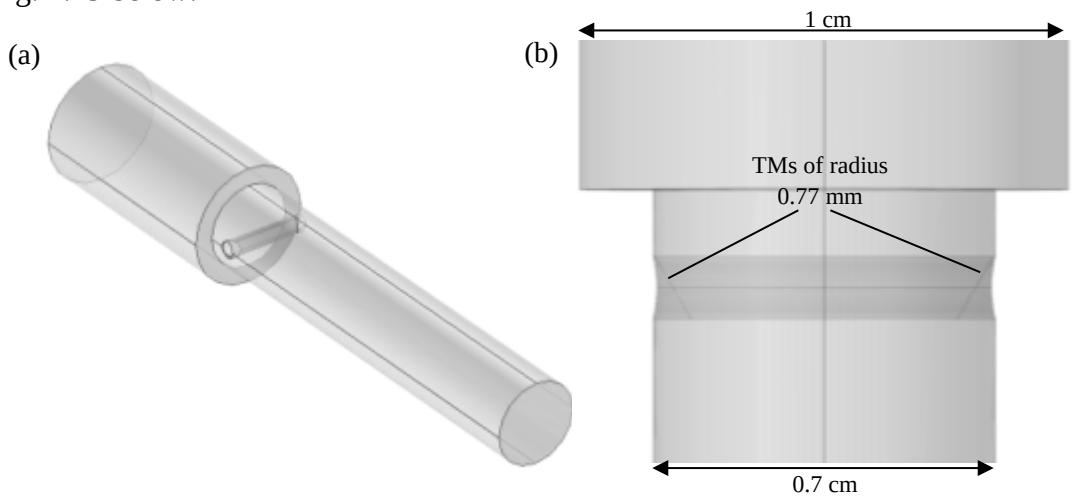

Figure 4.19 (a) Simplified model locust body with two ears and internal air chamber. (b) Zoom on region containing tilted model ears with annotated dimensions.

After adding a surrounding sphere as an additional air domain (to the cylinder between the ears) and constructing a high density mesh, the model had a total element count in excess of 1.6 million elements. Two acoustic-structure interactions

with a frequency analysis were computed, using a stimulus of an acoustic load incident on the left side of the body at 90° to the anterior-posterior axis of the body i.e. perpendicularly towards the space containing the left ear. Before executing the analyses a fixed boundary condition was applied to the external and internal surfaces of this ipsilateral ear to prevent the movement of the ear impacting on the internal sound since the intention was to investigate the impact purely of the movement of an ear contralateral to a sound source. The chosen frequencies for the analyses were 1 kHz and 20 kHz and a sound pressure level of 65 dB SPL. Four surfaces were defined namely the left exterior, left interior, right interior and right exterior and the pressure field as a complex number expression was extracted at each of these surfaces. The absolute value of this expression was the pressure amplitude in Pascals at the surface and the argument was the phase of the pressure wave at each surface in radians. Using Eq. [1.1], the pressure amplitude was converted into dB SPL. Fig. 4.20 below shows a snapshot in the cycle of the incident sound of frequency 1 kHz where red indicates a localised region of high pressure. Clearly the pressure amplitude external to the left ear is very close to the pressure amplitude external to the right ear in fact the computed difference in dB SPL between the sound pressure level at the external surface of the left ear and the external sound pressure level at the right ear was just -0.01 dB SPL. Bearing in mind the left ear is stationary, i.e. no sound is transmitting internally from the left side, clearly a huge majority of the incident sound wave has diffracted easily around the locust body at this frequency.

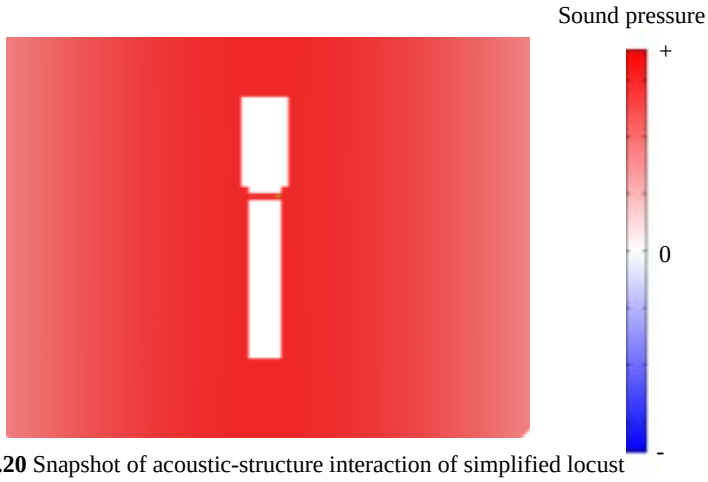

Figure 4.20 Snapshot of acoustic-structure interaction of simplified locust body, at stimulus frequency of 1 kHz.

The same analysis was performed at 20 kHz with the results shown in Fig. 4.21. At this frequency the locust body has a visible effect on the incident sound pressure wave and the sound pressure at each ear is clearly very different both in amplitude and phase at this snapshot in the cycle. Externally to the left ear the amplitude of the sound pressure level was 70.8 dB SPL, an increase of 5.78 dB on the incident pressure field value of 65 dB SPL, owing to a focussing of the sound due to reflections at the simulated body features. Conversely, exterior to the right ear, the amplitude of the sound pressure field was 61.7 dB SPL, 3.27 dB less than the amplitude of the stimulus. Resultantly there was a predicted difference of greater than 9 dB SPL between sound external to the ipsilateral ear and sound reaching the external surface of the contralateral ear i.e. a partial acoustic shadow created due to the complex interference pattern occurring as a result of reflection and diffraction at the boundaries between the fluid and solid domains.

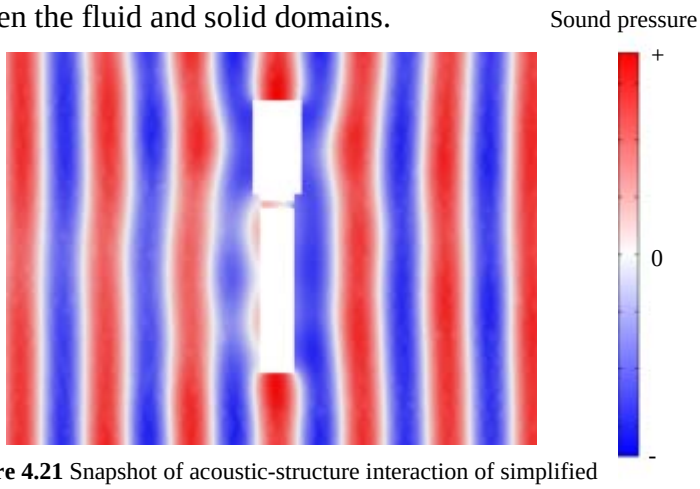

Figure 4.21 Snapshot of acoustic-structure interaction of simplified locust body, at stimulus frequency of 20 kHz.

By hiding the surrounding sphere of air, Fig. 4.22 was created showing a magnification of the internal propagation of sound purely within the interaural chamber as a result of the vibrating contralateral right ear. The displacement of this model tympanal membrane is overlapped and the response to the 1 kHz stimulus is at the top with the response at 20 kHz underneath. Consistent pressure field colour scales and deflection scale factors were used to produce a clear and fair comparison between the impact of the vibrating right ear on the sound reaching the internal surface of the left ear at each frequency. Darker shades of red indicate localised areas of high positive sound pressure and likewise darker shades of blue would indicate

areas of high negative sound pressure. Clearly the interaural sound pressure is far higher at 1 kHz than at 20 kHz due to the fact that the displacement magnitude of the contralateral ear is also far greater at 1 kHz. This fact is to be expected given the difference in the sound pressure level external to the contralateral ear at each of the two frequencies. Again the complex pressure fields were extracted and sound pressure levels calculated only this time at the internal surface of the ipsilateral left ear. For the 1 kHz stimulus this was found to be 64.5 dB SPL and at the 20 kHz stimulus the predicted value was just 56.7 dB SPL. In conclusion, the internal sound pressure level due to the contralateral ear vibrating at 1 kHz was just 0.5 dB below the stimulus amplitude value whereas when the ear responded to sound of frequency 20 kHz the internal sound pressure level was 5 dB less than that predicted externally at the right ear and a full 8.3 dB less than the 65 dB SPL stimulus.

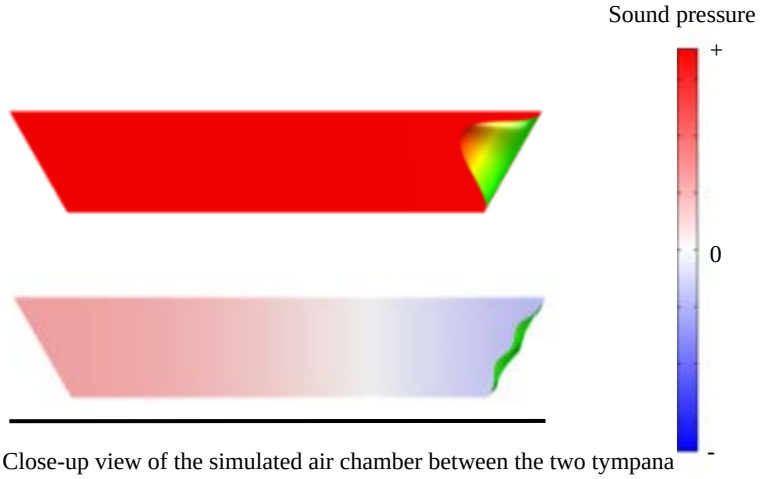

Figure 4.22 Close-up view of the simulated air chamber between the two tympana showing the exaggerated displacement of the right TM and consequential sound pressure distribution within the chamber, at 1 kHz (top) and 20 kHz (bottom). Scale bar is 0.7 cm.

4.7 Discussion

Simulating the locust TM as a reniform disc of uniform 50 µm thickness resulted in the prediction of several strong eigenmodes with shape reminiscent of components of the travelling waves measured on a real locust eardrum using LDV. Using FEM to simulate the frequency response of such a model tympanum resulted in the formation of many different travelling waves, with frequencies of 60 kHz, 80 kHz and 157 kHz being highlighted in subsection ***4.4.2***. Termination of each of the travelling waves on the uniform model TM occurred at the far right of the disc at each frequency, different from that observed on the real locust TM where higher frequencies are seen to terminate nearer the PV and low and medium frequencies travel beyond this point into the thicker region of the membrane. The absence of this phenomenon from this model is assumed to be due to the lack of the thickness changes across the real membrane and the location of sensory cell attachment areas. Corroborating this point is the contour thickness model in ***4.4.3*** where there was variability shown in the antinode positions when a non-uniform thickness is present. The modes of this changing thickness model show the PV to be located in a position relevant to areas of maximal deflection.

Initially, the observed frequencies where travelling waves formed on the uniform TM model appear far greater than the relevant frequencies of auditory sensitivity of a real locust however one must remember that this model TM was 50 µm thick, more than sixteen times thicker than the roughly 2-3 µm thick cuticle of the tympanum. Eigenmode analyses, using the analysis in ***3.2.1***, but parametrically sweeping an anisotropic Z direction scale factor from 0.5 to 1.2 with a 0.1 step i.e. creating model membranes from 25 µm to 60 µm thick, confirmed that the eigenfrequencies at all modes were directly proportional to the membrane thickness. Therefore assuming a model TM of thickness 3 µm, the corresponding scale factor is 0.06 and consequentially the travelling waves seen in Figs. 4.8, 4.9 and 4.10 are predicted at frequencies of 3.6 kHz, 4.8 kHz and 9.4 kHz respectively on a 3 µm reniform membrane, perfectly in line with frequencies where different travelling wave responses are observed on the real locust eardrum (see Table 4.1 column 1).

A circular disc model with a simulated Müller's organ resulted in a low frequency mode with the displacement confined to an area around the attachment points of the MO. Real locust tympana at low frequencies show deflection patterns confined to this same region.

A simulated cuticular shell was constructed and found to influence higher frequency sounds, incident on the model tympanum. Previously unstudied computationally, this phenomenon can perhaps be explained by calculating the wavelength of sound in air at each of the stimulus frequencies used in ***4.5.2***. At 5 kHz the wavelength of sound in air is approximately 69 mm (Eq. [1.3]), far greater than the dimensions of the modelled shell or membrane therefore a large fraction of the sound is expected to diffract around the structure. Sound waves of frequency 10 kHz have a wavelength of half this value in air i.e. 34.5 mm, and at this wavelength the incoming sound wave appears to be quite strongly influenced by the shell structure which would be expected to focus more sound towards the membrane, similarly to a curved reflector.

The combined influence of frequency-dependent TM vibration patterns and the dimensions of the external locust body on the internal sound between two tympanal ears was investigated using novel one-ear and two-ear models. At higher frequencies, less sound reached the outside of the contralateral ear due to partial acoustic shadowing which, in conjunction with the vibration shapes of the membrane at higher frequencies (less membrane surface area displaced maximally and with constant phase), results in a diminution of the sound reaching the internal surface of the ipsilateral tympanum. However it should be noted that computational models predicted the internal surface of the tympanum and the attached MO to be highly sensitive to sounds propagating within the interaural chamber, due in part to the increased surface area of the MO.

Some anomalies were observed in the FEM modelled tympanal membranes, where the modelled response differed greatly from that seen of the real locust ear. Firstly, to observe the travelling waves seen in previous Subchapters, the angle of incident sound required an off Z-axis component. In reality, the travelling wave response of the real locust has been found to be consistently independent of the angle of the respective sound source. However, testing of the finite element models

concluded that an angle of just 5° to the normal of the model membrane surface was enough to induce the travelling wave motion. Bearing in mind that the real locust membrane is not completely flat and is not angled parallel to the external surface of the body (but inwards with respect to the locust body), this combination along with the contribution of internal sounds with a fairly fixed stimulus angle could be enough to explain this phenomenon. Also worth noting is that the tympanum is partially obscured by the cuticular exoskeleton of the locust body which forms a shell-like cover, also adding to a pre-conditioning of any incident sound.

Secondly, at certain frequencies the travelling wave formed travelled in the opposite direction from expected, i.e. right to left when looking externally at a right locust ear. This phenomenon has never been observed on a locust TM and this travelling wave pattern could be supressed by the complex combination of the off-centred position of the mass of the MO and its attachment sites including the FB, the off-centred thin region and the phase relationship between external and internal sound pressure contributions. In addition, the damping effect of the internally located air sacs and abdominal fat etc. will also be influencing the response in a complex and hard to replicate manner.

The last anomaly is that when the model tympana were excited at the peaks in the modelled frequency response, standing waves often form on the modelled disc membranes. In reality standing waves are not observed on the locust TM except at the lowest frequencies where the overall response is a standing fundamental mode type pattern. One possible explanation is that the real TM is inhomogeneously damped, with off-centre thin and thick regions, an off-centre mass of MO, all contributing to the lack of standing waves. Movement of MO due to potentially phase-shifted internal sound coupled through the strong attachment of the EP to the membrane could also be a factor. At low to medium frequencies, where the ear is acting as a pressure gradient receiver, the phase relationship between the two components could result in the observed response. In addition, at higher frequencies many similar strength modes are predicted in very close proximity, therefore strong modal coupling interactions would be expected.

Chapter 5 : MEMS Microphone Structure

"*Nature is written in the language of mathematics*" – Galileo Galilei

This chapter introduces two silicon micro-electro-mechanical-systems micro-mirrors and assesses their potential as a directional microphone structure, through a combination of their operating modes. FEM and LDV methods introduced in previous Chapters are used to predict the eigenmodes of these structures and their corresponding eigenfrequencies. A modal investigation is then implemented using LDV with a view to experimentally testing the aforementioned computational predictions. Finally frequency response analyses are carried out both experimentally and computationally using LDV and FEM, to study a multi-degree-of-freedom MEMS structure's mechanical performance as a directional microphone. Part of the results presented in the following Chapter has formed a journal publication (see Appendix A).

5.1 Introduction

As discussed in Chapter 1, silicon MEMS based directional microphones have often taken inspiration from the unique directional hearing system observed in the parasitoid fly, *Ormia ochracea* (Miles et al., 1995; Yoo et al., 2002; Miles & Hoy, 2006; Liu et al., 2008; Touse et al., 2010; Lisiewski et al., 2011; Chen & Cheng, 2012). This fly localises a host cricket's acoustic signal (song) with reported accuracy better than 2°. The *Ormia's* ears are a tympanal hearing system, and the tympanal pits of each ear (location of the neural attachment) are separated by just 0.5 mm, yet the wavelength of the cricket song in air is an order of magnitude higher. The two tympana are mechanically coupled via an intertympanal bridge, which results in the combination of two major modes of vibration. Favourably for the fly, the consequence is that the perceived pressure intensity difference is significantly amplified.

These bio-inspired microphone designs have reported varying success however, in principle, any micromechanical device with sufficient degrees of freedom of movement may be capable of displaying some directional acoustic sensitivity. The purpose of this Chapter was to build on the protocol outlined in previous Chapters, using similar computational and experimental methods to analyse the potential mechanical directional performance of two single-crystal silicon (S-C Si) MEMS structures that were originally designed as twin-axis optical scanners. Although not designed as microphones or optimised for such applications, the MEMS structures displayed similar dimensions to those of the *Ormia* hearing system.

Single-crystal silicon is used throughout MEMS technology as the atomic structure and chemical properties result in MEMS devices displaying unique properties. The structure of S-C Si is such that there are no grain boundary associated defects meaning, theoretically, that the response of any fabricated device should be more consistent, predictable and accurate.

The structures analysed in this thesis were fabricated in the MEMSCAP Inc. (Durham, NC, USA [14]) commercial foundry using a multi-user silicon-on-insulator process (SOIMUMPs). Foundries such as MEMSCAP provide a cost-effective

solution for MEMS fabrication and development work because the processes are offered on a multi-user basis therefore several parties share fabrication and mask costs. An additional advantage of using a commercial foundry is that there already exists an established route to fabricating in large quantities by the same foundry.

A 10 μm layer of single-crystal silicon is attached, via a 1 μm oxide layer, to a 400 μm thick handle wafer, thus forming the starting substrate. The fabrication of the MEMS structure is completed using one or both of the following methods – top-down patterning involving etching of the silicon wafer from the surface to the oxide layer, and bottom-up patterning with etching through the posterior surface of the handle wafer to the oxide layer.

The first MEMS structure consisted of two circumferentially unclamped circular plates, 1 mm in diameter and 10 μm in thickness, directly attached to a suspension beam 3 mm long, 40 μm wide and 10 μm thick. The ends of the suspension beam are fixed to the substrate wafer at both ends. Fig. 5.1(a) displays a Scanning Electron Micrograph (SEM) of the structure. The defining dimensions can be seen clearly in Fig. 5.1(b), constructed in SOLIDWORKS 3-D CAD software.

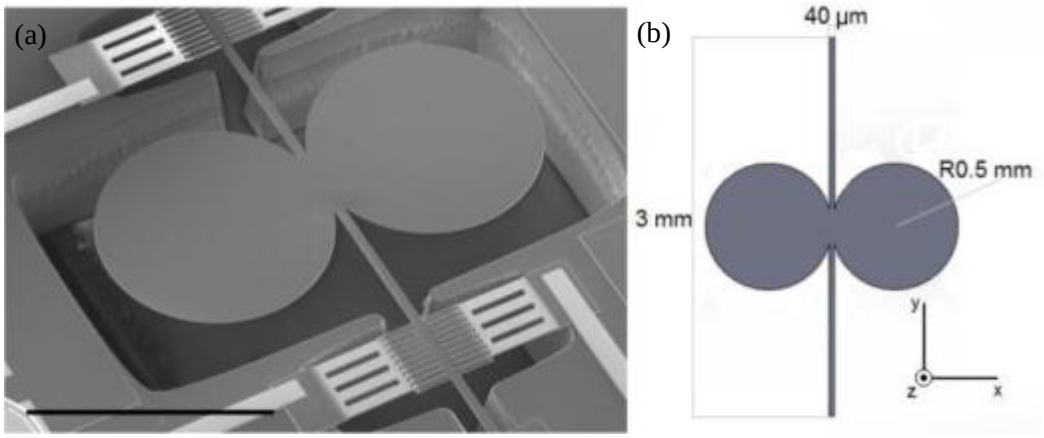

Figure 5.1(a) SEM image of device 1 on the left (Gordon Brown of the Centre for Microsystems and Photonics), scale bar represents 1 mm. (b) Dimensioned 3-D CAD model of device using SOLIDWORKS on the right complete with axes.

The second structure had two coupling bars which attach each disc to the central suspension beam. Each bar is 100 μm wide and 80 μm long. Again the thickness of the whole device is 10 μm. All other dimensions match those of device 1. Fig. 5.2 on the following page shows the SEM image and corresponding 3-D CAD geometry for device 2.

The optical scanning micro-mirrors were designed to oscillate at the mechanical resonance frequencies about two axes of rotation, with the motion initiated by means of the comb-drive actuators, visible in both SEM images. The comb drive fingers curl upwards from the plane of the device due to stress gradients arising from the processing. Owing to the vertical offset of the comb drive fingers, when a potential is applied across opposing sets of fingers in the comb drive there is a vertical component to the electrostatic force developed that can drive motion in either of the two mechanically resonant modes, according to the frequency of the drive signal.

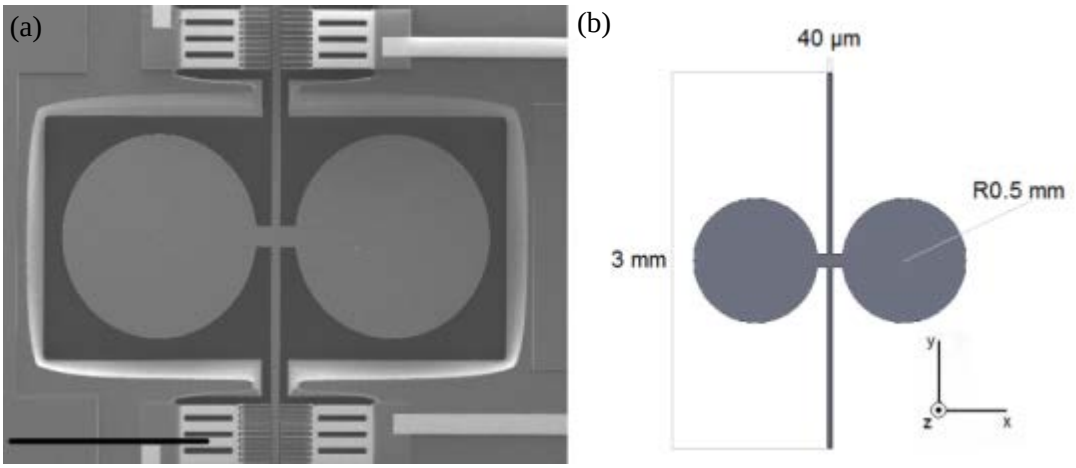

Figure 5.2(a) SEM image of device 2 on the left (Gordon Brown of the Centre for Microsystems and Photonics), scale bar = 1 mm. (b) SOLIDWORKS 3-D CAD model with dimensions and Cartesian axes on right.

To validate methods introduced in the previous Chapters and to assess the MEMS devices' potential as directional acoustic sensors, modal analysis of both structures was implemented and the mechanical directional sensitivity of device 1 further examined, both computationally by finite element analysis and physically using laser Doppler vibrometry.

5.2 Laser Doppler Vibrometry and Finite Element Modelling of the MEMS devices

5.2.1 Device Preparation

Both devices were situated on the same silicon die of 11 mm square cross-section and a thickness of 400 µm, along with two other devices which are not included in this study. Using double-sided adhesive tape, the die is fixed to an FR4 laminate printed circuit board (PCB) of dimensions 70 mm × 28 mm × 2.5 mm. Fig. 5.3 shows DSLR camera images (Canon EOS 550D, Tokyo, Japan) of the anterior and posterior of the die and PCB respectively. On the reverse of the PCB, a hole of approximate diameter 8 mm was drilled, allowing full exposure of the back surfaces of the structures to the laser spot of the micro-scanning vibrometer.

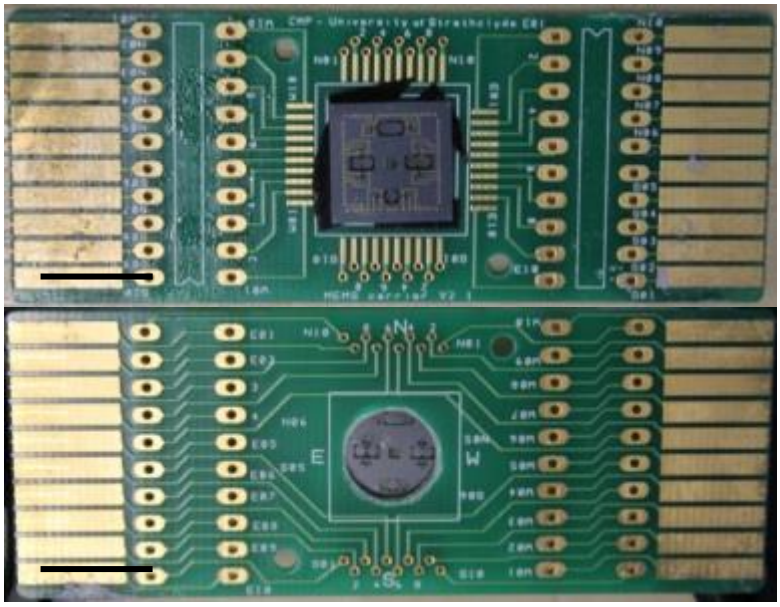

Figure 5.3 Photographs of the PCB, silicon die and devices, 1 left of centre and 2 right of centre on the top image. Scale bar = 1 cm.

5.2.2 Initial Finite Element Modelling of the MEMS Devices

Using finite element analysis, the frequency response of each device was explored computationally. For an initial modal analysis of each MEMS structure, the commercially available FEA software, COMSOL Multiphysics, was used. The first step was to construct 3-D finite element models of each structure and execute eigenfrequency studies. The eigenfrequencies of a device are the set of undamped, unforced, natural frequencies of vibration. A structure's eigenmodes are defined as the vibrational patterns or deflection shapes at each of these frequencies (see *2.2.3.2* for the theory behind eigenmode analysis).

Building the geometry of device 1 was the first requirement and due to the geometrical simplicity of the structure this was done within COMSOL's modelling environment. The device was constructed by first building the 2-D cross-section on the XY- work-plane, consisting of two circles and a rectangle, positioned accordingly, and these were merged using the union command, with the corresponding "keep interior boundaries" command unselected. The extrude work-plane command with an extrusion distance of 10 μm was used to complete the geometry.

The model materials were then specified and allocated to the appropriate domain, in this case, device 1. Initially COMSOL's embedded library of materials was used to provide the necessary material properties. This meant using the database's quoted properties for basic isotropic silicon of 2330 kgm^{-3} for the density, 131 GPa for Young's modulus and a Poisson's ratio of 0.27.

The next step was selecting the model domain settings including specifying any required boundary conditions. In the linear elastic material model subnode, isotropic was selected as material type. Both ends of the suspension beam were given a fixed constraint, issuing these boundaries with a prescribed permanent displacement of 0 in all directions. All other boundaries were left free.

Physics-defined meshing was used with a size setting of "finer" (two levels higher density meshing than the normal setting) due to the fact that the device is relatively thin and therefore contains some small boundary areas. This resulted in a mesh consisting of 71737 tetrahedral elements, corresponding to 430998 degrees of

freedom. All solver settings remained as default and the number of eigenmodes solved for was seven.

Fig. 5.4 shows the first 7 modes of device 1 and their corresponding eigenfrequencies.

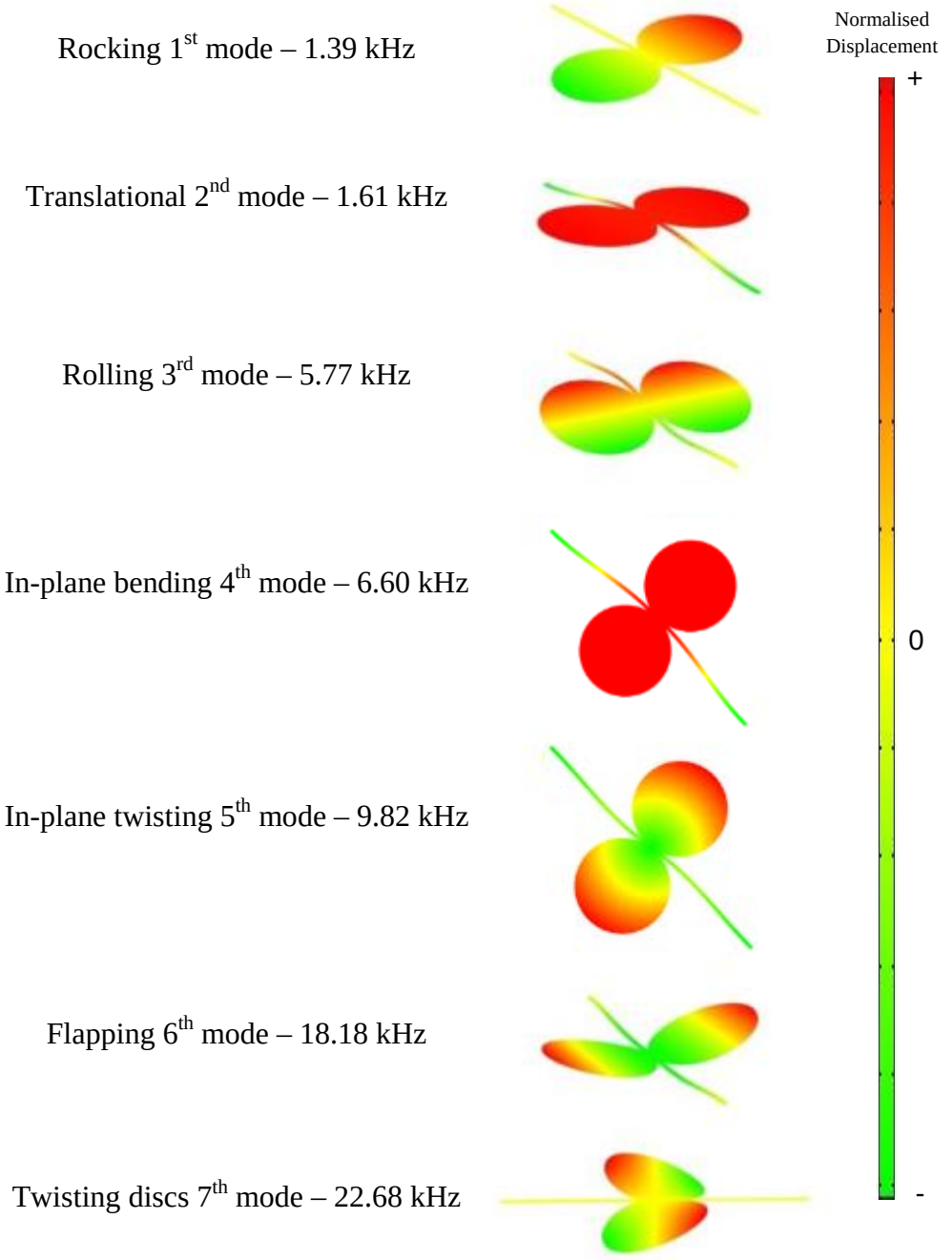

Figure 5.4 First 7 eigenmodes and the eigenfrequencies of device 1.

Device 2 was modelled using the same technique, with the only difference being the addition of 2 rectangles to the 2-D geometry cross-section to construct the coupling bars and then the position of the circular discs adjusted accordingly. The first 7 modes of device 2 and corresponding eigenfrequencies are below.

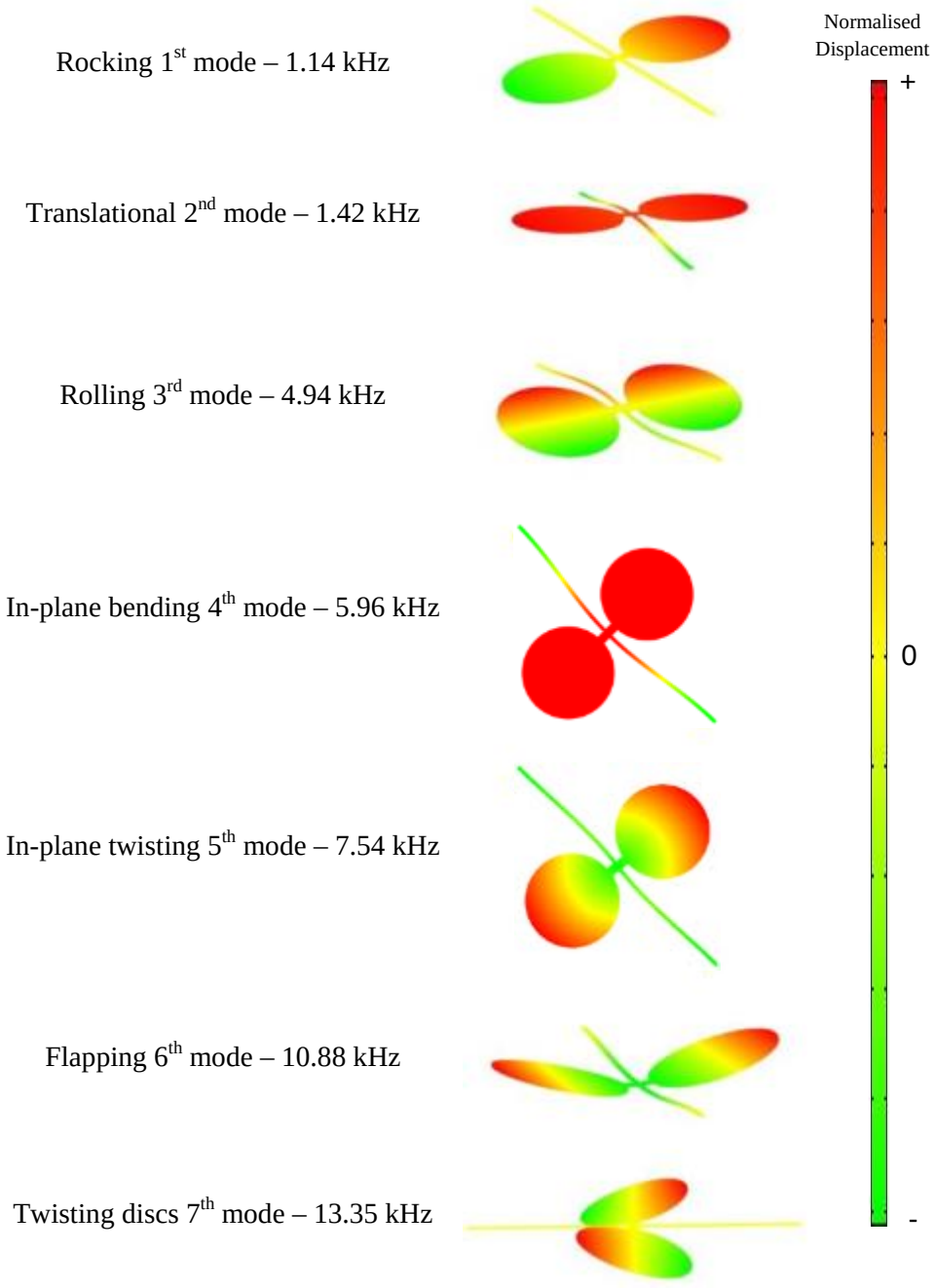

Figure 5.5 First 7 eigenmodes and the eigenfrequencies of device 2.

As in *3.2.1* the deformation is again exaggerated for visualisation purposes by displaying an enlarged displacement in each direction X, Y and Z. Initially the default solver setting was used for the output of eigenvectors i.e. normalisation via scaling against the RMS values. Therefore the colour scale for modes 1-3, 6 and 7 indicates an arbitrary normalised out-of-plane displacement field whereas for modes 4 and 5 only the in-plane displacement field is displayed (as the out-of-plane component is 0 for both of these modes). As mentioned previously, a comparative investigation of the amplitude of deflection at each mode cannot be made using simple eigenmode analysis alone.

Both devices display very similar mode shapes, as expected, due to their comparably alike structures. Consistently the eigenfrequencies of device 2, with the coupling bars, are all lower than those of device 1, with device 2's natural frequencies ranging from around 60 – 90% of the eigenfrequency of the equivalent mode of device 1. This indicates that the addition of coupling bars causes a decrease in stiffness of the structure, as well as an obvious slight increase in mass, as both contribute to a reduction of resonant frequencies. The first mode of both devices is of a rotational nature with the axis of rotation being the central suspension beam. Both discs are in antiphase of each other at this 'rocking' mode. Akin to the aforementioned rocking mode of the *Ormia ochracea* tympanal system (*1.4.2.3*), the mode shape is characterised by the fact that when one disc is at a maximum positive displacement, the opposite disc is at a maximum negative displacement. It is important to remember that the suspension beam also undergoes a torsional motion at this mode. As their second eigenmode, both structures have a translational mode characterised by an out-of-plane (or transverse) deflection of the whole device, with the phase of the displacement constant across the whole surface. The third natural mode of vibration of each device is another rotational mode, this time with the axis of rotation passing through the centre of each disc and crossing the beam perpendicularly, therefore the discs deflect in a rolling fashion. Computational modelling shows the next two eigenmodes, modes 4 and 5, both consist purely of motion in the plane of the device, i.e. when looking at both devices' fourth and fifth mode shapes above there is no displacement component in the plane perpendicular to the page. These two modes are described as an in-plane bending mode and in-plane

twisting mode respectively. For the first five modes of each device, device 2 has an eigenfrequency between approximately 77 – 90% of the eigenfrequency of the corresponding mode of device 1. Modes 2 to 6 of each device have not been reported to be present in the *Ormia* ear or microphone systems inspired by such. Eigenmode number 6 of both structures is a higher frequency translational mode where the discs are moving coherently in a flapping style and this mode is more akin to the translational mode observed in *Ormia*, believed to combine with the so-called rocking mode to contribute to *Ormia's* directional hearing capability. Finally, the 7th mode of the devices is another torsional vibration, with the axis of rotation again through the centre of each disc and perpendicular to the suspension beam only this time each disc is rotating 180° out of phase of the other, resulting in a twisting effect. For device 2, with the small coupling beams attaching the discs to the main suspension beam, these two higher frequency eigenmodes are approximately 60% lower in frequency than for device 1. Naturally the deflection shapes at these modes are heavily reliant upon the coupling between disc and central beam and clearly the addition of the small coupling bar significantly decreases the natural frequencies through reducing the strength of this coupling, effectively giving the discs more flexibility.

5.2.3 Modal Analysis of the MEMS Devices using Laser Doppler Vibrometry

Micro-scanning laser Doppler vibrometry (LDV) was used to observe the vibration of the devices in response to various acoustic stimuli, allowing the implementation of modal analysis. As described previously (**2.1** and **3.1**) LDV provides a non-contact, optical method for measuring the out-of-plane vibration velocities of structures, allowing the investigation of complex vibrational responses.

The Polytec PSV-300-F (Polytec: Waldbronn, Germany) with scanning head (OFV-056) was fitted with a specialised close-up attachment unit with integrated optics adapting the vibrometer for use with smaller sized samples such as the devices investigated here. When focussed onto the surface of a device, the diameter of the laser spot was just 3 – 5 µm and could be positioned with micrometre accuracy.

The PCB, as described in **5.2.1,** was used to mount the devices in a position which provided an unobstructed path for sound to propagate between the loudspeaker and the devices, which were held in place by two metal blocks, one bolted above and one bolted below the PCB, and additionally Blu-tack (Bostik-Findley, Stafford, UK) was placed on the reverse of the PCB to further improve the fixing of the devices. Laser access was facilitated through the drilled hole in the PCB, clearly exposing the entire underside of each device. The structures were orientated with their central suspension beams vertically, perpendicular to the floor, and therefore the devices' vibrating surfaces were perpendicular to the incident laser beam of the LDV.

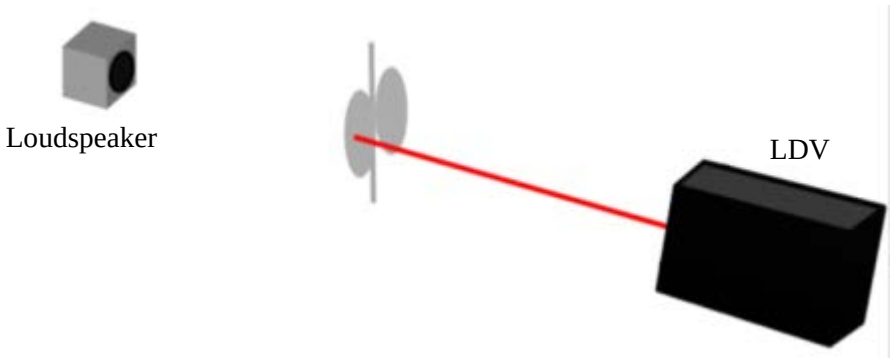

Figure 5.6 Schematic diagram of arrangement of loudspeaker, device and LDV.

Fig. 5.6 above and Figs. 5.1 and 5.2 all show the orientation of the devices more clearly, and 5.1 and 5.2 also show the chosen Cartesian axes used to define

device geometry throughout the thesis. This arrangement of sample and apparatus allowed the scanning of the surfaces of both devices with high spatial accuracy and the measurement of the transverse (out-of-plane) velocity of the device in the positive and negative Z directions.

The environmental conditions in the laser vibrometer room were a temperature of 23°C and relative humidity of 50%. Both the vibrometer itself and the sample devices were mounted on a floor panel isolated from the rest of the room to reduce unwanted structural vibrations.

Initially wideband periodic chirps were generated by an arbitrary waveform generator (Agilent 33220A; Santa Clara, USA), passed through an amplifier (Sony TA-FE570; Tokyo, Japan) and on to a loudspeaker (ESS Heil Air Motion Transformer; South El Monte, USA), located 500 mm from the devices. The low and high frequencies of the chirp were 1 kHz and 25 kHz respectively. Therefore the distance between the sound source and device was sufficiently far to ensure that the devices were in the far field of the source and therefore no significant near-field effects were present. Reference sound pressure was measured via a precision pressure microphone (Brüel & Kjær 4138; Nærum, Denmark), positioned approximately 10 mm from the device die, and connected to a preamplifier (Brüel & Kjær Nexus 2690; Nærum, Denmark). The same amplitude correction technique as mentioned in **3.1** was utilised to condition the sound stimulus. Fast Fourier Transform acquisition mode was also used and therefore the transverse velocity gain (in $ms^{-1}Pa^{-1}$) of the devices was measured in addition to a simultaneous investigation of the phase response, across the frequency spectrum contained within the chirp. Both devices were scanned with 100 – 200 scanning points, each averaged 15 times using the vibrometer software's complex averaging algorithm. Post-processing of this chirp response data allowed the identification of mode shapes and their corresponding frequencies. The next step was further investigation of any of these identified modes by a change in the acoustic stimulus to single frequency pure tones at these specific frequencies and the resulting modal shapes were measured accurately. Integrating the velocity gain at each of these identified modes resulted in values for the displacement gain of the devices when vibrating in a particular mode.

Figs. 5.7 and 5.8 show the devices' first 5 modes detected using LDV, and the corresponding frequency of these deflection shapes.

Rocking mode – 1.40 kHz

Translational mode – 2.20 kHz

Rolling mode – 7.39 kHz

Flapping mode – 20.51 kHz

Twisting discs mode – 23.30 kHz

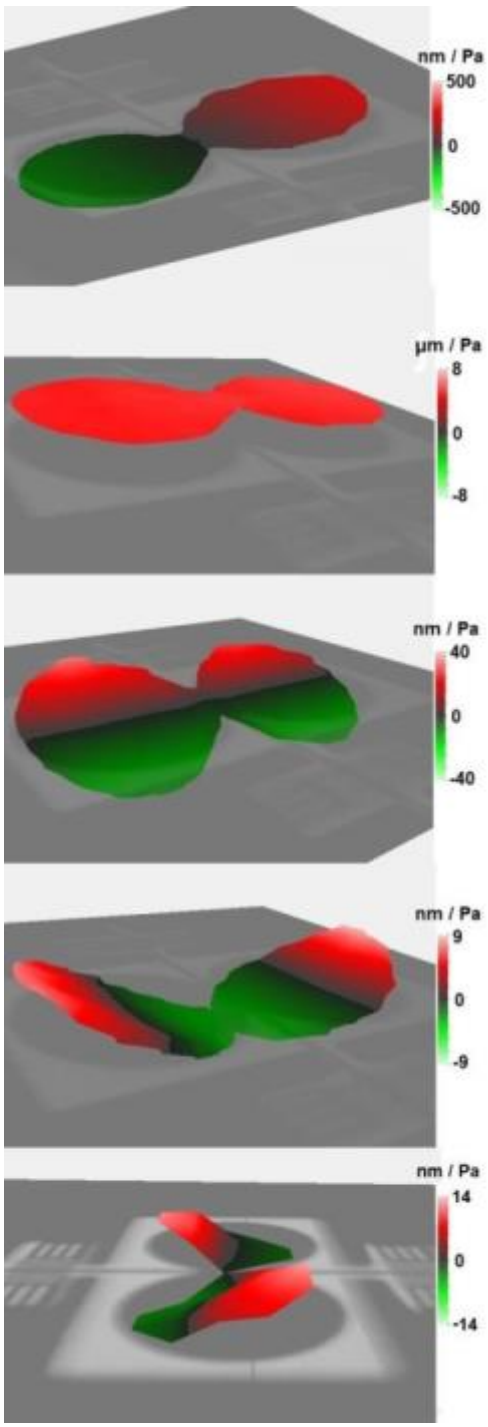

Figure 5.7 First 5 out-of-plane modes of device 1 observed by LDV.

Rocking mode – 1.13 kHz

Translational mode – 2.00 kHz

Rolling mode – 6.03 kHz

Flapping mode – 12.40 kHz

Twisting discs mode – 13.70 kHz

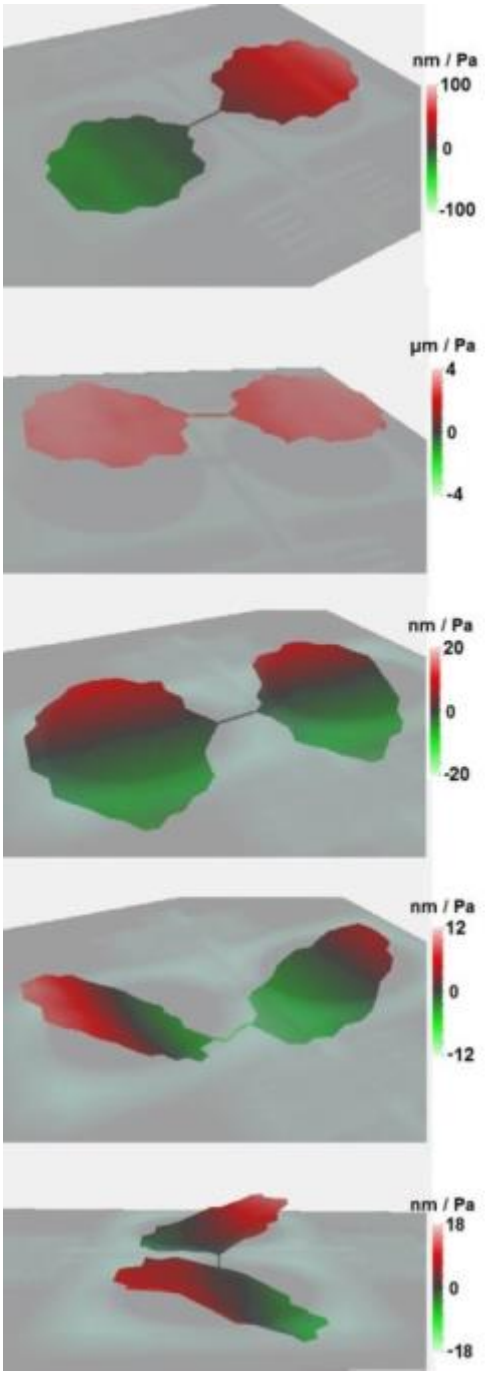

Figure 5.8 First 5 out-of-plane modes of device 2 observed by LDV.

Modal analysis of the vibration of the MEMS devices in response to pressure loads in the form of acoustic stimuli resulted in the same mode shapes being observed through laser vibrometry as those simulated using finite element analysis.

The characteristic rocking, translational, rolling, flapping and twisting modes were all observed. However, modes 4 (in-plane bending) and 5 (in-plane twisting) were not observed using laser vibrometry. This result was expected because the micro-scanning laser vibrometer used is capable of measuring vibrations in one dimension only, i.e. measuring transverse deflections, parallel to the laser beam itself. The incremental position in the frequency domain of each mode observed, relative to previous or subsequent modes, matched perfectly between the models and modal analysis experiments. Tables 5.1 and 5.2 below show the frequency comparison more clearly.

	Device 1 Modal Frequencies / kHz						
	1st	*2nd*	*3rd*	*4th*	*5th*	*6th*	*7th*
LDV	1.40	2.20	7.39	-	-	20.51	23.30
FEA – *Iso Si*	1.39	1.61	5.77	6.60	9.82	18.18	22.68

Table 5.1 Comparison of device 1's modal frequencies measured using LDV and computed using FEA.

	Device 2 Modal Frequencies / kHz						
	1st	*2nd*	*3rd*	*4th*	*5th*	*6th*	*7th*
LDV	1.13	2.00	6.03	-	-	12.40	13.70
FEA – *Iso Si*	1.14	1.42	4.94	5.96	7.54	10.88	13.35

Table 5.2 Comparison of device 2's modal frequencies measured using LDV and computed using FEA.

The rocking mode (1st mode), when observed using LDV, was found to be at 1.40 kHz and 1.13 kHz for devices 1 and 2, respectively. An eigenmode analysis of finite element models of devices 1 and 2 computed these same rocking modes at 1.39 kHz and 1.14 kHz for each structure, a very close match between model and experiment. However, for the majority of the modes (2, 3, 6 and 7) the correlation is not as close between the frequencies of the modes measured with LDV and the modelled eigenfrequencies.

Yet again all of the modes of device 2, when stimulated acoustically and observed using vibrometry, are lower in frequency than the corresponding modes of device 1. Closer inspection of the maximum displacement gain of the devices at each of their modes, indicated by the Figure legends on Figs. 5.7 and 5.8, shows some significant differences between modes. Specifically both devices were extremely

sensitive when stimulated at the frequency of their translational 2nd mode, 2.2 kHz and 2 kHz for devices 1 and 2 respectively. The maximum magnitude of the gain at this mode was 8 μmPa^{-1} for device 1 and 4 μmPa^{-1} for device 2 whereas all of the other modes showed maximum displacement gain amplitudes of anything between about 0.1 and 0.001 of this. It was noted that some modes were sometimes more difficult to excite than others, particularly the rocking and rolling modes (numbers 1 and 3) of both devices. By moving the direction of the loudspeaker from near the normal of the devices' centre to some angle in the X-axis direction (according to the axes on Figs. 5.1 and 5.2) the rocking mode was more readily excited as would be expected. Likewise decreasing or increasing the elevation of the loudspeaker from the norm of the same height as the devices was beneficial in strengthening the excitation of the rolling mode.

Further investigation into the poor correlation between some of the experimentally measured frequencies and computationally predicted eigenfrequencies of the modes of vibration was the next step. It must be noted that the S-C Si material properties used in the model made the assumption of isotropy of stiffness throughout the silicon structure. For S-C Si, used in the microfabrication of MEMS, this is known to be untrue therefore the next step is to allow for anisotropic properties of the material.

5.2.4 Finite Element Modelling of the Devices Incorporating Anisotropy

In the previous finite element modelling experiments, single crystal silicon was assumed to be isotropic and the value used for Young's modulus, *E*, in the material model settings was 131 GPa. The choice of *E* can significantly influence computational results and material property testing has shown a range from 130 to 188 GPa for *E* of silicon (Hopcroft et al., 2010). In reality the crystalline structure of S-C silicon means that the elastic response can differ depending on the orientation of a particular structure. Anisotropic material properties are explained more thoroughly in **1.3**.

Single-crystal silicon naturally forms a 'diamond' cubic structure and the lattice symmetry therein means the stiffness matrix of elastic constants which governs the stress-strain relationship for linear deformation of S-C Si can be simplified from a 4th rank tensor with 81 terms (general case for anisotropic 3-D problems) to a 6×6 matrix, with only 3 independent values.

COMSOL has the following elasticity matrix with 3 values, from literature (Hopcroft et al., 2010), built into the material library under the entry for anisotropic single-crystal silicon.

$$D = \begin{bmatrix} 165.6 & 63.9 & 63.9 & 0 & 0 & 0 \\ 63.9 & 165.6 & 63.9 & 0 & 0 & 0 \\ 63.9 & 63.9 & 165.6 & 0 & 0 & 0 \\ 0 & 0 & 0 & 79.5 & 0 & 0 \\ 0 & 0 & 0 & 0 & 79.5 & 0 \\ 0 & 0 & 0 & 0 & 0 & 79.5 \end{bmatrix} \quad [5.1]$$

Changing the material settings subnode to incorporate the above as the moduli of elasticity resulted in the new eigenfrequencies shown in Tables 5.3 and 5.4.

	Device 1 Modal Frequencies / kHz						
	1st	*2nd*	*3rd*	*4th*	*5th*	*6th*	*7th*
LDV	1.40	2.20	7.39	-	-	20.51	23.30
FEA – *Aniso Si*	1.61*	1.71*	5.81	6.59	9.82	18.51	26.71
*highlights switching of location of rocking and translational modes							

Table 5.3 Comparison of device 1's modal frequencies measured using LDV and computed using an anisotropic material model in FEA.

	Device 2 Modal Frequencies / kHz						
	1st	*2nd*	*3rd*	*4th*	*5th*	*6th*	*7th*
LDV	1.13	2.00	6.03	-	-	12.40	13.70
FEA – *Aniso Si*	1.40	1.42	5.01	5.95	7.55	11.05	15.83

Table 5.4 Comparison of device 2's modal frequencies measured using LDV and computed using an anisotropic material model in FEA.

For all but the 6th mode of both devices, changing from the isotropic material model for silicon to the anisotropic model silicon had a negative (or none in the case of the translational mode) impact on the correlation between computationally calculated eigenmodes and their LDV observed counterparts. Furthermore device 1 showed a complete switching of position between rocking mode and translational mode, something never observed in the vibrometry.

The stiffness matrix constants in [5.1] are determined with respect to specific Cartesian axes X, Y and Z. Conventionally, the matrix transform for [5.1] uses the principal crystallographic axes, i.e. the <100> directions in the case of cubic crystals. Taking a closer look at the structural arrangement of standard (100) silicon wafer used here (and commonly in MEMS devices), the X-Y axes (the <110> directions) should be aligned with the X-Y axes of the elasticity matrix (the <100> directions). Therefore, because of the orientation of the modelling workspace and that of the anisotropic stiffness matrix in COMSOL, there is a mismatch between the X-Y axes of the wafer and those of the elasticity matrix. Incorporating a 45° anti-clockwise rotation of the geometry of the devices within the simulation workspace, with the Z-axis as the axis of rotation and the device centres as rotation points, before applying the material model type, should overcome this mismatch (Hopcroft et al., 2010, Sections VIII & XI).

Tables 5.5 and 5.6 show a comparison of the LDV observed modal frequencies and the frequencies of the eigenmodes extracted from these new models, incorporating both the anisotropic stiffness matrix and rotation, for both device 1 and 2.

	Device 1 Modal Frequencies / kHz						
	1st	*2nd*	*3rd*	*4th*	*5th*	*6th*	*7th*
LDV	1.40	2.20	7.39	-	-	20.51	23.30
FEA – *Aniso Si + rotate*	1.41	1.83	6.53	7.47	11.11	20.45	23.54

Table 5.5 Comparison of device 1's modal frequencies measured using LDV and computed using an anisotropic plus rotation material model in FEA.

	Device 2 Modal Frequencies / kHz						
	1st	*2nd*	*3rd*	*4th*	*5th*	*6th*	*7th*
LDV	1.13	2.00	6.03	-	-	12.40	13.70
FEA – *Aniso Si + rotate*	1.17	1.63	5.56	6.75	8.51	12.27	13.84

Table 5.6 Comparison of device 2's modal frequencies measured using LDV and computed using an anisotropic plus rotation material model in FEA.

Closer inspection of the modal frequencies for both devices, as measured using LDV and predicted through FEA, shows that there is now a much closer correlation for modes 2 (translational), 3 (rolling), 6 (flapping) and 7 (twisting) as well as a remaining very close correlation for the rocking mode 1. These results suggest that these finite element models, which account for the anisotropy of S-C Si in the material model settings, and their accompanying eigenmode analyses, provide a fairly accurate prediction of the frequencies of 5 modes (the remaining 2 modes of each device were unable to be physically measured).

As mentioned in *5.2.2* the default solver setting for the scaling of the output of eigenvectors (and therefore the one used here) is RMS normalisation. Changing this to scaling against the model mass matrix in the advanced solver settings and rerunning the eigenmode analysis solver results in the computation of the modal mass participation factors (MPFs, defined in **1.3**), of which there are 3 translational MPFs for each mode, one for each Cartesian axis direction. The effective modal mass fractions in each axis direction are then calculated as in *3.2.1*. These EMMFs are an estimate of the amount of energy which is in a particular mode of the system. Tables 5.7 and 5.8 below show the calculated EMMFs for each mode of both devices, in the X, Y and Z directions.

	Effective Modal Mass Fractions of Device 1 / %						
	1^{st}	2^{nd}	3^{rd}	4^{th}	5^{th}	6^{th}	7^{th}
X	1.59×10^{-8}	2.41×10^{-8}	1.43×10^{-5}	48.94	2.99×10^{-8}	5.14×10^{-7}	7.51×10^{-7}
Y	1.77×10^{-8}	2.21×10^{-8}	1.36×10^{-5}	48.94	3.52×10^{-8}	6.85×10^{-8}	6.74×10^{-7}
Z	4.28×10^{-8}	97.81	4.99×10^{-9}	4.50×10^{-8}	2.67×10^{-8}	0.11	7.42×10^{-8}

Table 5.7 Effective modal mass fractions for modes 1 – 7 in X, Y and Z directions, of device 1.

	Effective Modal Mass Fractions of Device 2 / %						
	1^{st}	2^{nd}	3^{rd}	4^{th}	5^{th}	6^{th}	7^{th}
X	1.27×10^{-8}	6.59×10^{-12}	1.27×10^{-5}	48.87	4.99×10^{-8}	1.20×10^{-8}	1.63×10^{-8}
Y	2.97×10^{-9}	8.20×10^{-11}	1.14×10^{-5}	48.87	4.56×10^{-8}	1.79×10^{-8}	4.09×10^{-8}
Z	2.89×10^{-8}	97.51	1.30×10^{-11}	7.29×10^{-13}	6.29×10^{-8}	0.26	2.99×10^{-10}

Table 5.8 Effective modal mass fractions for modes 1 – 7 in X, Y and Z directions, of device 2.

Clearly the most dominant mode, when considering displacement in the Z-axis direction, is the translational mode number 2 of each device with EMMFs of nearly 98% for each device. Flapping mode number 6 is the second strongest mode when considering sound incident in the Z-axis direction. The 1st mode (rocking) and the 3rd mode (rolling) are very weak in comparison with Z direction EMMFs for both devices ranging from just 1.30×10^{-11} % to 4.28×10^{-8} %, and their proximity to the values for Z-axis stimulation of the in-plane modes a definite indication of the sheer domination of the translational mode. As expected, the strongest mode of both devices in the X- and Y- axis directions is the in-plane bending mode 4, with nearly 50% EMMF. It is worth noting that, due to the rotation of the geometry through 45° to properly account for the S-C Si crystal structure, the in-plane translational mode 4 is a deflection not directly in the X- or Y- axis directions but at 45° between the two axes, hence the approximate 49% : 49% split between $EMMF_{4\,x}$ and $EMMF_{4\,y}$.

Recalling the LDV measurement technique used to analyse these 2 devices, the vibrometer is capable of measuring only transverse vibrational deflections, i.e. those in the Z-axis direction, with the phase of displacement at each scanning point then used to determine the deflection shape. In combination with the above tables of EMMFs of the modes of each device, there is clear reasoning for the observation that both the rocking and rolling modes (1 and 3) were often difficult to excite and therefore measure. These values also begin to explain the greatly contrasting maximum displacement gain of both devices while vibrating in their translational modes compared to the other modes observed through LDV.

5.2.5 Finite Element Analysis of the Mechanical Directionality of Device 1

For a MEMS device to display mechanical directionality there is usually a requirement for a coupling of two or more modes of vibration of the device. This, combined with the results in the preceding subsection, guided the choice of the operating frequency with which to study the directionality of device 1. The choice of 1.2 kHz was made based on the fact it was in close proximity to the rocking mode of the device (1.4 kHz), but not exactly on the modal frequency as well as being far enough from the very strong translational mode at nearer 2 kHz. This explains the reasoning behind using an operating frequency below the rocking mode as an alternative to one between the two modes, because too close to the translational mode and any influence of the rocking mode would be diluted to the point of being negligible.

Mechanical directionality analysis using finite element modelling required the use of COMSOL's acoustic-structure interaction model with a frequency domain study type. As outlined in *2.2.3.3*, two domains were created within the model and allocated a specific domain type – solid (the device) and fluid (air). Coupling the fields of acoustics and structural mechanics required a sphere of air (of radius 80 mm) to be created around the device and the setting of several boundary conditions.

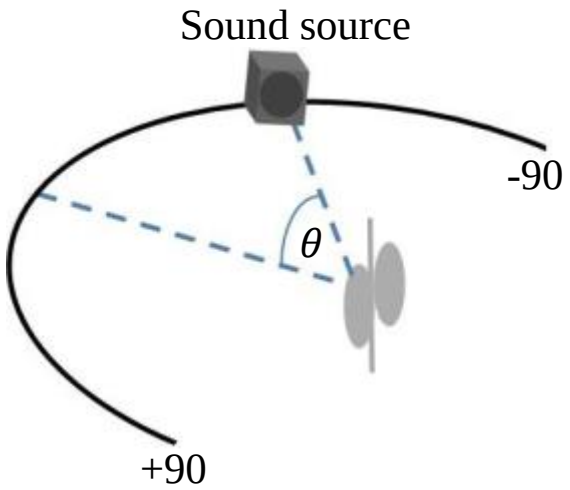

Figure 5.9 Definition of the sound source position angle θ.

Fig. 5.9 shows the position angle, θ, which was defined as the angle between the incident sound and the Z-axis normal to the device, measured through the XZ-plane. The stimulus was a simulated plane wave pressure field of amplitude 0.06 Pa (~70 dB SPL re 20 μPa) of frequency 1.2 kHz, applied to the external boundaries of the air domain. The incident sound wave was simulated using the method outlined in *2.2.3.3* with the azimuthal angle φ and elevation angle ϑ being used to define the angle of incidence via wave vector component calculations.

Formulating the model through the parameterisation of the angles and vector components in this way allowed double parametric sweeps (one nested inside the other) to be implemented, meaning automated and efficient computation of the response of the device at a range of incident sound position angles from -90° (closest to the right disc) through 0° (the device normal) to +90° closest to the left disc, with an angle step size of 5°. The same anisotropic material model as the second part of 5.2.3 was used for the S-C Si (i.e. stiffness matrix entered and geometry rotated through 45°). Because of the geometry rotation the parametric sweeps became $\varphi = \frac{\pi}{4}, \frac{5\pi}{4}$ for the outer and $\vartheta = \frac{\pi}{2}, \ldots, \pi$ with a step of $\frac{\pi}{36}$ for the inner. Additionally, the ends of the suspension beam were again given the fixed constraint boundary condition. The "Include geometric nonlinearity" feature was enabled as a study setting due to the nature of the suspension beam in the structure and the fact a fluid-structure interaction was involved.

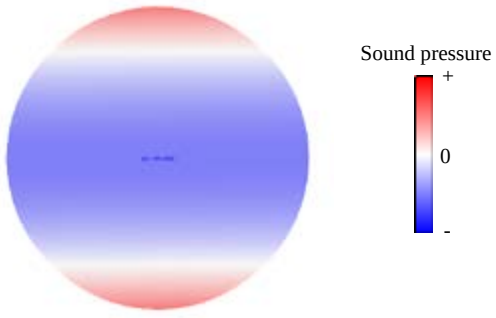

Figure 5.10 Snapshot showing incident sound wave in the air domain.

Fig. 5.10 above is a snapshot of the incident sound wave at $\theta = 0°$ showing the whole air domain and the device in the centre.

Fig. 5.11 shows two views of the dynamic cycle of the response of the device at $\theta = 0°$, with snapshots taken at phases of 0°, 90°, 180°, 270° and 360° of the cycle. Clearly the displacement across the device, specifically of the discs, is a constant at this stimulus angle throughout the cycle, with the whole device moving coherently. Worth noting is that the displacement scale legends at a cycle phase of 180° is the same as at 0° only inverted. The same is observed for cycle phases of 90° and 270°.

Fig. 5.12 displays the same only for an incident sound at $\theta = +45°$, i.e. from the direction of the top left corner of the first image. At this angle the rocking mode can be seen to interact with the translational mode and have some influence on the vibration pattern of the device. However it should be noted that at phases of 0° and 180° in the cycle the difference between the edge of the left disc and right disc is only 20 pm. Additionally the plan view images at these phase points are mirror images of each other and the displacement scales are almost the exact same, i.e. in any one whole cycle the maximum displacement of the edge of the left disc is very close to the maximum displacement of the edge of the right disc.

To investigate the directionality, the device directional intensity gain at each incident sound angle θ was defined as the ratio between the maximum transverse displacement of the edge of the right disc and the displacement of the edge of the left disc.

$$\text{Intensity gain}_{\theta} = \frac{z_r}{z_l} \qquad [5.2]$$

where z_r and z_l are the magnitudes of displacement of the edge of the right and left disc respectively.

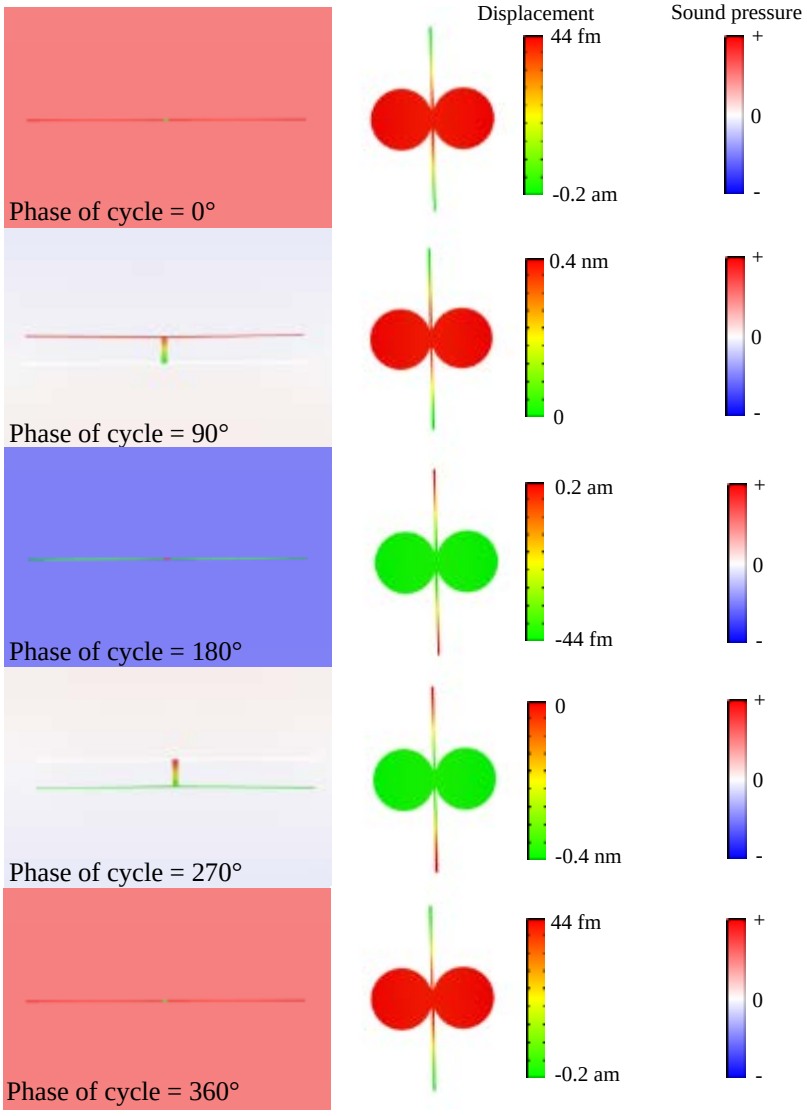

Figure 5.11 Two views of the instantaneous displacement at phases of 0°, 90°, 180°, 270° and 360° for sound incident at 0°.

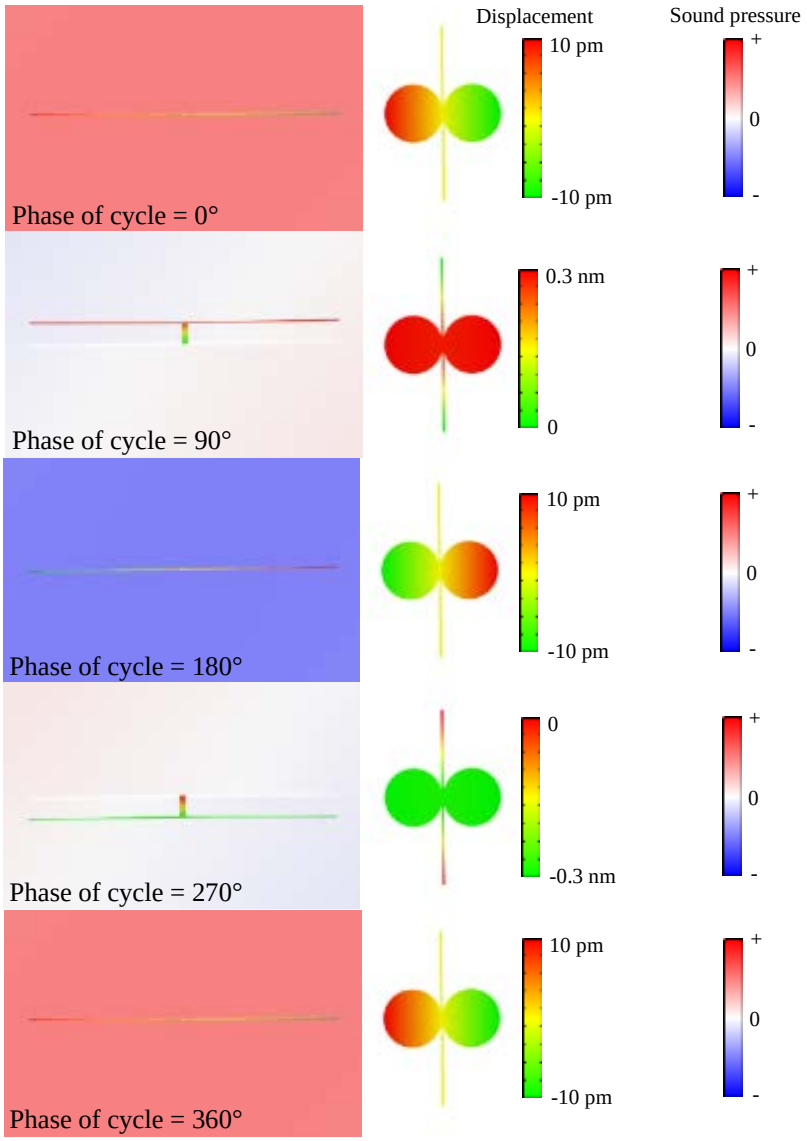

Figure 5.12 Two views of the instantaneous displacement at phases of 0°, 90°, 180°, 270° and 360° for sound incident at 45°.

COMSOL provides many post-processing options and the extraction of displacements and velocities at any user-defined points on the structure was a simple task. The intensity gain at each sound source angle θ from -90° to +90° with an angle step size of 5° was calculated and then plotted on Fig. 5.13. The symmetry of the device resulted in a symmetrical response across the range of angles of incident sound, characterised by the horizontal line through 1 shown for the directional intensity gain. At the two extremes, $\theta = -90°, +90°$ the device moves only very slightly (0.3 pm total displacement in all directions) and the z-displacement component is only 13 – 16 fm with the right hand disc very slightly favouring sound from -90°, i.e. an ipsilateral source, rather than a contralateral source at +90°.

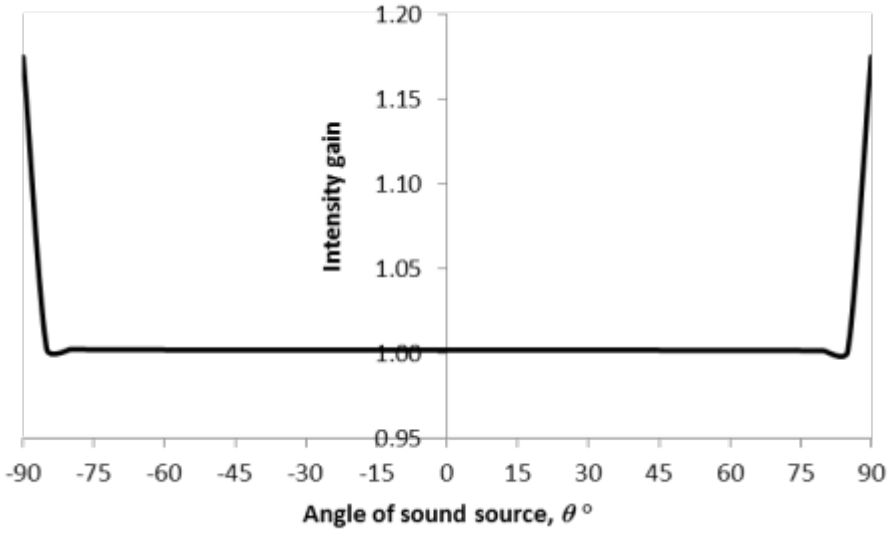

Figure 5.13 Simulated directional intensity gain versus angle of sound source at 1.2 kHz for device 1.

5.2.6 LDV analysis of the Mechanical Directionality of Device 1

All of the same equipment as used in 5.2.3 was utilised for experimentally measuring the mechanical directionality of the device. The device, LDV and loudspeaker were setup as shown in Fig. 5.14 and the sound source position angle θ was defined as previously, and measured using a custom-built goniometer. The distance between loudspeaker and device remained at 500 mm.

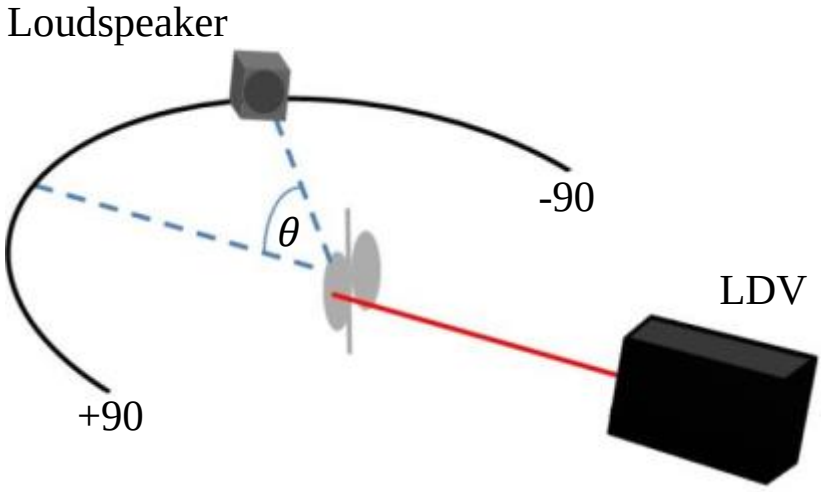

Figure 5.14 Schematic diagram of arrangement of LDV, loudspeaker and device.

A 1.2 kHz pure tone sound stimulus was used and, as in *5.2.3,* both the velocity of the device and the microphone reference signal were recorded. For every position angle, θ, from -90° (nearest right disc) through 0° (normal to the structure) to +90° (nearest left disc) with a step angle of 5°, single point measurements were made of the outer edge of the left disc and the outer edge of the right disc, each averaged 15 times with complex averaging. Computation of the transfer function of the device's velocity (ms^{-1}) to sound pressure (Pa) was implemented using FFTs with a rectangular window. The amplitude gain in $ms^{-1}Pa^{-1}$ is calculated from this and used to calculate the directional intensity gain, which is the ratio between the gain of the right disc and that of the left disc.

Fig. 5.15 shows snapshot scans at phases of 0°, 90°, 180°, 270° and 360° for a sound source position angle of 0°. The same disc on one side of the device clearly shows a greater displacement at both the positive and negative maxima, i.e. an asymmetric response unlike that seen in the finite element model in Fig. 5.12.

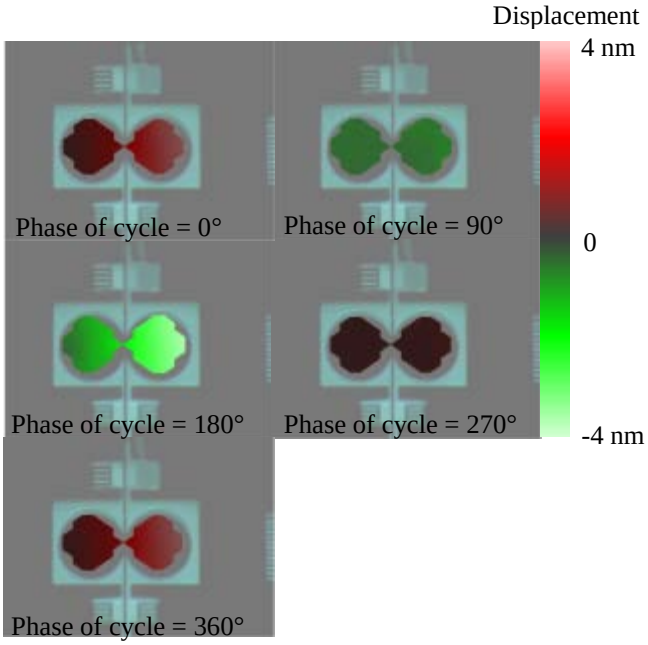

Figure 5.15 Measured instantaneous displacment snapshots at phases of 0°, 90°, 180°, 270° and 360° for sound source angle 0°.

Plotting the LDV measured directional intensity gain against the angle of sound source θ resulted in the grey line on Fig. 5.16. The intensity ratio of the right to the left disc is at a maximum for $\theta = -75°$ where the gain is between 2 and 2.5. For a sound source angle of 0° i.e. at the device's normal, the gain is approximately 0.6. At $\theta = 60°$ the gain converges to a minimum of about 0.1. These results and the snapshots above are in sharp contrast to those seen in Figs. 5.12 and 5.13.

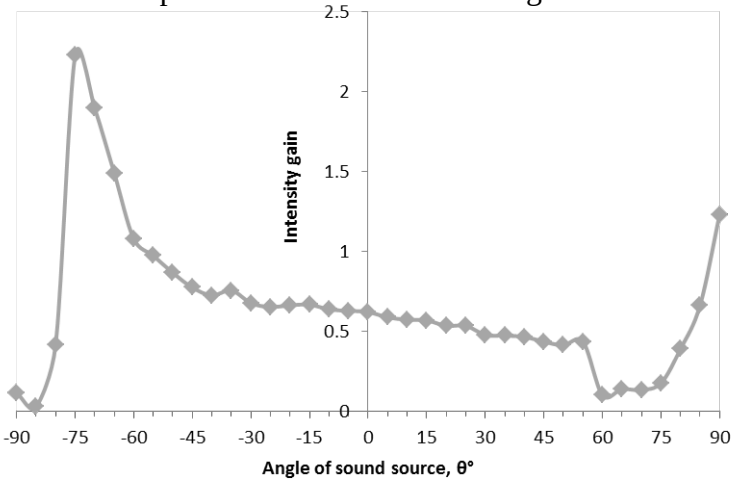

Figure 5.16 Measured directional intensity gain versus angle of sound source at 1.2 kHz for device 1.

5.2.7 FEA of the Mechanical Directionality of Device 1 with Die

The next step was to build the silicon die into the model and position the device as it was in reality, to investigate the effects of the die and device placement on the mechanical directionality response of the device. Fig. 5.17 shows a 3-D view of the new device plus die geometry and also a reverse plan view showing the incorporation of the hole behind the die as seen in Fig. 5.3.

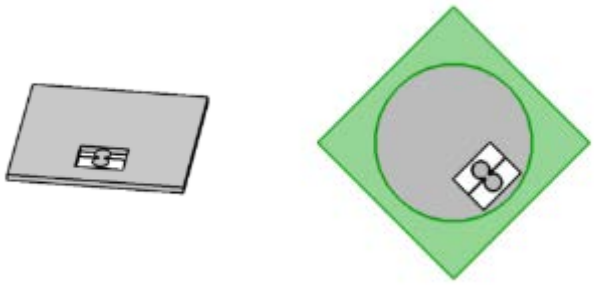

Figure 5.17 New geometry of device 1 and silicon die surround.

The same analysis as ***5.2.4*** was implemented using the exact same parameters with the only difference being the fixed boundary condition applied to the reverse of the silicon die, only outside the circle, i.e. the area shown in green on Fig. 5.17 right.

Fig. 5.18 shows plan views of the dynamic cycle of the response of the device on the die at $\theta = 0°$, with snapshots taken at phases of 0°, 90°, 180°, 270° and 360° of the cycle. There is now a visible difference between left and right disc, at all phases in the cycle with one disc always displaced more than the other, in an asymmetric fashion, throughout the whole cycle.

Snapshots from the same view for $\theta = 45°$ make up Fig. 5.19. The same asymmetry is visible here with one disc consistently having a greater displacement than the other throughout the cycle.

Recalculating the directional intensity gain using the same method outlined in ***5.2.4*** and plotting gain against the sound source angle θ results in the black dotted line on Fig. 5.20. The grey line is the LDV measured mechanical directionality intensity gain as seen in ***5.2.6***.

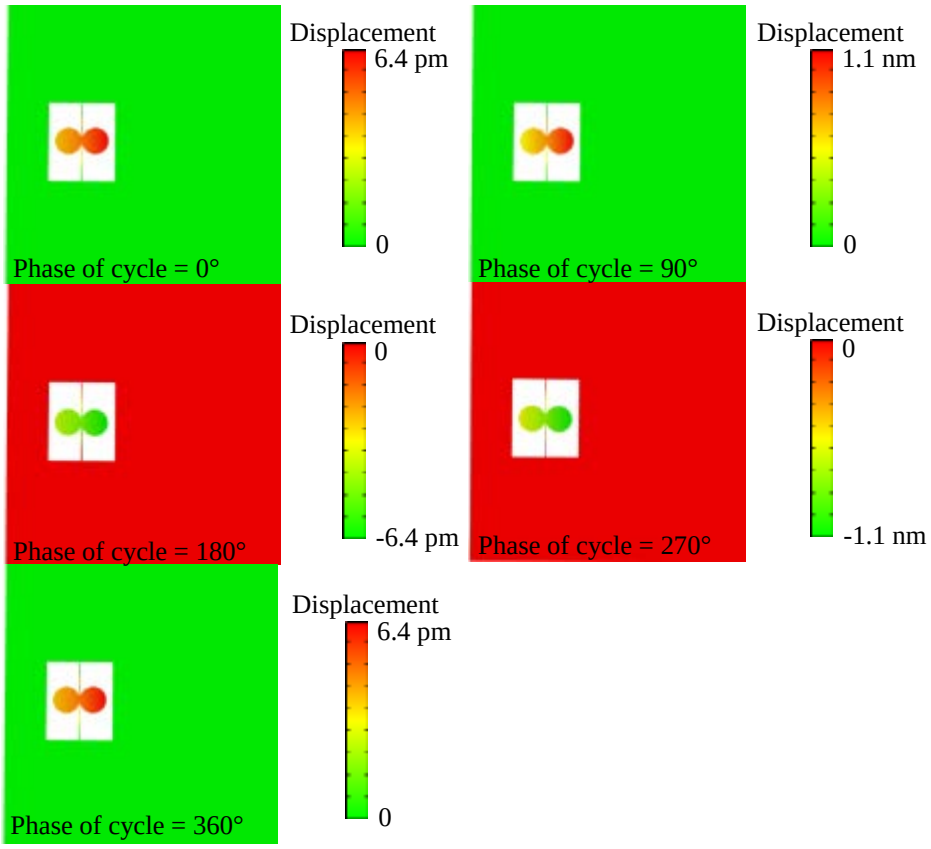

Figure 5.18 Device and die plan views of the instantaneous displacement at phases of 0°, 90°, 180°, 270° and 360° for sound incident at 0°.

The relationship between the directional intensity gain and sound source angle, as computed using FEA, follows the same pattern as that measured using LDV. Both reach a maximum at a large negative source angle, -85° in the case of FEA, where the gain is 4. At $\theta = 0°$ the gain, calculated from the finite element model of device plus die, is 0.5. This means that the left hand disc has a maximum displacement twice as large as the right hand disc at this incident sound angle. The modelled intensity gain converges to a minimum of 0.1 at +80°.

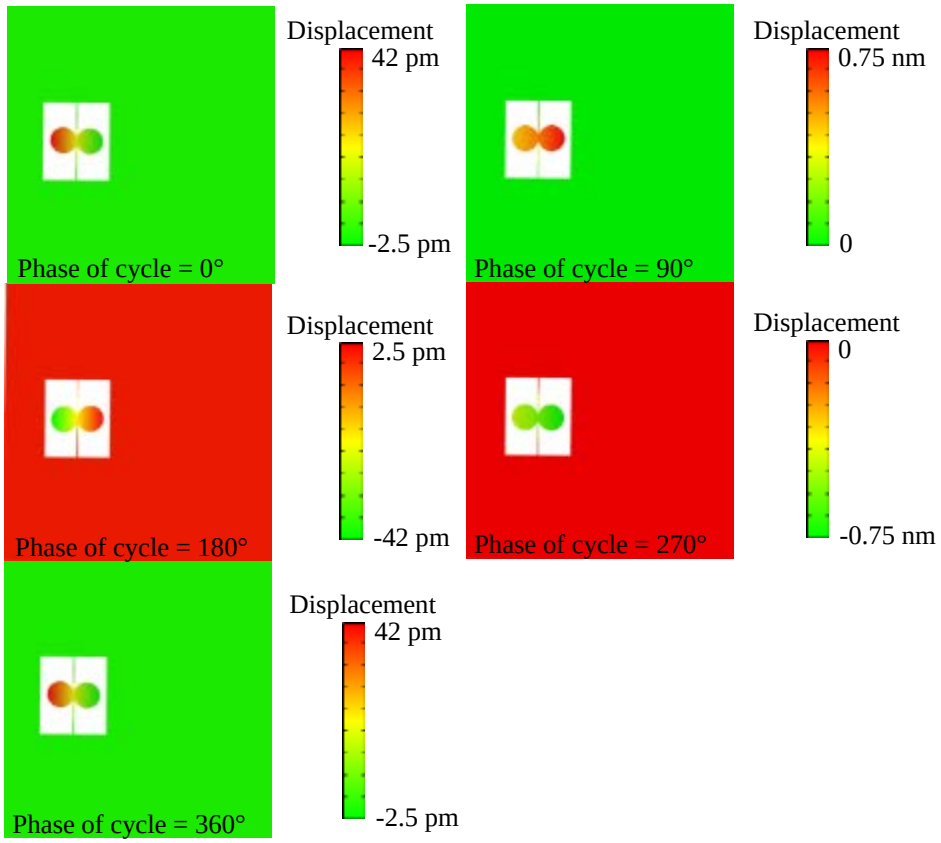

Figure 5.19 Device and die plan views of the instantaneous displacement at phases of 0°, 90°, 180°, 270° and 360° for sound incident at 45°.

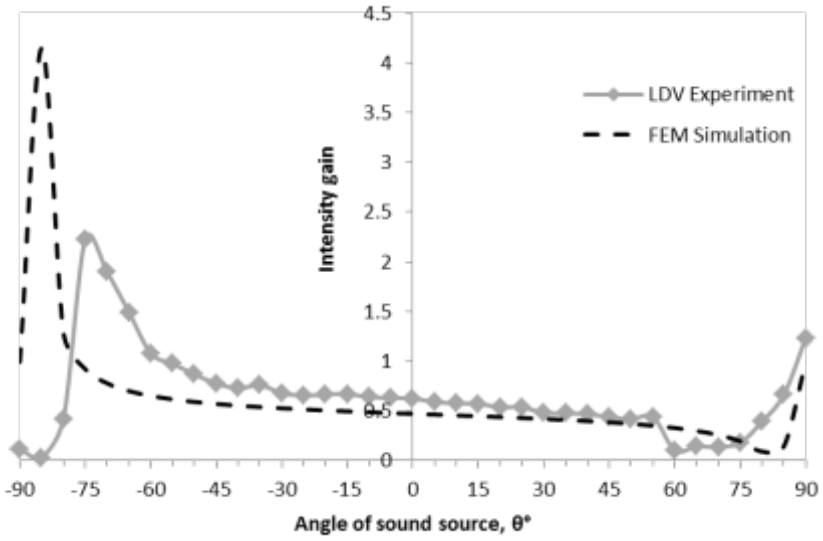

Figure 5.20 Simulated and measured directional intensity gain versus angle of sound source at 1.2 kHz for device 1.

5.3 Discussion

Using commercially available SOIMUMPS, two single-crystal Si MEMS devices were fabricated and investigated both computationally using FEM and experimentally using LDV. The first structure consisted of two equiradial circular discs fixed directly to a suspension beam. Short coupling beams attached the discs to the supporting beam in the second structure.

The same first five out-of-plane mode shapes were observed when using FEM as when using LDV. Reasonable correlation was observed between the estimated and measured resonant frequencies using both an isotropic and an anisotropic material model for silicon (as outlined in Hopcroft 2010). Measuring the correlation between the models and LDV experiments by calculating the average absolute value of the percentage difference between model eigenfrequency and observed frequency of the first five transverse modes showed an improvement from about 13% difference for the isotropic models to just 6% between model and experimental modal frequencies for the anisotropic material model. However, it should be noted that FEM mechanical eigenmode analyses consider only the undamped, unloaded vibrational modes of a solid structure. One main source of damping of devices with the structures seen here is squeeze-film damping (mentioned in ***1.5.2***) however since a hole was drilled through the mounting PCB then no other surface was in close proximity to either side of the devices, negating the influence of this effect.

Attached to the central suspension beams of the devices were comb structures, originally designed for actuation purposes (see Fig. 5.1(a)). Any effect of these small structures and their associated masses on the damping or stiffening of the structures was assumed negligible and therefore excluded from the modelling in this thesis. When using FEM to simulate the devices, any potential oxidation or humidity-related effects, as well as impurities in the S-C Si, were considered insignificant to the overall modelling results and out with the scope of the research. Great care was taken in ensuring that the FEM meshing density was sufficiently fine for both device models as well as the surrounding air domain for the second modelling application.

When the first device was stimulated at a specific working frequency, some interaction occurs between two close modes, called the rocking and translational modes. These combine in differing amounts depending on the angle of the sound stimulus. A predictable and repeatable relationship for the mechanical directionality was the outcome under investigation using LDV. Initially FEA of a model structure failed to display this same relationship due to oversimplification of the model device and the die on which it was mounted. Once the device's position on a surrounding silicon die was incorporated, both FEM simulations and LDV experimentation corroborated this relationship between angle of sound source and directional intensity gain. In reality, four devices were located on one die along with a centrally located comb structure (see Fig. 5.3). Nonetheless these extra features were not observed to significantly affect the accuracy of the modelling results and therefore were not included in the final acoustic-structure interaction model. For laser vibrometry, the die was also attached to a PCB which was then held top and bottom by two small metal blocks. Given the already multi-length-scale, high aspect ratio geometry involved in the finite element model, these additional objects were not incorporated into the final model, nor were they found to substantially affect the devices' modal analysis results or the mechanical directionality study. In the modelling, the attachment between die and PCB was also assumed to be a 100% perfectly fixed boundary.

Although the 1st device in this thesis displayed some form of mechanical directionality the extent of its performance appears limited by the relative sensitivity of the structure at the rocking mode compared to the translational mode. A suboptimal directional performance is achieved since the translational mode dilutes the rocking mode. However, the devices investigated here were not originally optimised as bio-inspired microphones yet they still exhibit strong sensitivity and some directional response. Therefore these findings and the methods used therein can help to guide future research on purposely designed biologically-inspired directional MEMS microphones.

Chapter 6 : Conclusions and Future Work

"*Science should make us the masters and possessors of nature*" – René Descartes

In this section, conclusions are formulated based on the results presented in Chapters 3, 4 and 5 with a view to consolidating the findings. Any anomalies or shortfalls in experimental and computational procedure are addressed along with the identification of potential future work in the field of insect ear inspired acoustic systems.

6.1 Conclusions

Mankind has long taken inspiration from the animal kingdom and today there are many everyday examples of bioinspired technology. Recently much work has been done in the field of bioinspired acoustic systems including the development of both microphones and loudspeakers. The first objective of this PhD thesis was to investigate an invertebrate hearing system, specifically that of the locust, for the purpose of improving the link between this highly evolved, environmentally conditioned, miniaturised, bioacoustic sensor and the design and fabrication of novel sensors and transducers.

After a comprehensive review of published literature on the locust tympanal hearing system, micro-scanning laser Doppler vibrometry was used to measure the mechanical response of the tympanal membrane to stimuli of various frequencies. Travelling waves with unique frequency-dependent form were measured on the membrane, with consistent frequency ranges and transition frequencies of each wave type, believed to be the underlying method with which the locust accomplishes frequency discrimination. These results corroborated previously published findings on the laser vibrometry of the locust tympanum. With the existence of consistent frequencies where the vibration shape changed rapidly from one travelling wave shape to another along with the identification of distinguishable features of each travelling wave pattern, an investigation of the eigenmodes of simulated locust tympana was the subsequent step.

Six eigenmodes of a circumferentially clamped uniform circular disc were computed using finite element modelling, along with the extraction of their corresponding eigenfrequencies and effective modal mass fractions. Analytical methods were used to verify these eigenfrequencies using the theory for the transverse modes of ideal circular plates. In-depth analysis of the FEM mesh performance resulted in very close correlation between the results computed using the finest mesh density and theory. Parametric sweeps were used to analyse the influence of disc radius and thickness as well as the Young's modulus, density and Poisson's ratio of the material, on the shape of the eigenmodes, their eigenfrequencies and the EMMF. All of these computed results matched the

theoretical relationship between the defining characteristics of a plate and its transverse modes.

Acoustic-structure interactions with a frequency response analysis were then employed to explore the possibility of travelling wave formation under the correct conditions, guided by the results of the eigenmode analyses. A mechanism was discovered for the formation of frequency-dependent travelling waves on the circular disc model locust tympana, and hence for the possibility of frequency discrimination in the locust ear. Using this novel method, such formation of travelling waves on model locust tympana are explained in a new fashion. Through a coupled-mode response, the locust ear models showed the formation of complex vibrations and the propagation of frequency-specific travelling waves. There is an apparent strong influence of the asymmetric modes on the response of the locust eardrum as a result of specialised material properties and system characteristics. In this way, analogies can be drawn between the locust tympanum and the tympani drum percussion instrument, studied by Edmund Bowles (1997). The author observed that pre-eighteenth century the drum was struck at or very near the centre which resulted in a dull thud, suitable only for outdoor ceremonial music. However when playing indoors, this method became obsolete as the desire grew for a clear, precise, and ringing tone. In consideration of the locust hearing system, off-centre thin and thick membrane regions with gradual interstitial thickness changes plus an off-centre mass in the form of the MO all contribute to a similar effect as that seen by the tympani drum when struck off-centre (now the most common method of playing) since the asymmetric modes are preferred due to the more musical sound as a result of harmonic interactions among other phenomena. These musical sounds also take significantly longer to diminish than those made using a central strike which excites only circularly symmetric modes. This provides a possible explanation for the observation of Windmill et al. (2008) that, when measured using LDV in the time domain, the locust tympanum vibrational response outlasts the stimulus by up to a factor of ten, owing to frictional forces and the lower damping of asymmetric modes.

Many aspects of the locust tympanal system were investigated computationally for the first time, including a smooth variable cuticle thickness

across the TM, a change of the outline shape of the model tympanum, the PV position, the presence of the MO and the effect of the overhanging cuticular shell.

For non-uniform model tympana, the vibration was found to favour the thinner section of a membrane, at least initially. The maximal displacement peak at some frequencies was found to rise and fall several times as a result of asymmetrical transitions in membrane thickness. In addition lower frequency travelling waves were found to travel further into thicker regions whereas the peaks in higher frequency travelling waves dissipated before reaching the thicker membrane regions.

Assuming an elliptical disc shape as a model locust tympanum did not provide any improvement over circular models. However, the real locust TM is reniform in shape and this feature appears to affect the vibration patterns in a complex spatial way. Firstly, the asymmetrical nature of a kidney-shaped membrane seems to alter the mode shapes by realigning the antinodes, slightly increasing the strength of the analogous modes of more primitively shaped membranes. In doing so the membrane shape facilitates the transfer of energy from incoming sound waves to mechanical vibrations which reach specific areas of the reniform model tympana. Constructing a complex 3-D CAD modelled geometry with smooth contoured thickness distribution also confirmed that the location of the PV coincided with the position of antinodes of multiple mode shapes of this model tympanum. Moreover this indicates that travelling waves, forming in such models, would reach maximal displacements and rapidly dissipate at such a location. Both of these are novel in

Incorporating a simplified Müller's organ as an interior attachment to a model tympanum resulted in the decrease of all eigenfrequencies and the appearance of a fundamental mode in the region of 0.5 kHz where the MO rocked in a motion coupled with the vibration of the membrane which deflected maximally in close proximity to the model MO. Due to the increased surface area and complex deflection shapes of the MO, the interior surface of the model TM plus MO also displayed a more than twofold increase in sensitivity to sound than the exterior surface. An analysis of the cuticular shell that partially covers the TM points towards the shell's purpose being to both protect the TM from any external damage and also pre-condition higher frequency sounds, hence increasing the sensitivity of part of the audible range of the locust.

The final study of the locust system was on the impact of membrane vibration shape on internal sound transmission along with the effect of a simplified locust body on an impinging sound field and specifically, the sound transmitted internally from a contralateral ear to the back of the opposite ipsilateral ear. Internal sound pressure level, relative to the level of the stimulus, displayed a decreasing relationship with increasing frequency across a specific range of frequencies, reaching a trough before increasing slightly again and appearing to level off (Figs. 3.57 and 3.58). Previously published data on sound source directionality experiments in real locusts (Michelsen, 1971c and Miller, 1977) reported this very same relationship shape. A possible explanation is a dependence of the internal sound pressure on the total area of maximal coherent deflection of the membrane as it transmits the sound. With regards to the impact of a locust body on an incident plane pressure wave, at 1 kHz no significant difference was observed between the sound pressure level externally at the contralateral ear and that externally at the ipsilateral ear, due to the locust body dimensions being insufficiently small in comparison with the wavelength of the sound stimulus. Furthermore, at this frequency a huge majority of the sound impinging on the contralateral ear was transmitted efficiently by the ear's vibrations, reaching the internal surface of the opposite eardrum. These results were in stark contrast to the results at 20 kHz where a decrease of more than 9 dB SPL was predicted externally between the contra- and ipsilateral ears respectively. Partial acoustic shadowing as the wavelength of the sound approaches the locust's dimensions is the most likely explanation for this observation. Coupled to this was the fact that this sound pressure level diminished significantly when transmitted internally by the contralateral ear due to a lack of a large amplitude coherent transverse deflection of this membrane.

Key to using finite element modelling to further the understanding of any biological system is to simplify the model within reason, while remaining as true to the system's natural characteristics as possible, including the use of accurate parameters to yield realistic results. Some assumptions were made when creating model locust tympana and studying them via finite element analysis. Firstly a stiff plate material model type was chosen over a tensed membrane model type, primarily because the stiff plate requires three mechanical properties, namely the Young's

modulus, Poisson's ratio and density, all of which can be extracted from published literature for many different arthropod cuticles including the class of Insecta and specifically the locust. As an initial trial this method minimised model unknowns and whenever possible the model results were compared to both real locust data and theoretical predictions. In addition to this assumption, the cuticle was assumed to be a linear elastic, isotropic material i.e. with constant properties in all directions. Although this provided a good initial estimate, the reality is that insect cuticle is known to be a complex, viscoelastic and anisotropic laminar material, taking on many different forms and compositions depending on the primary function of the structures where the cuticle is located. For example, super stiff sclerotised chitinous cuticle has been reported, capable of displaying complex characteristics. Moreover some of the sources of published data on the physical and mechanical properties of insect cuticle may now be dated due to more recent advances in a wide variety of experimental techniques in the field of materials science. Another simplification made throughout this chapter was the fact that the model tympana had no FB or ridge between thin and thick region. In addition to this, the damping effects of internal air-sacs and abdominal tissue were out with the scope of this study and these would be expected to affect all of the simulations, particularly those in ***4.6.1-4.6.2***.

The second objective of this thesis was to apply similar computational modelling and experimental measurement techniques to the suitability of see-saw style MEMS devices as directional microphone diaphragm structures. These dual-circular disc devices were not originally designed as biologically inspired microphones but they had similar dimensions to the ear of the parasitoid fly, *Ormia ochracea*.

Initial FEM eigenmode analyses of the first seven modes of these devices predicted five transverse out-of-plane modes, a first rocking mode where the discs rotate about the central suspension beam, a second translational piston mode, a third rolling mode, a sixth flapping mode and a final twisting disc mode. For both devices the remaining modes, four and five, were described as in-plane bending and twisting respectively. Initially an isotropic material type was used for modelling the MEMS devices' single-crystal silicon.

LDV was then used with the goal of experimentally measuring these same mode shapes and verifying their frequencies. All five of the out-of-plane modes of both devices were observed with laser vibrometry and the measured frequencies were compared with those predicted in the isotropic material models. Good correlation existed between the LDV observed and FEM predicted frequencies of the five out-of-plane modes with calculated Pearson correlation coefficients of 0.997 and 0.995 for devices 1 and 2 respectively.

In an attempt to improve this correlation further, particularly for the 2nd and 3rd modes which showed slightly poorer correlation than the others, the anisotropy of single-crystal silicon was incorporated into the modelling. Rather than the input of a single value for the Young's modulus of silicon, an elasticity matrix was utilised meaning the mechanical properties now vary in different axis directions. Initially the outcome of this switch was actually a deterioration of this correlation with new Pearson coefficients of 0.984 and 0.978 and the device 1 model even predicting a switch of the position of the 1st and 2nd modes. However, with the realisation that there was a misalignment of the principal crystallographic axes of the silicon with the model material axes, a 45° rotation of the 3-D geometry of both devices resulted in the prediction of greatly improved eigenfrequency values and consequently both new Pearson coefficients are 0.999.

Hypothesising that the coupling of two or more of the aforementioned modes would lead to some directional aspect of the vibrational response, FEA was then used to investigate this mechanical directionality of the first device, using acoustic-structure interactions with frequency responses. Nested parametric sweeps of the two angles defining sound source direction were used to rotate the sound position angle, θ, from -90° through the normal to +90° with a step of 5°, at a working frequency of 1.2 kHz and sound pressure field of amplitude 0.06 Pa. Extracting the predicted magnitude of the out-of-plane displacement of the right edge of the right disc and dividing it by the same value of the left, then plotting this intensity gain ratio on the Y-axis against the sound source angle on the X-axis, resulted in an almost a perfect horizontal straight line through 1 i.e. no significant directionality. Repeating this experiment using vibrometry resulted in a very different result, with the intensity gain peaking at a value of 2.25 near -75°, falling to intersect the Y-axis just above

0.5, then slowly dropping as the sound source position rotated anti-clockwise to a low of 0.1 at 60°, all in stark contrast to the computationally predicted relationship.

In an attempt to improve the realistic accuracy of the FEM, the surrounding die, a thin cuboid of square cross-section, was added to the model, greatly increasing the complexity by adding another length-scale into the geometry. Nonetheless the result was rewarding in that the model-predicted relationship between intensity gain and sound source angle changed dramatically, with features very closely matching the LDV measured relationship, in particular the presence of a prominent peak, a decreasing gain with anti-clockwise angle rotation and a Y-axis intercept of 0.5.

Clearly, two important points from this Chapter are that both material model type i.e. isotropic, anisotropic etc., and the complexity of the included geometry in a particular finite element model, have a big impact on the predictions made by the model and their correlation with experimentally measured data.

6.2 Future Work

While it is hoped that the studies in Chapters 3, 4 and 5 may serve as a basis for future research on both insect hearing systems and MEMS microphones, particularly those with a bioinspired influence, care must be taken when interpreting these results. First and foremost, as mentioned in **6.1**, arthropod cuticle is known to be a complex matrix of materials, with a wide range of possible properties and functional capabilities. Clearly there is much still to learn both about the fascinating mechanical properties of insect cuticles and also the methods required in modelling such materials. Rapid improvements have been made in measurement techniques and the modelling of complex materials and new techniques can be applied to the analysis of the tympanal cuticle of many insects to further enhance the understanding of this wonder material and its importance in the field of bioinspired acoustics.

With the goal of establishing a better understanding of the systemic function of each component of the locust tympanal ear, Chapter 4 encapsulated simulations of many features of the ear, all with a view to assisting in the design and testing of novel microphones. At least seven orders of Insecta are known to possess tympanal hearing systems and the nature of this study of the locust ear is such that application of these same modelling techniques to other insects including moths, cicadas and crickets would be fairly seamless. Therefore there exists huge potential for learning from these masters of materials science and acoustics engineering.

Obvious new iterations of the FEM of insect tympana include full frequency response analysis of the complex 3-D reconstructions of morphologically accurate geometries as well as the simulation of transient response models with multi-stimuli i.e. internal and external sound contributions. The cuticular shell of the locust was studied in Chapter 4, with an interesting finding about its dual-purpose nature. However caution should be applied when interpreting these results as the true impact of the shell may deviate slightly from this result as the shell dimensions are currently unstudied, in addition to the angle of the paired tympana and their embedding within the first abdominal segment. In combination with the internal air-sacs and other internal tissue, there is the opportunity for further investigations using new and

improving imaging techniques such as micro computed tomography X-ray scanners and scanning electron microscopes.

New high-precision position systems and sophisticated transducers could be used in conjunction with vibrometry to further study the locust's mechanism of directional hearing, feeding into the model results seen in ***4.6.1*** and ***4.6.2***.

Laser Doppler vibrometry was used extensively throughout this PhD research to measure the highly sensitive response of a real locust eardrum and the equally sensitive response of MEMS structures to similar stimuli. During the laser vibrometry experiments there were some known sources of error. Low frequency background noise was a problem in the vibrometry room, particularly for such highly sensitive S-C Si structures as those in this thesis. This noise source was somewhat negated using the complex averaging algorithm available in Polytec's acquisition software. This source of error as well as any unwanted potential reflections of sound could have been further eliminated through the use of a sound proof booth. The chamber would majorly reduce unwanted echoes through internal sound absorption along with greatly reducing the influence of exterior noise sources, in effect lowering the noise floor and therefore increasing the signal to noise ratio. One limitation of LDV was the fact that measurement can be made only in 1-D i.e. only transverse displacements in the plane of the incident laser beam can be measured. Modern 3-D LDV systems are now becoming widely available, potentially allowing for the accurate measurement of in-plane motion such as the FEM predicted but unobserved mode shapes four and five of the MEMS devices presented here, as well as the investigation of the complex multi-dimensional vibrations of insect tympana.

Chapter 5 was a study of two MEMS devices with a view to assessing their practicality as microscale directional acoustic sensors. One motive was to learn more about microfabricated microphone design features and provide an initial protocol for finite element modelling and experimental testing of such devices. Finding the important influence of the surrounding die on the deflection of these devices can benefit future studies of directional acoustic sensors made using MEMS microfabrication techniques by helping to create a guide of layout rules for MEMS dies. Although the final computational modelling results accurately predicted the modal response of these structures, this accuracy could have been further improved

by some in-depth material testing of the properties of the single-crystal silicon used to fabricate the devices.

All of the findings in this thesis can feed into the design, fabrication and testing of novel bioinspired MEMS microphones capable of displaying supreme directional sensitivity, tuning to specific frequencies and still able to withstand environmental conditions in the very same way as evolution has done for animals.

One big difference between the devices investigated in this PhD research and the ear of the parasitoid fly, *Ormia ochracea*, is the lack of circumferential clamping of the edges of the characteristic discs. Due to this fact, the vibrational response of each device was found to be dominated by the displacement of the characteristic long thin central suspension beams. This has proven to be a suboptimal design for acoustic sensors due to the dilution of the response directionality by a strong and super sensitive translational mode.

Finite element modelling was used to predict the response of simulated locust tympana in a bid to identify the important features leading to the observations made on the locust hearing system. This same technique was used to predict the mechanical response of silicon MEMS structures and assess their practicality as directional acoustic sensors. Both of these subjects are defined by their high aspect ratio geometries which lead to the necessary computation of very large mesh models. Recent major improvements in computational power and the efficiency of FEA software codes allow for the execution of parallelised, high memory utilising multi-length scale, multi-physics finite element models which manage to somewhat explain the phenomena observed in nature. High performance computing brings a completely new level of capabilities to the world of computational modelling but regardless there is always a limit to model size and therefore the achievement of realistic responses and observable phenomena when constructing finite element models of any real systems. As computing technology advances rapidly the ability to simulate more complex systems including large data input of variables, complex materials, more physical phenomena and the solving of both linear and non-linear physics and engineering problems. The result of this can only be an increased understanding of the mechanisms underlying physiological processes in the natural world, leading to even more advancements in the field of bioinspired technological solutions.

References

Aernouts, J., Soons, J. A. M. & Dirckx, J. J. (2010). Quantification of tympanic membrane elasticity parameters from in situ point indentation measurements: validation and preliminary study. *Hearing Research* **263**, 177-182.

Agache, P. G., Monneur, C., Leveque, J. L. & De Rigal, J. (1980). Mechanical Properties and Young's Modulus of Human Skin *in Vivo*. *Archives of Dermatological Research* **269**, 221-232.

Airey, J. (1910). The vibrations of circular plates and their relation to Bessel functions. *Proceedings of the Physical Society* **23**, 225-232.

Arthur, B. J. & Hoy, R. R. (2006). The ability of the parasitoid fly *Ormia ochracea* to distinguish sounds in the vertical plane. *Journal of the Acoustical Society of America* **120(3)**, 1546-1549.

Autrum, H. (1941). Über Gehör- und Erschütterungssinn bei Locustiden. *Zeitschrift für Vergleichende Physiologie* **28,** 580-637.

Bayliss, A., Gunzburger, M. & Turkel, E. (2015). Boundary Conditions for the Numerical Solution of Elliptic Equations in Exterior Regions. *SIAM Journal on Applied Mathematics* **42(2)**, 430-451.

Blanch, G. (1952). Notes on Zeros of $I_{n+1}(x)J_n(x) + J_{n+1}(x)I_n(x)$. *Mathematical Tables and Other Aids to Computation* **6(37)**, 58-59.

Blumstein D. T., Mennill D. J., Clemins P., Girod, L., Yao, K., Patricelli, G., Deppe, J. L., Krakauer, A. H., Clark, C., Cortopassi, K. A., Hanser, S. F., McCowan, B., Ali, A. M. & Kirschel, A. N. G. (2011). Acoustic monitoring in terrestrial environments using microphone arrays: applications, technological considerations and prospectus. *Journal of Applied Ecology* **48(3)**, 758-767.

Bowles, E. A. (1997). The Timpani and Their Performance (Fifteenth to Twentieth Centuries): an Overview. *Performance Practice Review* **10(2)**, 192-211.

Cade, W. (1975). Acoustically orienting parasitoids: Fly phonotaxis to cricket Song. *Science* **190,** 1312-1313.

Carrington, H. (1925). CXXXV. The frequencies of vibration of flat circular plates fixed at the circumference. *Philosophical Magazine Series 6* **50(300)**, 1261-1264.

Chen, C. & Cheng, Y. (2012). Physical Analysis of a Biomimetic Microphone With a Central-Supported (C-S) Circular Diaphragm for Sound Source Localization. *I.E.E.E. Sensors Journal* **12(5)**, 1504-1512.

Coro, F. & Kössl, M. (1998). Distortion-production Otoacoustic emissions from the tympanic organ in two noctuid moths, *Journal of Comparative Physiology A* **183**, 525-531.

Corti, A. (1851). Recherches sur l'organe de Corti de l'ouïe des mammifères. *Zeitschrift für wissenschaftliche Zoologie* **3**, 1-106.

Cui, W., Miles, R. N., Su, Q. & Homentcovsci, D. (2010). A bio-inspired miniature comb sense differential microphone diaphragm. *Proceedings of the American Society of Mechanical Engineers – International Mechanical Engineering Congress and Exposition* **10**, 143-148.

Devetak, D. (1998). Detection of substrate vibration in Neuropteroidea: a review. *Acta Zoologica Fennica* **209**, 87-94.

Edgecomb, R. S., Robert, D., Read, M. P. & Hoy, R. R. (1995). The tympanal hearing organ of a fly: phylogenetic analysis of its morphological origins. *Cell & Tissue Research* **282(2)**, 251-268.

Evans, E. F. (1992). Auditory Processing of Complex Sounds: An Overview. *Philosophical Transactions of the Royal Society B* **336**, 295-306.

Fay, J. P., Puria, S., Decraemer, W. F. & Steele, C. (2005). Three approaches for estimating the elastic modulus of the tympanic membrane. *Journal of Biomechanics* **38**, 1807-1815.

Fay, J. P., Puria, S. & Steele, C. R. (2006). The discordant eardrum. *Proceedings of the National Academy of Sciences* **103(52)**, 19743-19748.

Forrest, T. G., Read, M. P., Farris, H. E. & Hoy, R. R. (1997). A Tympanal Hearing Organ in Scarab Beetles. *Journal of Experimental Biology* **200**, 601-606.

Frings, H. & Frings, M. (1957). Duplex Nature of Reception of Simple Sounds in the Scape Moth, *Ctenucha virginica*. *Science* **126**, 24.

Gennisson, J. L., Baldeweck, T., Tanter, M., Catheline, S., Fink, M., Sandrin, L., Cornillon, C. & Querleux B. (2004). Assessment of elastic parameters of human skin using dynamic elastography. *I.E.E.E. Transactions on Ultrasonics, Ferroelectrics & Frequency Control* **51(8)**, 980-989.

Ghose, K. & Moss & C. F. (2006). Steering by Hearing: A Bat's Acoustic Gaze is Linked to its Flight Motor Output by a Delayed, Adaptive Linear Law. *Journal of Neuroscience* **26(6)**, 1704-1710.

Gibbons, C. & Miles, R. N. (2000). Design of a biomimetic directional microphone diaphragm. *Proceedings of the American Society of Mechanical Engineers – International Mechanical Engineering Congress and Exposition*.

Gnewikow D., Ricketts T. A., Bratt G. W. & Mutchler L. C. (2009). Real-world benefit from directional microphone hearing aids. *Journal of Rehabilitation Research & Development* **46(5)**, 603-618.

Göpfert, M. C. & Robert, D. (2000). Nanometre-range acoustic sensitivity in male and female mosquitoes. *Proceedings of the Royal Society of London B* **267**, 453-457.

Göpfert, M. C. & Robert, D. (2001). Active auditory mechanics in mosquitoes. *Proceedings of the Royal Society of London B* **268** 333-339.

Göpfert, M. C. & Robert, D. (2003). Motion generation by *Drosophila* mechanosensory neurons. *Proceedings of the National Academy of Sciences*, **100(9)**, 5514-5519.

Gordon, S. D., Jackson, J. C., Rogers, S. M. & Windmill, J. F. C. (2014). Listening to the environment: hearing differences from an epigenetic effect in solitarious and gregarious locusts. *Proceedings of the Royal Society of London B* **281**, 1-10.

Gorman, D. G., Reese, J. M., Horáček, J. & Dedouch, K. (2001). Vibration analysis of a circular disc backed by a cylindrical cavity. *Proceedings of the Institution of Mechanical Engineers, Part C* **215(11)**, 1303-1311.

Gray, E. G. (1960). The fine structure of the insect ear. *Philosophical Transactions of the Royal Society B* **243**, 10-94.

Guppy, A. & Coles, R. B. (1988). Acoustical and neural aspects of hearing in the Australian gleaning bat, *Macroderma gigas* and *Nyctophilus gouldi*. *Journal of Comparative Physiology A* **162**, 653-668.

Hensen, V. (1863). Zur Morphologie der Schnecke des Menschen und der Säugethiere. *Zeitschrift für wissenschaftliche Zoologie* **3**, 481-512.

Hopcroft, M. A., Nix, W. D. & Kenny, T. W. (2010). What is the Young's Modulus of Silicon? *Journal of Microelectromechanical Systems* **19(2)**, 229-238.

Horridge, G. A. (1960). Pitch discrimination in Orthoptera (Insecta) demonstrated by responses of central auditory neurones. *Nature* **185**, 623-624.

Jackson, J. C. & Robert, D. (2006). Nonlinear auditory mechanism enhances female sounds for male mosquitoes. *Proceedings of the National Academy of Sciences* **103(45)**, 16734-16739.

Jacobs, K., Otte, B. & Lakes-Harlan, R. (1999). Tympanal Receptor Cells of *Schistocerca gregaria*: Correlation of Soma Positions and Dendrite Attachment Sites, Central projections and Physiologies. *Journal of Experimental Zoology* **283**, 270-285.

Jensen, M. & Weis-Fogh, T. (1962). Biology and Physics of Locust Flight. V. Strength and Elasticity of Locust Cuticle. *Philosophical Transactions of the Royal Society B* **245**, 137-169.

Jerman, J. H. (1990). The Fabrication and Use of Micromachined Corrugated Silicon Diaphragms. *Sensors and Actuators* **A21- A23**, 988-992.

Ketten, D. R. (1994). Functional analyses of whale ears: Adaptations for underwater hearing. *I.E.E.E. Proceedings in Underwater Acoustics* **1**, 264-270.

Klocke, D. & Schmitz, H. (2011). Water as a major modulator of the mechanical properties of insect cuticle. *Acta Biomaterialia* **7**, 2935-2942.

Lane, K. A., Lucas, K. M. & Yack, J. E. (2008). Hearing in a Diurnal, Mute Butterfly, *Morpho peleides* (Papilionoidea, Nymphalidae). *Journal of Comparative Neurology* **508**, 677-686.

Lapadatu, D., Pyka, A., Dziuban, J. & Puers, R. (1996). Corrugated silicon nitride membranes as suspensions in micromachined silicon accelerometers, *Journal of Micromechanics and Microengineering* **6(1)**, 73-76.

Leissa, A. W. (1969). Vibration of plates. *NASA SP-160 Technical Report, Washington.*

Liang, X. & Boppart, S. A. (2010). Biomechanical Properties of *In Vivo* Human Skin From Dynamic Optical Coherence Elastography. *I.E.E.E. Transactions on Biomedical Engineering* **57(4)**, 953-959.

Lisiewski, A. P., Liu, H. J., Yu, M., Currano, L. & Gee, D. (2011). Fly-ear inspired micro-sensor for sound source localization in two dimensions. *Journal of the Acoustical Society of America* **129(5)**, EL166-171.

Liu, B., Zhang, L. and Gao, H. (2006). Poisson ratio can play a crucial role in mechanical properties of biocomposites. *Mechanics of Materials* **38(12),** 1128-1142.

Liu, H. J., Currano, L., Gee, D., Helms, T. & Yu, M. (2013). Understanding and mimicking the dual optimality of the fly ear. *Scientific Reports* **3**.

Liu, H. J., Yu, M. & Zhang, X. M. (2008). Biomimetic optical directional microphone with structurally coupled diaphragms. *Applied Physics Letters* **93(24)**, 243902.

Mahaffy, R. E., Shih, C. K., MacKintosh, F. C. & Käs, J. (2000). Scanning Probe-Based Frequency-Dependent Microrheology of Polymer Gels and Biological Cells. *Physical Review Letters* **85(4),** 880-883.

Malkin, R., McDonagh, T. R., Mhatre, N., Scott, T. S. & Robert, D. (2013). Energy localization and frequency analysis in the locust ear. *Journal of the Royal Society Interface* **11,** 1-8.

Mason, A. C., Oshinsky, M. L. & Hoy, R. R. (2001). Hyperacute directional hearing in a microscale auditory system. *Nature* **410(6829)**, 686-690.

Mehrgardt, S. & Mellert, V. (1977). Transformation characteristics of the external human ear. *Journal of the Acoustical Society of America* **61(6),** 1567-1576.

Meyer, J. & Hedwig, B. (1995). The influence of tracheal pressure changes on the responses of the tympanal membrane and auditory receptors in the locust *Locusta migratoria* L. *Journal of Experimental Biology* **198**, 1327-1339.

Michel, K. & Petersen, M. (1982). Development of the tympanal organ in larvae of the migratory locust (*Locusta migratoria*). *Cell and Tissue Research* **222(3)**, 667-676.

Michelsen, A. (1966). Pitch discrimination in the locust ear: observations on single sense cells. *Journal of Insect Physiolology* **12**, 1119-1131.

Michelsen, A. (1971a). Physiology of locust ear I – Frequency sensitivity of single cells in isolated ear. *Zeitschrift für Vergleichende Physiologie* **71**, 49-62.

Michelsen, A. (1971b). Physiology of locust ear II – Frequency discrimination based upon resonances in tympanum. *Zeitschrift für Vergleichende Physiologie* **71**, 63-101.

Michelsen, A. (1971c). Physiology of locust ear III – Acoustical Properties of the Intact Ear. *Zeitschrift für Vergleichende Physiologie* **71**, 102-128.

Michelsen, A. & Larsen, O. N. (1978). Biophysics of the Ensiferan Ear: I. Tympanal Vibrations in Bushcrickets (Tettigoniidae) Studied with Laser Vibrometry. *Journal of Comparative Physiology* **123**, 193-203.

Middlebrooks, J. C. (1999). Individual differences in external-ear transfer functions reduced by scaling in frequency. *Journal of the Acoustical Society of America* **106(3)**, 1480-1492.

Miles, R. N., & Hoy, R. R. (2006). The development of a biologically-inspired directional microphone for hearing aids. *Audiology & Neuro-otology* **11(2)**, 86-94.

Miles, R. N., Robert, D. & Hoy, R. R. (1995). Mechanically coupled ears for directional hearing in the parasitoid fly *Ormia ochracea*. *Journal of the Acoustical Society of America* **98(6)**, 3059-3070.

Miles, R. N., Su, Q., Cui, W., Shetye, M., Degertekin, F. L., Bicen, B., Garcia, C., Jones, S. & Hall, N. (2009). A low-noise differential microphone inspired by the ears of the parasitoid fly *Ormia ochracea*. *Journal of the Acoustical Society of America* **125(4)**, 2013-2026.

Miller, L. A. (1977). Directional Hearing in the Locust Schistocerca gregaria Forskål (Acrididae, Orthoptera). *Journal of Comparative Physiology A* **119**, 85-98.

Miller, L. A. & Surlykke A. (2001). How some Insects Detect and Avoid Being Eaten by Bats: Tactics and Countertactics of Prey and Predator. *BioScience* **51(7)**, 570-581.

Moir, H. M., Jackson, J. C., & Windmill, J. F. C. (2011). No evidence for DPOAEs in the mechanical motion of the locust tympanum. *Journal of Experimental Biology* **214**, 3165-3172.

Musicant, A. D., Chan, J. C. K. & Hind, J. E. (1989). Direction-dependent spectral properties of cat external ear: New data and cross-species comparisons. *Journal of the Acoustical Society of America* **87(2)**, 757-781.

Neville, A. C., Parry, D. A. & Woodhead-Galloway, J. (1976). The chitin crystallite in arthropod cuticle. *Journal of Cell Science* **21(1)**, 73-82.

Obrist, M. K., Fenton, M. B., Eger, J. L. & Schlegel, P. A. (1993). What ears do for bats: A comparative study of pinna sound pressure transformation in chiroptera. *Journal of Experimental Biology* **180**, 119-152.

Ono, N., Saito, A. & Ando, S. (2003). Design and experiments of bio-mimicry sound source localisation sensor with gimbal-supported circular diaphragm. *12th International Conference on Solid-State Sensors, Actuators and Microsystems* 935-938.

Ott, S. R. & Rogers, S. M. (2010). Gregarious desert locusts have substantially larger brains with altered proportions compared with the solitarious phase. *Proceedings of the Royal Society of London B* **277**, 3087-3096.

Popov, A. V. (1965). Electrophysiological studies on peripheral auditory neurons in the locust (In Russian, with an English summary). *Journal Evolutionary Biochemistry Physiology* **1**, 239-250.

Pumphrey, R. J. (1940). Hearing in Insects. *Biological Reviews* **15**, 107.

Pumphrey, R. J. & Rawdon-Smith, A. F. (1936). Hearing in Insects: The Nature of the Response of Certain Receptors to Auditory Stimuli. *Proceedings of the Royal Society of London B* **121**, 18-27.

Ramsauer N. & Robert, D. (2000). Free-flight phonotaxis in a parasitoid fly: behavioural thresholds, relative attraction and susceptibility to noise. *Naturwissenschaften* **87(7)**, 315-319.

Reissner, E. (1854). Zur Kentniss der Schnecke im Gehörorgan der Säugethiere und des Menschen. *Archiv für Anatomie, Physiologie und Wissenschaftliche Medicin* 420-427.

Ricketts, T. A. (2000). Impact of noise source configuration on directional hearing aid benefit and performance. *Ear & Hearing* **21(3)**, 194-205.

Robert, D. (1989). The Auditory Behaviour of Flying Locusts. *Journal of Experimental Biology* **147**, 279-301.

Robert, D., Miles, R. N. & Hoy, R. R. (1998). Tympanal mechanics in the parasitoid fly *Ormia ochracea*: intertympanal coupling during mechanical vibration. *Journal of Comparative Physiology A* **183(4)**, 443-452.

Robert, D., Read, M. P. & Hoy, R. R. (1996). The tympanal hearing organ of the parasitoid fly *Ormia ochracea* (Diptera, Tachinidae, Ormiini). *Cell & Tissue Research* **275**, 63-78.

Robles, L. & Ruggero, M. A. (2001). Mechanics of the Mammalian Cochlea. *Physiological Reviews* **81(3)**, 1305-1352.

Röder, K. D. (1966). Interneurons of the thoracic nerve cord activated by tympanic nerve fibres in noctuid moths. *Journal of Insect Physiology* **12**, 1227-1244.

Rosen, M. J., Levin, E. C. & Hoy, R. R. (2009). The cost of assuming the life history of a host: acoustic startle in the parasitoid fly *Ormia ochracea*. *Journal of Experimental Biology* **212(24)**, 4056-4064.

Scheeper, P., Olthuis, W. & Bergveld, P. (1994). The Design, Fabrication, and Testing of Corrugated Silicon Nitride Diaphragms. *Journal of Microelectromechanical Systems* **3(1)**, 36-42

Schwabe, J. (1906). Beiträge zur Morphologie und Histologie der tympanalen Sinnesapparate der Orthopteren. *Zoologica* **20**, 1-154.

Skals, N. & Surlykke, A. (2000). Hearing and evasive behaviour in the greater wax moth, *Galleria mellonella* (Pyralidae). *Physiological Entomology* **25**, 354-362.

Spiering, V. L., Bouwstra, S. & Fluitman, J. H. J. (1993). Realization of mechanical decoupling zones for package-stress reduction. *Sensors and Actuators A* **37-38**, 800-804.

Stephen, R. O. & Bennet-Clark, H. C. (1982). The anatomical and mechanical basis of stimulation and frequency-analysis in the locust ear. *Journal of Experimental Biology* **99**, 279-314.

Sueur, J., Windmill, J. F. C. & Robert, D. (2010). Sound emission and reception tuning in three cicada species sharing the same habitat. *Journal of the Acoustical Society of America* **127(3)**, 1681-1688.

Touse, M., Sinibaldi, J., Simsek, K., Catterlin, J., Harrison, S. & Karunasiri, G. (2010). Fabrication of a microelectromechanical directional sound sensor with electronic readout using comb fingers. *Applied Physics Letters* **96(17)**, 173701.

Ulanovsky, N. & Moss, C. F. (2008). What the bat's voice tells the bat's brain. *Proceedings of the National Academy of Sciences* **105(25)**, 8491-8498.

Vincent, J. F. V. & Wegst, U. G. K. (2004). Design and mechanical properties of insect cuticle. *Arthropod Structure & Development* **33**, 187-199.

Volandri, G., Di Puccio, F., Forte, P. & Carmignani, C. (2011). Biomechanics of the tympanic membrane. *Journal of Biomechanics* **44**, 1219-1236.

Wang W. J., Lin R. M., Zou Q. B., Li X. X. (2004). Modeling and characterization of a silicon condenser microphone. *Journal of Micromechanics & Microengineering* **14**, 403-409.

Wiener, F. M. & Ross, D. A. (1946). The pressure distribution in the auditory canal in a progressive sound field. *Journal of Acoustical Society of America* **18**, 401-408.

Windmill, J. F. C., Bockenhauer, S. & Robert, D. (2008). Time-resolved tympanal mechanics of the locust. *Journal of the Royal Society Interface* **5(29)**, 1435-43.

Windmill, J. F. C., Fullard, J. H. & Robert, D. (2007). Tympanal vibrations in noctuid moths. *Journal of Experimental Biology* **210**, 2637-2648.

Windmill, J. F. C., Göpfert, M. C. & Robert, D. (2005). Tympanal travelling waves in migratory locusts. *Journal of Experimental Biology* **208**, 157-168.

Windmill, J. F. C., Jackson, J. C., Tuck, E. J. & Robert, D. (2006). Keeping up with Bats: Dynamic Auditory Tuning in a Moth. *Current Biology* **16**, 2418-2423.

Yack, J. E. (2004). The Structure and Function of Auditory Chordotonal Organs in Insects. *Microscopy Research and Technique* **63**, 315-337.

Yack, J. E. & Fullard, J. H. (1993). What Is an Insect Ear? *Annals of the Entomological Society of America* **86(6)**, 677-682.

Yager, D. D. (1999). Structure, Development, and Evolution of Insect Auditory Systems. *Microscopy Research and Technique* **47**, 380-400.

Yoo, K., Gibbons, C., Su, Q. T., Miles, R. N. & Tien, N. C. (2002). Fabrication of biomimetic 3-D structured diaphragms. *Sensors and Actuators A: Physical* **97-98**, 448-456.

Yoo, K., Yeh, J. L. A., Tien N. C., Gibbons, C., Su Q., Cui, W. & Miles, R. N. (2001). Fabrication of a biomimetic corrugated polysilicon diaphragm with attached single crystal silicon proof masses. *11th International Conference on Solid-State Sensors and Actuators*, 130-133.

Bibliography

Akin, J. E. (2005). Finite Element Analysis with Error Estimators: An Introduction to the FEM and Adaptive Error Analysis for Engineering Students. *Elsevier*.

Blum, M. S. (1985). Fundamentals of Insect Physiology. *Wiley*.

Callister, W. D. (2007). Materials Science and Engineering: an Introduction. *Wiley*.

Chapman, R. F. (1998). Insects: Structure and Function. *Cambridge University Press*. p. 705.

Deiters, O. (1860). Untersuchungen über die Lamina spiralis membranacea. *Bonn, Henry & Cohen*.

Dusenberry, D. B. (1992). Sensory Ecology: How Organisms Acquire and Respond to Information. *W.H. Freeman & Company*. p. 19.

Grimaldi D. A. & Engel M. S. (2005). Evolution of the Insects. *Cambridge University Press*. Ch. 1.

Rockey, K. C. (1983). The Finite Element Method: A Basic Introduction. *London Granada*.

Rosen, S. & Howell, P. (1991). Signals and Systems for Speech and Hearing. *Academic Press*.

Rossing, T. D. (2007). Springer Handbook of Acoustics. *Springer*.

Sales, G. P. & Pye, D. (1975). Ultrasonic Communication by Animals. *Chapman and Hall*. 71-97.

Uvarov, B. (1966). Grasshoppers and Locusts: A Handbook of General Acridology, Vol. 1. *Cambridge University Press*.

Uvarov, B. (1977). Grasshoppers and Locusts: A Handbook of General Acridology, Vol. 2. *Cambridge University Press*.

Vater, M. & Kössl, M. (2004). Echolocation in Bats and Dolphins. *The University of Chicago Press.* 91.

Von Békésy, G. (1960). Experiments in Hearing. *McGraw-Hill, New York*.

Wainwright, S. A. (1976). Mechanical Design in Organisms. *Edward Arnold*.

Appendix 1 – Published Work

Conference Publications

The work in Chapters 3 and 4 of this thesis has been presented at the following conferences:

- Invertebrate Sound and Vibration
  2013, University of Strathclyde, UK – oral presentation.
- International Congress of Neuroethology
  2012, Maryland, USA – poster presentation.
- Invertebrate Sound and Vibration
  2011, Missouri, USA – poster presentation.
- Institute of Physics – Physics meets Biology
  2010, University of Oxford, UK – poster presentation.

Journal Publications

The work in Chapters 3 and 4 of this thesis is in preparation for journal publication.

The work in Chapter 5 of this thesis has been published in the following journal:
Mackie, D. J. et al., 2014. Directional acoustic response of a silicon disc-based microelectromechanical systems structure, *Micro & Nano Letters*, **9(4)**, 276-279.

Other Publications during PhD

Sueur, J., Mackie, D. & Windmill J. F. C., 2011. So Small, So Loud: Extremely High Sound Pressure Level from a Pygmy Aquatic Insect (Corixidae, Micronectinae), *PLoS ONE*, **6(6)**, e21089. Paper contributions: data analysis and reagents/materials/analysis tools.

Directional acoustic response of a silicon disc-based microelectromechanical systems structure

David James Mackie[1], Joseph Curt Jackson[1], James Gordon Brown[2], Deepak Uttamchandani[2], James Frederick Charles Windmill[1]

[1]*Department of Electronic and Electrical Engineering, Centre for Ultrasonic Engineering, University of Strathclyde, Glasgow G1 1XW, United Kingdom*
[2]*Department of Electronic and Electrical Engineering, Centre for Microsystems and Photonics, University of Strathclyde, Glasgow G1 1XW, United Kingdom*
E-mail: david.mackie@strath.ac.uk

Published in Micro & Nano Letters; Received on 14th November 2013; Revised on 12th March 2014; Accepted on 21st March 2014

A microelectromechanical systems (MEMS)-based structure capable of operating mechanically as a directional acoustical sensor is presented. The structure, fabricated through the commercially available SOIMUMPS foundry process, consists of two circular discs attached to a central suspension beam, fixed at both ends. The design of the structure resembles other directional MEMS microphones that mimic the directional hearing organ of the parasitoid fly, *Ormia ochracea*. Modal analysis and mechanical acoustic directionality analysis using both laser Doppler vibrometry and finite element modelling have been implemented. It is demonstrated that this coupled MEMS structure exhibits an acoustic directional response, with a one-to-one relationship between the relative vibration amplitudes of the two coupled discs and the angle of sound, from −75° to +60°.

1. Introduction: Microelectromechanical systems (MEMS) microphones are becoming increasingly common in portable devices such as hearing aids, smartphones and tablet computers, among other applications [1, 2]. Several advantages lie in using a MEMS device, notably size and the integration of electronic functionality such as filtering and amplification. In addition, the robust mechanical properties of silicon make it ideal for the demanding conditions experienced in the above applications [3]. Although MEMS technology has been applied in commercial microphones, achieving directionality within such devices is currently a subject of the research domain. The inclusion of directionality in a microphone system can provide an approach to reducing noise and thus promoting signal intelligibility, for example, in speech, or the ability to accurately locate sound sources, such as in environmental monitoring [4–6]. However, there are physical constraints to designing a directional microphone.

Traditional directionality (extending to localisation in three dimensions) in conventional microphone systems usually involves an array of two or more pressure receivers, whose separation is greater than the wavelength of the incident sound. Such systems use an estimate of the time difference of arrival (TDOA), or a relative phase difference, and sometimes the difference in sound intensity at each receiver as inputs to algorithms which compute the location of the sound source. When miniaturising such directional microphone systems, a problem arises as the separation between receivers becomes smaller than the wavelength of incident sound, such that the TDOA and pressure difference measurements become less accurate, leading to greater errors in source localisation. For example, the typical acoustic wavelength for audio applications is of the order of centimetres, therefore imposing a size constraint on the miniaturisation of traditional directional receiver arrays.

Inspiration for silicon MEMS-based directional microphones has often been taken from the unique directional hearing system observed in the parasitoid fly, *Ormia ochracea* [1, 7–12]. The *Ormia* deposits its eggs on and around a singing male cricket, which is then used as a food source by the larvae. The fly locates the cricket by localising the cricket's acoustic signal (song) with accuracy better than 2°. The pressure receivers, specifically the tympanal membranes, within the *Ormia* ear are separated by just 0.5 mm, yet the cricket host's calling song has a wavelength of the order of centimetres. A mechanical coupling arrangement between the pair of tympanal membranes, namely the intertympanal bridge, causes the combination of two major modes of vibration which, favourably for the fly, results in a significant amplification of the perceived pressure intensity difference. The two modes are usually described as a 'rocking' mode, where the two membranes deflect 180° out of phase, and a 'translational' in-phase mode [12, 13].

Several previous studies have applied MEMS technology to mimic the dynamics of the ear of *Ormia* [1, 7–12]. While various degrees of success have been reported, directional acoustic sensitivity should, in principle, be present in any micromechanical device with sufficient degrees of freedom of movement. In this Letter, we present findings on the directional response of a simple, single-crystal silicon MEMS structure that is similar in size and geometry to the fly ear, and the several bio-inspired directional MEMS microphones which have been previously reported. The modal analysis of the structure and its performance, mechanically, as a directional acoustic sensor are investigated both experimentally and computationally. The structure exhibits acoustic directionality, demonstrating the potential for such micromechanical devices to be utilised as directional microphones.

2. Methods: The MEMS structure consists of two circumferentially unclamped circular plates, each 1000 µm in diameter and 10 µm in thickness, which are directly attached to a suspension beam 3000 µm long, 40 µm wide and 10 µm thick, anchored at both ends. Fig. 1*a* shows a scanning electron micrograph (SEM) of the structure. The defining dimensions are shown clearly in Fig. 1*b*, created using SolidWorks three-dimensional (3D) CAD software (Dassault Systèmes SolidWorks Corp., Waltham, MA, USA). This structure was fabricated using a commercial multi-user silicon-on-insulator process (SOIMUMPs) offered by MEMSCAP Inc., Durham, NC, USA [14]. The starting substrate consists of a 10 µm layer of single-crystal silicon, attached to a 400 µm-thick handle wafer by an oxide layer of thickness 1 µm. Two methods are then used during the fabrication of the MEMS structure – patterning and etching of the silicon wafer from the top surface down to the

doi: 10.1049/mnl.2013.0677

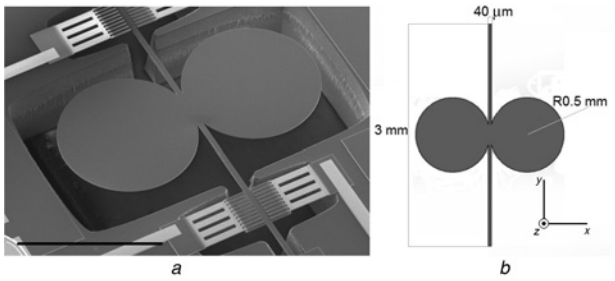

Figure 1 *Silicon MEMS structure*
a Scanning electron micrograph of the MEMS device (scale bar represents 1 mm)
b Dimensioned 3D CAD model of the device using SolidWorks

oxide layer, and patterning and etching through the bottom surface of the handle wafer substrate to the oxide layer.

2.1. Laser Doppler vibrometry (LDV): Modal analysis was carried out by observing the vibration of the structure with micro-scanning LDV, in response to various acoustic stimuli. LDV measures the structure's out-of-plane vibration velocity. The structure was located off-centre on a 11 mm × 11 mm die of thickness 400 µm fixed onto a 70 mm × 28 mm × 2.5 mm printed circuit board (PCB), with a centrally cut hole in the PCB exposing the bottom face of the structure. This enabled access to both sides of the mounted structure. The orientation of the structure was with the *xz* plane parallel to the floor and the *y*-axis perpendicular to the floor, according to Fig. 1*b*.

The scanning laser vibrometer (Polytec PSV-300-F; Waldbronn, Germany) has an OFV-056 scanning head and close-up attachment fitted yielding a positioning accuracy of 1 µm and spot diameter 5 µm. The vibrating surface of the structure was measured in steps of 50 µm. Acoustic frequency signals were generated [Agilent 33220A; Santa Clara, USA)], amplified (Sony TA-FE570; Tokyo, Japan) and passed to a loudspeaker (ESS Heil Air Motion Transformer; South El Monte, USA), positioned 500 mm from the structure. A precision pressure microphone (Brüel & Kjær 4138; Nærum, Denmark) connected to a pre-amplifier (Brüel & Kjær Nexus 2690; Nærum, Denmark) measured the sound pressure approximately 10 mm from the structure and was used to provide a reference signal for the vibrometer. Initially the acoustic signal generated consisted of wideband chirps of frequency range 1–25 kHz, to determine the frequency response of the structure. Modes identified during this process were subsequently investigated with single frequency pure tones to excite the mode and record an accurate mode shape.

Directional analysis involved the measurement of the velocity of the outer edge of each disc in response to a 1.2 kHz pure tone sound stimulus. The frequency was selected based on the modal analysis results, such that while it is relatively close to mode resonance frequencies, it is not a frequency corresponding to a specific mode (see Section 3). The position angle, θ, defined in the *xz* plane, is the angle between the loudspeaker and the *z*-axis. This angle was varied from −90° (closest to the right disc) through 0° (normal to the structure) to +90°, in 5° steps. Post-processing of this data using the fast Fourier transform with a rectangular window allowed computation of the transfer function of the structure velocity to sound pressure level (Pa). From this the amplitude gain in m/s/Pa was calculated (ratio of structure velocity to sound pressure). At each θ, the amplitude gain of the edge of the right-hand and left-hand discs was measured. The directional intensity gain was then defined as the ratio of these two amplitude gains.

2.2. Finite element modelling: COMSOL multiphysics was used to simulate the response of the MEMS structure. Modal analysis was implemented through eigenfrequency studies of a 3D finite element model (FEM) of the structure. This computes the undamped, unforced modes of vibration of the MEMS structure. The geometry was built within COMSOL's environment and two executions were run using different material model types. The first assumes purely isotropic silicon of density 2330 kg/m^3, Young's modulus 131 GPa and a Poisson's ratio of 0.27. In the second execution anisotropic single-crystal silicon was used allowing for the directional variation in the Young's modulus. The first six eigenmodes of each of these models were computed.

For computational directionality analysis, the structure, including the surrounding die, was modelled, with the hole behind the structure and a surrounding air domain incorporated. The material model type was the anisotropic silicon complete with crystal rotation, that is, the second setup mentioned previously. By coupling both the fields of acoustics and structural mechanics, an acoustic–structure interaction computes the two-way interaction between the mechanical response of a structure and an incident pressure wave in the surrounding fluid domain. An incident plane wave pressure field of amplitude 0.06 Pa (~70 dB sound pressure level re 20 µPa) was used in the model and, to match the experimental studies, an operating frequency of 1.2 kHz was chosen. By parameterising the defining angles of the load pressure wave, a double parametric sweep was executed allowing efficient calculation of the response of the structure at each angle, θ, required. Importantly, the geometric nonlinearity feature was enabled as a study setting because of the nature of the suspension beam in the structure.

Post-processing within COMSOL allowed the extraction of displacements and velocities (and other characteristics) at user-defined points on the structure such that the directional intensity gain, as defined in the laser vibrometry section 2.1 above, could be calculated for each angle of sound source, θ.

3. Results

3.1. Modal frequency analysis – measured against simulated: Fig. 2 shows the shape of the four out-of-plane modes of vibration found between 1 and 21 kHz using both finite element modelling (left) and laser vibrometry (right). Complementing this Figure is Table 1, collating the detected modes of vibration in both the experiment and the simulation. Analysis of the laser vibrometry data shows that the first mode of vibration is found at around 1.40 kHz. This mode can be described as a rotational mode with the suspension beam as the axis of rotation, that is, both discs moving 180° out of phase of each other, resulting in a so-called rocking mode. Executing an eigenfrequency study of the FEM of the structure, treating the silicon simply as an isotropic material, yields the rocking mode at 1.44 kHz (Table 1).

Eigenmode analysis of a FEM with a material model that includes the anisotropy of silicon yielded the first mode as the rocking mode at a frequency of 1.45 kHz.

Experimentally, the structure had a translational mode at 2.20 kHz and at this mode of vibration the structure appears to be more sensitive than at the lower frequency rocking mode (see the difference in the range of gain in Figs. 2*b* and *d*). This piston mode is found to have a frequency of 1.62 and 1.83 kHz for the isotropic model and the anisotropic model, respectively.

The correlation between the vibrometry results and the FEM results appears to be extremely strong for the model with anisotropic

Table 1 Modal frequencies of the structure calculated using vibrometry and finite element modelling

Mode		Modal frequency, kHz					
		First	Second	Third	Fourth	Fifth	Sixth
LDV experiment		1.40	2.20	7.39	NA	NA	20.51
FEM	Iso Si model	1.44	1.62	5.82	6.64	9.91	18.41
	Aniso Si model	1.45	1.83	6.56	7.50	11.16	20.64

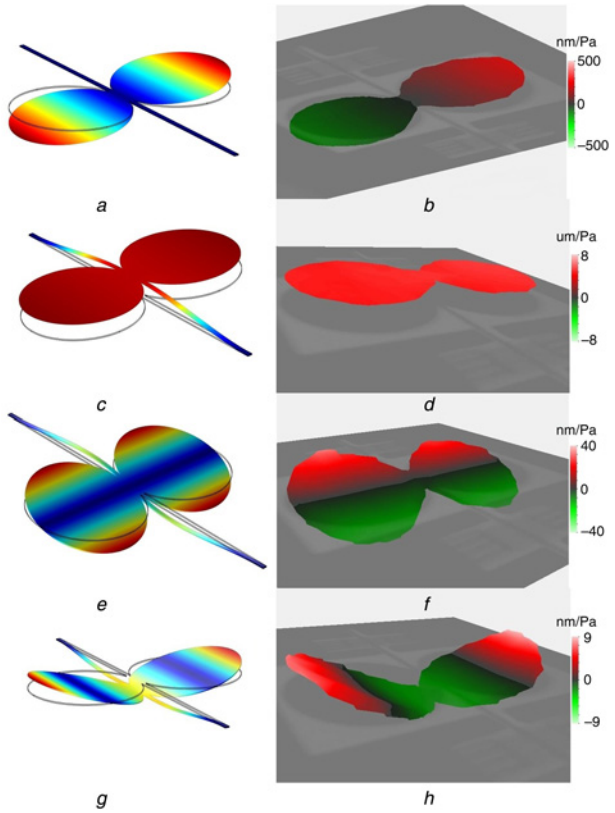

Figure 2 *First four out-of-plane mode shapes of the device*
a FEM simulated first (rocking) mode
b LDV measured first mode
c Second (translational) mode through FEM simulation
d Second mode as observed using LDV
e FEM computed third mode
f LDV measured third mode
g Fourth (flapping) mode as computed by FEM
h Fourth mode captured using LDV

Si combined with a rotation of the geometry within the workspace. Table 1 shows that this correlation continues across all four out-of-plane modes found during modal analysis using LDV, that is, rows 1 and 3 correlate well.

The third mode of vibration of the structure, described as a rotational mode with the axis of rotation through the centre of the two circular discs, is found to have a frequency of 7.39 kHz (LDV) and 6.56 kHz (FEM). Likewise, for the sixth mode, described as a flapping mode (see Figs. 2*g* and *h*), vibrometry shows it to have a frequency of 20.51 kHz and the model predicts a frequency of 20.64 kHz.

Modes four and five are in-plane twisting and in-plane bending modes which are undetectable using LDV in this way, since

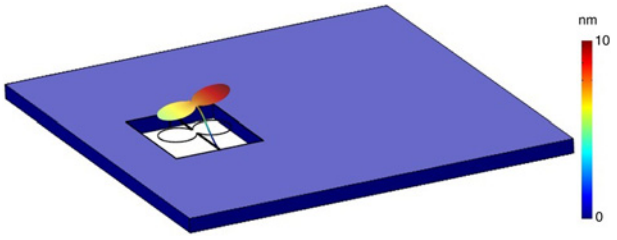

Figure 3 *Finite element analysis of the device using COMSOL's acoustic–structure interaction*
Incident sound is a plane wave of frequency 1.2 kHz, sound level of 0.06 Pa at an angle 20° to the normal from left to right
Instantaneous displacement of the device ranges from 5 to 10 nm at this moment in the cycle, whereas the die remains stationary in comparison

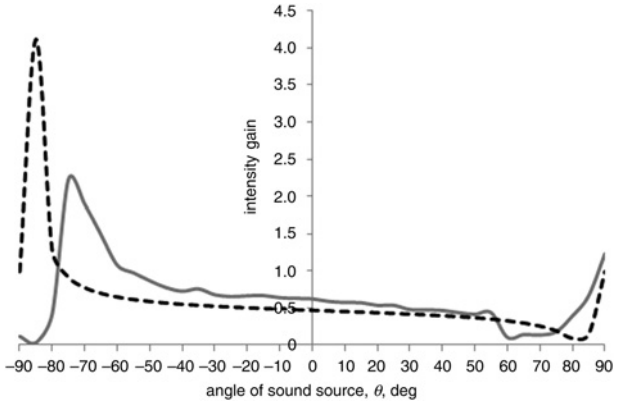

Figure 4 *Directional intensity gain (solid grey line) against sound source angle, θ, calculated from LDV data*
Broken black line is directional intensity gain against sound source angle, θ, computed using COMSOL Multiphysics
From approximately −75° to +60°, there is a one-to-one relationship between the relative vibration amplitudes of each disc and the angle of incidence

when vibrating in these modes the structure has no out-of-plane velocity component.

3.2. Directionality analysis: Laser vibrometry was also used to analyse the directionality of the structure as described in Section 2. Plotting the intensity gain calculated from vibrometer data against the angle of sound source, θ, results in the solid grey line shown in Fig. 4.

This experiment is repeated computationally as an acoustic–structure interaction in the frequency domain with COMSOL, as outlined in Section 2, using nested parametric sweeps to simulate all the same sound source angles (θ) used in the vibrometry measurements. Fig. 3, in which the vertical scale is multiplied by a factor of 1.5×10^5, shows a snapshot of the dynamic cycle of the simulated structure and die in response to a pure tone sound stimulus of 1.2 kHz, at a sound level of 0.06 Pa, at $\theta = +20°$. The deflection of the structure clearly displays a combination of both the rocking and translational modes, with a maximum displacement of 10 nm at the instant the snapshot was taken.

The broken black line in Fig. 4 represents the data from this FEM simulation, and displays a similar relationship to that observed from the LDV results. Both results display similar distinctive characteristics in that the intensity gain, or intensity ratio of the right disc to left disc, reaches a maximum at a large negative sound source angle θ, −85° for the model where the gain is 4, and −70° in LDV where the gain is between 2 and 2.5. Similarly the gain converges to a minimum of 0.1 at a high positive stimulus angle θ, 80° and 60° from FEM and LDV, respectively. Both the vibrometry and the modelling results display a gain of about 0.5 when the sound source is at $\theta = 0°$, or normal to the structure. A possible explanation for the relative difference in the position of maxima and minima between the experimental and simulated results is that while the simulation assumes a free-field, in the experiment various apparatus surrounds the device, for example, the laser vibrometer and fixtures for mounting the device.

4. Conclusion: A single-crystal silicon MEMS structure, consisting of two circular discs connected to a centrally supporting beam, has been fabricated using commercially available SOIMUMPs. Using both LDV and FEM to investigate the natural modes of vibration of the structure has resulted in observation of the same first four out-of-plane mode shapes. There is also close correlation between measured frequencies through both methods, particularly when correctly allowing for the anisotropy of single-crystal silicon. This is without consideration of damping characteristics. However, because the

doi: 10.1049/mnl.2013.0677

removal of a section of the PCB fully exposed the posterior surface of the structure, then a major contribution to damping in many MEMS structures of this style – squeeze-film damping – is eliminated.

When stimulated at an appropriate frequency, the structure appears to exhibit an interaction between two, spectrally close, modes called rocking and translational, which combine in differing proportions dependent on the angle of the sound source. The outcome of this effect is a predictable and repeatable relationship between the directional intensity gain and the angle of source. Both FEM simulations and LDV experimentation confirm this relationship. Therefore the structure is capable of performing as a directional microphone because of the coupling of two natural modes of vibration whose resonance frequencies are close.

The extent of how successfully this structure performs in terms of mechanical directionality may well be limited by the relative sensitivity of the structure to both the translational mode and rocking mode, that is, the translational mode somewhat dilutes the influence of the rocking mode, resulting in a sub-optimal mechanical directionality performance.

The simple MEMS structure presented here, while resembling biologically inspired microphones, was not optimised. However, it exhibits acoustic directionality, indicating that a variety of simple MEMS devices could have acoustic directionality not apparent during design or experimental characterisation, thus demonstrating the potential for such micromechanical devices to be utilised as directional microphones.

5. Acknowledgments: This work was supported by the Biotechnology and Biological Sciences Research Council, UK (grant BB/H004637/1), and the Engineering and Physical Sciences Research Council, UK (EP/H02848X/1).

6 References

[1] Miles R.N., Hoy R.R.: 'The development of a biologically inspired directional microphone for hearing aids', *Audiol. Neurootol.*, 2006, **11**, (2), pp. 86–94

[2] Wang W.J., Lin R.M., Zou Q.B., Li X.X.: 'Modeling and characterization of a silicon condenser microphone', *J. Micromech. Microeng.*, 2004, **14**, pp. 403–409

[3] Scheeper P.R., van der Donk A.G.H., Olthuis W., Bergveld P.: 'A review of silicon microphones', *Sens. Actuators A, Phys.*, 1994, **44**, (1), pp. 1–11

[4] Ricketts T.A.: 'Impact of noise source configuration on directional hearing aid benefit and performance', *Ear Hear*, 2000, **21**, (3), pp. 194–205

[5] Gnewikow D., Ricketts T., Bratt G.W., Mutchler L.C.: 'Real-world benefit from directional microphone hearing aids', *J. Rehab. Res. Dev.*, 2009, **46**, (5), pp. 603–618

[6] Blumstein D.T., Mennill D.J., Clemins P., *ET AL.*: 'Acoustic monitoring in terrestrial environments using microphone arrays: applications, technological considerations and prospectus', *J. Appl. Ecol.*, 2011, **48**, (3), pp. 758–767

[7] Yoo K., Gibbons C., Su Q.T., Miles R.N., Tien N.C.: 'Fabrication of biomimetic 3D structured diaphragms', *Sens. Actuators A, Phys.*, 2002, **97–98**, pp. 448–456

[8] Liu H.J., Yu M., Zhang X.M.: 'Biomimetic optical directional microphone with structurally coupled diaphragms', *Appl. Phys. Lett.*, 2008, **93**, (24), p. 243902

[9] Touse M., Sinibaldi J., Simsek K., Catterlin J., Harrison S., Karunasiri G.: 'Fabrication of a microelectromechanical directional sound sensor with electronic readout using comb fingers', *Appl. Phys. Lett.*, 2010, **96**, (17), p. 173701

[10] Lisiewski A.P., Liu H.J., Yu M., Currano L., Gee D.: 'Fly-ear inspired micro-sensor for sound source localization in two dimensions', *J. Acoust. Soc. Am.*, 2011, **129**, (5), p. EL166–71

[11] Chen C., Cheng Y.: 'Physical analysis of a biomimetic microphone with a central-supported (C-S) circular diaphragm for sound source localization', *IEEE Sens. J.,* 2012, **12**, (5), pp. 1504–1512

[12] Miles R.N., Robert D., Hoy R.R.: 'Mechanically coupled ears for directional hearing in the parasitoid fly *Ormia ochracea*', *J. Acoust. Soc. Am.*, 1995, **98**, (6), pp. 3059–70

[13] Robert D., Miles R.N., Hoy R.R.: 'Tympanal mechanics in the parasitoid fly *Ormia ochracea* : intertympanal coupling during mechanical vibration', *J. Compar. Physiol. A, Sens. Neural Behav. Physiol.*, 1998, **183**, (4), pp. 443–452

[14] Cowen A., Hames G., Monk D., Wilcenski S., Hardy B.: 'SOIMUMPs design handbook' (2011, 8th edn), http://www.memscap.com/products/mumps/soimumps/reference-material.htm, accessed 5 November 2013

OPEN ACCESS Freely available online

PLoS one

So Small, So Loud: Extremely High Sound Pressure Level from a Pygmy Aquatic Insect (Corixidae, Micronectinae)

Jérôme Sueur[1]*, David Mackie[2], James F. C. Windmill[2]

1 Muséum national d'Histoire naturelle, Département Systématique et Evolution, UMR 7205 CNRS Origine Structure et Evolution de la Biodiversité, Paris, France, **2** Department of Electronic and Electrical Engineering, Centre for Ultrasonic Engineering, University of Strathclyde, Glasgow, United Kingdom

Abstract

To communicate at long range, animals have to produce intense but intelligible signals. This task might be difficult to achieve due to mechanical constraints, in particular relating to body size. Whilst the acoustic behaviour of large marine and terrestrial animals has been thoroughly studied, very little is known about the sound produced by small arthropods living in freshwater habitats. Here we analyse for the first time the calling song produced by the male of a small insect, the water boatman *Micronecta scholtzi*. The song is made of three distinct parts differing in their temporal and amplitude parameters, but not in their frequency content. Sound is produced at 78.9 (63.6–82.2) SPL rms *re* 2.10^{-5} Pa with a peak at 99.2 (85.7–104.6) SPL *re* 2.10^{-5} Pa estimated at a distance of one metre. This energy output is significant considering the small size of the insect. When scaled to body length and compared to 227 other acoustic species, the acoustic energy produced by *M. scholtzi* appears as an extreme value, outperforming marine and terrestrial mammal vocalisations. Such an extreme display may be interpreted as an exaggerated secondary sexual trait resulting from a runaway sexual selection without predation pressure.

Citation: Sueur J, Mackie D, Windmill JFC (2011) So Small, So Loud: Extremely High Sound Pressure Level from a Pygmy Aquatic Insect (Corixidae, Micronectinae). PLoS ONE 6(6): e21089. doi:10.1371/journal.pone.0021089

Editor: Daphne Soares, University of Maryland, United States of America

Received December 2, 2010; **Accepted** May 19, 2011; **Published** June 15, 2011

Funding: This work was supported by a Royal Society (London) International Joint Project grant (JP080761). The funders had no role in study design, data collection and analysis, decision to publish, or preparation of the manuscript.

Competing Interests: The authors have declared that no competing interests exist.

* E-mail: sueur@mnhn.fr

Introduction

Animal communication is driven by competition between individuals and species [1–3]. The signal produced by an emitter should reach as many receivers as possible, whilst transmitting as much information as possible. To increase the range of their broadcast, animals can optimize the ratio of their signal to the background noise. One of the simplest strategies to achieve this is to produce a signal with a high amplitude that can override congener or other species songs, travelling the greatest distance across the habitat [4]. When considering acoustic communication, the production of a loud, and intelligible, signal is not an easy task even for human-built sound systems [5]. The system can be over-driven, distorting time and frequency parameters, and consequently impairing information transfer. In addition, animals are severely constrained by their morphological characteristics. Body size is one of the main mechanical constraints as a small sound source cannot produce a high level sound output [6,7]. This phenomenon explains why large mammals, such as whales or elephants, are known to be the loudest animals [8,9]. However, when these animals are scaled to their body size they may not produce the most efficient acoustic signals in terms of energy.

Acoustic communication is intensively studied in terrestrial and marine animals, but is neglected in freshwater species even when low visibility should favour acoustics as a way to exchange information. There are potentially an important number of aquatic insects that can sing underwater, but very few descriptions of their behaviour have been reported [10–16]. Water-boatman species belonging to the genus *Micronecta* (Corixidae, Micronectinae) are known to use sound for pair formation [14,15]. Only males produce species-specific sounds that attract females for mating [16–18]. Males can synchronize their calls generating a chorus [19]. This suggests a possible second role of male-male competition as observed in several other insects using sound to court females [2]. Here we report for the first time the acoustic behaviour of *Micronecta scholtzi* (Fieber, 1860), a common aquatic bug that produces an extremely loud courtship song. This insect is a few millimetres in length yet can produce sound audible from the riverside. This suggests the emission of intense signals departing from the body size to amplitude rule.

Materials and Methods

Specimens of *M. scholtzi* were collected in a river in Paris (France, 48°49.42′N–02°25.93′E) and in a pond in Morsang-sur-Orge (France, 48°40.03′N–02°20.59′E) from August to September 2009 and 2010. According to the national guidelines, no permission was required from authorities to collect specimens. Specimens were maintained in plastic water tanks (22*11*17 cm). Sex determination was not possible without manipulating individuals. As *M. scholtzi* is active only in groups, samples of five unsexed individuals were transferred to a fish net breeder (16.5*12.2*13 cm) which was positioned at the centre of a large plastic water tank (46*30*17 cm) with a water depth of 8 cm. The bottom of the tank was covered with gravel without any plants. This recording area provided a short distance between the insects and the hydrophone, and a relatively large distance between the hydrophone and the tank walls. This minimized sound wave

reflections that could have impaired recording quality. A Reson TC4033 passive hydrophone was placed at the bottom of the net breeder, in the centre. The hydrophone was connected to an Avisoft charge amplifier with an input capacitance of 1 nF and a 250 Hz high-pass input filter. Recordings were taken with a Marantz PMD 671 digital recorder at 48 kHz sampling frequency and 16 bit level digitization. All recordings were made at a water temperature of 23–24°C controlled with a Tetratex HT50 heater.

As *Micronecta* females do not produce sound [15], all sound recorded was considered as being produced by males. The calling songs of 13 males were recorded and 60 seconds of signal without background were selected for each male. Even if *M. scholtzi* call in chorus there is no fine synchronization of their signals. It was then possible to select a signal produced by a single animal excluding the risk of analysing several males together. Calling song parameters were analysed using *Avisoft SAS Lab Pro* [20] and *seewave* [21]. Temporal parameters were measured on the amplitude envelope. Frequency parameters were measured on the mean spectrum of a short-term Fourier transform with a frequency resolution of 43 Hz.

In order to produce an accurate measure of the sound-pressure-level (SPL), the recording equipment (hydrophone+charge amplifier+digital recorder) was calibrated in reference to a sound source emitting a signal at a known SPL. This was achieved by using one passive hydrophone (Reson TC4013) as an emitter and a second passive hydrophone as a receiver (Reson TC4033). This receiver hydrophone was connected to an Avisoft charge amplifier with an input capacitance set to 1 nF and a 250 Hz high-pass input filter, which in turn was connected to a Marantz PMD 671 digital recorder. The recording chain was therefore exactly the same as the one used to record the animals. The emitter output was a 10 kHz sine wave that was repeated for different acoustic amplitudes and for different Marantz PMD 671 manual recording input levels. Peak and root-mean-square (rms) of the digital values of the amplitude envelope were then calculated for each *M. scholtzi* recording selection. Average values were computed on this raw data before being converted to dB SPL in reference to 2.10^{-5} Pa to allow comparison with terrestrial animals (see below). As the distance between the animal and the hydrophone was not known, three estimations were assessed assuming the distance was minimal (0.05 cm), median (6.5 cm) or maximal (13 cm). Male body length was measured after recordings using the graticule of a binocular microscope Leica M205C with a precision of ±0.05 mm.

SPL values of *M. scholtzi* were compared with the values reported for 227 other species (2 reptiles, 3 fishes, 24 mammals, 29 birds, 46 amphibians and 123 arthropods) collected from the literature (Table S1). This includes 17 species (7.5% of 227) for which SPL values were estimated underwater. Two of this latter group were arthropods, namely the Crustaceans *Panulirus interruptus* and *Synalpheus parneomeris* (0.9% of 227). Only communication signals were considered, echolocation or debilitating sound was excluded. Different SPL values could be found for a single species. These values may come from different references or from variability across populations, sexes and signal types within a repertoire. The highest dB SPL value was selected in all cases. Peak measurements were converted into rms measurements by dividing them by $\sqrt{2}$ [22]. The SPL values found in the literature are all given in dB. However, they refer to measurements done at a different distance d and/or in reference to a different reference pressure P_0. To allow comparison across taxa, all data were first converted to sound pressure (Pa). Sound pressure data were then converted back to dB SPL with a reference pressure $P_0 = 2.10^{-5}$ Pa. Data were eventually converted to SPL data at a distance of 1 m by applying the attenuation inverse square law following the equation [23]:

$dB_{SPL@1m} = Y - 20 \times \log_{10}(1/d)$, where Y is the initial dB SPL value measured at a distance d.

Body length estimation was also documented for all species. As dB is a logarithmic scale, and as sound pressure scales with body mass rather than body length [5], the link between dB SPL and animal size was estimated between dB and the logarithm of body length cubed (*i.e.* $3 \times \log_{10}$(body length)). This was achieved for two sub-samples corresponding to the main characteristics of *M. scholtzi* acoustic communication system. The first sub-sample included all stridulating animals (57 arthropods and one fish). The second sub-sample included all underwater animals (three arthropods, three fish and 11 mammals). Because of the presence of outliers in the sample, both ordinary least squared (OLS) and robust regressions were computed [24,25]. All statistics were run using *R* with the additional package *robust* [26].

Results

The size of the *M. scholtzi* male was 2.3±0.1 mm (mean ± s.d., $n = 21$) (Fig. 1). The song consisted of a typical sequence repeated at a rate of 0.746±0.129 Hz ($n = 582$). Each sequence was composed of three parts differing in their temporal and amplitude parameters (Fig. 1). The first part was a repetition of 5.1±1.4 ($n = 582$) quiet echemes that lasted 84±19 ms ($n = 2994$) and were followed by a silence of 192± c cvv48 ms ($n = 2994$). The second part was a succession of 1.6±0.7 ($n = 582$) short and quiet echemes that lasted 16±3 ms ($n = 820$) followed by a silence of 101±21 ms ($n = 820$). The third part was a single loud echeme of a duration of 60±8 ms ($n = 582$). The frequency spectrum extended from 5 to 22 kHz with 50% of the signal energy between 9 to 11 kHz with a dominant frequency at around 10 kHz (1st part: 10.063± 1.122 kHz ($n = 2994$); 2nd part: 10.348±0.872 kHz ($n = 820$); 3rd part: 10.109±0.886 kHz ($n = 582$)). There was no frequency modulation along the signal, the frequency content of the different parts being similar.

The minimal, median and maximal amplitude level of the song were respectively estimated to be 36.7 (21.5–39.9) (mean (min – max)), 78.9 (63.6–82.2) and 85.0 (69.6–88.2) dB SPL rms *re* 2.10^{-5} Pa at 1 meter. Peak values were estimated to be 57.1 (43.6–88.2), 99.2 (85.7–104.6) and 105.2 (91.7–110.6) dB SPL rms *re* 2.10^{-5} Pa at 1 metre.

The average of the ratio dB/($3 \times \log_{10}$(body length)) for all animals documented was 6.9±3.0 ($n = 228$). A maximum value of 31.5 was estimated for *M. scholtzi*. Within the group of 58 stridulating animals, the OLS regression against dB and $3 \times \log_{10}$ (body length) indicated the following three species as outliers: (i) *M. scholtzi*, (ii) the miniature cricket *Cycloptiloides canariensis*, and (iii) the praying mantis *Mantis religiosa* (Fig. 2, $F_{1,56} = 7.44$, $R^2 = 0.10$, $p = 0.009$). *M. scholtzi* was isolated due to its high SPL and small size, while *C. canariensis* was isolated by its small size and low SPL, and *M. religiosa* by a particularly low SPL compared to its large size. Cook's distance associated with species leverage on the OLS model clearly identified *M. scholtzi* as the most extreme outlier (Figs. S1, S2). A robust regression, which is less sensitive to outliers, returns a regression line with a higher regression coefficient (Fig. 2, $F_{1,56} = 6.23$, $R^2 = 0.33$, $p = 0.011$).

Within the group of animals using sound underwater, the OLS regression had a p-value just above a 5% α risk (Fig. 3, $F_{1,15} = 3.60$, $R^2 = 0.14$, $p = 0.077$). The OLS regression indicated the following four species as outliers: (i) the snapping shrimp *Synalpheus parneomeris*, (ii) the weakfish *Cynoscion regalis*, (iii) the

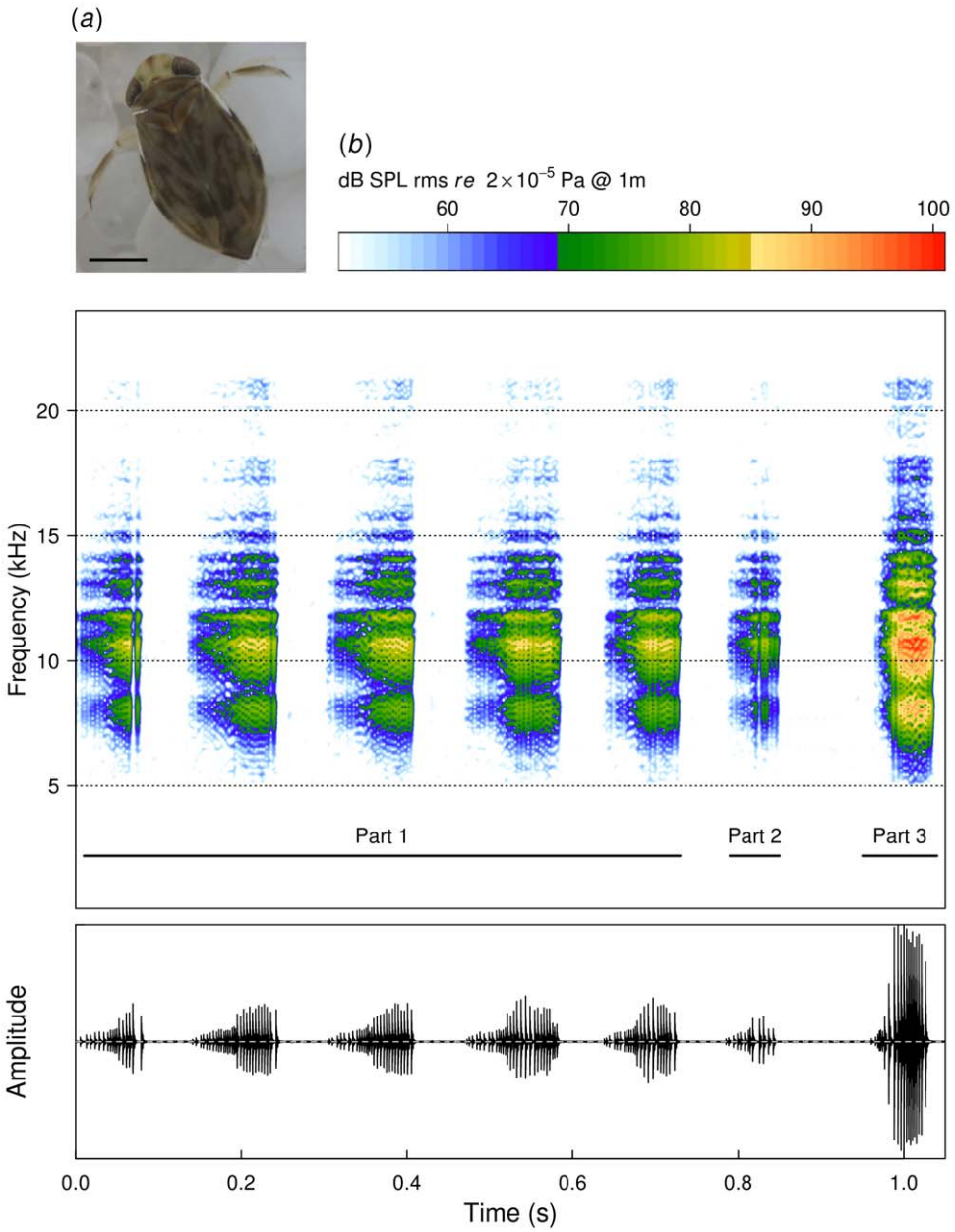

Figure 1. Habitus and calling song of *M. scholtzi*. (*a*) dorsal view of an adult (scale bar = 0.5 mm), (*b*) calling song consisting of three main parts differing in their temporal and amplitude parameters (oscillogram), but having a similar frequency structure (spectrogram and amplitude scale with an estimated maximum value of 101 dB SPL rms *re* 2.10^{-5} Pa at 1 meter).
doi:10.1371/journal.pone.0021089.g001

common bottlenose dolphin *Tursiops truncatus*, and (iv) *M. scholtzi*. *S. parneomeris* was isolated by its small size and high SPL, *C. regalis* by its medium size and low SPL, *T. truncatus* by its high SPL, and *M. scholtzi* by its very small size (Figs. S3, S4). A robust regression was significant and returned a regression line with a higher regression coefficient (Fig. 3, $F_{1,15} = 5.52$, $R^2 = 0.33$, $p = 0.017$).

Discussion

The water boatman *M. scholtzi* produces a complex calling song comprising three distinct parts with deep amplitude modulations, but no frequency modulation. However, the most striking feature of the song is its intensity. The song can be heard by a human ear from the side of a pond or river, propagating across the water-air interface. Estimating the sound intensity at a distance of one metre reveals a value of ~79 dB SPL rms. When considering peak values, *i.e.* the loudest part of signal, the intensity can reach 100 dB SPL. Whilst these values are far below those estimated for large mammals such as dolphins, whales, elephants, hippos, or bison, when scaled to body size, *M. scholtzi* has the highest ratio dB/body size. Even if such comparison might need to be adjusted with corrections taking into account different recording methods and conditions, *M. scholtzi* is clearly an extreme outlier with a dB/body size ratio of 31.5 while the mean is at 6.9 and the second highest value is estimated at 19.63 for the snapping shrimp *S. parneomeris*. This water bug might be the exception that proves the rule that stipulates that the size and the intensity of a source are positively related. This departure from the rule is apparent within the group

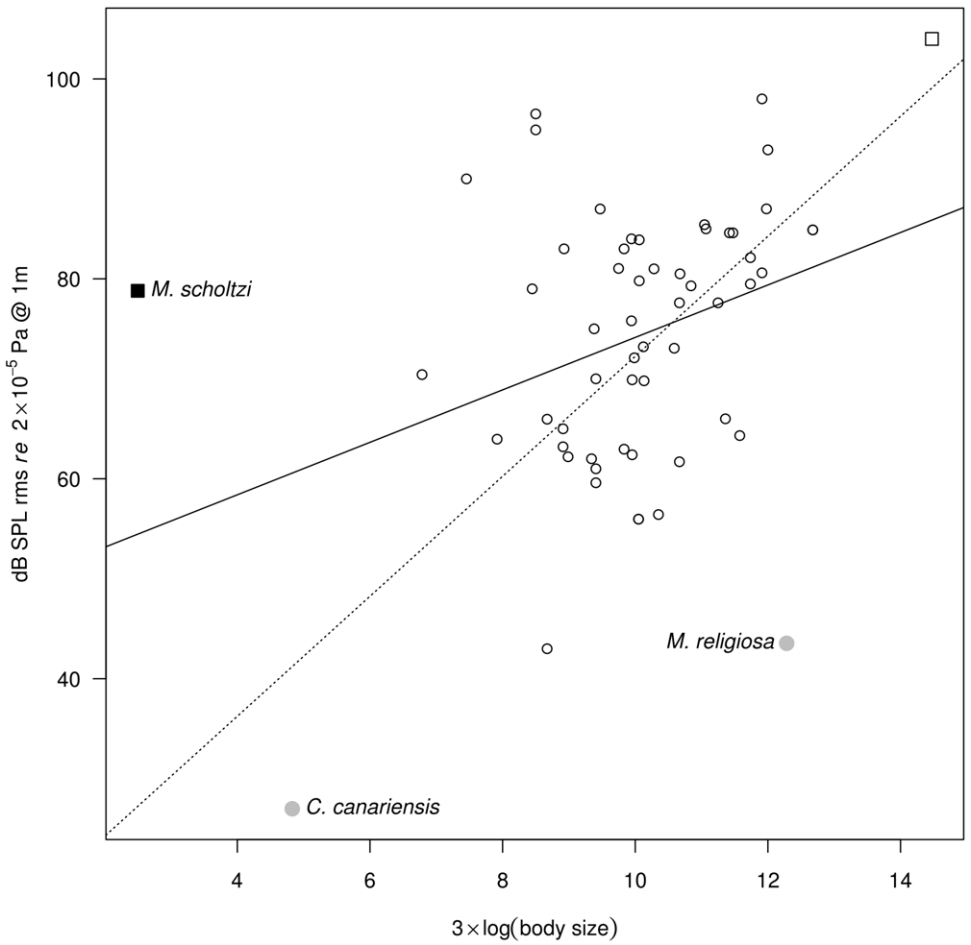

Figure 2. Regression between body size and SPL for stridulating animals. Terrestrial species are indicated with a circle and underwater species with a square. The species labelled with a plain symbol are identified as outliers following Cook's distance and leverage (electronic supplementary material, figures S1, S2). Regression lines: ordinary least squared regression (plain) and robust regression (dashed). Sample size: 57 arthropods and one fish.
doi:10.1371/journal.pone.0021089.g002

of stridulating animals. In this sub-sample, *M. scholtzi* is identified as an extreme outlier. No other recorded animals rival *M. scholtzi*. Two other arthropods were also identified as outliers; the Australian miniature cricket *C. canariensis* [27] and the Praying Mantis *M. religiosa* [28]. In both cases these are outliers for different reasons, as the Praying Mantis emits a much quieter song (~43 dB) than suggested by its size (~60 mm), and the miniature cricket is particularly small (~3 mm) and quiet (~30 dB). When considering aquatic animals, whatever the mode of sound production they use (*i.e.* drumming, friction, stridulation or vocalisation), *M. scholtzi* appears as an outlier mainly due to its very small size compared to fish, mammals or even crustacean species communicating underwater. Producing loud sound underwater is easier than in the air due to impedance-matching between the source, here the body part of the animal that generates vibrations, and the transmission media (water) [23]. This might explain why *M. scholtzi* appears as the most extreme outlier when compared to stridulating species that are terrestrial (except one fish), and is identified as only the fourth outlier when considering underwater species. Oxygen uptake of *Micronecta* has not been studied in detail but air is stored around their body by hydrofuge hairs. The ventral side is indeed covered with an air layer [29]. This suggests that the stridulating mechanism might be in contact with air but not water. This could induce a complex micro acoustic environment with reflections and refraction due to impedance differences between air and water.

The mechanism behind the intense sound production of *M. scholtzi* is not clearly identified. The sound is produced by rubbing a *pars stridens* on the right paramere (genitalia appendage) against a ridge on the left lobe of the eighth abdominal segment [15]. This sound emission system does not measure more than 50 μm in length, and there are no obvious body or external resonating systems that could amplify the sound, as observed in insects, amphibians, mammals and birds [30–35]. The high sound output (~124 dB) observed in *Panulirus* spiny lobsters has been explained by the use of stick-slip friction instead of a classical stridulation [36,37]. This mechanism might occur in *M. scholtzi*, but to observe the micro-mechanics of such a small system remains a significant challenge.

Could we try to interpret why *M. scholtzi*, and presumably other *Micronecta* species [17], produce such loud sounds? An increase of signal amplitude in reaction to a rise of the background noise, known as the Lombard effect, has been documented for various birds and mammals, including man [4]. However, this amplitude rise is only observed over the short-term. Here the high amplitude level is a long-term process that might result from intra-specific competition. *Micronecta* male stridulation has been proven to be a

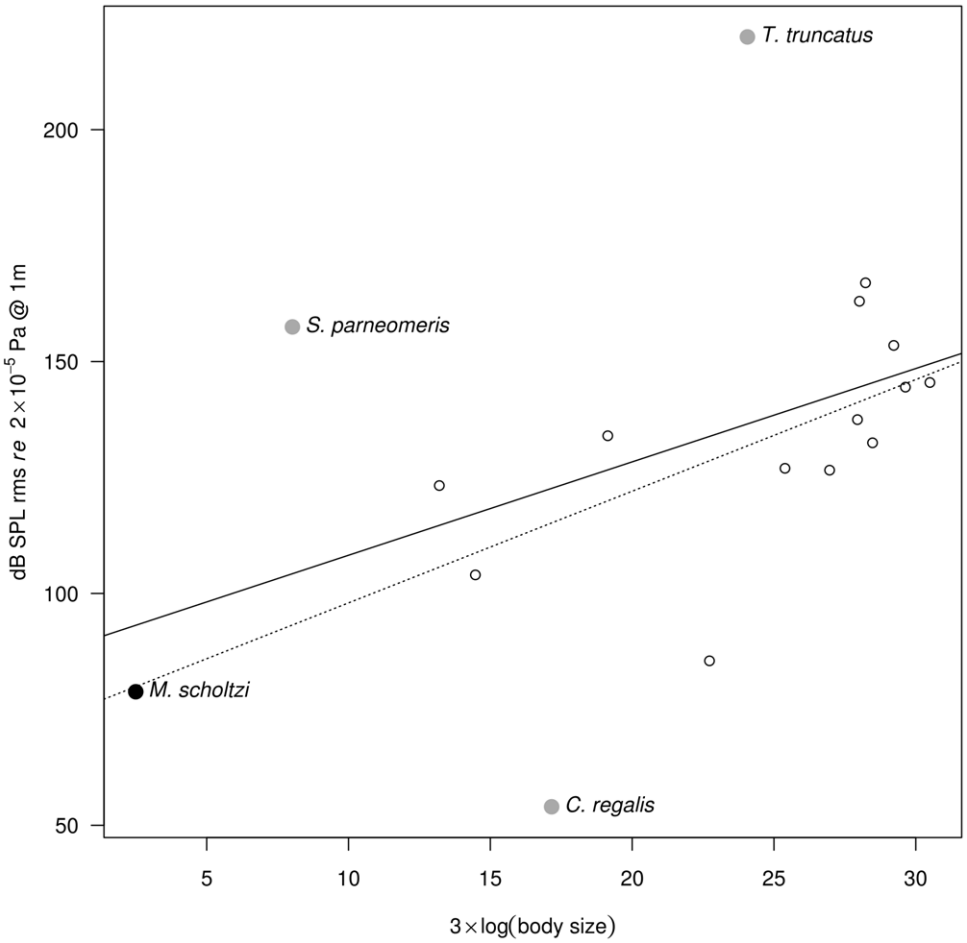

Figure 3. Regression between body size and SPL for underwater animals. The species labelled with a plain symbol are identified as outliers following Cook's distance and leverage (electronic supplementary material, figures S3, S4). Regression lines: ordinary least squared regression (plain) and robust regression (dashed). Sample size: three arthropods, three fish, 11 mammals.
doi:10.1371/journal.pone.0021089.g003

sexual signal addressed to the female, which can use the signal to select a conspecific male (species identification) [17] and to select a male among other conspecific males (sexual selection) [15]. The extreme SPL level of this signal could be compared to the extremely high complexity of some bird songs, particularly long mammal antlers, complex insect horns, or the brightly coloured integumentary system found in almost all animal groups. All of these exaggerated secondary sexual ornaments are thought to be a by-product of a runaway or Fisherian sexual selection [38,39], especially in the case of insect acoustic signals [40,41]. A signal produced at high amplitude can potentially override the signals emitted by competitors during chorusing bouts and hence facilitate male localisation by the choosing female [1–3,42]. Acoustic competition can then lead to loud signal levels. However, such a runaway process can be counterbalanced by natural selection if the extreme signal tends to have adverse effects. The extreme signal might be too costly in terms of energy or too risky in terms of predation. An obvious acoustic display could attract predators that localise their prey through audition [43,44]. Predators and parasitoids can strongly constrain song evolution and can even lead to a disappearance of the acoustic sexual signal [45]. Nothing is known about predation on *M. scholtzi*, but the extreme SPL value suggests the absence of such an evolutionary limiting factor. Male of *M. scholtzi* may have no auditory predator, or escape such a predator more efficiently than other acoustic species. The hypothesis of a runway selection being at the origin of *M. scholtzi* loudness still needs to be tested with observations on competition behaviour between males and with an estimation of the predator guild associated with males. Eventually, playback experiments based on the broadcast of pairs of similar signals with similar time and frequency pattern, but different SPL values, could test female preference for loud over soft calls.

Supporting Information

Figure S1 Cook's distance of each of the 58 stridulating animals (57 arthropods and one fish) included in an OLS model. Three species were identified by the model: the praying mantis *Mantis religiosa*, the miniature cricket *Cycloptiloides canariensis* and the water-boatman *Micronecta scholtzi*.
(TIFF)

Figure S2 Scatterplot of leverage and standardized residuals of the model. As in Fig. S1, the following three species are identified as outliers: the praying mantis *Mantis religiosa*, the miniature cricket *Cycloptiloides canariensis* and the water-boatman *Micronecta scholtzi*. *M. scholtzi* has the highest leverage.
(TIFF)

Figure S3 Cook's distance of each of the 17 animals calling underwater (freshwater or marine habitats)

included in an OLS model. Four species were identified by the model: the snapping shrimp *Synalpheus parneomeris*, the weakfish *Cynoscion regalis*, the common bottlenose dolphin *Tursiops truncatus* and the water-boatman *Micronecta scholtzi*.
(TIFF)

Figure S4 Scatterplot of leverage and standardized residuals of the model. As in Fig. S3, the following four species are identified as outliers: the snapping shrimp *Synalpheus parneomeris*, the weakfish *Cynoscion regalis*, the common bottlenose dolphin *Tursiops truncatus* and the water-boatman *Micronecta scholtzi*.
(TIFF)

Table S1 Species list and references used to assess sound pressure level (dB L) and body size relationship. Underwater recordings are denoted with an asterisk (*) before species name.
(PDF)

References

1. Bradbury JW, Vehrencamp SL (1998) Principles of animal communication. Sunderland: Sinauer Associates. 882 p.
2. Greenfield MD (2002) Signalers and receivers. Mechanisms and evolution of arthropod evolution. Oxford: Oxford University Press. 414 p.
3. Gerhardt HC, Huber F (2002) Acoustic communication in insects and anurans. Chicago: University of Chicago Press. 531 p.
4. Brumm H, Slabbekoorn H (2005) Acoustic communication in noise. Adv Stud Behav 35: 151–209.
5. Leach M (2003) Introduction to electroacoustics and audio amplifier design. DubuqueIA: Kendall/Hunt. 298 p.
6. Bennet-Clark HC (1998) Size and scale effects as constraints in insect sound communication. Phil Trans R Soc Lond 353: 407–419.
7. Fletcher NH (2004) A simple frequency-scaling rule for animal communication. J Acous Soc Am 115: 2334–2338.
8. Au WWL (1993) The sonar of dolphins. New York: Springer-Verlag. 292 p.
9. Poole JH (1999) Signals and assessment in African elephants: evidence from playback experiments. Anim Behav 58: 185–193.
10. Jansson A (1973) Stridulation and its significance in the genus *Cenocorixa* (Hemiptera, Corixidae). Behaviour 46: 1–36.
11. Aiken RB (1982) Sound production and mating in a waterboatman, *Palmacorixa nana* (Heteroptera: Corixidae). Anim Behav 30: 54–61.
12. Prager J, Streng R (1982) The resonance properties of the physical gill of *Corixa punctata* and their significance in sound reception. J Comp Physiol A 148: 323–335.
13. Theiss J (1982) Generation and radiation of sound by stridulating water insects as exemplified by the Corixids. Behav Ecol Sociobiol 10: 225–235.
14. Aiken RB (1985) Sound production by aquatic insects. Biol Rev 65: 163–211.
15. Jansson A (1989) Stridulation of Micronectinae (Heteroptera, Corixidae). Ann Ent Fennici 55: 161–175.
16. King IM (1976) Underwater sound production in *Micronecta batilla* Hale (Heteroptera: Corixidae). J Aust Ent Soc 15: 33–43.
17. King IM (1999) Acoustic communication and mating behaviour in water bugs of the genus *Micronecta*. Bioacoustics 10: 115–130.
18. King IM (1999) Species-specific sounds in water bugs of the genus *Micronecta*. Part 1. Sound analysis. Bioacoustics 9: 297–323.
19. King IM (1999) Species-specific sounds in water bugs of the genus *Micronecta*. Part 2. Chorusing. Bioacoustics 10: 19–29.
20. Specht R (2004) Avisoft-SAS Lab Pro. Avisoft, Berlin.
21. Sueur J, Aubin T, Simonis C (2008) Seewave: a free modular tool for sound analysis and synthesis. Bioacoustics 18: 213–226.
22. Fletcher NH (1992) Acoustic systems in biology. Oxford: Oxford University Press. 333 p.
23. Hartmann WM (1998) Signals, sound, and sensation. New York: Springer. 647 p.
24. Yohai VJ (1987) High breakdown-point and high efficiency robust estimates for regression. Ann Stat 15: 642–656.
25. Renaud O, Victoria-Feser MP (2010) A robust coefficient of determination for regression. J Stat Plann Infer 140: 1852–1862.
26. R Development Core Team (2010) R: A Language and Environment for Statistical Computing. Vienna, Austria, http://www.R-project.org, last access 25/05/11.
27. Dambach M, Gras A (1995) Bioacoustics of a miniature cricket, *Cycloptiloides canariensis* (Orthoptera : Gryllidae : Mogoplistinae). J Exp Biol 198: 721–728.
28. Hill SA (2007) Sound generation in *Mantis religiosas* (Mantodea: Mantidae): stridulatory structures and acoustic signal. J Orthopt Res 16: 35–49.
29. Parsons MC (1976) Respiratory significance of the thoracic and abdominal morphology of three Corixidae, *Diaprepocoris*, *Micronecta*, and *Hesperocorixa* (Hemiptera: Heteroptera: Hydrocorisae). Psyche 83: 132–179.
30. Forrest TG (1991) Power output and efficiency of sound production by crickets. Behav Ecol 2: 327–338.
31. Bennet-Clark HC (1999) Resonators in insect sound production: how insects produce loud pure-tone songs. J Exp Biol 202: 3347–3357.
32. Duellman WE, Trueb L (1986) Biology of amphibians. BaltimoreMaryland: Johns Hopkins University Press. 670 p.
33. Lardner B, Lakim Bin M (2002) Tree-hole frogs exploit resonance effects. Nature 420: 475.
34. Suthers RA (2010) Sound Production: vertebrates. In: Breed MD, Moore J, eds. Encyclopedia of animal behavior. Oxford: Academic Press. pp 293–303.
35. Suthers RA, Roderick A (2009) Signal production and amplification in birds. In: Squire L, ed. The new encyclopedia of neuroscience, vol 8. Oxford: Academic Press. pp 815–825.
36. Patek SN (2001) Spiny lobsters stick and slip to make sound. Nature 411: 153–154.
37. Patek SN, Baio JE (2007) The acoustic mechanics of stick-slip friction in the California spiny lobster (*Panulirus interruptus*). J Exp Biol 210: 3538–3546.
38. Fisher RA (1930) The genetical theory of natural selection. Oxford: Oxford University Press. 272 p.
39. Andersson M (1994) Sexual selection. Princeton: Princeton University Press. 624 p.
40. Alexander RD, Marshall DC, Cooley JR (1997) Evolutionary perspectives on insect mating. In: Choe JC, Crespi BJ, eds. The evolution of mating systems in insects and arachnids. Cambridge: Cambridge University Press. pp 4–31.
41. Ryan MJ, Kime N (2003) Selection on long distance acoustic signals. In: Simmons A, Fay R, Popper A, eds. Handbook of auditory research; acoustic communication. Berlin: Springer Verlag. pp 225–274.
42. Limousin D, Greenfield MD (2009) Evaluation of amplitude in male song: female waxmoths respond to fortissimo notes. J Exp Biol 212: 4091–4100.
43. Zuk M, Kolluru GR (1998) Exploitation of sexual signals by predators and parasitoids. Quart Rev Biol 73: 415–438.
44. Windmill JFC, Jackson JC, Tuck EJ, Robert D (2006) Keeping up with bats: dynamic auditory in a moth. Curr Biol 16: 2418–2423.
45. Zuk M, Rotenberry JT, Tinghitella RM (2006) Silent night: adaptive disappearance of a sexual signal in a parasitized population of field crickets. Biol Lett 2: 521–524.

Acknowledgments

We thank Fernand Deroussen for his advice regarding collecting localities. We are indebted to Thierry Aubin, Rohini Balakrishnan, Renaud Boistel, Isabelle Charrier, Fernando Montealegre-Z, Eric Parmentier, Ryo Nakano, Allen F. Sanborn, and Takuma Takanashi for providing information regarding the SPL of other species. We are grateful to Joseph C. Jackson for his comments on the manuscript. We thank two anonymous referees for their helpful comments on the manuscript.

Author Contributions

Conceived and designed the experiments: JS JFCW. Performed the experiments: JS JFCW. Analyzed the data: JS DM JFCW. Contributed reagents/materials/analysis tools: JS DM JFCW. Wrote the paper: JS JFCW.